Response of the Brahmaputra River to Tectonic Deformation and Paleohydrological

Events in the Foreland Bengal Basin

By

Jennifer Lynne Pickering

Dissertation

Submitted to the Faculty of the

Graduate School of Vanderbilt University

in partial fulfillment of the requirements

for the degree of

DOCTOR OF PHILOSOPHY

in

Environmental Engineering

August, 2016

Nashville, Tennessee

Approved:

Steven L. Goodbred, Jr., Ph.D.

Janey Smith Camp, Ph.D.

James H. Clarke, Ph.D.

Jonathan Gilligan, Ph.D.

Jessica L. Oster, Ph.D.

আমার সোনার বাংলার জন্য

For my golden Bengal

ACKNOWLEDGMENTS

my giggle count up even in times of distress.

Finally, and perhaps most importantly, I am deeply indebted to my undergraduate advisor, Warner Cribb, and mentor, Beth Weinman, for getting me into Bengal, the land of superlatives, in the first place.

TABLE OF CONTENTS

LIST OF TABLES

LIST OF FIGURES

LIST OF ABBREVIATIONS

Acs	Amalgamated, Cross-stratified, Sand
Chl	chlorite
CMP	common midpoint
D50	median particle diameter
DEM	Digital Elevation Model
GLOF	glacial lake outburst flood
Gpsa	Graded, Poorly Sorted Alluvium
GSD	grain size distribution
Gt	goethite
HBM	Holocene Basinal Muds
HOM	Holocene Overbank Muds
Hs	Homogeneous Sand
Hssm	Heterolithic Sand, Silt, Mud
Ill	illite
IRSL	Infrared Stimulated Luminescence
K	kurtosis
Kln	kaolinite
MIS	Marine Isotope Stage
MODIS	Moderate Resolution Imaging Spectroradiometer
PBM	Pleistocene Basinal Muds
PBT	Pleistocene Bogra Terrace
PGM	Penultimate Glacial Maximum
PJT	Pleistocene Jamulpur Terrace
POM	Pleistocene Overbank Muds
PSR	Pleistocene Sherpur Remnant
Qtz	quartz
SEM	Scanning Electron Microscope
SG	average specific gravity
Sk	skewness
Sme	smectite
SNR	signal to noise ratio
SRTM	Shuttle Radar Topography Mission
TWT	two-way time
X	mean grain size
XRD	X-ray diffraction/diffractometer
XRF	X-ray fluorescence (spectrometer)
h	channel depth
Q_w	water discharge
v	mean flow velocity
w	channel width
σ	grain sorting (spread)
τ_c	critical shear stress
τ_*	Shields parameter

Chapter 1

Introduction

The Bengal basin is a remarkable landscape, fully deserving of its appellation "the Land of Superlatives" (Fig. 1.1). Having formed in response to the largest tectonic orogeny on modern Earth, the world's third largest river system has been infilling the Bengal basin since the early Miocene, constructing the world's largest delta. This tripartite river system carries an astonishing 1 billion tons of sediment (Milliman and Syvitski, 1992) from the Himalaya through the Bengal delta down into the Bay of Bengal, which is, naturally, the largest submarine fan in the world. The landscape itself supports a staggering number of inhabitants, nearly 300 million people across West Bengal and Assam, India and Bangladesh, an area of $\sim$315,000 km^2 that is one of the most densely populated regions on the planet.

Because of the extremity of geologic processes operating in the Bengal basin, it is an interesting location to target for studies of fluvio-tectonic or fluvio-climatic interaction. The tectonic deformation surrounding the basin is ongoing, so the response of rivers large and small to this deformation can be studied over timescales ranging from millions to thousands of years to decades. Additionally, the Bengal basin has been south of the maximum latitudinal extent of glacial coverage (roughly the 40th latitudinal parallel in the Pleistocene) throughout the Quaternary, so the sedimentary record is "complete" in the sense that the stratigraphy is the net result of only fluvial deposition and erosion, without episodic glacial erosion as in other systems.

This landscape of extremes is not an ideal place to study fluvial behaviors or relationships of scale if the intent is to apply what is learned to general fluvial theory. The shear size and sediment load of this system makes it an end-member among fluvial systems, with the ability to record the fluvial response to momentous external forcings over varying timescales. As such, it is an ideal location for studying the potential responses that
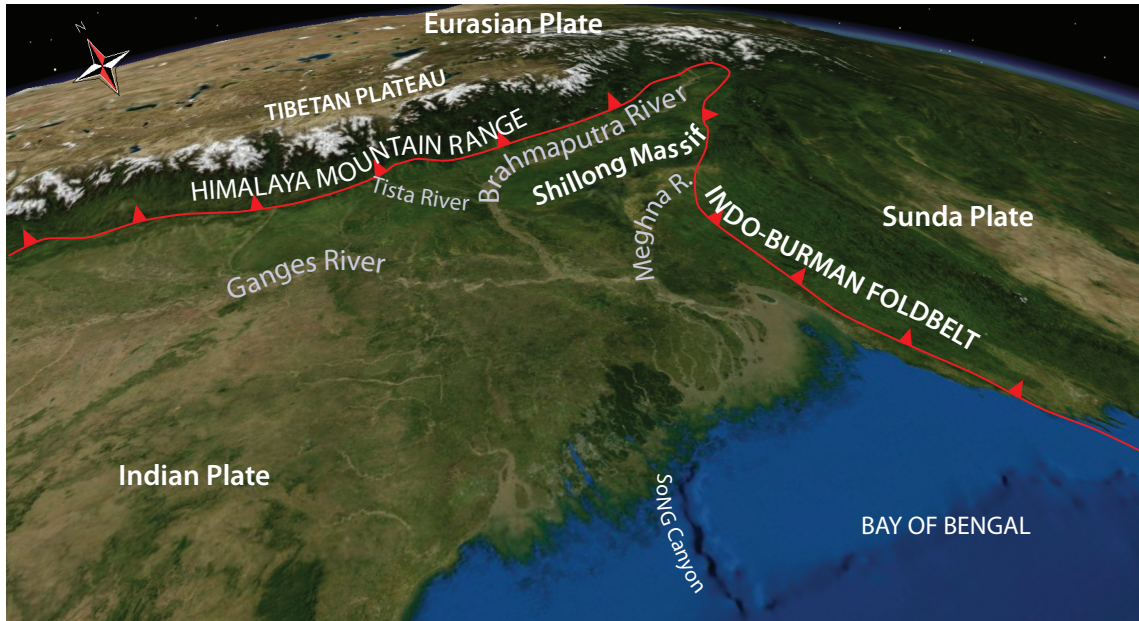
Figure 1.1: Oblique view of the region studied for this project. The Bengal basin is the area southwest of the plate boundaries (in red), where the Ganges, Brahmaputra, and Meghna rivers converge. Major tectonic structures, rivers, and offshore features are labeled.

rivers might have to external agents of change like tectonic deformation and glacioeustatic variability.

1.1   Significance and Rationale

The focus of this dissertation is the Brahmaputra River, the largest of the three main rivers that feed the Bengal basin. Prior to this work, studies specifically addressing the Brahmaputra have largely addressed its geology over three timescales:

1. characterization of the **modern** river system, including its hydrology, bank migration rates, planform morphology, and sedimentology (e.g., Coleman, 1969; EGIS, 1997; Goodbred and Kuehl, 1998; Best et al., 2007; Garzanti et al., 2010; Baki and Gan, 2012; Wilson and Goodbred, 2015),

2. understanding the **Holocene** river system, including the sediment budget as well as

channel switching on 100–1000 year timescales (e.g., Goodbred and Kuehl, 1999; Stanley and Hait, 2000; Allison et al., 2003; Khan and Islam, 2008; Srivastava et al., 2009; Goodbred et al., 2014; Pickering et al., 2014),

3. establishing the paleogeography of the Brahmaputra during the **Miocene through Pleistocene**, typically between 7–18 Ma (Uddin and Lundberg, 1999; Alam et al., 2003; Uddin and Lundberg, 2004; Chirouze et al., 2013; Robinson et al., 2013), and more recently up to ∼2 Ma (Cina et al., 2009; Najman et al., 2016).

Investigations into the paleogeography of the river during the Pleistocene (the last ∼2.5 Ma) have historically been lacking. From the onset of this dissertation project, it was my intention to bridge that knowledge gap between the Miocene Brahmaputra and the Holocene Brahmaputra by establishing the evolution of the system throughout the Pleistocene.

Additionally, because the change in the river course from the Miocene to the present was caused by the deformation of a regionally important tectonic structure, future results from this project (dates of key geologic deposits, expected summer 2016) will provide age constraints for the timing of uplift of the structure in question (which, although not the focus of this thesis, is a contentious topic among geologists working in the region).

Finally, this dissertation contributes to an overarching goal shared by the Quaternary geology community: to understand how environmental triggers, specifically tectonic deformation and climate variability, interact with rivers to influence the evolution of the delta.

1.2   Bengal Basin Geologic Setting

The Brahmaputra River flows eastward along the north-sloping side of the Himalaya Mountain range and then bends abruptly southward around the the eastern syntaxis (a peak called "Namche Barwa"), before it exits the mountains and enters the Bengal basin. There it transitions from bedrock-controlled to a braided alluvial river and opens onto the Assam valley. For the next ∼900 km, the Brahmaputra maintains a braided planform as it

flows through Assam, India, winding southward around the western margin of the Shillong Plateau, pinned against the Tista megafan. Continuing south between the Bogra and Madhupur terraces, the Brahmaputra finally joins the Ganges River in Bangladesh on a southerly course to the Bay of Bengal.

The foreland Bengal basin is a structural depression that formed during the Paleogene in response to prior and ongoing crustal shortening of the Himalaya (Alam et al., 2003). The basin has been occupied by the Ganges-Brahmaputra delta throughout the Holocene (Goodbred and Kuehl, 2000b) and by ancestral Ganges-Brahmaputra rivers since at least the Miocene (Uddin and Lundberg, 1999; Alam et al., 2003; Uddin and Lundberg, 2004). The Shillong Plateau pops up out of this basin, where the Indian plate, which is actively subducting beneath the Eurasian and Burman plates (Steckler et al., 2016), transitions from oceanic to continental crust. As a result of this triple plate convergence, the region is extensively faulted and subject to significant seismic activity, making the Brahmaputra River particularly susceptible to fluvio-tectonic interactions.

The Shillong Plateau is an actively uplifting anticlinal structure (Clark and Bilham, 2008), some 30,000 km^2 in area, that routes the Brahmaputra River around its western margin. The Shillong Plateau comprises three main physiographic regions: the Jaintia Hills in the east, the central Khasi Hills, and the Garo Hills in the west, with variably hilly topography ranging from ~1960 m in the east to ~25 m in the west. This anticlinal landscape consists of uplifted Precambrian basement plateau with intermontane valleys, highly dissected Cenozoic sedimentary hills of varied topography that flank the high plateau, and Quaternary alluvial plains that fringe the northern and western hills.

The westernmost hills of the Shillong Plateau, the Garo Hills, are discussed in Ch. 4. The elevation of these hills range from ~500 m in the northeast, up to ~1400 m in the uplifted central region along the Dapsi fault, down to ~25 m in the low-lying southwest (Fig. 1.2). The blind (buried) Dapsi thrust fault, trending NW-SE, offsets >1000 m of topography on the upthrown side of the fault and separates the Garo Hills into two general zones: a
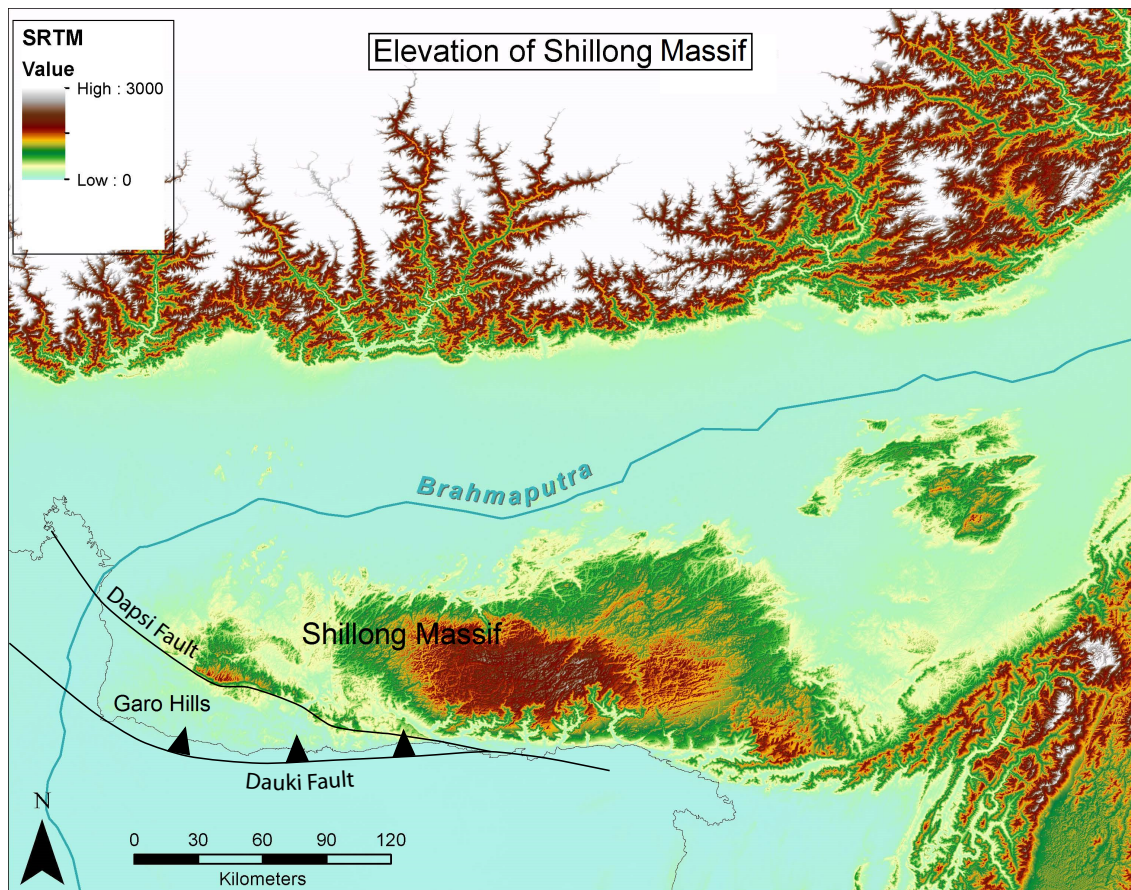
Figure 1.2: Digital elevation model (DEM) of Shillong Plateau with Brahmaputra River in Assam, India for reference.

N-NE-dipping monocline of uplifted basement rock on the up-thrown (northeast) side of the fault, and a gentler monocline of both unconsolidated and consolidated sedimentary deposits on the down-dropped (southwest) side of the fault. With a few exceptions, sediment samples for this dissertation were collected on the southwest side of the fault, but the entire regional structure is important to the Brahmaputra's paleogeographic evolution. The Dauki fault, another blind thrust, generates significant topographic relief along the southern margin of the Shillong Plateau. Numerous other faults, including the Dhubri, the Brahmaputra, the Oldham, and the Chedrang, are projected in and around the western Garo Hills (e.g., Oldham, 1899; Molnar, 1987; Rajendran et al., 2004), but none of these faults are well understood.

The Brahmaputra braidbelt and its floodplain in northern Bangladesh are bound on the east by the southwest Garo Hills and on the west by the high topography of the Tista fan. Once the river flows through this constricted area, however, it is free to migrate laterally or avulse between old and new channel paths, constructing or incising its alluvial fan. Indeed, throughout the Holocene, the reach of the Brahmaputra just south of the Tista fan and the Garo Hills has alternated between two courses: a southeasterly path that closely hugs the southwest Garo Hills and flows south of the Shillong massif (locally called the Old Brahmaputra River), and the modern path (locally called the Jamuna River) that more directly flows into the Bay of Bengal (Goodbred and Kuehl, 2000b; Pickering et al., 2014).

1.3   Research Questions and Approach

River channels are conduits for fluid and sediment transport that convey material shed from upland sources to lowland sinks, and their pathways are more or less mobile at different locations along such source-to-sink systems (Schumm, 1977). Alluvial (non-bedrock) reaches of a river exist where its channel beds and banks are mobile, relative to the landscapes through which it flows. This means an alluvial river has the potential to respond rapidly to environmental perturbations like climate events or tectonic deformation (e.g.,

Blum and Törnqvist, 2000).

Processes both internal to (autogenic) and external from (allogenic) the river basin itself can influence a river to change the shape of its bed and banks or even change its course altogether (e.g., Holbrook et al., 2003; Stouthamer and Berendsen, 2007; Leeder, 2011). Internal processes are the flow dynamics and depositional mechanics associated with the river itself, whereas external triggers can be changes in climate or tectonic setting that are independent of the river. These processes have been recognized since the 1960s (Beerbower, 1964), and understanding the effects of external triggers on intrinsically mobile river systems has been a goal of fluvial sedimentologists for at least the last 2 decades (e.g., Kraus, 1999; Ardies et al., 2002; Stouthamer and Berendsen, 2007; Kim, 2011). Toward that end, the broad objective of this dissertation is to investigate climatic and tectonic influences on a large alluvial system by studying the history of sediment deposition and erosion that has been preserved in the sediments the river has constructed throughout the latter half of the Pleistocene epoch.

Central to this objective was the definition of geometries of the fluvial deposits. To define the alluvial architecture (the layout of channel sands and floodplain muds in the subsurface), both borehole (buried) and outcrop (uplifted) sediments deposited by the Brahmaputra River were analyzed. This required lithofacies and provenance (sediment source) analyses to confirm that these sediments were indeed deposited by the Brahmaputra. Establishing age control was also necessary to transform the preserved spatial stratigraphy into a detailed history of river behavior. To date, ∼400 boreholes associated with this project have been drilled. In addition to these sediment samples, a fluvial multichannel seismic reflection survey was acquired in 2011. These datasets were integrated to define the alluvial architecture of the study area. A summary of completed fieldwork within this study area is given in (Fig. 1.3).
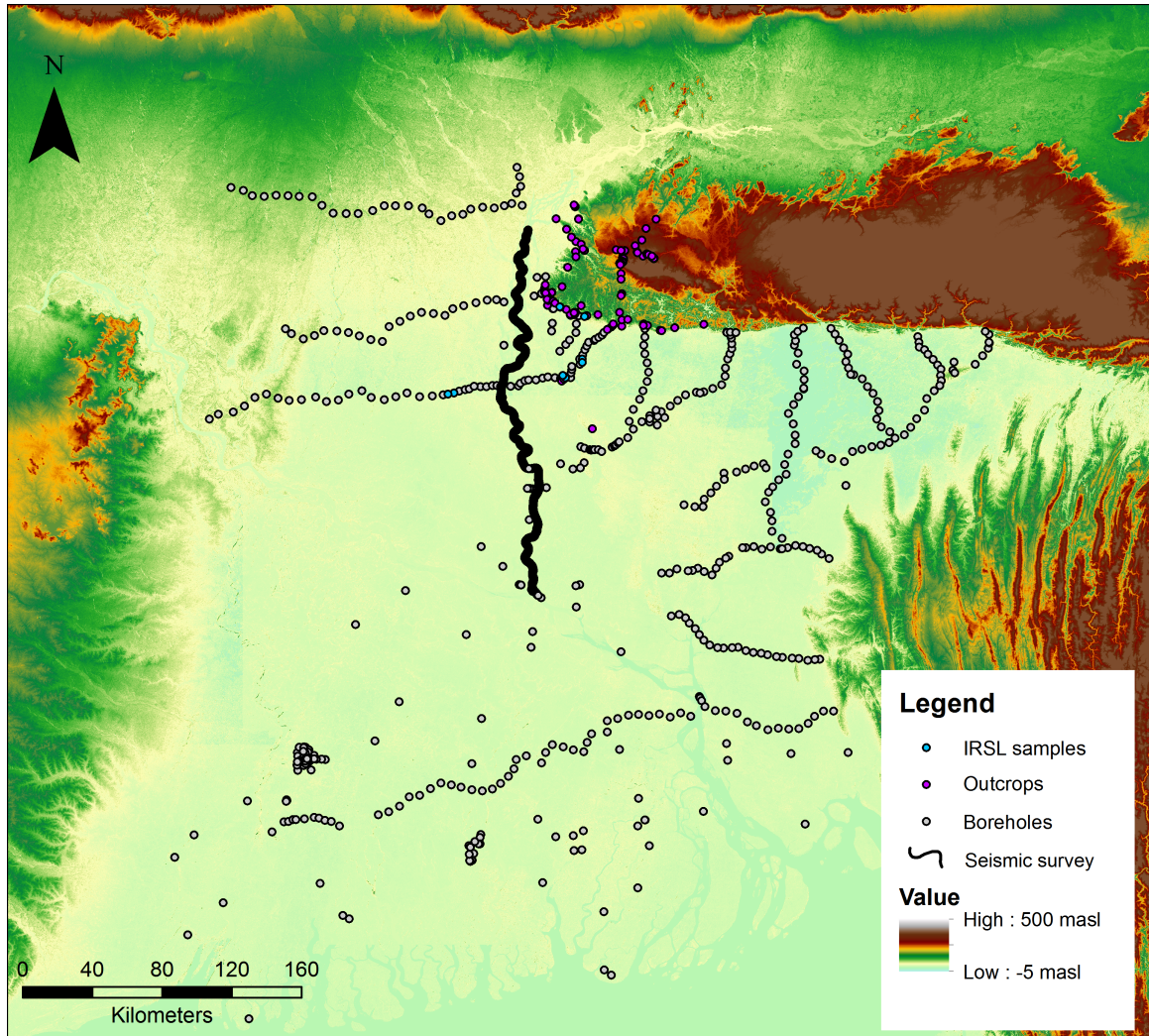
Figure 1.3: Overview of data acquired for this project: lithology logs from 544 boreholes and 127 outcrops, as well as a 255-km seismic line. The Digital Elevation Model (DEM) was generated from the 90 m resolution Shuttle Radar Topography Mission (SRTM) dataset.

1.4 Dissertation Components

This work comprises three papers that address the paleogeography of the Brahmaputra River and the external influences that controlled its whereabouts and behavior over three different timescales. This work builds on my Masters thesis, which established the history of Brahmaputra channel course switching throughout the Holocene, published in *Geomorphology* under the title *Late Quaternary sedimentary record and Holocene channel avulsions of the Jamuna and Old Brahmaputra River valleys in the upper Bengal delta plain*. The three substantive chapters that make up this dissertation built on this earlier work, in an attempt to extend the known history of Brahmaputra River channel switching and paleogeography beyond the Holocene, into the Pleistocene.

Chapter 2, *Impacts of Glacial-Lake Paleofloods on Valley Development since Glacial Termination II: A Conundrum of Hydrology and Scale for the Lowstand Brahmaputra-Jamuna Paleovalley System*, describes the last lowstand buried valley morphology in the paleohydrological context of the time, exposing a paleohydrological-valley scale conundrum: if the Brahmaputra-Jamuna valley formed in response to sea-level lowering at the end of the Pleistocene, why does it have such a broad valley floor (similar to U-shaped valleys formed by glaciers, as opposed to V-shaped valleys formed by river incision)? This paper is currently undergoing edits with co-authors and will be submitted to *Quaternary Science Reviews* in 2016.

Chapter 3, entitled *Landform Evolution of Late Pleistocene to Recent Terraces of the Brahmaputra-Jamuna River in the Upper Bengal Basin* is currently under review for the journal *Basin Research*. This chapter extends our understanding of the paleogeography of the Brahmaputra by a few hundred thousand years, by assessing the relative weathering of the terraces that surround the Brahmaputra and linking each one to a specific marine isotope stage. This relative chronology also exposes the latest Pleistocene trajectory of the Brahmaputra river, during which time the river migrated principally from west to east. In addition, sediments buried beneath these terraces are currently being dated using the

Infrared Stimulated Luminescence (IRSL) technique, so the relative chronology established in this chapter will be tested, resulting in an absolute chronology of terrace deposition.

Chapter 4, *Influence of Regional Fluvio-Tectonic Interactions on Downstream Sediment Dispersal: Uplift-Controlled Depositional Lobes of the Paleo-Brahmaputra River*, describes the deflection of the river from its location in the eastern basin, prior to uplift of the western margin of the Shillong Plateau, to a more westward location in response to the uplift, and finally to its location in the central part of the basin today. In this paper, stratigraphic evidence is presented that shows that the Brahmaputra was gradually forced westward across the emergent Shillong Plateau. Along with sediment samples from the terraces in Chapter 3, now-uplifted Brahmaputra sediments are currently undergoing IRSL age analyses, the results of which will better constrain timing of uplift of the lower, western portion of the Shillong Plateau and the transience of the Brahmaputra in response to this uplift.

Grain size data used to interpret lithofacies throughout this dissertation are given in App. A, geochemical data used to interpret fluvial provenance are given in App. B, and geochronological data used to interpret timing of deposition are given in App. C. Qualitative statistical classifications of sediment samples referenced in Ch. 3 are given in App. D. Locations and facies of outcrops presented in Ch. 4 can be found in App. E.

As will become apparent in the following pages, the stratigraphy of Bengal records some important environmental triggers that have caused major changes in the flow path of the Brahmaputra River. These triggers are both tectonic and paleohydrologic in nature, and they tend to trigger a fluvial response that perpetuates, effectively establishing a new norm in the system. In Chapter 5, I summarize the major findings of the previous chapters and discuss how these findings contribute to the field of stratigraphy, as well as the overarching conclusions regarding the role that environmental forcings played in the evolution of this large river system.

Chapter 2

Impacts of Glacial-Lake Paleofloods on Valley Development since Glacial
Termination II: A Conundrum of Hydrology and Scale for the Lowstand
Brahmaputra-Jamuna Paleovalley System[1]

2.1   Abstract

The basal unconformity of the Brahmaputra-Jamuna paleovalley, first identified during
a 1976 geotechnical drilling campaign aimed at determining feasibility of bridge construc-
tion, has been imaged along a 255-km fluvial seismic survey. The valley floor is defined
by a planar gravel unit up to 10 m thick and 40 km wide with boulders up to 30 cm in
diameter, overlying Pleistocene-aged diluvial sands of Brahmaputra provenance. Timing
of deposition of the basal unit is constrained by radiocarbon ages; the diluvial unit below
the gravel layer contains material dated to 28 ka, and the valley fill alluvium above the
gravel unit contains material dated to 9 ka at a similar latitude. This age bracket is coin-
cident with paleoflood events that originated in a glacially-dammed lake that formed along
the flow path of the Brahmaputra River in Tibet. These floods resulted in high discharge
(up to 10^6 m^3/s) flows that were routed through the existing Brahmaputra-Jamuna lowstand
valley, effectively excavating the valley and transporting and depositing the gravel unit. In
a sequence stratigraphic framework, these findings are important because they reveal an
observable example of an unconformity that formed in response to an upstream driver (i.e.,
incision happened in response to a forcing that originated in the upstream catchment rather
than at the coastline in response to sea-level lowering) in a very short amount of time. As
such, this unconformity represents a geologically instantaneous time surface that can be
used as a marker for stratigraphic correlation.

---

[1]This chapter was written for publication with co-authors MS Diamond, C Grall, SL Goodbred,
RS Sincavage, C Paola, J Martin, L Palamenghi, T Schwenk, and V Spieß.

2.2 Introduction

Rivers, especially along more mobile alluvial reaches, have the potential to respond rapidly to changes in environmental boundary conditions like climate events or tectonic deformation (Blum and Törnqvist, 2000; Dalrymple, 1994). These perturbations are recorded downstream in the form of changes in clast size transported through the system and changes to the channel geometry (Armitage et al., 2011; Castelltort and Van Den Driessche, 2003; Romans et al., 2014). Classic sequence stratigraphy suggests that under circumstances where the perturbation results in a relative base level reduction, the change in channel geometry may manifest as downcutting, creating a basal incision surface and eventually leading to the development of an incised valley (e.g., Posamentier et al., 1988; Posamentier and Vail, 1988; Posamentier, 2001; Shanley and McCabe, 1994; Van Wagoner et al., 1990; Zaitlin et al., 1994).

Recent research has changed our understanding of incised valley (hereafter "paleovalley" *sensu* Blum and Törnqvist, 2000) formation, emphasizing the processes by which paleovalley bounding surfaces formed, i.e. channel extension toward the retreating shoreline by either decreasing the channel slope or by prograding the coastal plain out to the shelf, depending on the nature of the preexisting system (Blum et al., 2013). Likewise, physical experiments have shown that channel extension toward an emergent shoreline causes episodic channel incision and valley floor narrowing with protracted periods of lateral migration that widen the valley (Martin et al., 2011; Strong and Paola, 2008).

Traditionally, the primary focus of sequence stratigraphy has been on the influence of relative base level changes on the genesis of a basal erosional unconformity (or sequence boundary), typically focusing on downstream-driven incision (Blum and Törnqvist, 2000; Vail et al., 1977; Van Wagoner et al., 1990). There is no question that relatively rapid base level fall has the potential to form deep incision surfaces through upstream-migrating readjustment of the channel-bed gradient (e.g., Aslan and Blum, 1999; Blum and Price, 1998). However, other processes that might induce large-scale erosion remain understud-

ied, especially upstream-driven incision that may be interpreted as lowstand incision from preserved stratigraphy (Ethridge et al., 1998; Shanley and McCabe, 1994). For example, Milana and Tietze (2002) isolated the effect of increased stream discharge on a basin margin in a flume experiment, whereby increased discharge generated incised channels and an erosional system-tract boundary comparable to a sequence boundary. Other researchers have convincingly shown that stratigraphic surfaces generated by fluvial erosion responding to decreasing base level can be composite, diachronously-formed surfaces (e.g., Martin et al., 2011; Strong and Paola, 2008), an idea that has challenged the fundamental and long-standing idea that erosional unconformities represent a time surface that separates overlying younger sediments from older sediments below (Van Wagoner et al., 1988).

Amidst the ongoing discussion of the formation and nature of stratigraphic unconformities (e.g., Blum et al., 2013; Holbrook and Bhattacharya, 2012; Holbrook, 2001), we present a paleovalley delineated by a basal erosional surface that was initially incised due to sea-level lowering, but largely excavated by enhanced stream discharge that was capable of transporting boulders along the entire length of the system. The result is a basal stratigraphic surface with an anomalously large width dimension. This floor consists of a longitudinally and laterally continuous, planar (i.e., relatively flat in the cross-stream dimension) unit of gravel including boulders, in an otherwise sandy system. We consider high discharge paleoflood events, which were regularly transmitted to the basin margin throughout the Quaternary, to have contributed to the development of this wide paleovalley. Ultimately, the basal unconformity created by these floods not only represents an example of upstream-driven valley incision, but also one example in which an erosional unconformity does essentially represent an instantaneous (rather than composite) time surface.

Stratigraphic evidence for similar paleoflood events is ubiquitous in high latitudes (a review of 41 locations documented worldwide is presented in Carling, 2013); most of these events are associated with ice-dam failure around the time of the recent glacial termination. For example, along the Tsangpo-reach of the Brahmaputra River catchment near the

eastern syntaxis of the Himalaya (Fig. 2.1), there is growing evidence for repeated floods, occasionally very large ones, triggered by the drainage of ice-dammed lakes during the last interstade and glacial termination (Hu et al., 2015; Huang et al., 2014; Lang et al., 2013; Liu et al., 2015; Montgomery et al., 2004; Zhu et al., 2013). In other high-latitude systems, is it possible that valley widening by glacial lake outburst floods (GLOFs) has augmented initial (downdip) valley incision that occurs in response to falling sea-level?

By combining new borehole lithology and seismic-reflection data with preexisting geotechnical well logs, we define for the first time the geometry and bounding-surface lithology of the infilled lowstand Brahmaputra-Jamuna paleovalley system. Results reveal the paleovalley to be >80 km-wide at the ground surface, with a 40 km-wide boulder-floored basal unconformity that lies as deep as 90 m below modern sea-level 130 km upstream of the shoreline. Compared to other systems, this paleovalley and its basal unconformity are extremely wide, suggesting an extended period of formation (Blum et al., 2013), yet radiocarbon ages reveal that the boulders that make up the unconformity were deposited in the early Holocene. We present several lines of evidence that indicate that the valley system was widened and the boulder surface was deposited by the extreme discharge of glacial-lake early Holocene paleoflood events rather than incision via monsoon-driven river discharge and morphodynamic channel widening.

2.2.1   Background

The Brahmaputra River originates high in the Himalaya and flows as the Yarlung-Tsangpo along the northern flank of the mountain range through the Tibetan plateau before descending into the Tsangpo Gorge where it abruptly turns southward and exits the Himalaya (Fig. 2.1). The river then flows west through the Assam Valley as the Brahmaputra, where its path is still controlled by bedrock until it traverses the western margin of the Shillong Plateau and enters Bangladesh, where it flows as the Jamuna River southward to the Bay of Bengal. The modern Brahmaputra-Jamuna is a large, braided stream that is currently
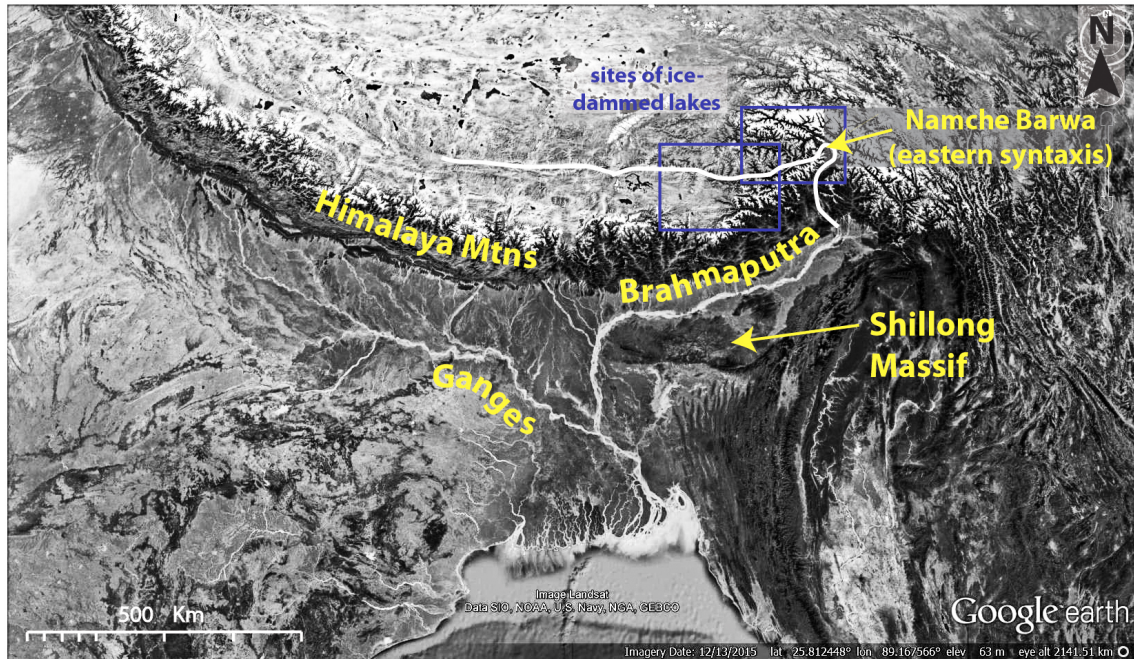
Figure 2.1: Himalayan-Brahmaputra River system. Sites of ice-dammed lakes are in blue. Satellite image from Google Earth.

flowing through a wide paleovalley that the river has infilled throughout the Holocene.

The development of the Brahmaputra-Jamuna paleovalley, including aggradation of sediments prior to incision, has been ongoing since just after glacial Termination II, the transition between the penultimate glacial maximum (PGM) and the Marine Isotope Stage (MIS) 5e highstand. Sea-level and climate (i.e., insolation and monsoon strength) during MIS 5e (roughly 120–130 ka) were similar to, although slightly higher than, today (Fig. 2.2), and fluvial aggradation would have constructed a pre-incision landscape similar to that of the modern. After the MIS 5e highstand, there were 4 episodes of falling sea-level that may have contributed to the erosional unconformity that forms the base of the Brahmaputra paleovalley: MIS 5d, MIS 5b, MIS 4, and MIS 2 (Fig. 2.2D). Each of these episodes of falling sea-level resulted in on the order of 50 m base level reduction (Berger et al., 2015; Grant et al., 2014; Siddall et al., 2003). MIS 5d and 5b were relatively brief lowstands (lasting a few thousand years each), whereas MIS 4 and 2 were relatively prolonged lowstands (lasting ∼10 ka each). While fluvial incision is not implicit for any given base level fall

(c.f. Blum et al., 2013), the Ganges-Brahmaputra subaerial delta is connected via shallow water to the nearshore Swatch of No Ground canyon, which might tend to favor incision with base level fall.

However, recent theoretical and experimental work suggests that the magnitude of relative sea-level change affecting a delta must be greater than the scale of autogenic scour within that delta, or else the stratigraphic signal generated by the change in sea-level is not likely to be preserved (Jerolmack and Paola, 2010). Large systems, including the Brahmaputra, produce autogenic scours that are likely to "shred" the stratigraphic signal when the magnitude of sea-level change is on the order of 10–35 m, instead requiring fluctuation magnitudes on the order of $\sim$100 m for the stratigraphic signal to be preserved (Li et al., 2016). Even treating these experimental results as rough guidelines, discrete episodes of falling sea-level since the PGM do not exceed 60 m, and while some remnants of incised topography may endure, an extensive erosional unconformity is unlikely to have been preserved in a system of this size. Alternatively, if the cumulative magnitude of base-level lowering is taken as the governing scale of scour necessary to preserve the stratigraphic signal, an extensive erosional unconformity may persist in this system since the cumulative sea-level change is $\sim$100 m. In either case, the magnitude of base-level lowering was only marginally sufficient to produce incision great enough to persist in the stratigraphy.

Further complicating paleovalley formation is the reduced relative to modern but still moderate precipitation after MIS 5 (discerned from speleothem records, insolation, and Bay of Bengal salinity data: Fig. 2.2A–C). This reduced but moderate precipitation coupled with enhanced sedimentation as Himalayan glaciers reached their maximum extent during MIS 3 (Owen et al., 2002) would have dispersed sediment to the system, aggrading channels and serving as a "topographic reset" or at least distorting the erosional signal of the lowstands. These conditions are coincident with multiple episodes of megafan aggradation in the upper reaches of the foreland basin, evidence that the interstadial climate in the Himalaya system fostered sediment deposition (Goodbred, 2003b). This is further corroborated by high car-

bonate content in upper Bengal Fan cores, which indicates that siliciclastic sediment input to the offshore fan was decreased during MIS 3 and 4 (Weber et al., 2003), likely due to sediment storage in megafans and on the subaerial delta. Moreover, MIS 5 and MIS 3 are characterized by prominent sea-level midstands (Fig. 2.2D), incapable of generating deep incisional surfaces.

To briefly summarize the effects of glacioeustatic cycles since glacial termination II on Brahmaputra-Jamuna paleovalley development, the MIS 5e highstand would have infilled the PGM paleovalley, generating a relatively flat topographic surface similar to the delta today. Environmental conditions in this system following the MIS 5e highstand were not cumulatively conducive to the formation of a large, wide incised valley. The "lowstand paleovalley" of the Brahmaputra-Jamuna has thus been generated (incised) during MIS 2, the Last Glacial Maximum (LGM), leading up to the Holocene climate that has since infilled the paleovalley with nearly 100 m of alluvium.

2.2.2 The Conundrum

The paleohydrological regime during the MIS 2 incisional period, however, was characterized by relatively low water discharge, Q_w, during a weakened monsoon. Indeed, the monsoon was suppressed since the onset of MIS 4, about 75 ka (Goodbred, 2003a; Prell and Kutzbach, 1987). Recent speleothem records from caves in China that have been linked to the Indian Summer Monsoon (Cai et al., 2015) indicate reduced precipitation relative to modern since MIS 5 (Fig. 2.2A). Speleothem data from Hulu cave (Fig. 2.2A) and salinity data from the Bay of Bengal (Fig. 2.2C) depict remarkably similar trends, which, interpreted as precipitation proxies, show that precipitation has been greatly reduced relative to modern since the onset of MIS 4 until the LGM; even at the onset of MIS 2, regional precipitation was significantly reduced (>25%), according to multiple proxies and models (e.g., Cullen, 1981; Goodbred, 2003a; Prell and Kutzbach, 1987). Acknowledging that the ^{18}O to ^{16}O ratio variability may not be explicitly linked to monsoon strength (Dayem et al., 2010), flu-
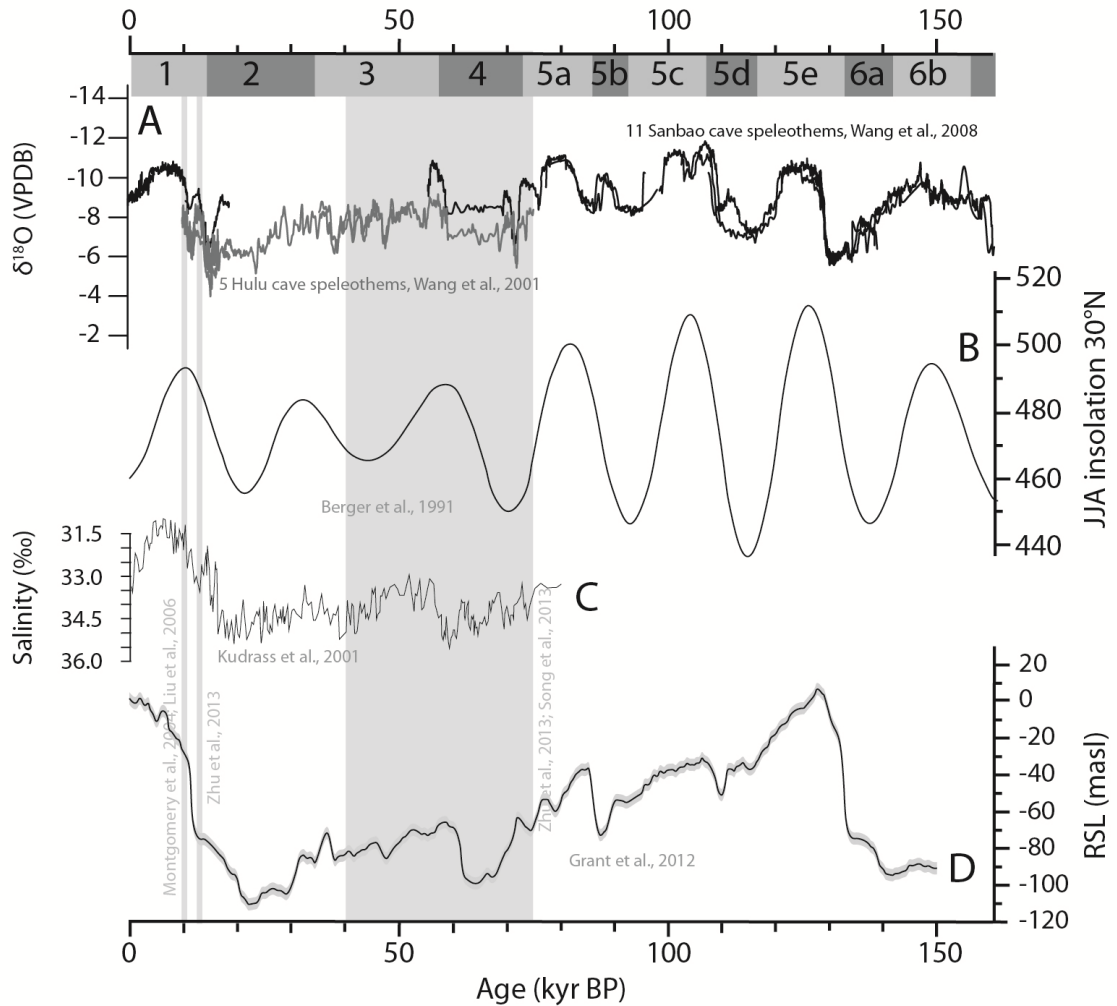
Figure 2.2: Marine isotope stages (MIS) and climate proxies for the last 150 ka. A) Speleothem oxygen-isotope records from Hulu (eastern China) and Sanbao (central China) caves. Data from Wang et al. (2008, 2001). Variations in isotope ratio represent changes in properties of rainfall including amount, source, and temperature. B) Model of insolation from Berger and Loutre (1991); June, July, and August insolation is averaged. C) Salinity in the Bay of Bengal from Kudrass et al. (2001). D) Maximum probability of relative sea-level rise (RSL) from Grant et al. (2012). Vertical shaded areas represent periods of ice-dammed lakes along the Tsangpo reach of the Brahmaputra (Liu et al., 2015; Montgomery et al., 2004; Zhu et al., 2013).

vial Q_w into the Bengal basin is largely monsoon-modulated, and has been reduced relative to today since the last peak at MIS 5a until about 15 ka, after the LGM, when monsoon precipitation increased (Fig. 2.2C, Kudrass et al., 2001).

Formation of the broad, gravel unit that paves the base of the Brahmaputra-Jamuna paleovalley would require high Q_w, capable of initiating incision and transporting those boulders. The valley dimensions suggest an extended period of erosion, but the hydrologic regime at the time was characterized by low Q_w from MIS 4 until after the LGM. How then did this valley develop during a climate and hydrologic regime that was inconsistent with the flow conditions required to form it?

To reconcile this discrepancy, we refer to paleoflood records from this time. Over the last decade, an increasingly robust history of glacial lake outburst paleoflood events in the upper reaches of the Tsangpo-Brahmaputra has been compiled by documenting and dating sediments and terraces of glacially dammed lakes (Huang et al., 2014; Lang et al., 2013; Montgomery et al., 2004; Song et al., 2013). Similar flood events are ubiquitous worldwide during the Late Pleistocene and early Holocene, especially in mountainous high-latitude regions (Baker, 2013), and downstream evidence of these types of events has included coarse gravel fluvial deposits (Rudoy and Baker, 1993). In order to reconcile the paleohydrological-valley morphology conundrum, we invoke these flood events, which were routed through the existing Brahmaputra-Jamuna lowstand valley, and we suggest that they served to widen the initial incised valley floor by scouring the existing riverbed topography and depositing a gravel unit along the length of the valley.

2.3   Methods

2.3.1   Determination of Buried Valley Geometry

The three-dimensional geometry of the Brahmaputra-Jamuna valley, i.e. dimensions of the western and eastern valley walls and the depth to the valley base from the northern border
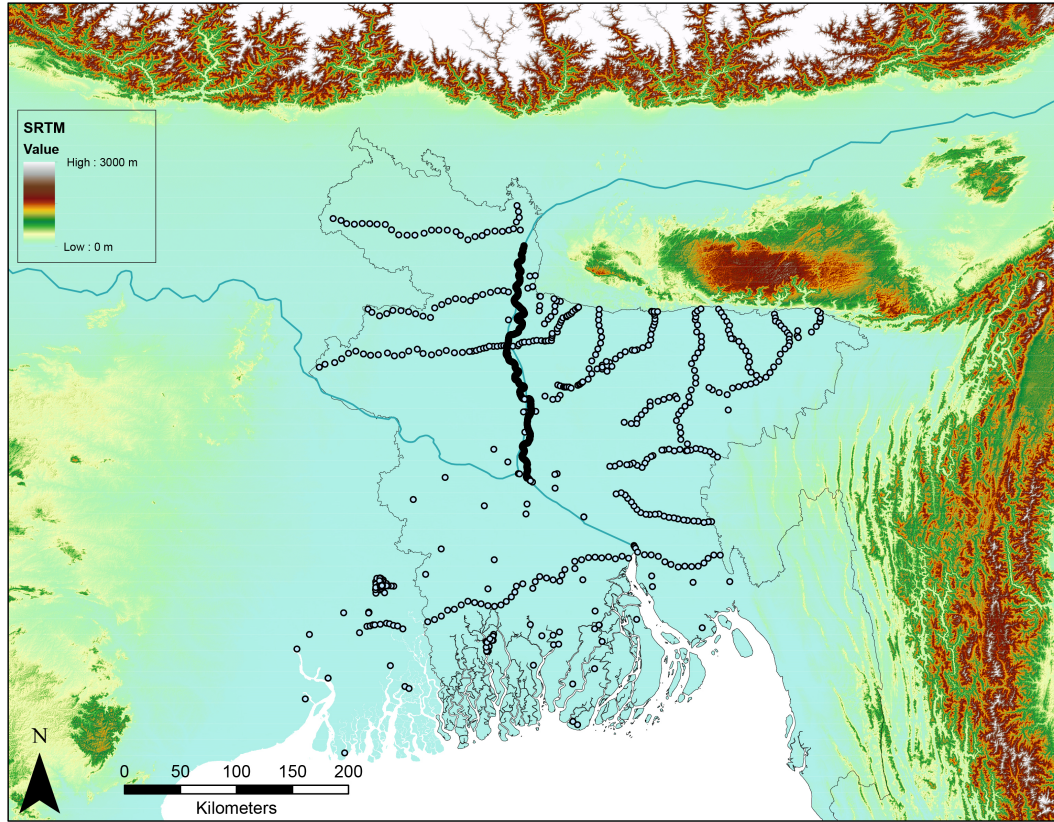
Figure 2.3: Overview of boreholes drilled and seismic survey acquired during BanglaPIRE project. Digital elevation model (DEM) is generated from the Shuttle Radar Topography Mission (SRTM) 90 m resolution grid. Geopolitical boundary of Bangladesh is outlined and serves as references for Figs. 2.4 and 2.5.

of Bangladesh down to ~130 km inland from the coast, was determined by stratigraphic analysis of boreholes and a seismic reflection profile along the mainstem of the modern river. All data available for this project, including the seismic profile, recent boreholes drilled, and sites of the prior geotechnical wells are shown in Figure 2.3.

A network of closely-spaced boreholes (3–5 km spacing, 5 cm diameter) comprising four transects was drilled using a reverse circulation method capable of penetrating >90 m below the surface (Pickering et al., 2014). The contact between overlying Holocene valley fill and underlying Pleistocene diluvium was interpreted in conjunction with absolute ages and based on the presence of one or more of the following:

1. reduced (gray) sediments overlying oxidized (brown, red, orange, or mottled) sediments,

2. deformable muds overlying stiff, non-deformable, brown to red-colored muds, representative of floodplain paleosols (further explanation given in Ch. 3),

3. depth of refusal of drilling where the lowermost sediments extracted before refusal were pebble to cobble sized clasts, interpreted as the basal Holocene unit reported by the Japan International Cooperation Agency (1976).

Interpretations were corroborated by radiocarbon ages of organic material found within each unit, wherein organic material within the Holocene unit was dated to <11 ka cal BP and organic material within the Pleistocene unit was beyond the limit of detection of the dating method (>48 ka) or >11 ka cal BP. Strontium geochemistry, indicative of sediment provenance (Goodbred et al., 2014), was used to verify lateral extent of the Holocene valley fill along the western boundary where the Brahmaputra-Jamuna and Tista rivers have historically overlapped in vertical succession.

2.3.2 Multichannel Seismic Reflection Survey and Data Processing

During the 2011 monsoon season, a 255-km fluvial multichannel seismic dataset was acquired to determine the depth to the base of the Holocene unit beneath the Brahmaputra-Jamuna River, the first survey to image the lowstand valley from the India-Bangladesh border to the confluence with the Ganges (Padma) River. The two-dimensional seismic acquisition was optimized for shallow water depth, flow current, and the complexity of the navigation along the river. A small single streamer of 48 hydrophones with 1 m spacing was used with a GI Gun source of 0.1L, generating a high-frequency signal in the spectrum of 100-600 Hz.

Post-acquisition seismic processing was performed using Schlumberger Vista (previously Gedco) and IHS Kingdom software. In order to improve the signal to noise ratio

(SNR) at the depth of the main unconformity, a 15 m common midpoint (CMP) bin size was used. A bulkshift function was applied to every shot in order to correct a CMP coordinate problem that resulted from motion of the streamer in the water column. Broad bandpass frequency filters (30/60–900/1300 Hz) and spherical divergence gains were applied to the data, and after meticulously picking velocities from 1480 m/s (riverbed) to 1600 m/s (strong reflector present along entire survey), the data were corrected for normal moveout and stacked. Ad-hoc static correction of the arrival time of the direct wave was applied to obtain an accurate correlation with the lithology logs from multiple surveys within a 1 km radius. Two-dimensional white noise and F-K (frequency-wave number) filters were then applied to the stacked profiles before migration in the time domain.

Seismic horizons were correlated to strata identified in the lithology logs of both new boreholes from this project and well-described preexisting geotechnical borings from the Jamuna Bridge feasibility study (Japan International Cooperation Agency, 1976). Positions of seismic profiles and boreholes were georeferenced using a GPS device during both navigation and drilling. The physical properties from the JICA-S1 well were used to calculate a synthetic seismogram. This seismogram was compared to the seismic traces to evaluate the correlation between the sedimentary units and the seismic signal.

2.4 Results

2.4.1 Brahmaputra Paleovalley Architecture

2.4.1.1 Three-Dimensional Valley Geometry

Borehole lithology of the upper <100 m of sediments in the west-central Bengal basin reveals a generally sandy stratigraphy where the river traverses the western margin of the Shillong Plateau, with significant mud preserved about 300 km downstream from the apex of the modern fan delta (Fig. 2.4 and 2.5; grain size data given in App. A). Holocene Brahmaputra alluvium unconformably overlies latest Pleistocene Brahmaputra alluvium (geochem-

22

ical data used to determine fluvial provenance are given in App. B and described in detail in Ch. 4). Geotechnical well logs (Japan International Cooperation Agency, 1976) revealed that the unconformity is marked by an early Holocene basal unit comprising a "well-graded gravelly bed with as big gravels as human head" (stratum Al1: Fig. 2.6) juxtaposed atop a soft but dense sand and gravel conglomerate (D50=0.6 mm) of latest Pleistocene age (stratum Du3: Fig. 2.6). The top of this unit is characterized by a density contrast at 45 m depth at the JICA S-1 well site, which is correlated to the strong reflection observed on the seismic signal at a similar depth. To evaluate this, a synthetic seismogram was generated at the well site and projected onto the seismic data (for more details on the synthetic seismogram refer to Grall et al., 2016). Demarcating the base of the valley, the Holocene-Pleistocene unconformity is imaged along the entire length of the seismic survey, sloping from ∼40 m below the water level upstream to ∼90 m below the water level at the downstream confluence of the modern Ganges and Brahmaputra rivers (Fig. 2.4).

Upstream, where the river traverses the western margin of the Shillong Plateau, the paleovalley is ∼55 km wide at the land surface and ∼60 m deep (Fig. 2.5A–B), or roughly 5x the width of the modern braidbelt. In relation to ancient valley fills worldwide, the Brahmaputra paleovalley is very wide (Gibling, 2006), and the valley maintains this extreme width downstream. About 50 km south of the northernmost transect, where the Brahmaputra is no longer confined by surrounding topography, the paleovalley widens to ∼65 km and 70 m deep (Fig. 2.5C, Pickering et al., 2014). Another 60 km downstream, the paleovalley maintains its width but deepens to almost 90 m deep (Fig. 2.5D). Finally, another 150 km downstream where there is virtually no higher topography to confine the river, at about 130 km inland from the coast, the paleovalley dimensions increase to >80 km wide and >90 m deep (Fig. 2.5E). This is about 8 times the width of the modern braidbelt; for comparison, the Ganges valley is ∼35 km wide in the same transect, despite the modern rivers having similar widths (Patrick, 2016). The Brahmaputra paleovalley is exceptionally wide; today, even the most extreme monsoon floods do not completely inundate the width of the valley

(NASA Modis Rapid Response Team, 2007).

2.4.2 Holocene Basal Gravel Unit

Drilling operations encountered depth of refusal for many of the boreholes of this study at the depth of the basal gravel unit, where clasts returned reached 5 cm in diameter, limited only by the diameter of the drill pipe (Fig. 2.8), and sometimes these clasts appeared to be freshly fractured, suggesting perhaps an even greater clast diameter. These gravels make up the uppermost sediments of the basal Holocene unit—the Al1 unit from the Japan International Cooperation Agency (1976) project, as well as the main unconformity imaged along the seismic survey. The average width of the basal gravel unit is roughly 40 km wide based on borehole data from Transects C and D (Fig. 2.5), and comparison of the morphology of these with Transects A and B shows that width of the valley does not change significantly in the downstream direction until Transect E (Fig. 2.5), about 130 km inland from the coast.

The geotechnical report (Japan International Cooperation Agency, 1976) likewise notes the "good continuity" of the gravel unit, which is up to 10 m thick, and indeed the stratigraphic interpretation of 6 cross-stream cores spanning about 15 km width (redrawn in Fig. 2.5D) shows no sign of lateral thinning of the gravel unit; instead the unit appears to thicken away from the modern channel centerline. This broad, planar surface of basal alluvium above the unconformity of the paleovalley is a remarkably coarse-grained gravel unit, "consist[ing] mainly of big boulders having the estimated maximum diameter of about 30 cm" (Fig. 2.6), and extending flatly throughout the cross-stream transect. Transport of these boulders would require flow properties of significantly greater magnitude than the paleohydrological regime of the time could produce, which we explore below.
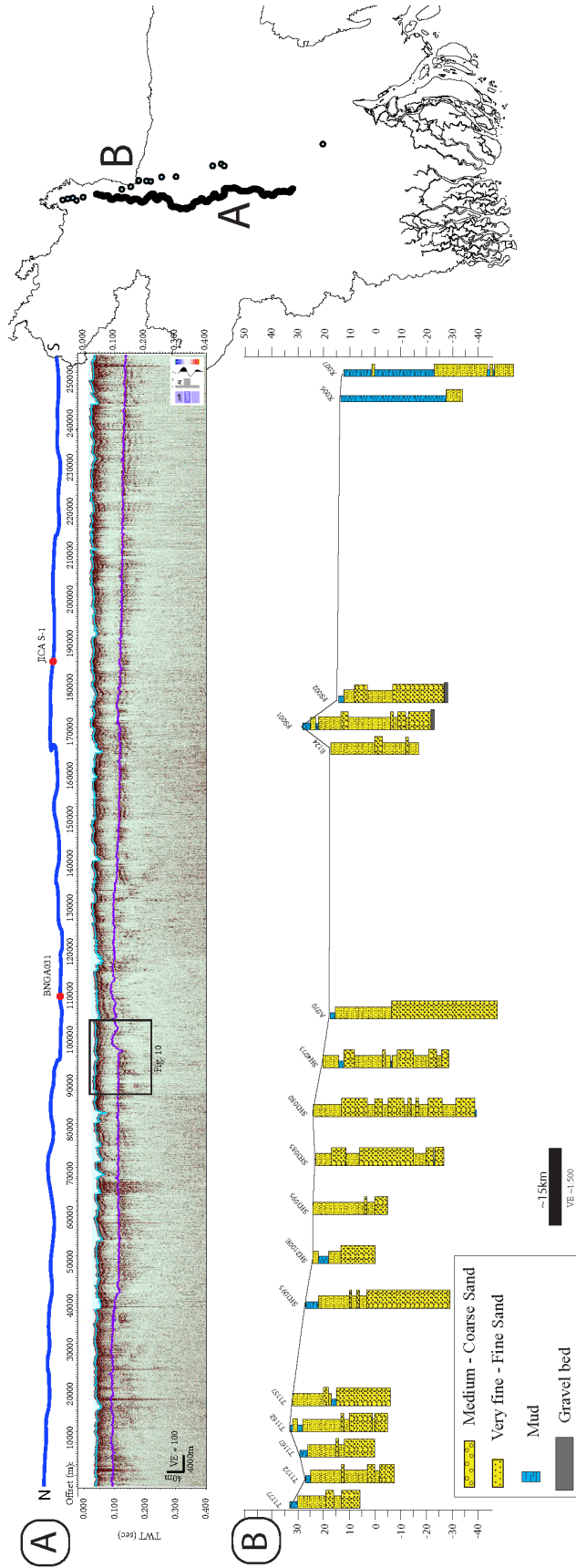
Figure 2.4: A) 255-km seismic reflection survey image. The river course is shown in blue above the seismic line for reference. The Holocene-Pleistocene unconformity is interpreted in purple. On the map, the seismic survey is shown by the thick black line. B) North to south longitudinal transect beside the Brahmaputra river. Borehole locations are shown by dots on the map. Note that the horizontal scale is only an approximation.
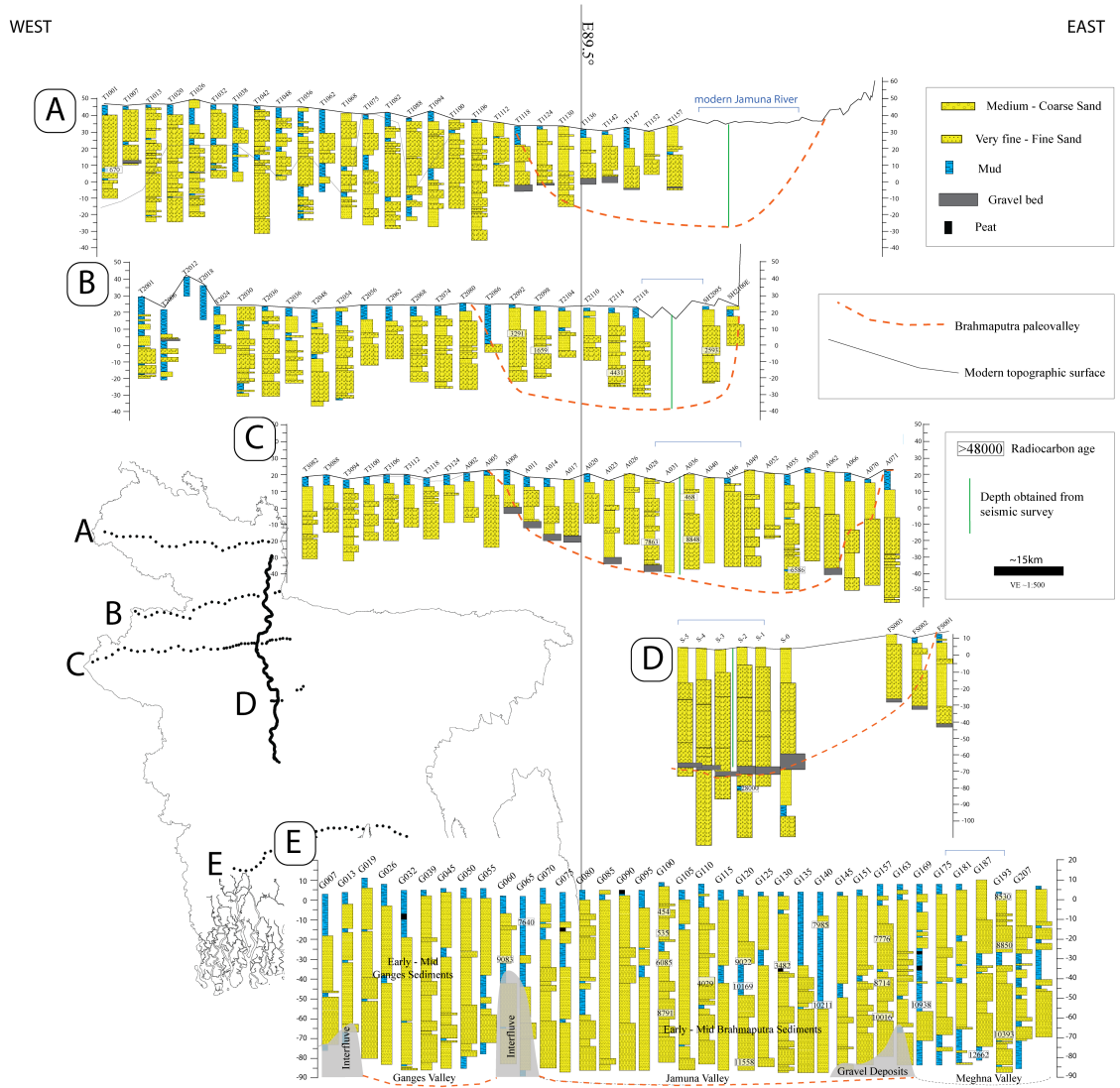
Figure 2.5: Five cross-valley borehole transects. Locations of each transect are shown on the map; boreholes are represented by dots; and the seismic line, for reference, is given by the thick black line on the reference map. Note that the horizontal borehole scale is an approximation.

2.5   Discussion

2.5.1   Paleohydrologic Conditions Necessary to Transport Gravels

We now consider whether the valley system attributes are consistent with glacial lake flood outburst events, of which some events reached 'megaflood' scale ($>10^6$ m^3/s), documented in the upstream catchment of the Brahmaputra system. We estimate uniform flow properties, including the critical shear stress (τ_c), channel depth (h), mean flow velocity (*v*), and water discharge (Q_w) for a range of grain sizes and channel dimensions using four equations:

$$\tau_c = \tau_* \rho g (SG - 1)(D50), \tag{2.1}$$

$$h = \frac{\tau_c}{\rho g m}, \tag{2.2}$$

$$v = \sqrt{\frac{\tau_c}{c_f \rho}}, \tag{2.3}$$

$$Q_w = hvw, \tag{2.4}$$

where τ_* is the Shields parameter (the shear stress necessary to initiate motion of a given particle), *SG* is the specific gravity of the material being transported, and c_f is an empirically derived bed roughness coefficient. Given the composition of the gravel unit, described as "granite-gneiss, siliceous sandstones, slates, quartzites, limestones, and [rarely, soft Pleistocene shale]" (Japan International Cooperation Agency, 1976), we use 2.7 g/cm^3 for *SG*. We consider a range of median grain sizes, from 20 mm (the minimum *D50*, measured during the geotechnical drilling and based on a limited sample diameter of 86 mm and adjusted for the clast size recovered during excavation for pylon installation) up to 150 mm (the probable maximum *D50*, considering the geotechnical report lists 300 mm diameter boulders as the maximum clast diameter). We calculate τ_* for each *D50* grain size after Ponce (1989).

Calculations were made using a conservative minimum channel width, *w*, of 5000 m,

which is approximately half the width of the modern channel, as well as a maximum width of 40,000 m, which is the average width of the gravel layer at the base of the paleovalley. The minimum channel width approximates the channel at the time of initial incision, whereas the maximum channel width represents the channel after deposition of the gravel unit. However, it is likely that the discharge routed through this system during the early Holocene was a series of events, rather than a single event, and the width of the channel would have evolved with time. Thus, we calculate a range of plausible scenarios.

While the shear stress required to transport particles is a complex parameter to measure, at a first order, the shear stress required to set these boulders in motion along the bed of the Brahmaputra-Jamuna paleovalley scales with the shear stress of megaflood events. Results, given in Table 2.1, show that even to move particles of 50 mm median diameter over this relatively low transport slope, significant discharge greater than modern would have been necessary. The peak discharge estimated for the early Holocene floods based on the volume of the glacially-dammed lakes estimated by mapping lacustrine terraces is 5 x 10^6 m^3/s (Montgomery et al., 2004), warranting classification as a megaflood. For comparison, the mean annual discharge of the modern Brahmaputra-Jamuna River is $\sim$2 x 10^5 m^3/s (Best et al., 2007). For the last lowstand, a conservative 25% reduction in discharge would produce $\sim$1.5 x 10^5 m^3/s, a flow with the competence to move sediment for only the most conservative scenarios in Table 2.1. More reasonably, a median grain size of 80 mm at the base of a valley some 40 km wide would require the discharge of a megaflood, as well as a channel height comparable to the depth of the valley.

2.5.2 Flood Height and Velocity Estimates Scale with Valley Dimensions

Using the empirical dimensions of the valley along the 4 upper transects (Fig. 2.5A–D) and a range of bed roughness coefficients (c_f) to represent the full spectrum of possibilities, we model the flood height generated by these events across each of the upper valley cross-sections. Because we use the full valley dimensions in our model, and because the

Table 2.1: Calculated flow properties based on clast size of gravel unit, slope of paleovalley, and channel width estimates.

$D50$ (mm)	τ_c (Pa)	h (m)	v (m/s)	Q_w (m³/s) if channel width=5000 m	Q_w (m³/s) if channel width=40000 m
20	19.7	10	1.4	7.02×10^4	5.62×10^5
50	49.1	25.1	2.2	2.78×10^5	2.22×10^6
80	78.6	40.1	2.8	5.62×10^5	4.50×10^6
100	98.3	50.1	3.1	7.85×10^5	6.28×10^6
150	147.4	75.2	3.8	1.44×10^6	1.15×10^7
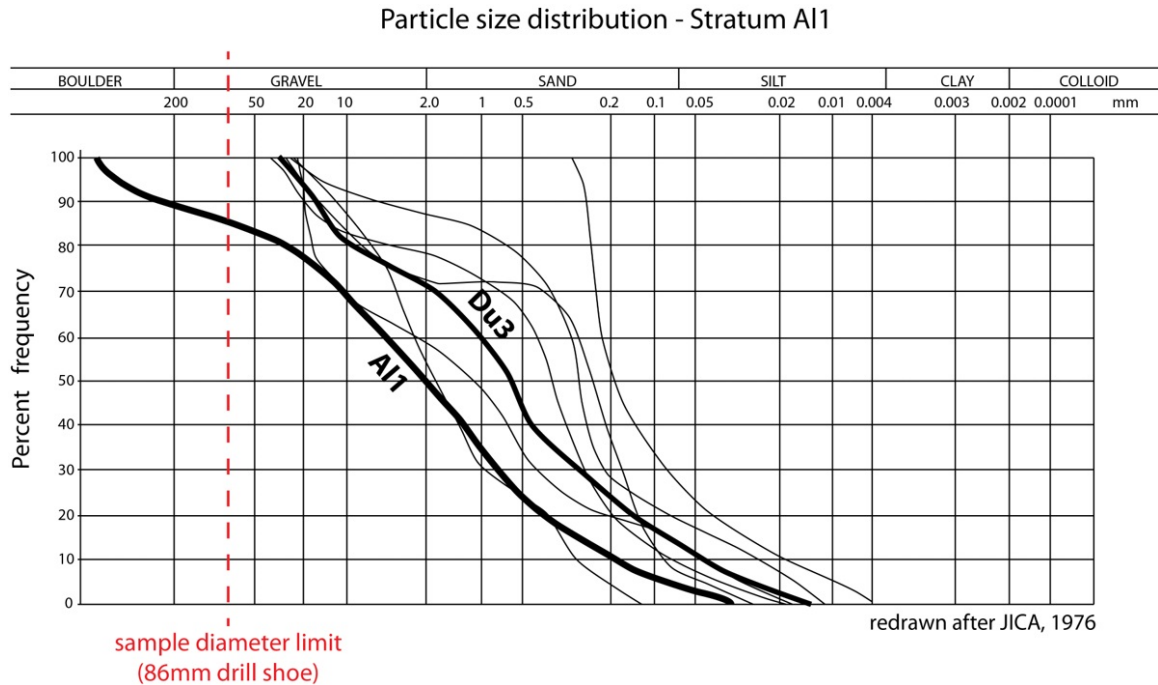
Figure 2.6: Grain size distributions of stratum Al1, the early Holocene gravel unit, and stratum Du3, the late Pleistocene sand unit. Note the sample diameter limit of 86 mm. Redrawn after Japan International Cooperation Agency (1976).
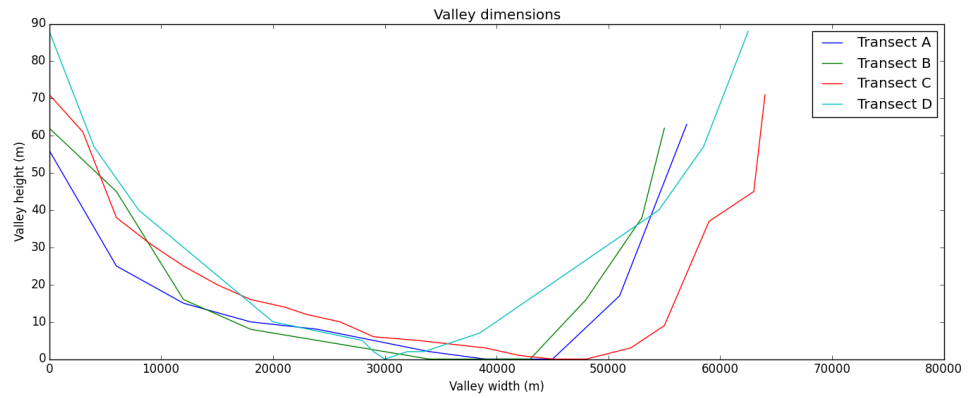
Figure 2.7: Valley width and height (above valley thalweg) at the 4 upstream-most cross-stream transects (see Fig. 2.5 for reference). Transect E is not plotted because the depth of teh valley is not constrained beyond that it is >90 m deep.

Figure 2.8: Images of pebbles and cobbles lodged in the drilling shoe.

calculated Q_w range for the 40,000 m width is in agreement with the empirically-derived flood discharge estimate based on the volume of the lake observed in the upstream catchment (Montgomery et al., 2004), we model discharge up to 5 Sv (Sverdrup, or 1 x 10^6 m^3/s). We also consider a GLOF discharge as low as 3 Sv because, if the flood events were recurring, some of those events were likely much lower in magnitude. Using a range of Manning roughness coefficients from 0.0–0.1, calculated from the Manning formula and comparable to the roughness coefficient used in other studies (e.g., references within Burr et al., 2009), the flood height that would have been generated given the geometry of the Brahmaputra-Jamuna paleovalley reconstructed herein ranges from about 4–60 m high (Fig. 2.9), the maximum of which is roughly coincident with the depth of the paleovalley. Modeled uniform flow velocity results are also given in Fig. 2.9, where the median flood water velocity is shown by the white contours and the maximum flood water velocity is shown by the black contours. These values, ranging from <2 m^3/s up to >3.5 m^3/s are comparable to the calculated velocities in Table 2.1.

The discharge volumes and flow velocities calculated herein are based on depositional evidence in the downstream system, specifically the flow properties required to transport gravel-sized clasts as well as the geometry of the valley downstream that would have acted as a conduit for the floods. These results are of a similar magnitude to independent estimates based on mapping the terraces of the glacially-dammed lakes that were the upstream sources of the floodwater (Montgomery et al., 2004). Because these upstream-driven and downstream-driven calculations converge upon common volumes and velocities, and especially because the height of these floods is generally equivalent to the depth of the paleovalley, we suggest that these paleoflood events were instrumental in forming the Brahmaputra-Jamuna paleovalley.
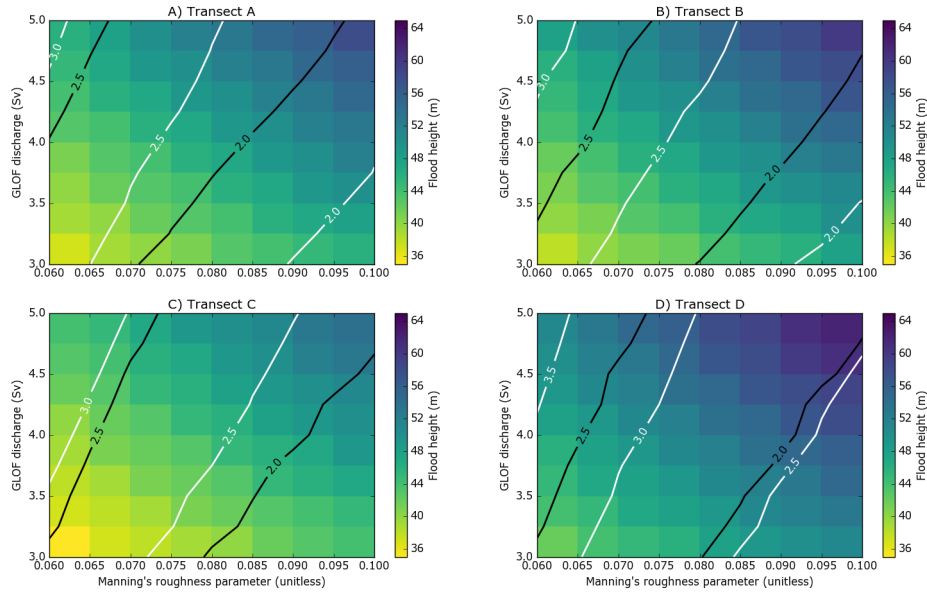
Figure 2.9: Spread of possible flood water heights for plausible bed roughness estimates and GLOF discharge estimates. Flood height is shaded according to the scale at right, median flood water velocity is shown by the black contours, and maximum flood water velocity is shown by the white contours, both given in m/s.

2.5.3 Comparison with Other Systems

Acknowledging that highstand bedrock and alluvial paleovalleys are often much larger than their modern channel counterparts (Gibling et al., 2015; Schumm and Ethridge, 1994), the width of a basal valley unconformity should (to the first order) scale with the size of teh fluvial system and the amount of time over which the valley has been forming (Blum et al., 2013). The basal unconformity of the Brahmaputra-Jamuna paleovalley is ~40 km wide, composed of a gravel unit up to 10 m thick. Although there are no guidelines to suggest how long it would take to form such a wide valley base, it should at least be comparable to other systems that formed under similar environmental conditions and under a similar glacioeustatic regime.

The lowstand Ganges paleovalley is ~35 km wide at the same latitude, in fact, along the same transect (Fig. 2.5E) where the Brahmaputra-Jamuna paleovalley is >80 km wide.

These systems are both monsoon-driven, and their modern sediment loads are very similar, $\sim$520 x 10^6 t/yr for the Ganges and $\sim$540 x 10^6 t/yr for the Brahmaputra (Milliman and Syvitski, 1992), so it is curious that their valley dimensions are not more similar. Another system of similar modern magnitude is the Amazon River. Ria lakes in the modern Amazon system, the troughs of which formed during the LGM in response to sea-level lowstand, are on the order of 20 km wide (Irion et al., 2010), much less than half the width of the Brahmaputra paleovalley. In the ancient record as well, very few valley fills reach the scale of the Brahmaputra-Jamuna paleovalley system; examples that come close include Carboniferous valley fills in Germany (Hampson et al., 1999) and east-central North America (Archer and Greb, 1995; Greb and Chestnut, 1996), both features that formed during high-frequency glacial transition, similar to Quaternary climate (Veevers and Powell, 1987).

2.6   Summary and Implications

Because of the broad shape of the Jamuna valley, the presence of the laterally extensive early Holocene gravel unit, and the incompetent paleohydrological regime during the valley's formation, we propose that the valley was widened during the series of early Holocene megaflood events widely recognized in the literature. These paleoflood events augmented the paleohydrological regime, providing enough energy to deposit and transport the boulder-sized clasts that make up much of the gravel unit, and draining of these sediment-laden previously-dammed lakes may have contributed to more rapid aggradation within the Brahmaputra-Jamuna paleovalley during the early Holocene.

From the process-driven viewpoint of Blum et al. (2013), the genesis of a valley and its associated bounding surface does not necessarily occur in response to a single regressive event, but instead it represents a compilation of responses to variations in base level through time; as detailed by many current researchers in references herein, the erosional unconformity that defines the base of a stratigraphic valley therefore does not necessarily represent what the topography of that valley looked like before infilling. This implies that

the erosional base of a valley is a time-transgressive (diachronous), composite feature, as many researchers have suggested. However, in the instance that a megaflood event (or series of events) created the valley bounding surface, that surface may actually represent a relatively instantaneous point in geologic time.

Chapter 3

Landform Evolution of Late Pleistocene to Recent Terraces of the

Brahmaputra-Jamuna River in the Upper Bengal Basin[1]

3.1 Abstract

Floodplain paleosols and geologic deposits of antecedent landforms, as well as recent

floodplain sediments associated with the Brahmaputra avulsion belt in north-central Bangladesh

preserve cycles of deposition and weathering near the apex of the Brahmaputra-Jamuna fan

delta. In the absence of absolute sediment ages, this stratigraphy and weathering history can

be used to decipher the relative chronology of sediment deposition and terrace formation

in the avulsion belt. Holocene sediments in this region are well dated, but pre-Holocene

deposits have not been resolved beyond 48000 yr BP, the limit of detection of radiocar-

bon dating. As such, terraces have previously been considered uniformly as Pleistocene-

aged. We use detailed sediment analysis of discrete geomorphic domains, encompassing

both fluvial overbank and basinal foredeep environments, to establish the relative chronol-

ogy of terrace formation and elucidate patterns in the long-term (>10 ka) trajectory of the

Brahmaputra-Jamuna River. Across all domains, compositional trends indicate extensive

weathering in Pleistocene-aged units compared to Holocene-aged units. Under magnifi-

cation, the Pleistocene sediments generally display a higher amount of anhedral (as op-

posed to euhedral) crystals, a function of chemical weathering. Clay mineralogy results

show that the basinal foredeep has been receiving sediments sourced from a different par-

ent material than the Brahmaputra's overbank sediments in the avulsion belt across the

Holocene–Pleistocene time boundary. Each geomorphic domain and associated facies has

---

[1]This chapter was written as a manuscript with co-authors JC Beam, AK Covey, JC Ayers, and
SL Goodbred. It is currently in review at Basin Research.

a characteristic mineralogical and microtextural signature, which combined outline a relative chronology of terrace formation, i.e., floodplain deposition and subsequent stranding by the paleo-Brahmaputra River. Unlike the Holocene trajectory of the Brahmaputra-Jamuna, the Late Pleistocene river trended eastward, first depositing and stranding the westernmost terrace sediments and subsequently moving eastward toward the Shillong Plateau. This reconstruction of terrace formation yields the first interpretation of the river's trajectory in the Late Pleistocene, an important step in temporally constraining the evolution of the Brahmaputra during the last glacial period in response to the regional tectonic framework.

3.2   Introduction

The use of an integrated systems, or "source-to-sink" model for linking sedimentary processes with geomorphic landforms has risen to prominence in continental margin studies over the last two decades (e.g., Nittrouer and Driscoll, 1999; Goodbred, 2003a; Allen, 2008; Davidson et al., 2011; Romans and Graham, 2011). This approach has facilitated the calculation of sediment budgets worldwide (e.g., Milliman and Meade, 1983; Syvitski et al., 2005), and floodplains and terraces have been established as important depocenters in the midstream sediment routing system (e.g., Granet et al., 2010; Wittmann et al., 2011; Clift and Giosan, 2013; Rogers et al., 2013).

Because the stability timescale of a floodplain scales with the size of its catchment (Métivier et al., 1999; Sømme et al., 2009), floodplain-turned-terrace sediments in large deltas have the potential to provide perhaps the longest terrestrial record of source-to-sink history. To establish an integrated long-term history of delta evolution, fine-grained sediments that have been stored within Holocene floodplains, antecedent Pleistocene terraces, and an interior sub-basin of the Brahmaputra fluvial fan have been analyzed to establish the relative chronology of deposition of the landforms through which the modern river flows.

The subaerial Bengal (Ganges-Brahmaputra) delta, at 2–24 km thick (Hiller, 1988; Larson et al., 2015; Mitra et al., 2005), has been amalgamating in the Paleogene structural Ben-

gal basin since at least Neogene times (Uddin and Lundberg, 1999). As such, landforms within the subaerial delta have been subject to dozens of cycles of erosion and overprinting, resulting in a complex composite morphology. Compounding this complexity, alluvium enters the delta from multiple major sources—the Ganges, Brahmaputra, Tista, and innumerable smaller but important rivers. In addition, the delta is located at the intersection of two sub-perpendicular collisional mountain ranges, creating topographic relief and high gradients capable of actuating changes in the flow paths of these large rivers. Despite recent strides in understanding the delta's latest Quaternary evolution (Goodbred and Kuehl, 2000a) and Holocene fluvial avulsion history (Goodbred et al., 2014; Pickering et al., 2014), the evolution of the basin prior to the Last Glacial Maximum (LGM) remains unclear.

The goal of this study is to establish the relative depositional chronology of the pre-Holocene Brahmaputra floodplains toward a broad understanding of the river's migrational trajectory in the context of the regional tectonic framework and Late Pleistocene climate. Fine-grained sediments were analyzed to decipher clues about the sediment source and weathering history of landforms in upper Bengal, in order to determine the origin and sequence of deposition of Brahmaputra terraces. By appending this relative chronology of pre-Holocene terrace formation to the known Holocene avulsion history, a generalized account of the Brahmaputra's flow path for the Late Pleistocene has been established.

Expanding upon a published borehole transect from the Brahmaputra avulsion braidbelt (Pickering et al., 2014), lithology and bulk geochemistry were used to assess the degree of weathering of fine-grained sediments from different morphostratigraphic units in and around the braidbelt. Microtextural morphology and clay mineralogy were then used to assess pedogenesis and weathering within 3 comparable geomorphic zones, resulting in a relative chronology of landform evolution of the features that make up the upper delta plain. Results are discussed in the context of the paleo-Brahmaputra's long-term pattern of spatial mobility within the regional environmental framework.

3.2.1 Regional Setting

Where the Brahmaputra River exits the Himalayas it enters the Assam valley as a mixed bedrock-alluvial stream. After flowing westward for ∼900 km, it abruptly turns southward, pinned between the western margin of the Shillong Plateau on the east bank and by the Tista alluvial fan on the west bank (Fig. 3.1). South of the Tista confluence in Bangladesh, the Brahmaputra is referred to as the "Jamuna" ("Brahmaputra-Jamuna" is used herein when referring to this portion of the river). The Brahmaputra-Jamuna continues south between the Bogra and Madhupur terraces and finally joins the Ganga (or "Ganges") to become the Podda (or "Padma") River on a southerly course to the Bay of Bengal.

South of the reach constricted by the Tista fan and Shillong Plateau, the Brahmaputra-Jamuna is free to migrate and flood the adjacent land where antecedent topography does not preclude it from doing so. This reach contains the Holocene Old Brahmaputra avulsion node, where the two main channels are bifurcated by the Jamulpur Terrace, and have spent the Holocene trading or sharing occupation (for the comprehensive avulsion history see Pickering et al., 2014). This upper delta plain avulsion belt is the focus of our study (Fig. 3.2).

The lateral extent of the Brahmaputra avulsion belt is limited by high topography. The surrounding uplands are pre-Holocene weathered floodplains, typically 3–5 m higher than the adjacent alluvial valleys. From west to east, these are the Bogra Terrace, the Jamulpur Terrace, and the Sherpur Remnant (Fig. 3.2). Since Morgan and McIntire (1959), most researchers accept that highlands in Bengal (including the Madhupur and Barind tracts) were deposited during the Pleistocene, although reliable ages of deposition have yet to be reported in publicly available literature. Indeed, only a handful of reliable pre-Holocene ages have been reported at all, from deposits buried beneath Holocene alluvium (Japan International Cooperation Agency, 1976; McArthur et al., 2008; Pate, 2008; Sarkar et al., 2009; Stanley and Hait, 2000; Umitsu, 1987).
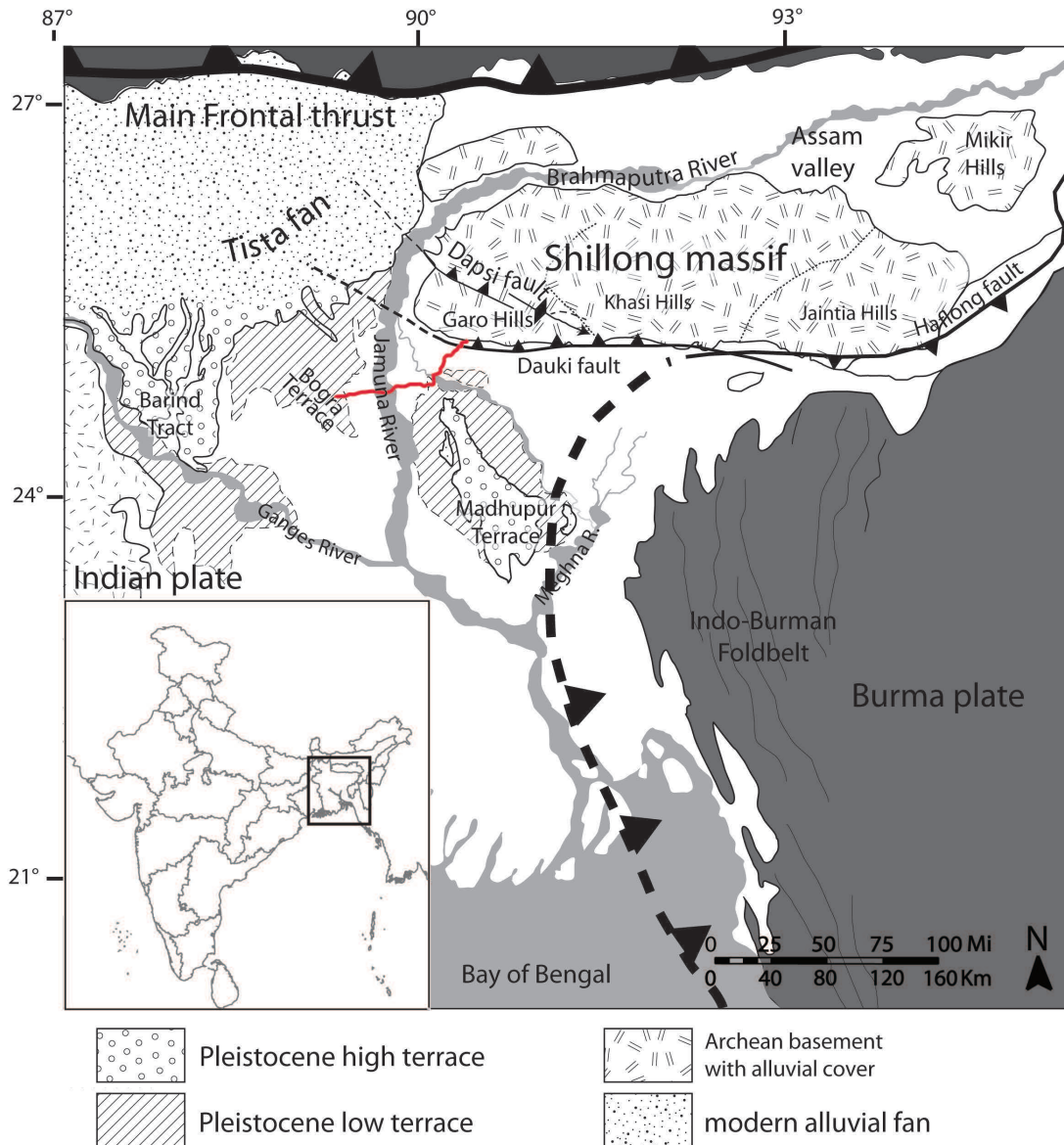
Figure 3.1: Physiographic map of the upper Bengal basin, showing major rivers and relatively high and low terraces. The transect of boreholes sampled in this study is shown in red.
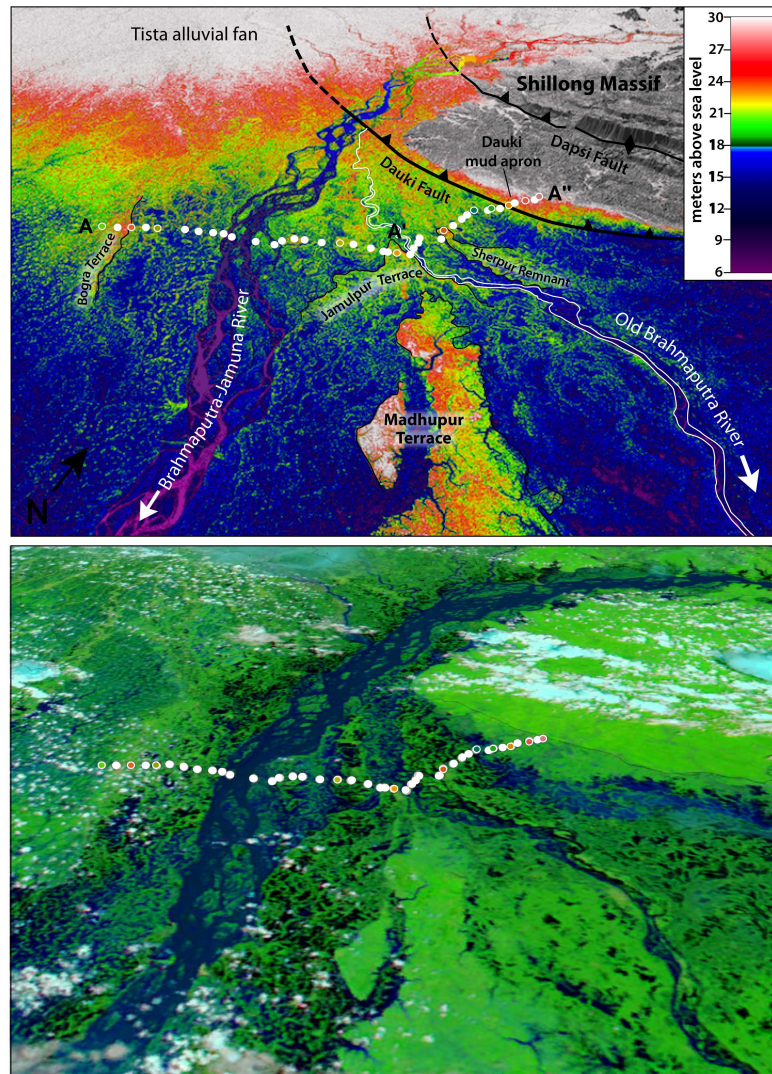
Figure 3.2: Top: Oblique view of the study area, represented as Shuttle Radar Topography Mission (SRTM) digital elevation model (DEM). Geomorphic boundaries and major faults are labeled. The borehole transect is represented by white circles, and colored circles represent boreholes from which samples for this study were collected, where the color corresponds to the surface elevation of the borehole. A–A' and A'–A" transects are shown in cross section in Fig. 3.3. Bottom: Same view of the study area, represented by Moderate-resolution Imaging Spectroradiometer (MODIS) image captured on August 5, 2007 during peak monsoon flooding during an exceptionally wet year. This image depicts the extent of land receiving overbank flooding during peak discharge.

3.3 Methods

The shallow stratigraphy of the Brahmaputra avulsion belt was defined prior to this study based on sediment grain size, geochemical provenance signatures, and radiocarbon dates of a 41-borehole transect (Fig. 3.2, Pickering et al., 2014). Of the 980 samples analyzed for grain size in that study, 180 samples yielded mean diameters <62.5 μm. The surface-weighted mean diameter was used to define the cut-off between fine- and coarse-grained particles because the volume-weighted mean was often too coarse to accurately represent the lithology of the sample (Pickering et al., 2014).

Statistical calculations were performed for all 180 fine-grained samples using the open-source GRADISTAT program (Blott and Pye, 2001). The graphical statistics method of (Folk and Ward, 1957) was utilized in order to accurately represent skewness and kurtosis; results are given geometrically in metric units. The mean grain size (X), sorting (spread, σ), skewness (symmetry or lean toward one side of the mean, Sk), and kurtosis (a measure of the shape of the distribution, representing how much of the sample is concentrated around the mean, K) are reported in App. D.

Major oxide weight percents were determined for sediment powders using a benchtop Oxford Instruments MDX 1080+ X-ray fluorescence (XRF) mass spectrometer (Pickering et al., 2014). The element ratio of K/Si relative to Al/Si is a proxy for chemical weathering in this system (Lupker et al., 2013); data are reported with reference to their chronostratigraphic units.

A subset of 17 of the 180 fine-grained samples were imaged by Scanning Electron Microscope (SEM) and clay mineralogy was determined using X-ray diffraction (XRD) (Fig. 3.3). These samples were selected to represent each of the subfacies of the transect, in order to identify compositional and textural differences across spatial and temporal boundaries.

Saturated cohesive mud plugs extruded while drilling were stamped onto glass slides; the transferred sediment was then carbon-coated. Slides were imaged using a Tescan Vega 3

Figure 3.3: Distribution and relative development of paleosols in A) Brahmaputra-Jamuna valley (A–A'), and B) Old-Brahmaputra valley (A'–A"). Location of 17 samples analyzed for XRD clay mineralogy and SEM magnified textural morphology indicated by red stars.

LMU SEM with a backscattered electron detector and a standard view field of 150 μm at 20 kV accelerating voltage. Textural differences between the Holocene-aged and Pleistocene-aged samples were observed, yielding a qualitative comparison of euhedral versus anhedral overall crystal morphology.

Powder X-ray diffraction scans were obtained as non-oriented powders sieved below 2 μm on a Scintag X1 θ/θ automated powder XRD with a copper (Cu) target, a Peltier-cooled solid-state detector, and a plastic sample holder with well dimensions 25 mm x 25 mm x 2 mm. Each sample underwent a set of 3 analyses: (1) the air-dried sample was analyzed for smectite + illite and kaolinite + chlorite clay minerals; (2) the sample was glycolated for 12 hours at 60°C to expand the smectite layers for analysis; (3) the sample was heated at 550°C to break down illite and analyze chlorite. Estimates of the relative abundance of clay minerals were determined for illite, smectite, chlorite, and kaolinite by measuring the mineral peak area and dividing by the mineral intensity factor, after Biscaye (1965). Presence or absence of goethite was also noted, and the ratio of quartz to clay was estimated by the use of a zinc oxide internal standard and comparison of peak areas to a standard curve of known quartz concentrations.

3.4   Results

Two major lithofacies have been described across the Brahmaputra avulsion belt: the Brahmaputra Valley facies, comprising the Braidbelt Sands and Overbank Muds subfacies, and the Dauki Foredeep facies. These were further divided into Holocene and Pleistocene chronostratigraphic units based on radiocarbon ages, oxidation state, and position relative to prominent floodplain paleosols (Pickering et al., 2014: Table 1). Results herein build upon the fine-grained units of the Brahmaputra Valley and Dauki Foredeep facies.

3.4.1 Chemical Weathering

Despite having reasonable age control for the Dauki Foredeep facies and the Braid-belt Sands of the Brahmaputra Valley facies (Pickering et al., 2014), there are no absolute ages for the Overbank Muds below the Holocene–Pleistocene contact. However, chemical weathering of sediments above and below the contact was assessed by tracking the ratio of mobile K to immobile Si in sediments from each facies over time.

For the modern Himalayan frontal rivers, a plot of K:Si versus Al:Si defines a linear trend with a slope nearly 1:1 (Lupker et al., 2013: Fig. 3a). Figure 3.4 is a plot of those sediments from the modern Himalayan rivers and the Brahmaputra in Bangladesh from Lupker et al. (2013) for reference, along with the buried Holocene Brahmaputra overbank sediments from this study. Note the progressive decrease in slope from modern Himalayan frontal rivers (slope = 0.28) to modern Brahmaputra in Bangladesh (m = 0.17) and buried Holocene Brahmaputra sediments (m = 0.17) to Pleistocene Brahmaputra sediments (slope = 0.06) from this study. This indicates K depletion over time as potassium feldspar and other primary K-minerals such as muscovite weather to form K-poor clay mineral phases such as kaolinite.

Likewise, the Dauki Foredeep facies shows a similar decrease in trend; the slope of the Pleistocene Dauki Foredeep sediments is decreased relative to the Holocene Dauki Foredeep sediments, also indicative of weathering. Note the similarity in slope for the two Holocene units and the two Pleistocene units, respectively (Holocene Brahmaputra = 0.17 vs. Holocene Dauki Foredeep = 0.11, Pleistocene Brahmaputra = 0.06 vs. Pleistocene Dauki Foredeep = 0.03). Sediments from each of the facies are plotted separately because they have different provenances, and the Dauki Foredeep sediments, derived from the Shillong Plateau, consist of recycled, i.e. older, fluvial deposits.
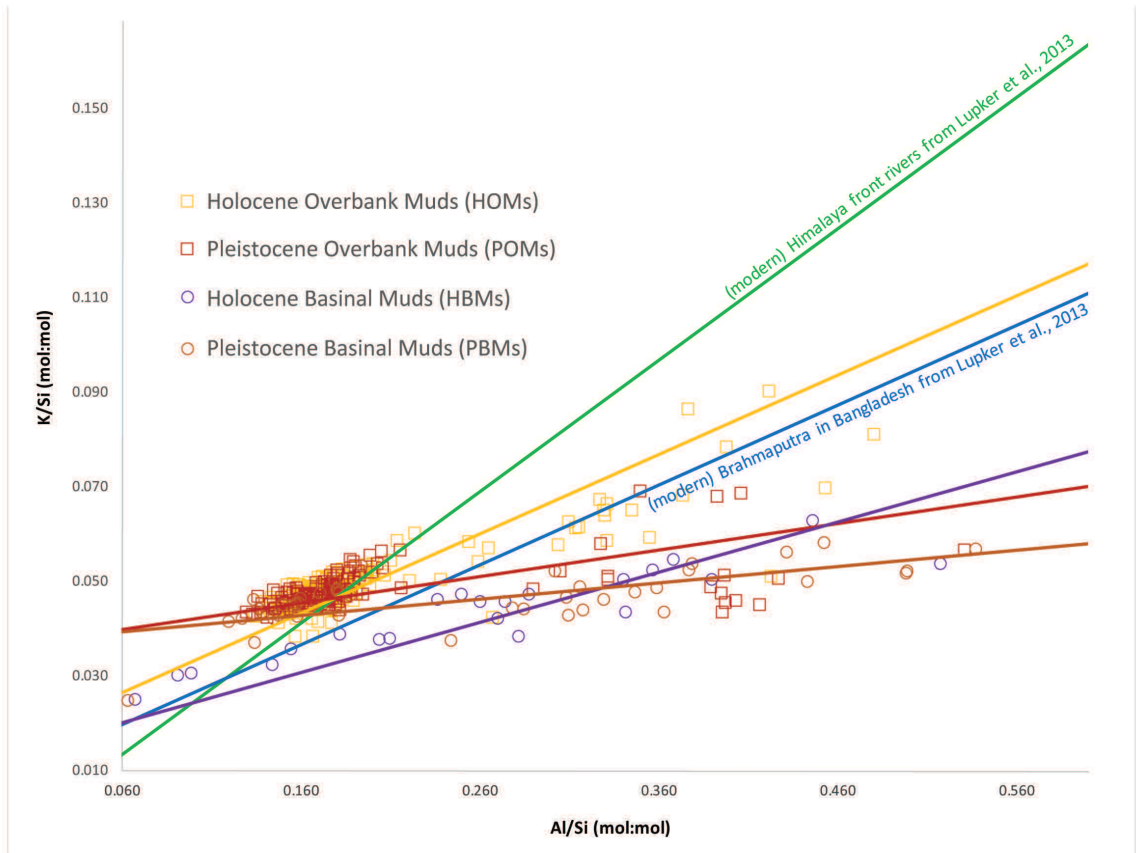
Figure 3.4: Compositional variability of K/Si in Himalayan system from Lupker et al. (2013), with Holocene and Pleistocene sediments from the Brahmaputra Valley and Dauki Foredeep facies of this study.

3.4.2 Grain Size Trends

Aggregate grain size statistics show remarkable homogeneity across the transect. The average sample is a poorly sorted, coarse silt with a symmetrical, mesokurtic grain size distribution (GSD), and this holds true across the transect with few exceptions (App. D). First, sediments from the western and eastern margins of the transect are the least sorted (σ = 3.77—4.08 for Dauki Foredeep and Bogra Terrace, cf. σ = 3.09—3.55 range for all other sediments) of any of the fine-grained sediments sampled. On the western side of the transect at the Bogra Terrace, very poorly sorted GSDs suggest that the river is reworking coarser sediment as it is occupying the western margin of the fan, eroding into the coarser Tista fan. On the eastern side of the transect at the Dauki Foredeep, lesser sorting is a result of the shorter transport distance from the adjacent Garo Hills into the foredeep.

Second, the Pleistocene-aged sediment GSDs (along with the Holocene Dauki Foredeep sediment GSDs) have a unique grain size bin not present in Holocene-aged sediments: About 30% of the 180 fine-grained samples analyzed contain sub-micron (<1 µm) grains, and all but two of those samples are Pleistocene-aged. Samples containing sub-micron grains are interpreted as sediments that have undergone secondary clay mineral formation, resulting from prolonged chemical weathering.

3.5 Lithofacies

Utilizing the facies described by Pickering et al. (2014), the microtextural morphology (Fig. 3.5) and clay mineralogy (Fig. 3.6) of the fine-grained units were further analyzed, yielding a more detailed classification of the fine-grained facies of the Brahmaputra avulsion belt in the upper delta plain. These descriptions are given below and summarized in Table 3.1.
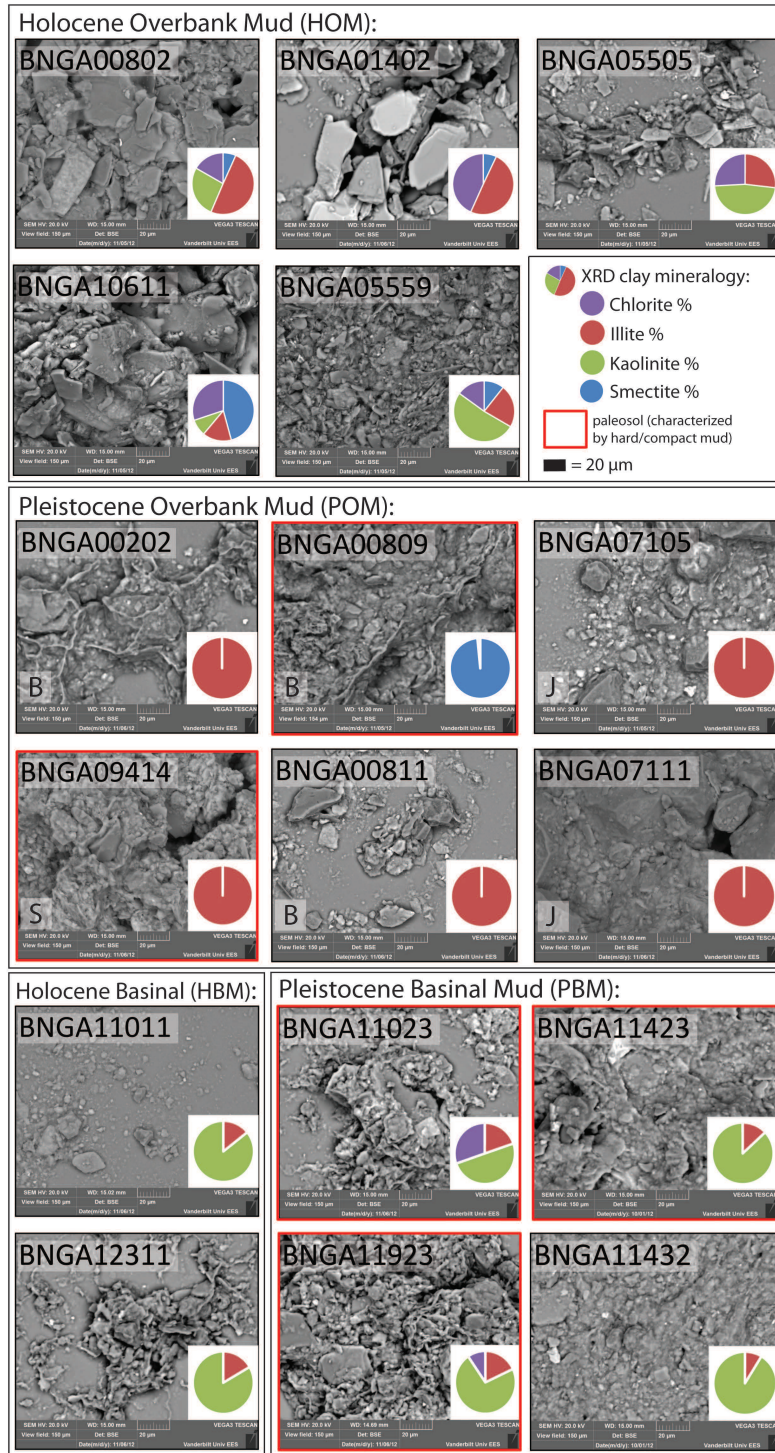
Figure 3.5: SEM images of samples

Scanning electron microscope (SEM) images of 17 samples, grouped by morphostratigraphic units. POM units are labeled with "B" for Bogra Terrace, "J" for Jamulpur Terrace, and "S" for Sherpur Remnant. Pie charts indicate relative amounts of chlorite, illite, kaolinite, and smectite. Horizontal view field is 150 μm for all images.
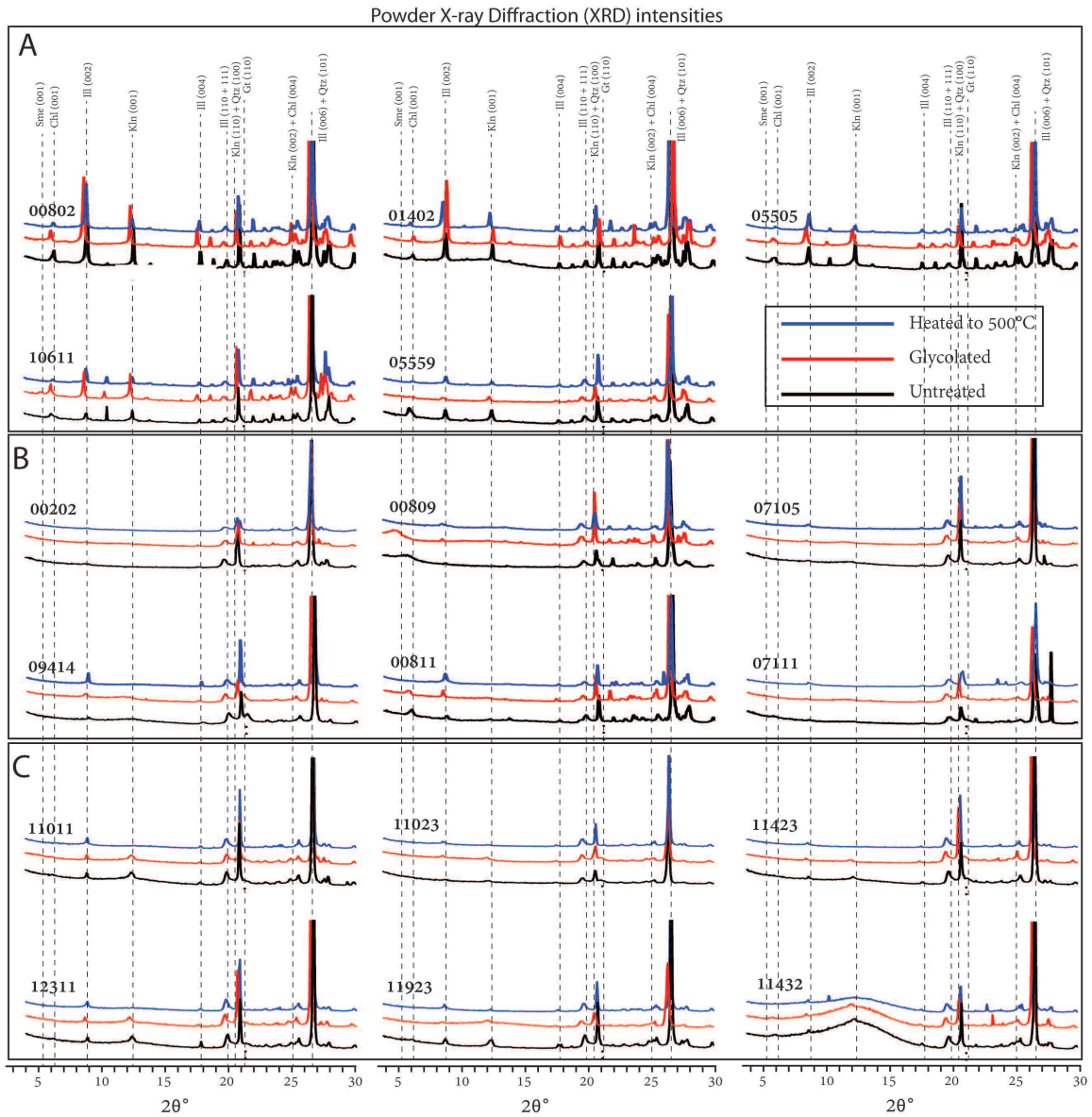
Figure 3.6: X-ray diffraction (XRD) scans of non-oriented powders for 17 samples labeled for comparison with Figures 3 and 5. A) Holocene Overbank Muds (HOMs); B) Pleistocene Overbank Muds (POMs); C) Dauki Foredeep Muds (HBMs & PBMs). Sme = smectite, Ill = illite, Chl = chlorite, Kln = kaolinite, Qtz = quart, and Gt = goethite.

Table 3.1: Summary of chronostratigraphic facies of the upper Bengal delta plain.

Chronofacies	Lithology	Mudcap Thickness	Plasticity (Paleosol proxy)	Microtexture	Mineralogy
Holocene Overbank Muds (HOMs)	Poorly sorted coarse silt; typically, blue-gray or dark gray-brown	1—5 m	highly plastic	uniformly euhedral with relatively large crystals (up to ~50 μm)	contain chorite, illite, kaolinite, and smectite
Pleistocene Bogra Terrace (PBT)	Very poorly sorted coarse silt, friable; yellow-gray to yellow-brown; oxidized below 2-3 m depth	11 m	low plasticity at 9—10 m depth; second unit of low plasticity at 40—48 m depth (below sand package)	anhedral, except one sample directly below paleosol	uniformly illite, except one paleosol sample is uniformly smectite
Pleistocene Jamulpur Terrace (PJT)	Poorly sorted coarse blue-gray mottled silt; hydromorphic below 2-3 m depth	12 m	moderate to very low plasticity at 5—9 m depth	anhedral with few euhedral crystals; euhedral crystals have a granular habit	uniformly illite
Pleistocene Sherpur Remnant (PSR)	Poorly sorted coarse silt of variable color; from top: yellow-gray above dark gray above blue-gray above red-brown above yellow-brown; oxidized below 9 m depth	18 m	moderately plastic	anhedral with few euhedral crystals; euhedral crystals have a granular habit	uniformly illite
Holocene Basinal Muds (HBMs)	Poorly sorted coarse silt; highly variable color, including yellow-gray, red-brown, blue-gray, black, green, brown-gray, and tan silts	up to 20 m	highly plastic	mixed euhedral-anhedral; euhedral crystals are <20 μm	dominantly kaolinite with some illite
Pleistocene Basinal Muds (PBMs)	Poorly sorted coarse silt; highly variable color, including gray, red-brown, blue-gray, dark gray, green-gray, and brown silts	up to 55 m	thick (up to 20 m) deposits of low to very low plasticity	anhedral with few euhedral crystals have a platy habit	dominantly kaolinite with illite and chlorite

Brahmaputra Valley facies (fine-grained fraction) — Pleistocene Overbank Muds (PBT, PJT, PSR)

Dauki Foredeep facies (HBMs, PBMs)

49

3.5.1 Brahmaputra Valley Facies

3.5.1.1 Holocene Overbank Muds

The Holocene Overbank Muds (HOMs) facies consists of thinly bedded, deformable, dark-colored silts interspersed throughout Brahmaputra braidbelt sands as preserved flood-plain deposition (Pickering et al., 2014). Under magnification, these silts display a uniformly euhedral mineral habit with relatively large crystals (up to $\sim$50 μm, Fig. 3.5). The average clay content of HOMs is $\sim$71%. Clay mineralogy is a suite of inherited minerals that includes chlorite, illite, kaolinite, and smectite phases, with no dominant mineral trends; this mixed composition is similar to clay mineral distributions found in Holocene fluvial overbank deposits throughout the delta (Aftabuzzaman et al., 2013; Heroy et al., 2003; Tennant, 2005).

3.5.1.2 Pleistocene Overbank Muds

Unlike HOMs, the Pleistocene Overbank Muds (POMs) outcrop at the surface, capping interfluves of the Brahmaputra-Jamuna and Old Brahmaputra rivers. POMs contain grains smaller than 0.69 μm, whereas HOMs do not; this is the result of secondary (authigenic) clay mineral formation, evidence of weathering, i.e. surface (or near-surface) exposure. In general, POMs are oxidized and consist of lower plasticity sediments than their Holocene counterparts. These low plasticity sediments are interpreted as floodplain paleosols formed during lowstand exposure; the LGM paleosol can be correlated across the Bengal delta and beyond (Alam et al., 1997; Hoque et al., 2012; McArthur et al., 2008; Williams, 2014). However, multi-layer and composite paleosols also exist, and it is worth reiterating that paleosols in the Brahmaputra avulsion belt represent multiple cycles of sea level highstand (aggradation) and lowstand (exposure). As such, these are composite landforms that have recorded multiple glacial-interglacial cycles within the Pleistocene.

The POMs are subdivided into three units, based on their geographic locations: (1) Bo-

gra Terrace, forming the western boundary of the Brahmaputra-Jamuna, (2) Jamulpur Terrace, the interfluve that bifurcates the Brahmaputra-Jamuna and Old Brahmaputra courses, and (3) the Sherpur Remnant, in the eastern portion of the transect, the interfluve that bifurcates the two sub-valleys of the Old Brahmaputra course (Pickering et al., 2014).

3.5.1.2.1 Bogra Terrace Muds

The Pleistocene Bogra Terrace (PBT) consists of very poorly sorted, friable, coarse silts that cap brown, deeply leached, fine to medium sands and silts. The mudcap sediments are oxidized to a yellow-gray or yellow-brown color. Despite this, PBT sediments do not contain detectable goethite. The shallow stratigraphy comprises a compound paleosol, defined as multiple weakly developed paleosols vertically separated by insignificantly weathered sediments by (Kraus, 1999). In this case, the upper unit is a thin, relatively weakly developed paleosol at 9—10 m depth, and the lower paleosol is much thicker and more extensively developed, from 40—48 m depth. These two paleosols are separated by a package of deeply leached fluvial sand with a mixed Brahmaputra-Tista provenance signature (Pickering et al., 2014).

Sediments from this unit display an anhedral crystal habit, with the exception of one sample, which was collected from directly below the upper paleosol (sample BNGA00811, Fig. 3.5). Sediments within the PBT average ∼78% clay content, which is primarily illite, except the paleosol sample, which is primarily smectite with a trace amount of illite. Illite is not often considered a highly altered mineral, but the dominance of smectite in the paleosol sample indicates some weathering has taken place (Gardiner and Miller, 2004). The relatively uniform mineral composition of these sediments reflects the intensity of weathering the soils have undergone (Fig. 3.6); the weathering process has converged, resulting in transformation toward a single phase mineral (Duchaufour, 1982; Velde, 1992).

3.5.1.2.2 Jamulpur Terrace Muds

The Pleistocene Jamulpur Terrace (PJT) consists of poorly sorted, coarse silt capping

brown fine to medium sand. The mudcap sediments are mottled blue-gray gleysols characterized by a completely reduced matrix and concentrated zones resulting from redox reactions, forming rings around clay nodules or root channels. Hydromorphic soils here comprise very low plasticity sediments at 5—9 m depth interpreted as a moderately thick, cumulative paleosol, or a unit that formed as thin, incrementally deposited strata that underwent steady pedogenesis (Kraus, 1999). Pleistocene Jamulpur Terrace sediments have a generally anhedral crystal habit with some large granular (almost equant) crystals interspersed throughout the anhedral matrix (Fig. 3.5). Like the PBT, these sediments are composed predominantly of illite, indicating clay mineral neoformation. Unlike the PBT, PJT sediments average only ∼70% clay content and contain detectable goethite (Fig. 3.6), indicating extensive leaching.

3.5.1.2.3   Sherpur Remnant Muds

The Pleistocene Sherpur Remnant (PSR) consists of a relatively thick (18 m) mudcap atop reddish-brown very fine to fine sand. Color of the silts is variable, beginning with yellow-gray at the surface, followed by a dark gray organic layer at 6 m depth. A blue-gray mottled cumulative paleosol begins at 8 m depth, grading into oxidized red to yellow-brown silt at 18 m depth. The entire paleosol exhibits moderately low plasticity, but muds of this unit are slightly more deformable than those of the PBT or PJT, indicating that the PSR unit has undergone relatively less intense weathering compared to the other two terraces. Like the PBT and PJT sediments, PSR sediments have a generally anhedral crystal habit (Fig.3.5) and the clay mineral fraction (∼77%) is composed predominantly of illite but contains detectable goethite (Fig. 3.6), indicating extensive leaching.

3.5.2 Dauki Foredeep Facies

3.5.2.1 Holocene Basinal Muds

The upper ~20 m of strata in the Dauki Foredeep sub-basin are Holocene-aged deposits (Pickering et al., 2014). Strata of the Holocene Basinal Muds (HBMs) are very heterogeneous and include coarse, angular sands as well as finer basinal muds. The Dauki Foredeep is seasonally flooded and contours the southern margin of the Shillong Plateau along the Dauki thrust fault (Fig. 3.2); as such it accommodates seasonal precipitation and overflow of south-flowing rivers that drain the Garo Hills (southwest Shillong Plateau), which generates the stratigraphy of coarse angular sands interspersed within fine units (Pickering et al., 2014). Fine-grained units are highly deformable, poorly sorted, coarse silts with highly variable color, including yellow-gray, red-brown, blue-gray, black, green, brown-gray, and tan deposits. Under magnification, these silts are a mix of euhedral and anhedral crystal habits, and the euhedral crystals are typically <20 μm (Fig. 3.5). The average clay content of HBMs is ~66%, which is dominated by kaolinite (normalized to ~85%) with some illite (normalized to ~15%); goethite is detectable in these samples, evidence that these Holocene-aged sediments are older, recycled alluvium.

3.5.2.2 Pleistocene Basinal Muds

Pleistocene Basinal Muds (PBMs) consist of poorly sorted, coarse silts of various colors, similar to HBMs. These are very thick deposits, up to 55 m in the northernmost area of the transect. The contact between the Holocene and Pleistocene units was demarcated by the presence of a thick (up to 20 m) composite paleosol of low to very low plasticity. Radiocarbon ages confirmed that this composite paleosol represents pre-Holocene deposition (Pickering et al., 2014). Under magnification, these muds have a predominantly anhedral crystal habit with few euhedral crystals interspersed; euhedral crystals have a platy habit (Fig. 3.5). The average clay content of PBMs is ~74%, which is, like the HBMs, primarily

kaolinite (normalized to ~50–90%) with smaller percentages of illite (normalized to ~10–20%) and chlorite (normalized to ~10–30% when present), with goethite detectable in half of the samples.

3.6   Sediment Chronostratigraphy

The HOM facies has a mixed clay composition that includes chlorite, illite, kaolinite, and smectite; the POM facies is composed largely of illite and smectite mineral phases, sometimes containing goethite; and the Dauki Foredeep facies, both the HBMs and PBMs, are composed dominantly of kaolinite (Fig. 3.5). In general, illite and chlorite are associated with physical weathering, or erosion by transport, suggestive of a young clay mineral that has not undergone extensive chemical weathering after deposition or only early diagenesis (Dunoyer De Segonzac, 1970; Gardiner and Miller, 2004; Weaver and Pollard, 1973). Conversely, smectite and kaolinite are associated with more intense chemical weathering in general and in particular in this system (Debrabant et al., 1993; Derry and France-lanord, 1996). Indeed in this system, Colin (2006) classify smectite and kaolinite as pedogenic clays, and feldspar, quartz, illite, and chlorite as primary minerals.

Clearly evident from radiocarbon ages, the Holocene Overbank Muds (HOMs) and Holocene Basinal Muds (HBMs) represent the most recent and synchronous sediment deposition(Pickering et al., 2014). However, in terms of mineral alteration these two units are distinctly different. The HOMs are less altered than the HBMs, which are dominated by illite and kaolinite (Fig. 3.5). The dominance of kaolinite does not vary across the Holocene-Pleistocene contact in the Dauki Foredeep, indicating that both HBMs and PBMs have inherited their more altered mineralogical state from the adjacent Shillong Plateau.

The POMs, on the other hand, are composed uniformly of illite or smectite (Fig. 3.6), indicative of mineral alteration; the relative homogeneity of the POM sediments suggests that they have undergone in situ weathering, compared to the more heterogeneous HOM mineralogy. It is clear that the Holocene sediments of both the Brahmaputra Valley and

Dauki Foredeep facies represent more recent deposition than the Pleistocene sediments based on radiocarbon ages and lack of paleosol development. However, the relative ages of the Pleistocene units cannot be deciphered from compositional data or mineral phase alteration because the PBMs inherited their advanced pedogenic mineral phases, evidenced by the similar mineralogy of Holocene and Pleistocene Dauki Foredeep basinal muds.

3.7 History of Pleistocene Terrace Development

Thus paleosol development, morphology, and elevation of the exposed Pleistocene landforms are used to reconstruct their relative timing of formation, yielding the first interpretation of the Brahmaputra River's trajectory over Late Pleistocene phases of eustasy and tectonic deformation of the Bengal basin.

3.7.1 Degree of Paleosol Development within Each Unit

Each of the Pleistocene landforms is characterized by a paleosol with distinctive characteristics. The Bogra Terrace is characterized by a compound paleosol, the upper and lower units of which are separated by meters of heavily leached (eluviated) sandy silts. The deep weathering profile of this terrace suggests that these deposits have not been reworked by the Brahmaputra or local rivers since at least the previous highstand. In other locations, a shallow paleosol of Pleistocene age would be interpreted as the LGM lowstand paleosol (cf. Ghosal et al., 2014; Hoque et al., 2012; McArthur et al., 2008: e.g.). However, due to the continuous weathered profile, the PBT tread has likely been exposed considerably longer than since the LGM. No other terrace feature in the study area has as thick of an eluviation zone nor a compound (double) paleosol sequence. For these reasons we consider the PBT to be the oldest of the Pleistocene landforms along this transect in the northern Bengal basin. A composite paleosol represents periods of non-steady deposition punctuated by periods of negligible erosion (Kraus, 1999); as such the sediments that constitute this terrace represent levee deposits of the paleo-Brahmaputra.

The PBT surface has only been eroded on its eastern boundary, and thus represents the westernmost extent of the Brahmaputra channel belt since at least the last sea-level highstand. The last lowstand exposure surface is preserved about 9 m below the surface, and this paleosol is correlative with the paleosol recognized at 30–45 m depth in other boreholes south of the Ganges river about 100–150 km downstream of PBT, which comprise sediments of Brahmaputra origin (Goodbred et al., 2014; Hoque et al., 2014; Ullah, 2010). The paleoslope defined by the PBT surface to the buried paleosol in the lower delta is 2 x 10^4, the same slope of the modern fan delta floodplain (Wilson and Goodbred, 2015). Further, the scarp defining the eastern boundary of the PBT is found to extend due south to the lower delta, where it is buried by Holocene sediment (Hoque et al., 2014; Patrick, 2016).

As distinct as the PBT is among the regional terraces, differentiating the Jamulpur Terrace (PJT) and the Sherpur Remnant (PSR) is more difficult. Each of these terraces is characterized by a cumulative paleosol, representing steady sediment accumulation with minimal erosion, typically in floodplains or floodbasins distal to the mainstem (Kraus, 1999). Consideration of the morphologies of the PJT and PSR surfaces reveals similarly-shaped bifurcating interfluves of comparable elevation (Fig. 3.2), suggesting that they are genetically related and were coevally exposed (Blum and Törnqvist, 2000). The PJT sediments exhibit slightly lower plasticity than the PSR samples, consistent with induration caused by secondary mineral formation and pore space reduction. Differences in the thickness and stiffness of each terrace's mudcap may be explained by their relative proximity to the Dauki Foredeep: The PSR is closer to the foredeep and thus may be subject to a slow but not inconsequential rate of subsidence, as suggested by north-dipping Pleistocene surface toward the Dauki fault. Modest accommodation at the PSR is readily filled with overbank fine sedimentation, resulting in a thicker mudcap that is uniformly, moderately stiff compared with the thinner but very stiff mudcap atop the PJT sediments.
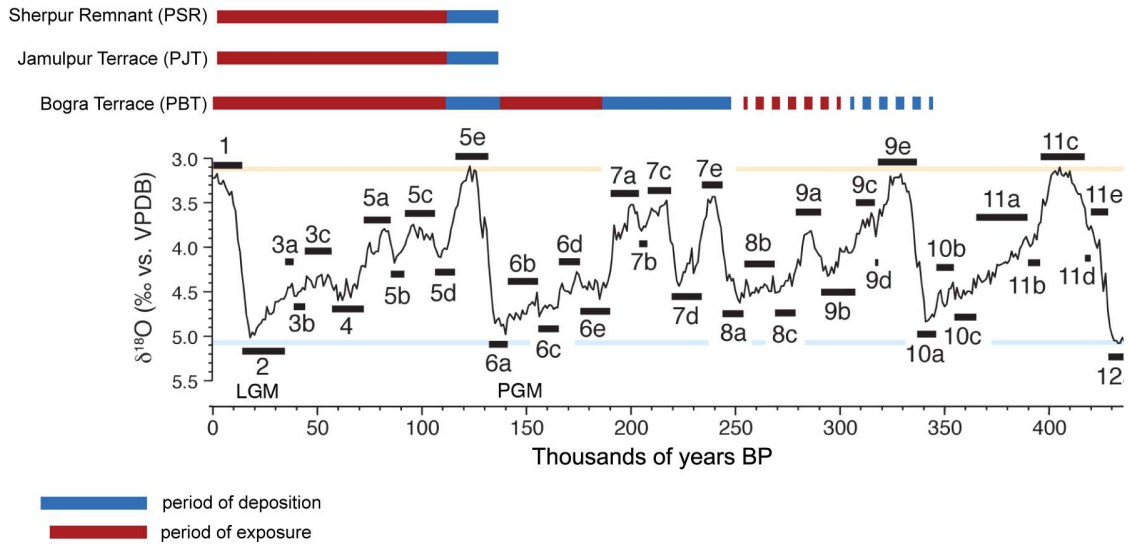
Figure 3.7: Marine isotope stages (MIS) of the last 500,000 years modified from Railsback et al. (2015) with interpreted periods of deposition and exposure from terrace landforms of this study. Dashed lines represent uncertain but possible periods of deposition.

3.7.2 Chronology of Terrace Development

Assuming the uppermost unit (at 9 m depth) of the compound paleosol of the PBT represents the exposed weathering surface during the last sea-level lowstand (roughly MIS 2), the lower unit then represents the exposed surface during the penultimate sea-level lowstand (roughly MIS 6). It follows that deposition of the sediments constituting this terrace were deposited intermittently since MIS 7 or earlier through MIS 5e, with minimal post-LGM deposition in the upper few meters. Figure 3.7 shows these phases of deposition and exposure for each terrace with reference to the marine isotope stages during which they occurred.

The PBT sediments are more weathered than the PJT and PSR sediments, the latter two being coeval. The PJT and PSR sediments then must have been deposited during MIS 5e, the last sea-level highstand prior to the current highstand that followed a significant lowstand, capable of generating the accommodation space required to deposit tens of meters of floodplain sediment in the upper Bengal basin. Exposure of these terraces followed MIS

5, continuing to present.

Based on the sequence of formation of the POM terraces, it appears that the general trajectory of the Brahmaputra River trended eastward toward the Shillong Plateau, first depositing the sediments that would become the PBT, then depositing the sediments that would become the PJT and PSR. Given the hundreds of thousands of years over which these processes occurred and the potentiality for non-deposition and erosion, the trajectory of migration of the Brahmaputra within its fan as evidenced by the deposition and subsequent stranding of these terraces can only be very broadly generalized. However, the trend of the river to move eastward toward the Dauki foredeep and the Sylhet Basin is the logical long-term (10^5 ka) trajectory, considering the regional tectonic framework, in which the Shillong Plateau is overthrusting the upper delta plain, creating a zone of subsidence along the Dauki fault.

3.8   Summary and Conclusions

In order to understand the long-term trajectory of the Brahmaputra River in its upper delta plain, sediments from fine-grained, cohesive, upland units of the marginal foredeep basin and interfluvial landforms of the Brahmaputra avulsion belt were analyzed, resulting in a relative chronology of terrace formation, i.e. floodplain deposition and exposure by the Brahmaputra River.

Sediments of the westernmost Bogra Terrace were deposited during MIS 7 and 5e, with exposure occurring after each highstand. Sediments of the Jamulpur Terrace and Sherpur Remnant were deposited no later than MIS 5e, with exposure occurring during and since the subsequent lowstand. The relative chronology of deposition of these landforms demarcates the trajectory of the river throughout the Late Pleistocene, during which time the river migrated principally from west to east, toward the Dauki foredeep, a subsidence attractor created by Shillong Plateau overthrusting.

Chapter 4

Influence of Regional Fluvio-Tectonic Interactions on Downstream Sediment

Dispersal: Uplift-Controlled Depositional Lobes of the Paleo-Brahmaputra River

4.1   Abstract

Unlike most of the world's major rivers, the Brahmaputra follows an especially anfractuous flow path as it winds around the eastern syntaxis of the Himalaya and again around the Shillong Plateau, an actively growing doubly plunging antiform. Considered herein is the interaction between the Brahmaputra River and this regionally important antiform by examining the stratigraphy in the delta downstream from the fluvio-tectonic interaction preserved in uplifted outcrops and buried sediments spanning the entire subaerial delta. Analysis of sediments from 118 outcrops and 143 boreholes reveal 3 general zones of deposition governed by unique fluvio-tectonic regimes. In the eastern delta, deformed subsurface sediments as well as uplifted sediments on the western escarpment of the plateau document a zone of deposition that was occupied during incipient uplift of the western margin, presumably before the expression of surface topography was sufficient to preclude the river from flowing through this region. In the western delta, up to 65 km west of the modern river, Brahmaputra sediments dominate the subsurface stratigraphy, despite relatively high topography which should act as a barrier to fluvial deposition, indicating that the river was being routed westward in response to uplift of the western margin of the Shillong Plateau. In the central delta, relatively young sediments form and fill the Brahmaputra-Jamuna paleovalley along the path of steepest descent, suggesting that the river has equilibrated since westward deflection by the uplifting antiform. These results document regional fluvio-tectonic interaction on a major world river and suggest that the river is able to overcome the

effect of tectonic deflection over a hundred-thousand-year timescale with sufficiently high discharge. We propose that tectonic influence may control the course of the river during periods of relatively low discharge, but given enough discharge, the river is able to erode the margin of the active uplift, following the steepest route to base-level.

4.2   Introduction

Because rivers are inherently mobile, they can potentially record changes to environmental boundary conditions in the stratigraphy they generate. These system changes can be either internally (autogenically) or externally (allogenically) generated (e.g., Holbrook et al., 2003; Stouthamer and Berendsen, 2007; Leeder, 2011). External forcing mechanisms are those influences that are independent of the river, such as changes in climate or tectonic setting. A major goal of fluvial stratigraphy is to understand the consequences that environmental forcings have on intrinsically mobile river systems. To broaden our understanding of how rivers interact with their environments, the objective of this study is to investigate the stratigraphy generated by an alluvial system that traverses the margin of a landscape undergoing surface uplift, while considering the role of glacioeustasy on the generation of that stratigraphy.

For rivers in uplifting terrains, orogenesis, occurring over timescales on the order of 10^6–10^9 years) controls the environmental framework of the system by affecting basin characteristics, such as topography, sediment availability, even climate (Schumm et al., 2000). However, rivers directly respond to land surface elevation changes at the local to regional level, with different responses at each scale; most studies have focused on the role of local deformation, despite the potential for extracting detailed stratigraphic histories from regional structures (Holbrook and Schumm, 1999).

Regional deformation tends to occur over 10^3–10^4 years, coincident with the observational gap that exists beyond documented history (up to 10^2 years at most) through 10^4 years ago, which results from the lack of a geochronometer refined enough to reliably un-

ravel the stratigraphic record younger than 10^4 years (Miall, 2014). Observations over this 'meso-timescale' are essential in connecting modern fluvial processes to the ancient fluvial record, a topic that has recently become a major focus of sedimentology (e.g., Davidson et al., 2011). Delta tank experiments have the potential to bridge this gap, as they can be scaled up to the meso-timescale, but they must be compared to observations from natural systems to inform scalable models for geologic interpretation.

Herein is presented a study of regional-scale fluvio-tectonic interaction between the Brahmaputra River and the adjacent Shillong Plateau, an actively deforming antiform south of the eastern Himalaya (Fig. 4.1); this interaction is recorded in about half a million years of stratigraphy along the uplifted margin and in the delta downstream. The timescale over which this has occurred provides a perhaps unprecedented opportunity to study the recent (Holocene) river response to ongoing land surface uplift in the geologic context of this river's own uplifted (Pleistocene) sediments. We observe and document spatial changes in the distributive lobes of the Brahmaputra through multiple glacial-interglacial stages during incipient to ongoing surface uplift of the western escarpment of the Shillong Plateau. This study thereby links modern process to preserved stratigraphy and contributes a detailed observation-based fluvial history, including the difficult to observe meso-timescale, to the field of fluvio-tectonics.

4.2.1 Background

The Brahmaputra River flows eastward through the Tibetan Himalaya, then abruptly turns southwestward into Arunachal Pradesh (India), then south into Assam where it flows westward until the westernmost extent of the Shillong Plateau. At the margin of this antiform, the river duly turns south into Bangladesh before flowing into the Bay of Bengal. Of the world's major rivers, the course of the Brahmaputra is among the most anfractuous. From a qualitative perspective, only a few rivers compare: The Ordos Loop of the Huang He (Yellow River) is one example, where the river traverses the Loess Plateau and cir-
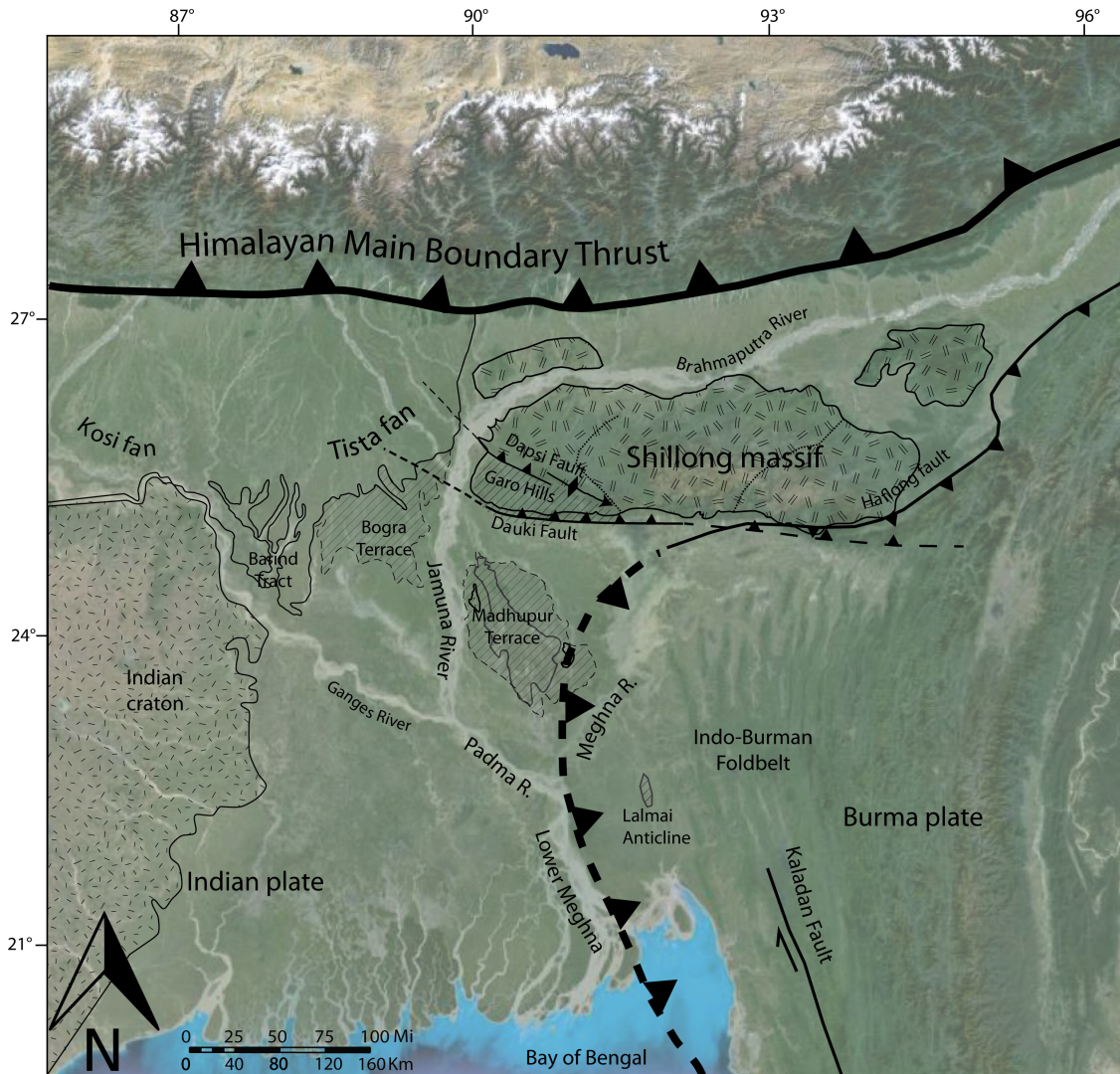
Figure 4.1: Regional setting of Himalaya and Indo-Burman Range tectonic convergence. The Brahmaputra, Ganges, and Meghan rivers converge in the Bengal basin, in the foreland of the two thrust boundaries. Regionally important physiographic features are labeled.

cumnavigates the Ordos Desert; The Samara Bend of the Volga River, around the Zhiguli Mountains is another example; The Orinoco and Congo Rivers also have high variances from their directional means owing to their semicircular flow paths as they circumnavigate the Guiana Highlands and the Cuvette Centrale, respectively. The Brahmaputra River, however, has a very dramatic non-unidirectionality, with a 180° hairpin turn, known as the Great Bend, around the eastern syntaxis of the Himalaya, as well as this 90° turn southward into Bangladesh around the Shillong Plateau. This winding flow path is the result of the evolution of the paleo-Brahmaputra River in response to structural deformation related to uplift of the eastern Himalaya and the Shillong Plateau.

4.2.1.1 Regional Drainage Development and Tectonic Setting

Two main tectonic events are responsible for the development of the Brahmaputra River as it exists today: the establishment of the Brahmaputra during early Himalayan convergence, as well as later re-routing of the river around the Shillong Plateau. Multiple studies (Brookfield, 1998; Uddin and Lundberg, 1999; Alam et al., 2003; Uddin and Lundberg, 2004; Rüber et al., 2004; Britz, 2009; Cina et al., 2009; Robinson et al., 2013; Bracciali et al., 2015) support initial establishment of the Brahmaputra River having occurred in the Miocene when the Yarlung-Tsangpo, the uppermost reach of the modern Brahmaputra that flows eastward through Tibet, disconnected from the Irrawaddy River and was subsequently captured by the Lohit-Brahmaputra as deformation of the eastern Himalayan syntaxis commenced.

Likewise, the structural control of the Shillong Plateau on the flow path of the Brahmaputra has been implicit in the literature for decades (Johnson and Alam, 1991; Uddin and Lundberg, 1999), but the specific timing of when uplift rerouted the Brahmaputra has only recently been well constrained. Exhumation of the Shillong Plateau has occurred in two phases since the mid-late Miocene (Bilham, 2001; Biswas et al., 2007), with the early phase dominated by relatively slow exhumation and the erosion of overlying sediment. Only since

the Pliocene or later does it appear that basement rock was relatively rapidly and fully exhumed with continued uplift generating high topography of the modern system, causing drainage reorganization of the Brahmaputra by about 2 Ma (Najman et al., 2016). Since then the Brahmaputra has traversed the north flank of the antiform turning southward only at the western extent of the uplifted plateau. Uplift of the Shillong Plateau, however, is ongoing (Ferguson et al., 2012; Islam, 2012) and because the Brahmaputra closely follows the western margin of the antiform, the river and the land surface deformation are likely interacting.

The interaction of this regionally important uplifting antiform with the Brahmaputra River is considered here by examining the stratigraphy preserved in the delta downstream from the fluvio-tectonic interaction. We readily identify from borehole transects and uplifted outcrops three phases of sediment deposition related to uplift of the western escarpment of the Shillong Plateau: (1) deposition along a flow path that existed during the incipient stage of surface expression of the western margin, (2) deposition that occurred in response to uplift of the western margin, which deflected the river westward, and (3) deposition along the modern flow path, which appears to currently be in a state of equilibrium since the river was deflected.

4.3 Methods

The methods and results of many of the boreholes utilized in this chapter have been discussed in detail in the preceding chapters and elsewhere (Ch. 2 and 3 in this dissertation; Ullah, 2010; Goodbred et al., 2014; Pickering et al., 2014; Williams, 2014; Hartzog, 2015; Wilson and Goodbred, 2015; Patrick, 2016). In the interest of brevity, the reader is referred to those works for detailed drilling, sampling, and laboratory methodologies. To summarize, sediments collected from boreholes underwent grain size and geochemical provenance analyses, and radiocarbon dates obtained from organic material recovered from sediment samples were used to determine ages of Holocene units and to broadly classify

deposits older than 48 ka (the limit of detection of radiocarbon dating) as Pleistocene-aged. Geochronological results are summarized in App. C.

4.3.1 Stratigraphic Analysis

Stratigraphic data utilized herein include sediment samples from 143 subsurface boreholes (up to 95 m deep, sampled every 3 m, with ∼3–5 km spacing), divided into 12 mostly west to east transects that span the entire subaerial Bengal delta. In addition, 118 outcrops along the western escarpment of the Shillong Plateau, covering a land area of ∼1500 km^2, were surveyed and sampled. Outcrops were mapped and described in the field using an iPad equipped with both American GPS and Russian GLObal NAvigation Satellite System (GLONASS) capabilities, as well as GIS Pro software. Initial field investigations revealed that 63 of these outcrops were composed of fluvial sediments, some of which were composed, to varying degrees, of very thick-bedded, cross-stratified, fine to medium-grained sands, suggesting deposition by a very large stream with a distal sediment source, an environment that is incompatible with the current physiography of the western Shillong Plateau. Thus, an initial hypothesis was developed: alluvium matching this description was deposited by a large river and subsequently uplifted. The field approach was tailored to confirm or negate this hypothesis. In two follow-up field seasons. The objective was to map and describe in detail these alluvial outcrops.

4.3.1.1 Facies Analysis of Outcropping Alluvium

Stratigraphic analysis of outcropping deposits was approached hierarchically by first observing sediment body dimensions, then measuring bedset and bed thicknesses where possible, followed by analysis of internal bedform structure, and finally describing sediment attributes, including grain size, sorting, and rounding. Sediment body and bedding unit dimensions are an indication of depositional energy as well as environment stability (Miall, 2000); beds were described according to the thickness scheme of Blatt et al. (1980),

in which very thick strata are >1 m, thick strata are 30—100 cm, medium strata are 10—30 cm, and thin strata are 1—3 cm thick. Bedform analysis followed the criteria outlined by Allen (1963, 1965), wherein bedforms were characterized by grouping, magnitude, environment, lower bounding surface, and lithology. Finally, an in-field assessment of the degree of weathering was made for alluvial outcrops based on the weathering scale presented in Table 4.2.

Where cross-stratification was observed, this became the primary focus of field analysis because bedforms provide a basis for understanding channel dimensions (e.g., Cheel, 2005). Determining channel geometry from bedforms is, however, only possible if enough facies information is obtainable, and this becomes even more difficult when reconstructing large channels (10^3—10^5 m wide) due to inadequate outcrop exposure (Miall, 1985). Empirically-derived relationships allow channel cross-sectional area to be estimated from bedforms, but these require assumptions about velocity and channel depth (e.g., Rubin and McCulloch, 1980) or only pertain to rivers of a certain magnitude or planform, e.g., meandering rivers (Reinfelds and Bishop, 1998). Because our hypothesis hinged upon deposition by a large fluvial system, we used bedforms of the modern Brahmaputra-Jamuna as a basis for determining channel scale; in the modern system, dunes make up 40—100% of bedforms, depending on flow stage (Roden, 1998), and the average dune dimensions are 1 m in height with a 37 m wavelength Best et al. (2003). Figure 4.3 shows several examples of planar beds (A and D) and cross-stratification (C), which were used for qualitative comparison.

4.3.1.2   Facies Analysis of Subsurface Sediments

Stratigraphic analysis of buried sediments was determined by measuring the particle size of sediments sampled during borehole drilling. Grain size was analyzed using a Malvern Mastersizer 2000E, results of which define packages of generally sandy stratigraphy with minor gravel and localized mud units. Due to the nature of the unconsolidated sediments and

the drilling technique utilized, no information about bed thickness, bedforms, or sedimentary structures is available for buried sediments. However, radiocarbon dates in addition to sediment rheology (i.e., plasticity of mud deposits, see Ch. 3) enable identification of Holocene and Pleistocene sediment sequences.

4.3.1.3   Provenance of Borehole Sediments

In the case of borehole sediments in the upper Bengal delta proximal to the Shillong Plateau, fluvial provenance can, for the most part, be readily determined in hand sample based on sedimentological attributes and overall color (Fig. 4.2). Sediments originating in the upstream catchment of the Brahmaputra River, for example, are sourced from trans-Himalayan monzonites and thus have a different mineral composition than sediments originating from the Shillong Plateau. In Figure 4.2A, the sand on the left was transported by the Brahmaputra, and the sand on the right was transported by a local stream draining the Shillong Plateau. Attributes like color, rounding, and sorting are quick indications of whether a large river like the Brahmaputra transported the sediments from the Himalaya to the basin, or alternatively, the sediments were transported by a smaller, local river draining the Shillong Plateau.

Away from the influence of the plateau, differentiating fluvial provenance requires geochemical analysis because several major rivers transport sediments into the delta, and while these may have some slight color differences, particle rounding and grain size sorting are generally similar. However, bulk sediment geochemistry, and strontium concentration in particular, has proven effective in differentiating fluvial provenance in the Bengal delta because the sediment load of each river has a unique Sr concentration range with little overlap among rivers (e.g., Singh et al., 2006; Garzanti et al., 2010; Goodbred et al., 2014). These ranges, or provenance signatures, are given in Table 4.1. Typically, if the Sr concentration of a group of samples falls between 2 of the ranges, it is interpreted as a zone of sediment mixing between the rivers, assuming spatial compatibility. Note that independent tests of

Table 4.1: Ranges of bulk sediment Sr concentrations determined by XRF mass spectrometry for different fluvial sources in and around the Bengal Basin.

Fluvial provenance	Range of Sr concentration (ppm)	Source
Brahmaputra mainstem	>140	Goodbred et al. (2014)
Ganges mainstem	<100	Goodbred et al. (2014)
Tista River	<90	Ullah (2010) & this paper
Barak-Surma-Kushyara	60—90	Williams (2014)
Locally-sourced Shillong streams	<85	Pickering et al. (2014)
Indo-Burman foldbelt	<60	Williams (2014)

this dataset show that there is no significant correlation between bulk Sr concentration and grain size (Goodbred et al., 2014); thus sands and muds may be considered together when interpreting provenance from bulk Sr geochemistry.

4.3.1.4 Provenance of Exposed Outcrops

Where sediments have been exposed to weathering, fluvial provenance cannot be identified by analyzing bulk Sr concentration. Strontium readily substitutes for Ca and is primarily contained in Ca-plagioclase minerals in the Brahmaputra system (Garzanti et al., 2010); Ca-plagioclase is among the most easily weatherable minerals (e.g., Anbeek et al., 1994), so outcrops that have been exposed to weathering may contain considerably less Sr by weight percent than buried sands. We therefore do not attempt to determine fluvial provenance geochemically; instead we consider indications of fluvial source and scale, including lithology, deposit size and structure, and bedform scale, which differ considerably for large rivers, like the Brahmaputra, versus smaller streams in areas of high relief, like those draining the Shillong Plateau.

4.3.2 Sediment Burial Age Dating

Based on facies analyses of subsurface and outcropping alluvium, samples for luminescence burial dating were collected from 2 outcrops and 4 boreholes. Outcrops sampled were those of the amalgamated, cross-stratified, sand body facies (described in Sec. 4.4.1)
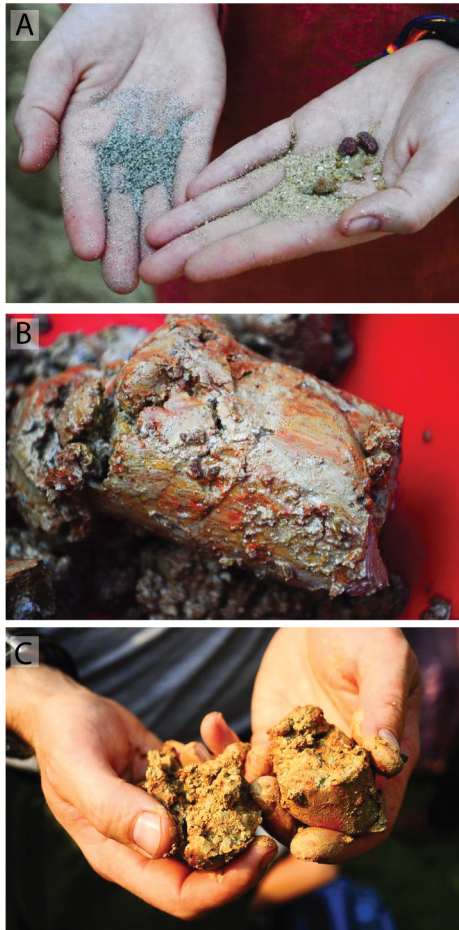
Figure 4.2: A) Comparison of recent Brahmaputra sand (left) with Shillong-sourced fluvial sediments (right). Note color difference as well as grain size and sorting contrast. B) Deeply weathered clay from the Madhupur Terrace mudcap, which was in the floodplain of the Brahmaputra River prior to uplift and exposure. C) Weathered clay of the Jamulpur Terrace mudcap, which was (and still is) in the Brahmaputra floodplain during the Latest Pleistocene.

Figure 4.3: Examples of stratified bedforms on a longitudinal bar exposure on the modern Brahmaputra River. A: Upper image is given for scale and to show young vegetation, a proxy for persistence timescale of the longitudinal bar. B: Notice the scale of the crossbeds behind the men. C: Close view of different types of bedforms. D: Low-angle planar crossbeds atop subplanar bedforms.

Table 4.2: Relative weathering stage criteria used in assessing and interpreting alluvial outcrops of the Garo Hills.

Weathering stage	Outcrop sediment characteristics
Stage 0	"modern" – unconsolidated, individual grains may be weathered, but no outcrop-scale weathering apparent
Stage 1	unconsolidated, may be oxidized, but no Fe-concretions or laterite formation, no obvious evidence of hydrolysis (no authigenic clay formation or kaolinite dust, micas still in tact)
Stage 2	may be consolidated but not lithified, may be oxidized, may have Mn nodules & oxidation marks along spiral "planes", but no laterite or authigenic clay
Stage 3	may be lithified, often oxidized, may have authigenic clay development, laterite beds may be present
Stage 4	deeply weathered – oxidized throughout, red-pink-purple discoloration, authigenic clay present

in order to determine their depositional (burial) age, which represents the last time that a large-scale river flowed across the now uplifted western escarpment of the Shillong Plateau. Borehole samples targeted 3 Pleistocene-aged terraces of the Brahmaputra River, including the Bogra and Jamulpur Terraces and the Sherpur Remnant (discussed in detail in Ch. 3), as well as a borehole ∼2 km southeast of several amalgamated, cross-stratified, sand bodies, on the adjacent floodplain. The latter borehole was selected to constrain timing of offset between the now uplifted outcrops and the adjacent, potentially correlative buried sediments.

Sample collection from outcrops was achieved by climbing on the face of the outcrop to the highest possible position (usually still 2–3 m below the mudcap) and digging into the exposure to the maximum depth possible without causing calving of the unlithified sediments. A steel pipe of 5 cm diameter and 30 cm length was sealed on one end with opaque vinyl and pounded into the excavated area, filling the pipe with sediment. A tarpaulin was enclosed around the area, the pipe was then extracted, and the other end was sealed while remaining under the tarp.

The sampling technique for borehole sediments was a modification of the reverse-circulation

drilling technique used for borehole sample collection. Borehole sampling depths ranged from 9—20 m, targeting the first sands encountered below the surficial muds. To collect the sample to be dated, we used a modified auger with extension rods to sample boreholes down to a maximum of 20 m depth. The auger was coupled to a 30 cm long steel pipe of 3 cm diameter (small enough to fit inside the 5 cm diameter drill pipe); the pipe was fabricated to split in half vertically in order to contain a 30 cm long PVC liner, which was fastened closed and stabilized by 3 teeth on the bottom of the steel pipe, angled inward, allowing sediment to be forced into the pipe but containing it once inside. The auger was inserted inside the borehole drill pipe; when the auger and coupled sampler reached the bottom of the borehole, a sledgehammer was used to strike the auger head, forcing the auger downward for 30 cm more. Extraction of the auger was achieved using a braced fulcrum and lever that forced the auger upwards, and the PVC liner was extracted under a tarp and in sealed in opaque vinyl.

Samples were processed and analyzed at the TL-OSL Laboratory at the Physical Research Laboratory in Ahmedabad, India, under filtered red light conditions. Using standard laboratory protocol (Wintle, 1997; Aitken, 1998), the coarse sand fraction of quartz and potassium feldspar were extracted, chemically treated to remove carbonate and organic material, rinsed and dried at 45˚C for 24 hours to avoid fading of the luminescence signal that can occur at higher temperatures. Grains 90—150 µm were then sieved, and feldspars were separated for measurement of post Infra-Red Infra-Red Stimulated Luminescence (pIR-IRSL) after Buylaert et al. (2009). For all dating measurements, pIR-IRSL SAR protocol after Thiel et al. (2011) was used.

4.4   Results and Interpretation

4.4.1   Sedimentary Facies of Outcrops of the Garo Hills

Alluvial deposits of the western escarpment of the Shillong Plateau are divided into four facies: (1) Amalgamated, Cross-stratified, Sand bodies (Acs); (2) Homogenous Sand bodies (Hs); (3) Heterolithic Sand, Silt, Mud bodies (Hssm); and (4) Graded, Poorly Sorted Alluvial bodies (Gpsa). Additionally, massive silt outcrops are interspersed throughout the study area, but these lack internal structure; it is likely that these deposits are floodplain or overbank deposits, but without additional information this cannot be confirmed. Instead, we focus on the 4 facies associated with fluvial channels in order to test the hypothesis; attributes of these facies are described in the following paragraphs and summarized in Table 4.3.

The Amalgamated, Cross-stratified, Sand (Acs) facies, constituting 12 outcrops along the margin of the escarpment, is characterized by laterally continuous (the maximum lateral continuity measured in the field was 300 m, but it was limited by exposure on both ends) deposits with 5—30 m exposed vertically. Cross-strata occur in grouped, large-scale sets (dcm—m scale) with non-erosional bases. The lower bounding surface is typically planar or trough-shaped, and internal lithology is homogenous, fine to medium sand. Sediments of these outcrops are typically well-sorted, comparable to sediments of the Brahmaputra Braidbelt Sands of Pickering et al. (2014), and thus are interpreted as large-scale, braided river bar deposits (Fig. 4.4).

The Homogeneous Sand (Hs) facies, constituting 24 outcrops along the escarpment, is characterized by laterally continuous (up to 100 m, limited by exposure) outcrops 10 or more m high. Sedimentary structures are not discernible in these massive units, but they are typically composed of well-sorted, fine to medium sands, and are interpreted as likely to have been deposited by a large-scale river, but additional information is necessary to confirm this interpretation.

The Heterolithic Sand, Silt, Mud (Hssm) facies is characterized by decimeter scale lateral continuity and vertical height of several meters, with measurements for both often limited by heavy vegetative cover. These units are composed of thin, grouped, small-scale (cm–dcm) bedsets with non-erosional bases. The lower bounding surface is typically planar, and internal bed lithology is usually homogenous. These units are interpreted as floodplain landscapes dominated by silt deposition with sand introduced during seasonal or large-scale flooding events.

The Graded, Poorly Sorted Alluvial (Gpsa) facies consists of isolated exposures with occasional thin, low-angle cross-beds. In most cases, these deposits are normally graded, but in some locations somewhat evenly spaced (roughly tens of cm apart) gravel layers occur within silt or sand matrices. Sediments of these unit are often very poorly sorted and frequently sub-rounded to sub-angular. These units comprise both modern, proximally-sourced streams draining the Shillong Plateau, as well as substantially weathered, older deposits. Fig. 4.4 shows 3 examples of these types of sediments.

4.4.2   Sedimentary Facies of Subaerial Bengal Delta Sediments

In general, sand packages are typically >30 m thick, up to 95 m in some boreholes, often containing interspersed gravel deposits. Mud units are thin (<5 m thick) relative to the scale of sand units except where Pleistocene muds are exposed at the land surface, in which case the units are up to 20 m thick. These attributes indicate deposition by a large river, and the thickness of fluvial packages in particular suggests an aggradational environment; we therefore consider these thick fluvial sands to represent sea-level highstand deposition, when the combination of high sediment load associated with interglacial climates as well as post-lowstand accommodation would be capable of generating these thick sequences. Sediment package dimensions and lithologic attributes of subsurface facies are consistent with the Brahmaputra Valley facies[1] presented in Pickering et al. (2014), which is subdivided

---

[1] "Brahmaputra Valley facies" is somewhat a misnomer, as Pleistocene Braidbelt Sands occur outside of the bounds of the valley; indeed, sands deposited by the Brahmaputra during the Pleistocene
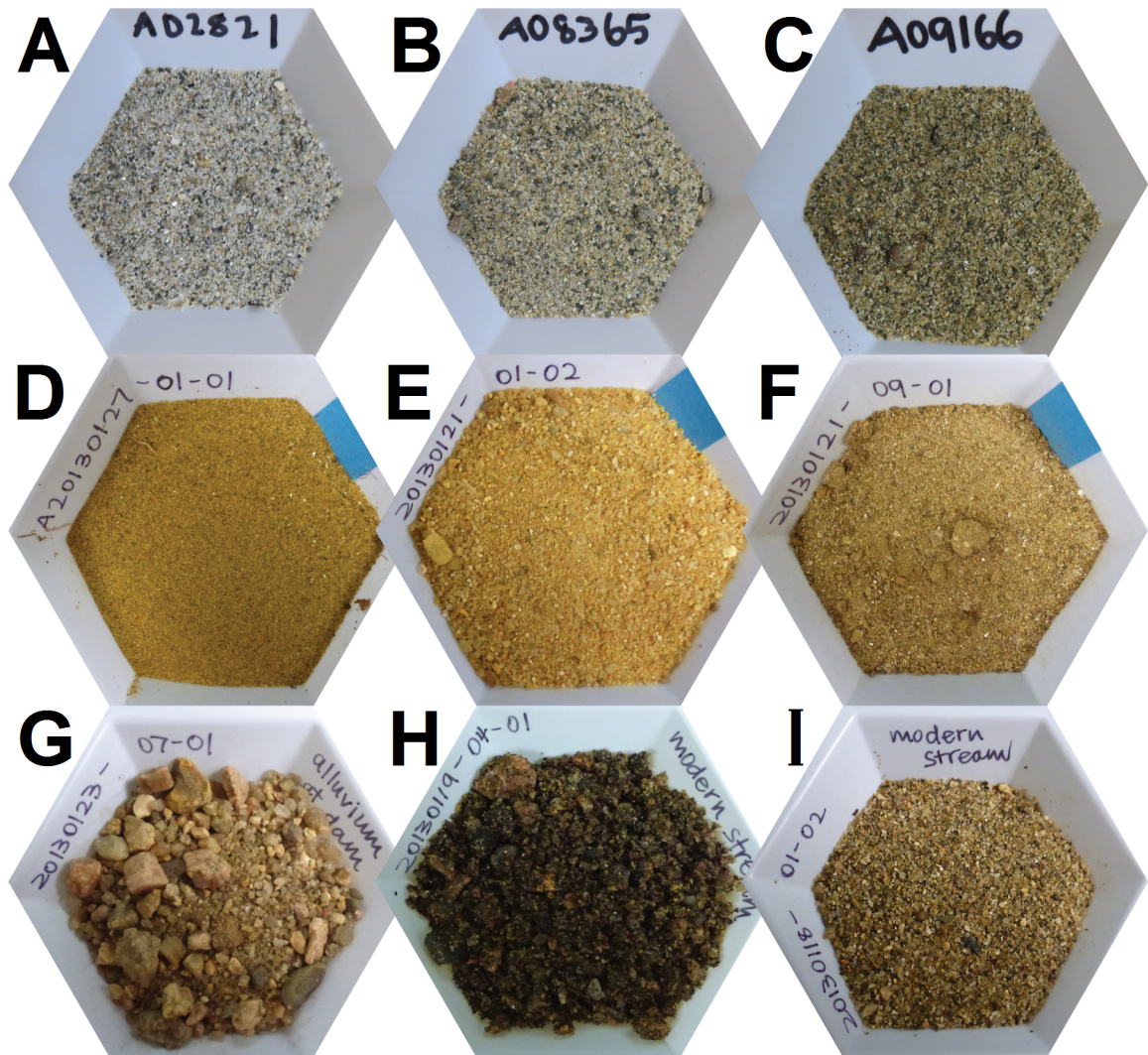
Figure 4.4: Images depict characteristic alluvial sediments from three different facies: Holocene and Pleistocene Braidbelt Sands; Amalgamated, Cross-stratified Sands (Acs); and Graded, Poorly Sorted Alluvial bodies (Gpsa). A) Holocene Braidbelt Sands. B and C) Pleistocene Brahmaputra Braidbelt Sands. D–F) Samples of Acs facies of uplifted marginal Garo Hills. G–I) Samples of modern streams draining the interior Garo Hills, belonging to the Gpsa facies.

Table 4.3: Facies descriptions of outcropping alluvium of the Garo Hills.

Facies	Spatial distribution	Deposit dimensions	Sedimentary structures	Dominant grain size	Sediment sorting	Interpretation
Amalgamated, cross-stratified, sand bodies (Acs)	Along outermost margins of uplifted terrain, up to 5 km upslope from topographic margin; typically, 20—50 m elevation	Up to ~300 m lateral, more typically ~50—100 m; 5—30 m vertical; measurements limited by exposure	Tabular (m-scale) to trough thick (30—50 cm) cross-beds and low-angle dunes (10—50 cm)	Fine to medium sand	Well-sorted	Braided river channel bars
Homogenous sand bodies (Hs)	Along outermost margins of uplifted terrain, up to 5 km upslope from topographic margin; typically, 20—50 m elevation	Up to ~100 m lateral, often >10 m vertical; measurements limited by exposure	Sedimentary structures not discernible (massive units)	Fine to medium sand	Well-sorted	Undifferentiated large river deposits
Heterolithic sand, silt, mud bodies (Hssm)	Widespread southwest of Dapsi fault, up to 10 km upslope from topographic margin; typically, 45—80 m elevation	Typically, tens of m lateral, 3—5 m vertical; often heavily vegetated	Thin (<20 cm), subplanar beds in sand units; silts and muds may contain ripples; occasional flaser bedding	Fine sand, mud, silt	Well-sorted within beds	Overbank or floodplain deposition associated with seasonal flooding
Graded, poorly sorted alluvial bodies (Gpsa)	Found locally near drainage networks along topographic margin as well as upslope; elevations range from 40—180 m	5—10 m lateral, up to a few m vertical	Occasional thin (<30 cm) tabular cross-beds	Gravels, sand, silt	Poorly sorted	Proximally-sourced flashy streams

into Holocene and Pleistocene Braidbelt Sands, both packages generally deposited during highstands, as well as Holocene and Pleistocene Overbank Muds. However, geochemical results reveal that sediments were not uniformly deposited by the Brahmaputra River across the delta.

4.4.3 Sedimentary Provenance

In order to correlate genetically related fluvial deposits, we utilize methods for determining fluvial provenance. In the following section, we present evidence that now uplifted sediments of the Acs facies (and possibly also the Hs facies) were deposited by a river of large magnitude. As discussed in Sec. 4.3.1.4, large river deposits of the western escarpment of the Shillong Plateau must have been deposited by the Brahmaputra if they are younger than 2 Ma. Therefore, where uplifted alluvium has been deposited by a large river, and

---

are widespread across the subaerial Bengal delta as results of fluvial provenance analysis indicate.

these deposits are shown to be younger than 2 Ma, we interpret Brahmaputra provenance. Geochemical provenance results for Holocene and Pleistocene sediments in the subaerial delta are also presented.

4.4.3.1 Outcrops of the Garo Hills

The low-lying (20–150 m, Fig. 4.10) hummocks of the Southwest Garo Hills comprise fluvial sands and silts that outcrop where either seasonal rivers, runoff channels, or development of roads and agriculture have exposed them. Along the margins of the topographic expression of the Shillong Plateau, these low-lying hills are composed primarily of the Amalgamated, Cross-stratified Sand (Acs) and the Homogenous Sand (Hs) facies. The interior hills, towards but still south of the Dapsi fault, are more commonly indurated but friable sediments of the Heterolithic Sand, Silt, Mud facies or occasional bedrock. Proximal stream sediments of the Graded, Poorly Sorted Alluvial (Gpsa) facies are interspersed throughout both the marginal and interior hills. For the most part, sediments southwest of the Dapsi fault are not lithified; however, at the southwestern corner of the Garo Hills, a very weathered and presumably older 100 km^2 remnant of shale bedrock outcrops (Fig. 4.10).

With the exception of that remnant bedrock exposure, the hills surveyed on the outermost margins of the topographic expression of the antiform consist entirely of non-indurated, fluvial sediments of the Acs, Hs, Hssm, and Gpsa facies. In general, these hummocks can be up to tens of meters high and typically an order of magnitude greater in lateral extent. These sediments are often oxidized but relatively unweathered in comparison to sediments found more interior to the Shillong Plateau, toward the Dapsi fault. Because secondary clay mineral formation is not evident and relatively weatherable mica minerals remain intact, we interpret Late Quaternary deposition; forthcoming luminescence dates will validate (or invalidate) this interpretation.

About half of the exposures surveyed along the margin belong to the Acs facies and are characterized by large-scale fluvial bedforms, ranging from tabular to trough cross-beds
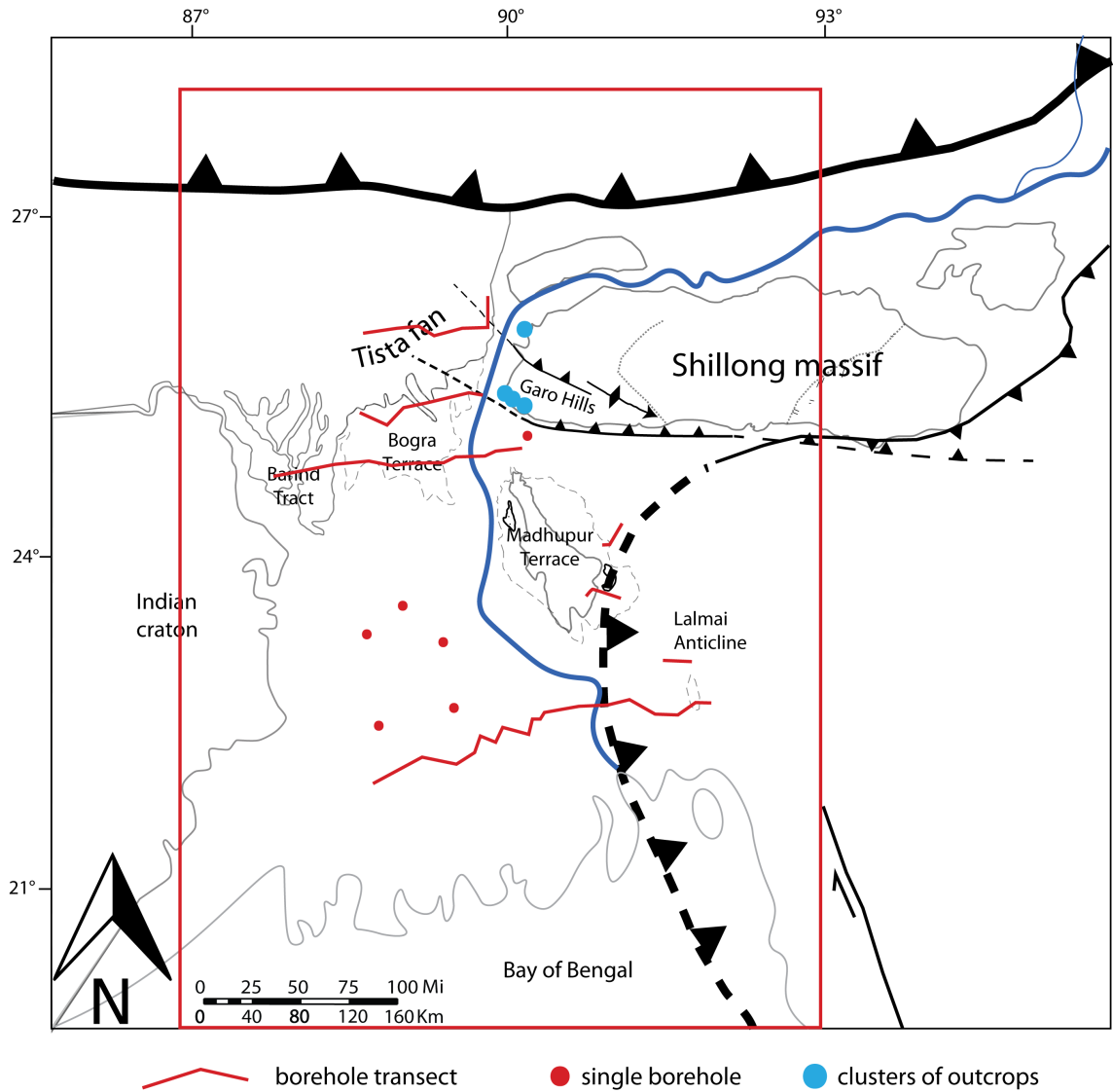
Figure 4.5: Location map of borehole transects and outcrops presented in Sec. 4.4. The red box outlines the areas shown in Figs. 4.7, 4.8, and 4.9.

and low-angle dunes. Tabular cross-bed sets are meter-scale from lower bounding surface to bar top; trough cross-beds are more typically 30–50 cm from bottomset to topset, but occur in grouped sets >1 m in height; and low-angle to subplanar bedforms range from 10—50 cm per dune, also occurring in sets >1 m in height. In order to justify our interpretation that deposits of the Acs facies were deposited by a large river, and assuming they were deposited less than 2 Ma, we present detailed images and bedform descriptions for 3 exemplary outcrops belonging to the Acs facies in Figures 4.11, 4.12, and 4.13.

Figure 4.11 (outcrop ID: 20151014-03) shows an exposed sedimentary face some 130 m in length. Not pictured, the exposure continues to the southeast (left in the figure) for another 120 m, although the face is poorly exposed due to thick vegetation cover. The outcrop face pictured was cleaned over the course of one day and sampled and imaged the following day. This outcrop is about 20 m high at the hummock peak. Fig. 4.11C shows an adult man at right and a pair of sandals in the foreground for scale. Fluvial bedforms are laterally continuous across the two main sections that were cleaned (enlarged in Fig. 4.11B and D), characterized by subplanar to low-angle strata, where each bedset is on the order of 0.5–1 m thick. Sediments at this exposure are homogeneous, clean, fine to medium micaceous quartz sands. The thick to very thick cross-beds and lithologic attributes of the sediments indicate deposition by a large-scale river. Evidenced by the abundance of colluvium, these sediments are not indurated and are easily displaced when disturbed, an indication that this is Quaternary fluvial deposition. A sample for luminescence dating was collected at the location shown in Fig. 4.11E.

Figure 4.12 (outcrop ID: 20130127-07) shows a hummock exposed by a small, presumably ephemeral stream (pictured in the foreground). Here the upper half of the outcrop is characterized by low-angle bedforms about 0.5 m thick. The lower half of the outcrop is characterized by very thick tabular cross-beds, roughly 30° from the horizontal, suggesting minor or no overall tilt to the outcrop during uplift. Sediments at this exposure are oxidized, clean, well-sorted, fine to medium quartz sands, with tiny (∼2 mm diameter)
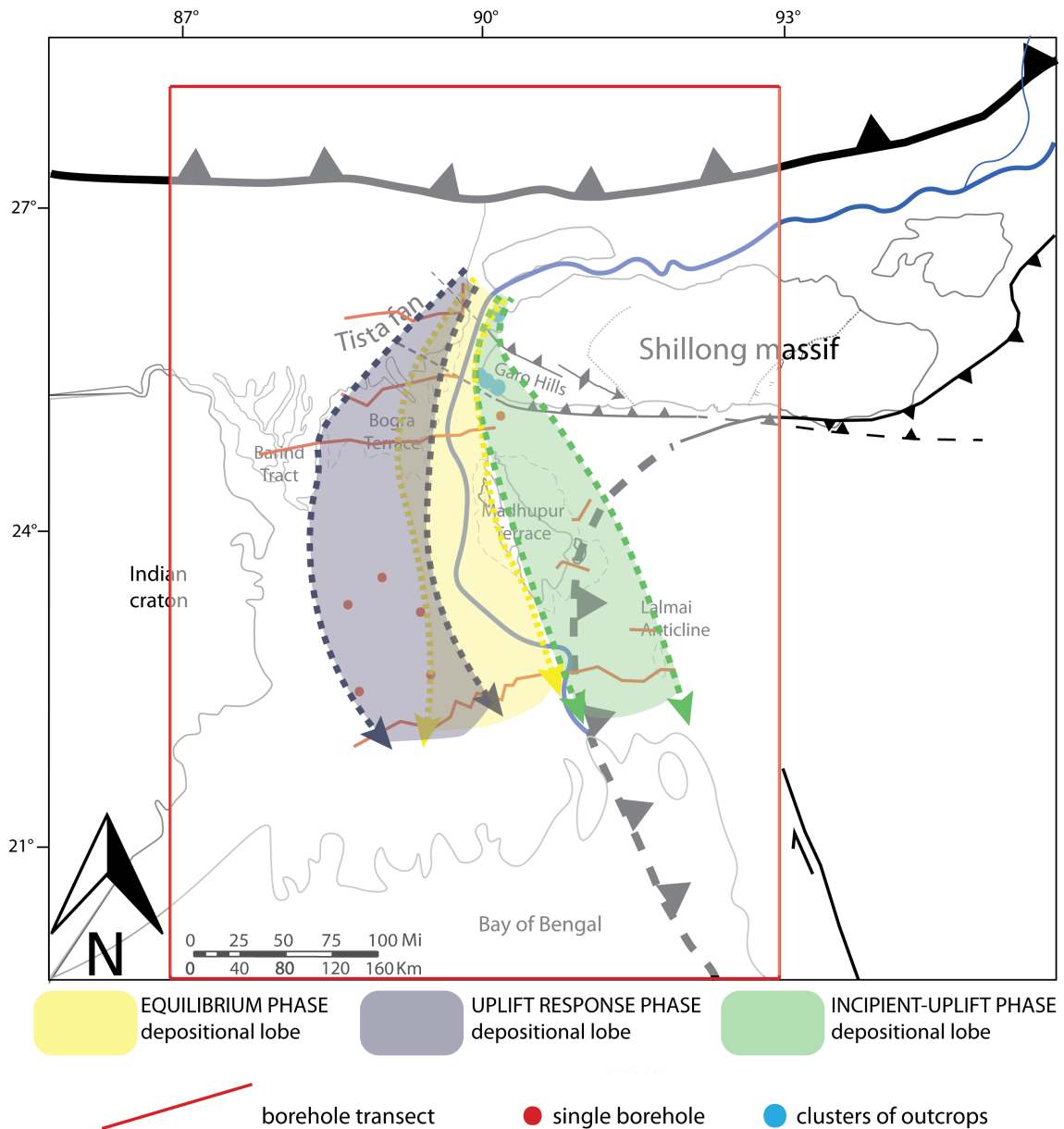
Figure 4.6: Stratigraphic results reveal three major phases of sediment deposition in the Bengal basin. The easternmost lobe (green) represents the Pleistocene depositional lobe before uplift of the western margin of the Shillong massif, the westernmost lobe (in dark gray) represents the depositional lobe that developed in response to uplift of the western margin of the Shillong massif, and the central lobe (in yellow) represents the post-uplift phase of deposition. The red box serves as reference for the following three figures, in which stratigraphic results used to demarcate the three lobes are presented.

manganese nodules that disband when removed from the outcrop face. These sediments are more compact than those of outcrop 20151014-03 (Fig. 4.11), but likewise are not indurated nor lithified. Again, bedform scale and sediment lithology indicate deposition by a large river; although this outcrop appears slightly more oxidized than that of the outcrop in Fig. 4.11, the lack of induration and secondary clay mineral formation suggests Quaternary deposition.

Figure 4.13 (outcrop ID: 20131123-02) shows an exposure roughly 30 m wide and 5—10 m in height consisting of fine to medium well-sorted, micaceous quartz sands. The sand of this outcrop has been recently excavated for the purpose of building up roadways, something we encountered frequently during fieldwork; local practice is to first build up the roadway with homogenous sand, then cap it with gravel and tar. In Fig. 4.13A, the upper portion of the outcrop is relatively oxidized, whereas the lower portion is not, probably because the lower portion was only very recently exposed for mining. In the lower non-oxidized portion of the outcrop, both tabular and trough cross-beds are easily discernible (Fig. 4.13D, e.g.). In the upper half of the exposure, however, oxidation has made it difficult to make out the bedforms, but they are vertically continuous across the weathering horizon (Fig. 4.13C).

These and other outcrops of the Acs facies are interpreted as large river braidbelt deposits that have been uplifted relatively rapidly as indicated by the elevation offset from the adjacent modern delta plain and the generally good preservation of the outcrops. Despite dramatic precipitation during the summer monsoon season, the 1–3 m thick mudcaps above these fluvial sands appear to slow erosion; however, locals report calving of large sections of the faces of these outcrops each rainy season and colluvial deposits at the base of the outcrops corroborates this.

The Acs facies, interpreted to be of large-river origin, occurs only on the outer margin of the topographic expression of the Shillong Plateau (Fig. 4.10). Given the very proximal location of these deposits to the modern Brahmaputra River, it is hard to imagine that any

other large-scale braided river occupied this area of the basin recently enough to deposit those sediments. However, without a means to test the provenance of these sediments, that they are of Brahmaputra origin remains an interpretation.

4.4.3.2 Buried Sediments of the Subaerial Bengal Delta

In the following three sections, fluvial provenance determined by bulk Sr concentration measurements obtained from borehole samples of 12 transects are presented in 3 sections, grouped by their position relative to the modern Brahmaputra-Jamuna River: the central delta, which includes the modern river and recent paleovalley; the western delta, which encompasses the subsurface west of the modern river; and the eastern delta, which encompasses the subsurface east of the modern river. The contact between the Holocene and Pleistocene units was defined using a combination of radiocarbon ages obtained from organic material, the presence or absence of paleosols, and the degree of oxidation of the units, as in the preceding chapters. A detailed discussion of the methods used to determine this contact is presented in Sec. 2.3.1. Geochemical results in the following 3 sections are presented with regard to sediment provenance (for lithologic sections of these transects, refer to Ch. 2 and Ch. 3, as well as Pickering et al. (2014); Williams (2014); Sincavage et al. (2015); and Patrick (2016)).

4.4.3.2.1 Fluvial Architecture of the Central Delta Geochemical provenance results delineate depositional pathways for specific rivers within the delta. Each pathway consists of genetically related sediments that make up sediment packages of variable thickness and width, depending on the scale of the river depositing the material. The central delta is dominated by Brahmaputra River deposition within both Holocene and Pleistocene fluvial sediments, with minor deposition by the Tista and Ganges rivers. Fig. 4.4.3.2.1 reveals a central corridor of deposition characterized by the Holocene Brahmaputra paleovalley, which is ~55—>80 km wide and ~40—>90 m deep, distinguished by amalgamated, typ-

ically high-Sr (>140 ppm) sands (Ch. 2 and Pickering et al., 2014). In all 4 transects that capture the stratigraphy of the central delta, Sr concentrations generally increase from west to east, owing to the dominance of the Ganges and Tista rivers in the west and the Brahmaputra River in the east.

The northern Transect C1 (Fig. 4.7) defines the paleovalley of the Brahmaputra at the apex of the delta; here the valley has been infilled by both Tista and Brahmaputra deposits; not unexpectedly, Tista deposition, characterized by low-Sr (<90 ppm) dominates the western portion of the paleovalley, with Sr ranging from <60–~110 ppm, while mixed Tista-Brahmaputra sediments, typically >110 ppm but occasionally as low as 90 ppm fill the central to eastern valley.

Further downstream and south of the topographic expression of the Tista fan, at Transect C2 (Fig. 4.7), borehole sediments define high-Sr Brahmaputra deposition within the paleovalley, as well as outside of the bounds in sediments below the western Pleistocene surface that defines the paleovalley. As in Transect C1, a relatively thick (20—30 m) package of low-Sr sands is present within the western portion of the Brahmaputra paleovalley, perhaps deposited when the mainstem Brahmaputra followed a more easterly course in the mid-Holocene (Pickering et al., 2014; Goodbred et al., 2014; Sincavage et al., 2016).

Transect C3 (Fig. 4.7), further south still, grades from slightly lower-Sr deposits in the western part of the transect (90—100 ppm at the surface and 120—140 ppm in the subsurface) to dominant high-Sr Brahmaputra stratigraphy in the eastern part of the valley. Brahmaputra deposition is continuous across the Holocene-Pleistocene boundary on both sides of the paleovalley, having constructed the Late Pleistocene landscape and later incising it (Ch. 2) as well as infilling the Holocene valley.

Transect C4 (Fig. 4.7), at the southern end of the system, shows a more complete picture of river mixing throughout the Holocene. In the central part of the transect, early Holocene Brahmaputra deposition (high-Sr, almost exclusively >140 ppm) dominates within the paleovalley. Here these high-Sr deposits trend eastward upward through the stratigraphic

section indicating that the river migrated eastward as the Holocene progressed, to its modern position, which is the farthest east the Jamuna path of the Brahmaputra has been during the Holocene. West of the Brahmaputra paleovalley, the Ganges paleovalley is infilled with low-Sr (<100 ppm) sands. Curiously, basal deposition within the Ganges valley is slightly higher (~100–120 ppm), perhaps an indication that the Brahmaputra contributed sediment to the Ganges system during the early Holocene. East of the Brahmaputra paleovalley, low-Sr (<110 ppm) sediments dominate the lower stratigraphy, with the exception of localized Brahmaputra deposition (discussed in Sec. 4.4.3.4). Above the Pleistocene surface, Sr-geochemistry of sediments is depressed (90–>140 ppm) but generally higher (120—140 ppm) in the shallow stratigraphy and lower (90—120 ppm) closer to the Pleistocene surface.

In summary, fluvial provenance of the central delta stratigraphy defined by these 4 transects (Fig. 4.7) is dominated by Brahmaputra-sourced sediments within and beneath the paleovalley, which is flanked on the west by more Pleistocene Brahmaputra deposition in the central delta. In the upper delta, the Tista contributed substantially to sediments that infill the western paleovalley, and in the lower delta, the Ganges dominates stratigraphy west of the paleovalley.

4.4.3.3 Fluvial Architecture of the Western Delta

In the modern landscape, the western portion of the delta is characterized by the relatively high topography of the Tista fan and Barind Tract. In the western half of the northern transect, which captures stratigraphy of the Tista fan (Fig. 4.8:W1), thick (~70 m) fluvial packages are dominated by low-Sr (<90 ppm) Tista sediments. Across this transect, Sr concentrations decrease toward the west (up to >140 ppm in the east and roughly <60—90 ppm in the west), indicating decreasing sediment input by the Brahmaputra toward the west. This suggests that the Tista fan has acted as a topographic barrier, precluding Brahmaputra deposition during the Upper Pleistocene and Holocene. However, a few isolated packages of mixed Tista-Brahmaputra sediments (Sr ranges of 100—140 ppm) occur west of the
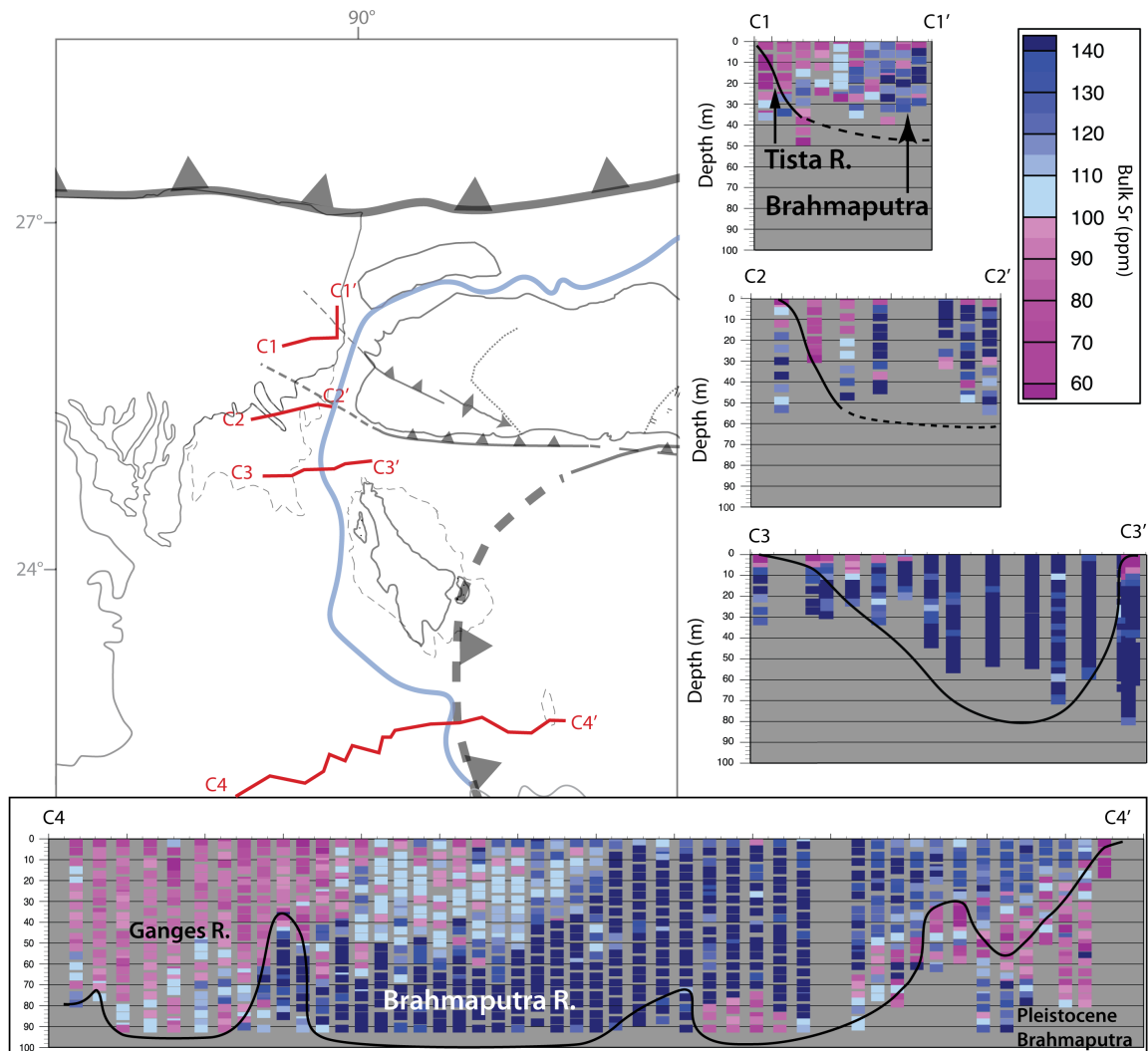
Figure 4.7: At left, the map shows the locations of borehole transects (denoted by red lines) that were used in identifying the central depositional lobe of the Brahmaputra River. At right, the 4 borehole transects are shown by their bulk strontium concentration, a proxy for fluvial provenance; the black line in each transect represents the Holocene-Pleistocene contact.

Brahmaputra paleovalley beneath the Pleistocene surface. These are encountered at 35 m depth and 60—70 m depth. These isolated packages of mixed-fluvial deposition document westward erosion at the apex of the delta into the Tista fan by the Brahmaputra River during the Pleistocene.

South of the Tista fan, however, the stratigraphy is dominated by Brahmaputra sediments. In Transect W2 (Fig. 4.8), a wide swath of deposition by the Brahmaputra is evidenced by Sr ranges of 110–>140 ppm. These occur west of the Holocene valley, buried beneath a thin cover of low-Sr Tista sediments. Likewise, sediments of Transect W3 (Fig. 4.8 are capped by a thin (<10 m) veneer of Ganges and/or Tista sourced sediments, with widespread high-Sr sediment deposition by the Brahmaputra below about 10 m depth. Five isolated boreholes (Fig. 4.8: W4—W8; Ullah, 2010: Fig. 3.1) in the modern Ganges delta, confirm that this pattern of Brahmaputra sediment deposition in the western portion of the delta during the Pleistocene continues south. These results are significant because at no time during the Holocene has the Brahmaputra River been this far west in the delta due to the relatively high topography of the Tista fan and Barind Tract.

4.4.3.4 Fluvial Architecture of the Eastern Delta

In the eastern portion of the delta, separated from the central corridor by the raised topography of the Pleistocene Madhupur Terrace, the subsurface character is less straightforward than in the western and central delta. In the east, the subsurface is more heterogeneous in terms of sediment lithology as well as subsurface architecture, comprising both braidbelt sands and overbank muds, as well as both erosional valleys and deformed anticlinal structures. The stratigraphy of the eastern delta is is not easily generalized. In the northernmost transect (E1, Fig. 4.4.3.4) relatively thick (~30 m) successions of mud are preserved in both Holocene and Pleistocene units; these mud packages separate equally thick packages of braidbelt sands. Sediments of this transect are not dominated by high-Sr Brahmaputra deposition. Instead Brahmaputra deposits are isolated to 2 main packages: the upper fill
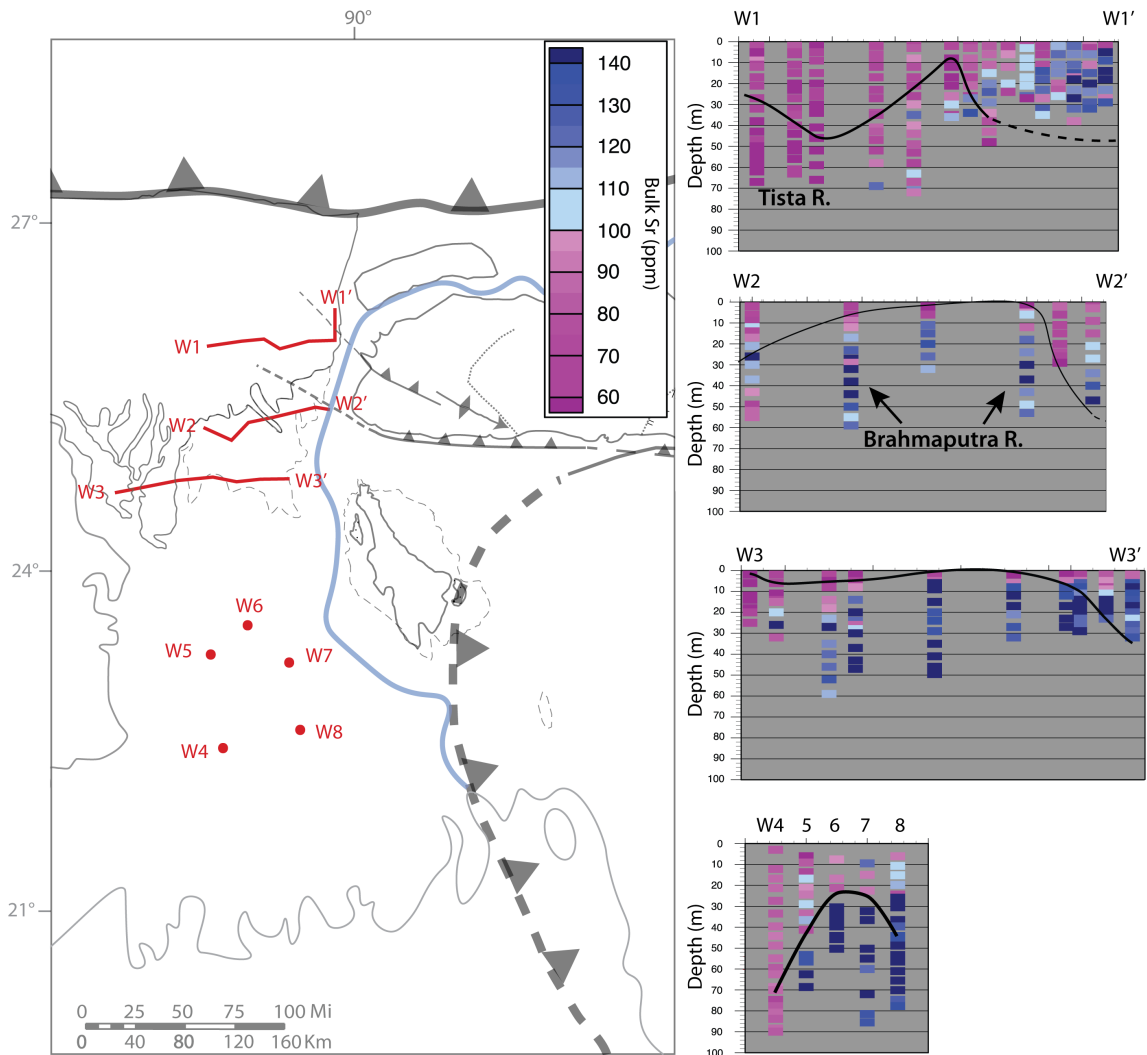
Figure 4.8: At left, the map shows the locations of borehole transects (denoted by red lines) that were used in identifying the western depositional lobe of the Brahmaputra River. At right, the 4 borehole transects are shown by their bulk strontium concentration, a proxy for fluvial provenance; the black line in each transect represents the Holocene-Pleistocene contact.

of the Old Brahmaputra paleovalley down to about 25 m depth, as well a package of Pleistocene sediments below about 50 m depth. These 2 packages, however, are characterized by somewhat depressed Sr concentrations, ranging from 110–>140 ppm. This is likely the result of mixing with local rivers, including the Barak-Surma-Kushyara system and Indo-Burman foldbelt streams (Williams, 2014).

Transect E2 (Fig. 4.9) similarly contains relatively thick mud deposits, both in the shallow stratigraphy and below the Pleistocene contact. However, much of the preserved Pleistocene stratigraphy is characterized by braidbelt sands >60 m thick. A 5 km wide package of these thick sands in the west-central portion of this transect is characterized by relatively high-Sr (>120 ppm) Brahmaputra sediments, evidence that a major occupation of the Brahmaputra was routed through this region in the Pleistocene.

Transect E3 (Fig. 4.9) likewise documents Brahmaputra deposition during the Pleistocene. Beneath the Lalmai Anticline, a structure with 40—50 m of surface relief, a 50-m thick unit of high-Sr (120–>140 ppm) Brahmaputra sediments buried beneath the Pleistocene contact has been uplifted toward the modern surface. The provenance signature of the Brahmaputra sediments is "pure", i.e. >140 ppm—not mixed or weathered, indicating that these deeply buried Brahmaputra sediments have been brought to the surface relatively recently. While the deformed Holocene-Pleistocene contact may not be as old as the antiform itself, the 40—50 m of topography and buried sediment on top of the contact suggest that the Brahmaputra sediments buried below are of significantly older age.

Along the same transect, a unit of Brahmaputra-sourced sands has infilled the Old Brahmaputra paleovalley. While high-Sr Holocene sediments that have infilled the smaller paleovalleys can be attributed to periodic avulsions of the Brahmaputra into the Old Brahmaputra flow path during the Holocene (Pickering et al., 2014), each of the 4 transects in the eastern delta contain high-Sr Brahmaputra sediments below the Holocene-Pleistocene contact. These deposits can be grouped into one of two types:

1. Pleistocene Brahmaputra deposits that have been truncated by Holocene valley in-

cision (as in Transect E1, the western portion of Transect E2, and minor incision in Transect E4; Fig. 4.9), interpreted as Latest Pleistocene Brahmaputra deposition,

2. or Pleistocene Brahmaputra deposits that have been brought nearer to the surface by upward deformation (as in Transect E2 beneath the deformed contact and Transect E3 beneath the surface expression of the Lalmai anticline), interpreted as older than those in the former group.

We propose that the older unit, deeper, now uplifted unit of Brahmaputra sediments in the eastern delta can be correlated with the Amalgamated, Cross-stratified Sand facies of the Southwest Garo Hills outcrops. This proposed interpretation can be substantiated with burial age dates of these buried sediments. Regardless, the Brahmaputra clearly followed a substantial flow path into the eastern delta during the Pleistocene, probably much before the western delta course became dominant. This may have encompassed multiple episodes of deposition, constructing thick sequences of sediment during relative sea-level highstands and incising valleys during relative lowstands.

4.5   Discussion

4.5.1   Sequence of Deposition

Sedimentary deposits of Brahmaputra origin are widespread across the subaerial Bengal delta; three main depocenters, or lobes of deposition, have been identified in the stratigraphy. In the western portion of the delta, radiocarbon (and forthcoming luminescence) ages indicate that sediments were deposited by the Brahmaputra River exclusively during the Pleistocene, and the river has not deposited a significant amount of sediments there during the Holocene. In the central delta, along the modern Brahmaputra-Jamuna corridor, the river deposited Pleistocene sediments which were later incised, and with the exception of occupations of the Old Brahmaputra flow path in the eastern delta (Pickering et al., 2014; Sincavage et al., 2016), the river has predominantly occupied this central corridor through-
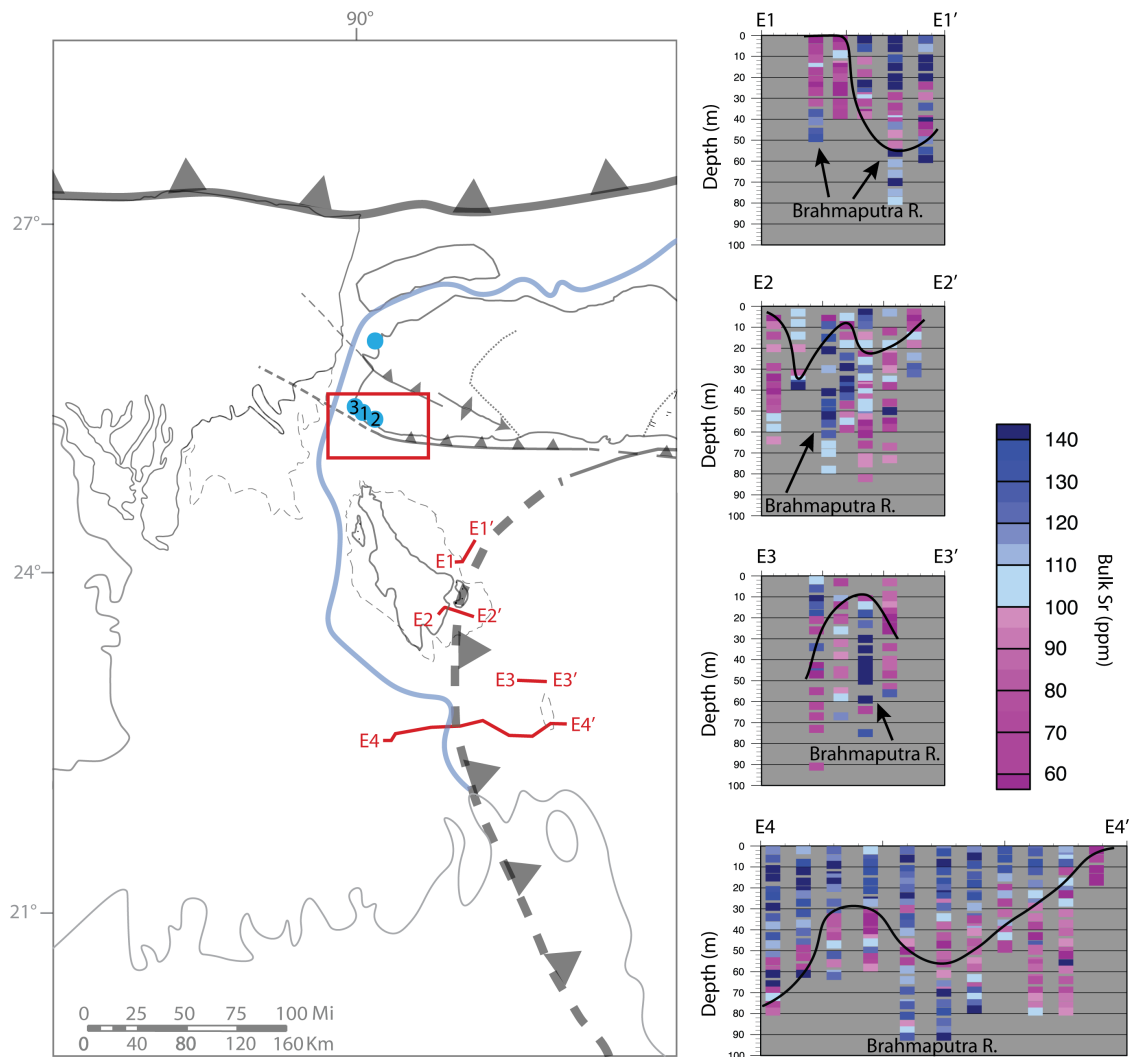
Figure 4.9: At left, the map shows the locations of uplifted outcrops (denoted by blue circles) and borehole transects (denoted by red lines) that were used in identifying the eastern depositional lobe of the Brahmaputra River. The outcrops outlined in the red box are those shown in Figs. 4.11, 4.12, and 4.13. At right, the 4 borehole transects are shown by their bulk strontium concentration, a proxy for fluvial provenance; the black line in each transect represents the Holocene-Pleistocene contact.
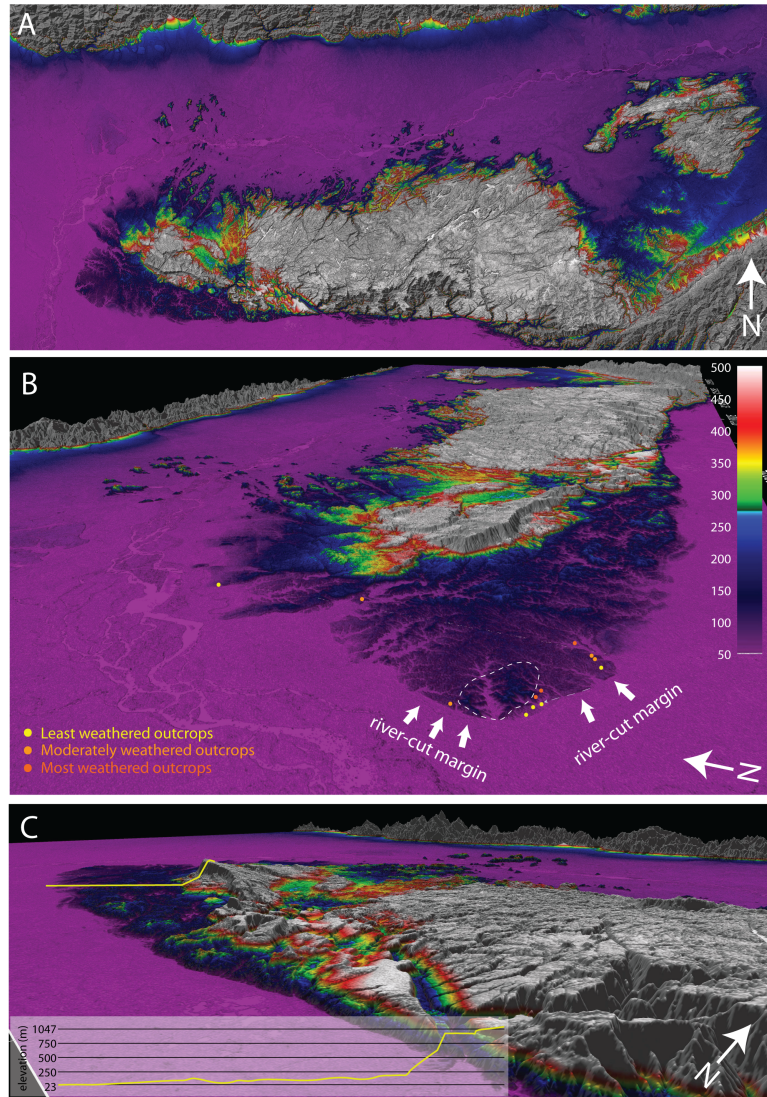
Figure 4.10: Digital elevation models (DEM) of Shillong anticline. A) North-oriented planform view of Shillong anticline. B) Oblique angle looking south-southeastward at the western margin of the Shillong anticline. Outcrops that have been interpreted as deposited by a Brahmaputra-scale river have been shown. C) Oblique angle looking north-northwestward at the southern margin of the Shillong anticline along strike of the Dapsi fault.
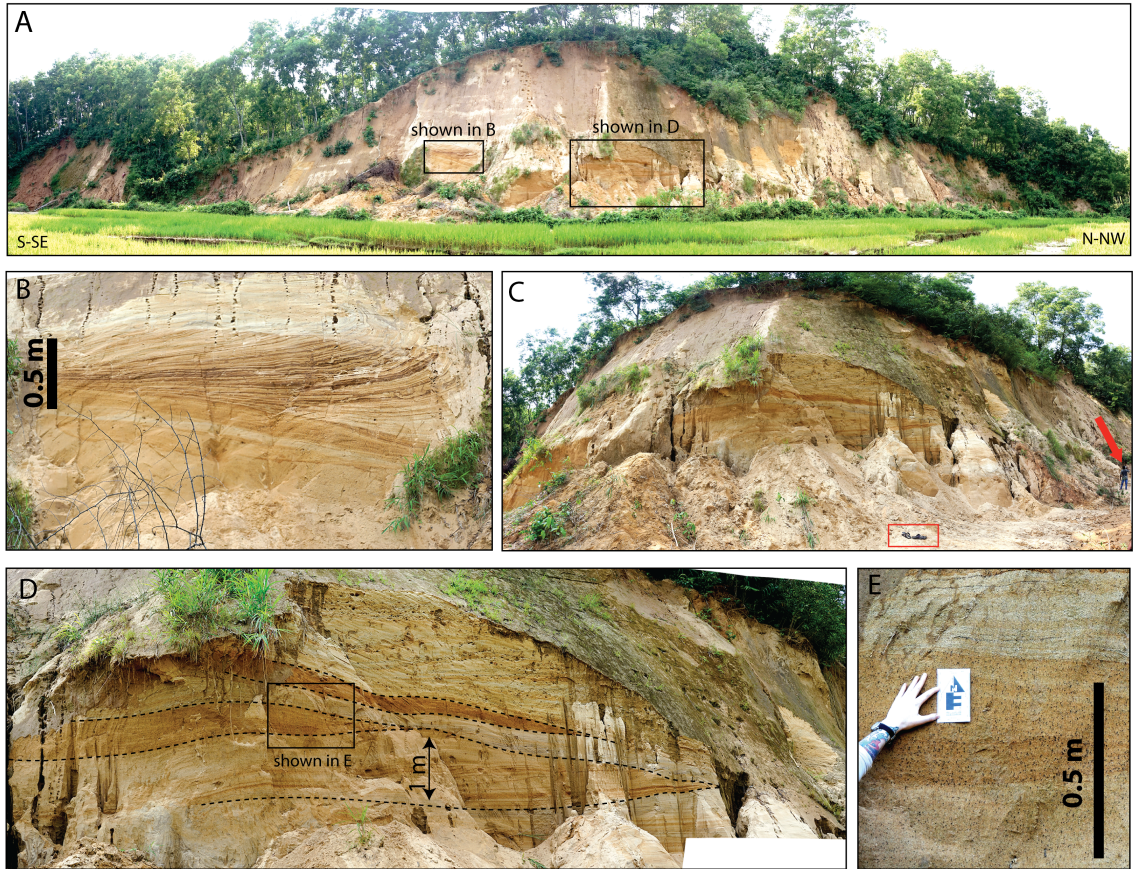
Figure 4.11: Outcrop ID 20151014-03: 130 m x 20 m exposure. A) Outcrop view showing scale and lateral extent of this face (not pictured: exposure continues 120 m toward southeast). B) High resolution image of high angle trough cross-strata above low angle dune. Location context given in A. C) Northwest (right) side of outcrop with adult male and sandals given for scale. D) Image showing lateral extent of bedforms. These also connect to the lower beds shown in B. E) High resolution image of subplanar bedforms with 10 cm arrow on card for scale.
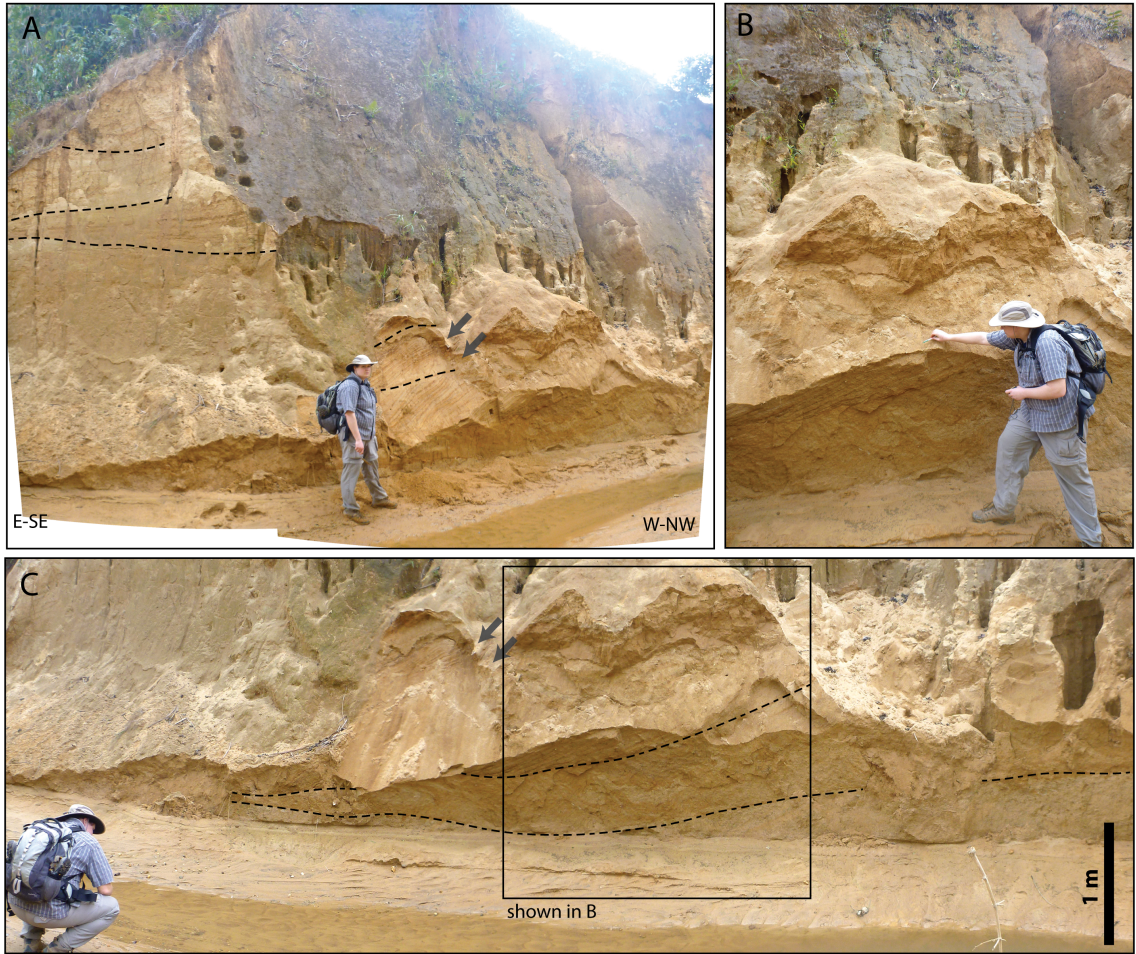
Figure 4.12: Outcrop ID 20130127-07: Roughly 8–10 m high exposure. A) Photomosaic of outcrop exposed by ephemeral stream. Note position of 2 gray arrows referencing same location on outcrop in C. B)Exposed bedform is 50 cm high. Outcrop context is given in C. C) Laterally continuous bedform. Flow direction is to the left (east-southeast) in the photo.
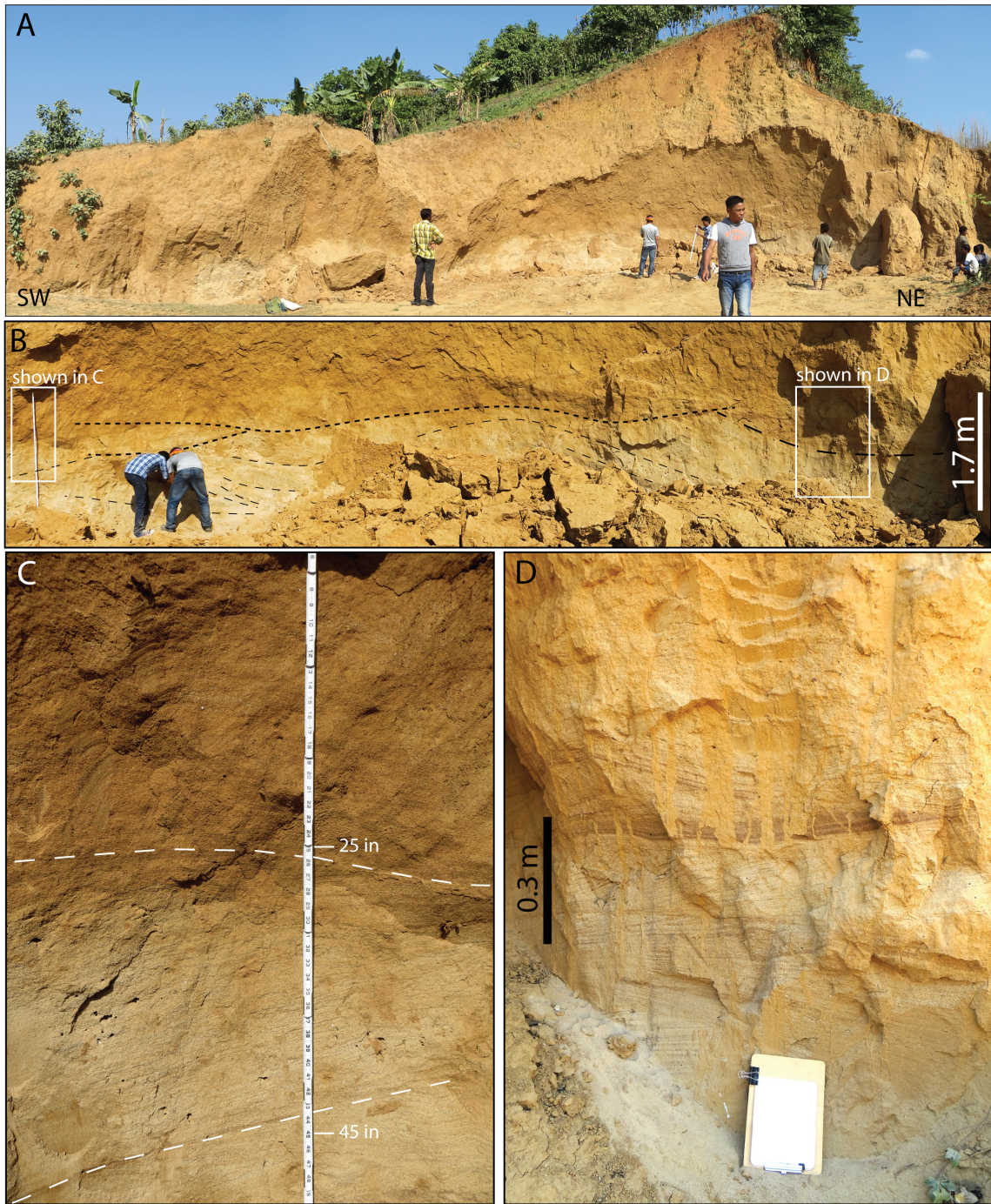
Figure 4.13: Outcrop ID 20131123-02: 30 m x 10 m sand exposure. A) Full outcrop view showing scale and lateral extent. Adult males for scale, approximately 1.75 m. B) Interpreted section of bedform units with reference positions for C and D. C) Cross-strata are vertically continuous across the weathering horizon. Yardstick shown for scale; units are in inches. D) High resolution view of cross-stratification. Flow direction is not consistent throughout the outcrop, typical of braided river bars.

out the Holocene. While the eastern delta was less frequently occupied by the Brahmaputra during the Holocene, fluvial provenance results document a substantial flow path into the eastern delta during the Pleistocene, and those sediments that were deeply buried and subsequently brought nearer to the surface are older than those in the western and central depocenters.

Thus the sequence of lobe deposition by the Brahmaputra River has been determined by stratal position of subsurface deposits relative to the Holocene-Pleistocene contact and as well as sediment burial ages, and degree of sediment weathering (Ch. 3); first, deposition of the buried lobe of the eastern delta occurred, followed by the western delta as the major sediment depocenter, and finally the major depositional zone shifted to the central delta. Below, this sequence of deposition is discussed in the context of eustatic sea-level and the regional tectonic framework.

4.5.2   Three Phases of Fluvial Response to Tectonic Uplift

The apex of the Brahmaputra-Jamuna fluvial fan is spatially coincident with the blind continuations of both the Dapsi and Dauki faults (Fig. 4.1), which underlie the river. These and countless other nearby faults associated with deformation of the Shillong Plateau are active (e.g., Bilham, 2001; Kayal et al., 2006; Bilham et al., 2013). Uplift of the Shillong Plateau is not spatially uniform; recent geodetic work has shown that the Shillong crustal block is rotating clockwise about a pole west of the Brahmaputra and Assam Valley (Vernant et al., 2014), which means the rate of shortening along the plateau grades from fastest in the east to slowest in the west. Western Shillong additionally is characterized by more faults than eastern Shillong, so motion is split across multiple faults. Ultimately this has resulted in the eastern portion of the antiform having roughly twice the vertical relief of the western portion, and assuming uplift varies proportionally to shortening, the rate of uplift across the antiform should be decreasing toward the west.

We propose a tectonic influence upon the Brahmaputra River over the timescale imposed

by the westward-advancing uplift of the Shillong Plateau. We suggest that uplift of the western portion of the antiform has gradually and episodically forced the Brahmaputra River westward at the apex of the fan. This westward deflection upstream results in a pattern of downstream deposition from the deepest portion of the delta in the east, to the western delta, followed by periods of eastward erosion during times of high discharge when the river is able to erode eastward into the Shillong Plateau.

4.5.2.1 Eastern Depositional Lobe: Deposition Along the Axis of Maximum Subsidence During Incipient Uplift

This eastern section of the delta was the primary depocenter of the river prior to Pleistocene-aged rerouting of the paleo-Brahmaputra around the western edge of the Shillong Plateau (Uddin and Lundberg, 1999). The westward propagation of the Indo-Burman foldbelt combined with uplift of the Shillong Plateau caused a major reorganization of paleo-Brahmaputra drainage about 2 Ma (Najman et al., 2016; Govin, 2015). Subsurface stratigraphy of the delta reveals that after the timing of initial rerouting around the Shillong Plateau, the river reestablished this eastern lobe as the major zone of deposition. We propose that the river was subsequently forced out of this foredeep in response to active tectonics associated with uplift of the western Shillong margin.

The eastern depositional pathway includes several post-depositionally uplifted Brahmaputra River deposits including the outcrops of the Southwest Garo Hills (Sec. 4.4.3.1), sediments buried beneath the apparently deformed Holocene-Pleistocene contact near the southwestern extent of the Madhupur Terrace (Fig. 4.9: Transect E2), and those buried beneath the Lalmai Anticline (Fig. 4.9: Transect E3). This lobe represents deposition along the zone of maximum subsidence in the foredeep of the advancing Indo-Burman foldbelt, during which the Brahmaputra constructed a thick fluvial sequence, >60 m thick. In more recent times, i.e., Latest Pleistocene and Holocene, fluvial sediments have continued to infill this basin, but geochemical results indicate that these sediments are typically of mixed flu-

vial provenance, originating from the Brahmaputra as well as the Barak-Surma-Kushyara system and local Indo-Burman foldbelt streams (Williams, 2014). During the Holocene, the Old Brahmaputra River has occupied this section of the delta multiple times (Sincavage et al., 2016; Pickering et al., 2014), but it has not served as the main depocenter for Brahmaputra deposits since the timing of deposition of the flow path that constitutes the Brahmaputra deposits of the Southwest Garo Hills and the deformed sediments beneath Madhupur Terrace and Lalmai Anticline.

4.5.2.2 Western Depositional Lobe: Fluvial Response to Uplift of the Western Margin of Shillong Plateau

Subsurface sediments with a high-Sr provenance signature along the western portion of the delta, up to 65 km west of the current location of the Brahmaputra-Jamuna, represent the westernmost extent of the Brahmaputra River in the delta plain during the Pleistocene. The presence of widespread paleosols in the stratigraphy of this portion of the delta is indicative of the relative age of these sediments (Ch. 3). We propose that this deposition was the result of a major shift of the river westward, in response to episodic uplift of the western margin of the Shillong Plateau.

The stratigraphy of the western lobe of the delta indicates that the Brahmaputra River was being pushed into the Tista fan. At the apex of the delta, the Brahmaputra provenance signature does not dominate the stratigraphy; instead mixed-sourced sediments are found in the stratigraphy at 35 and 60 m depth. However, just south of the topographic extent of the Tista fan, Brahmaputra sediments dominate the stratigraphy with only a thin veneer of Tista and Ganges sediments in the shallow (< 10 m) stratigraphy. The presence of this 50—60 m thick (which may be even thicker, but the known stratigraphy is limited to the depth of these boreholes) and $\sim$65 km wide swath of Brahmaputra sediments is surprising, considering the physiography of the delta: the Tista fan presents a topographic barrier that would presumably preclude Brahmaputra sediments from being deposited this far west without the

influence of an external forcing; additionally, the more central Jamuna path that the river follows today and the eastern Old Brahmaputra path present courses of steeper descent as well as greater rates of subsidence than the western delta.

4.5.2.3 Central Depositional Lobe: Fluvial Equilibrium Attained by Eroding Eastward into Shillong Plateau

The central lobe of deposition is characterized by the dominant flow path that the Brahmaputra River has followed during the Latest Pleistocene and Holocene. The base of the Holocene valley is defined by a prominent gravel unit that was deposited during a period of high-discharge flood events (Ch. 2). We propose that this depositional path is the major course the river follows during times of relatively high discharge when it is able to erode into the margin of the Shillong Plateau. Indeed, just two centuries ago the Brahmaputra followed a more eastern course during which time it closely traversed the southwestern margin of the antiform (Fig. 4.14) and flowed into the eastern delta. The smooth river-cut margins along this corner of the plateau (Fig. 4.10) are a testament to the erosional power of the river, perhaps having recently exposed many of the outcropping Brahmaputra-scale sediments along this margin.

The modern river seems to have equilibrated after westward deflection in response to uplift of the western margin of the Shillong Plateau. Uplift of the Shillong Plateau antiform is of course ongoing, but perhaps high discharge associated with a strengthened monsoon and paleoflood events during the early Holocene helped to shift the major depositional zone of the river eastward toward the central delta where it is focused today.

4.6 Summary and Conclusions

Stratigraphic evidence in the subaerial Bengal delta documents the effect that a regional anticline has had on downstream sediment dispersal of the Brahmaputra River. The depositional lobes presented in this chapter represent the overall fluvio-tectonic regime during
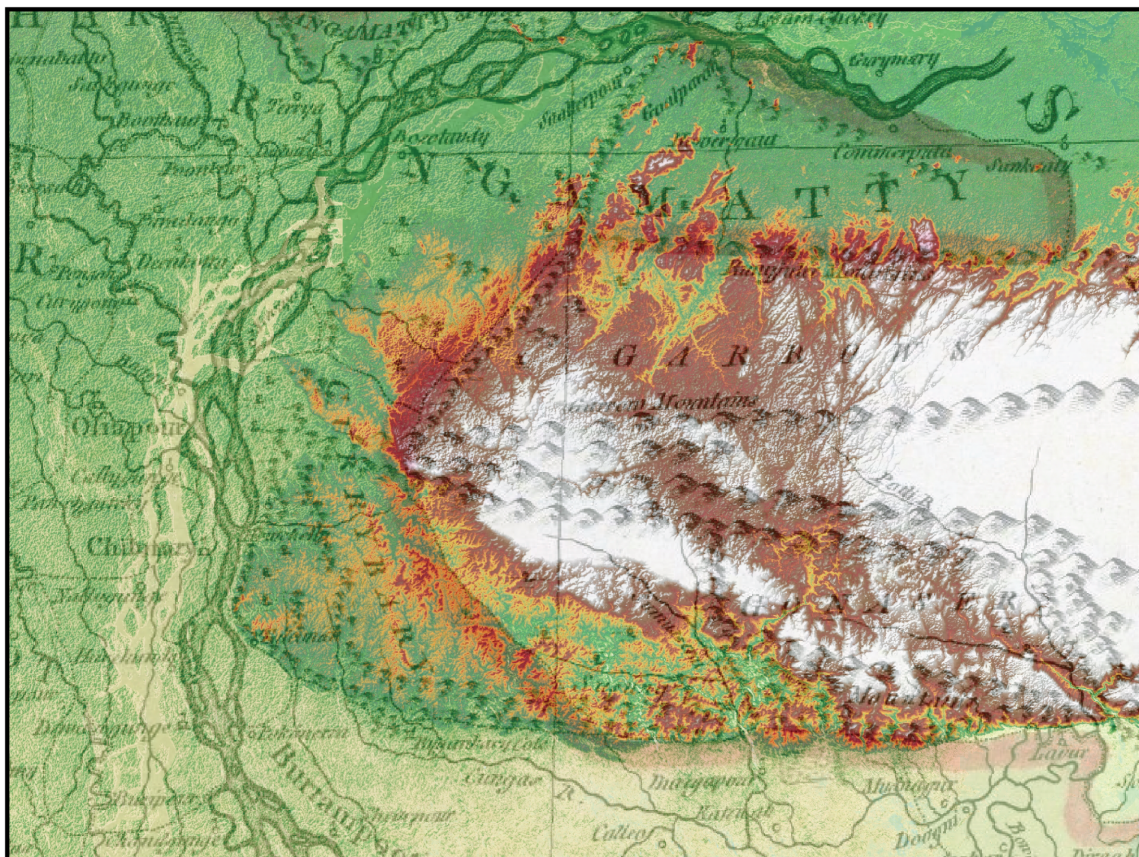
Figure 4.14: ASTER GDEM of Western Shillong Plateau georeferenced to 1776 historical map by Rennell and Dury (1776) to show location of Old Brahmaputra River, which was directly adjacent to the southwestern margin of the Garo Hills.

the time of deposition. We acknowledge that both the dynamics of river path selection as well as tectonic uplift activity are internally complex processes with some level of stochastic behavior that is not captured in stratigraphy of this resolution. However, we observe three distinct zones of deposition, for which we propose three stages of fluvial deposition in response to tectonic uplift.

In the eastern portion of the delta, relatively deeply buried Brahmaputra sediments have been folded and brought nearer to the surface coincident with north-south oriented folds associated with the westward propagating advance of the Indo-Burman foldbelt. With respect to the southwestern-most margin of the Shillong anticline, sediments in this eastern lobe were deposited during a period of incipient uplift, before the Shillong anticline and local folds generated enough topography to preclude the river from depositing sediments at these locations. Once exhumation generated enough topography to preclude deposition, however, the river moved westward, eroding into the relatively high topography of the adjacent Tista fan. Perhaps in conjunction with increased discharge during the Latest Pleistocene and Holocene, the river has eroded eastward into the margin of the Shillong anticline, defining a central depositional lobe in the recent stratigraphy. The thickness of Brahmaputra sediments in in each of these depositional zones indicates deposition during relative sea-level highstands, indicating that long term trends (10^5–10^6 years) may be preserved only in highstand stratigraphy; fluvio-tectonic interactions are likely ongoing during lowstands, but reduced discharge prevents the river from generating substantial stratigraphy for preservation.

Chapter 5

Conclusions

5.1   Summary and Conclusions

At the onset of this dissertation project I aimed to investigate external influences on river flow path selection and sediment dispersal to the delta in a large, braided river system. In Ch. 2, I presented a case for extreme paleohydrological events as the unequivocal driver influencing the preserved stratigraphy of the "lowstand" paleovalley of the Brahmaputra River. In Ch. 3, I presented the stratigraphy of terraces that have been created and stranded by the Brahmaputra in response to longer term glacioeustatic cycles. Finally, in Ch. 4, I considered the role that tectonic uplift of a regionally important structure played on the general flow path of the Brahmaputra during incipient uplift, in response to that uplift, and after the river had seemingly equilibrated to that uplift.

Prior to this project, our collective knowledge of the paleogeography of the Brahmaputra River contained many historical gaps. The approximate flow path and depocenter of the river during the Miocene was known thanks to the early perceptive work of Uddin and Lundberg (1999), which was refined by Allen et al. (2008), Galy et al. (2010), and Robinson et al. (2013) among others. The whereabouts of the river over the past 7–3 million years was established by Cina et al. (2009) and Chirouze et al. (2013), and recent work by Govin (2015) and Najman et al. (2016) seeks to bridge the historical gap of the past few million years. Work by Allison et al. (2003), Goodbred and Kuehl (2000b), and Pickering et al. (2014) sought to establish the flow path history of the river since the Last Glacial Maximum through the Holocene, but the paleogeography of the river through much of the Quaternary remained unknown. The work done for this dissertation has helped to bridge that gap—we have now established where the river was from the present back to about half a million years
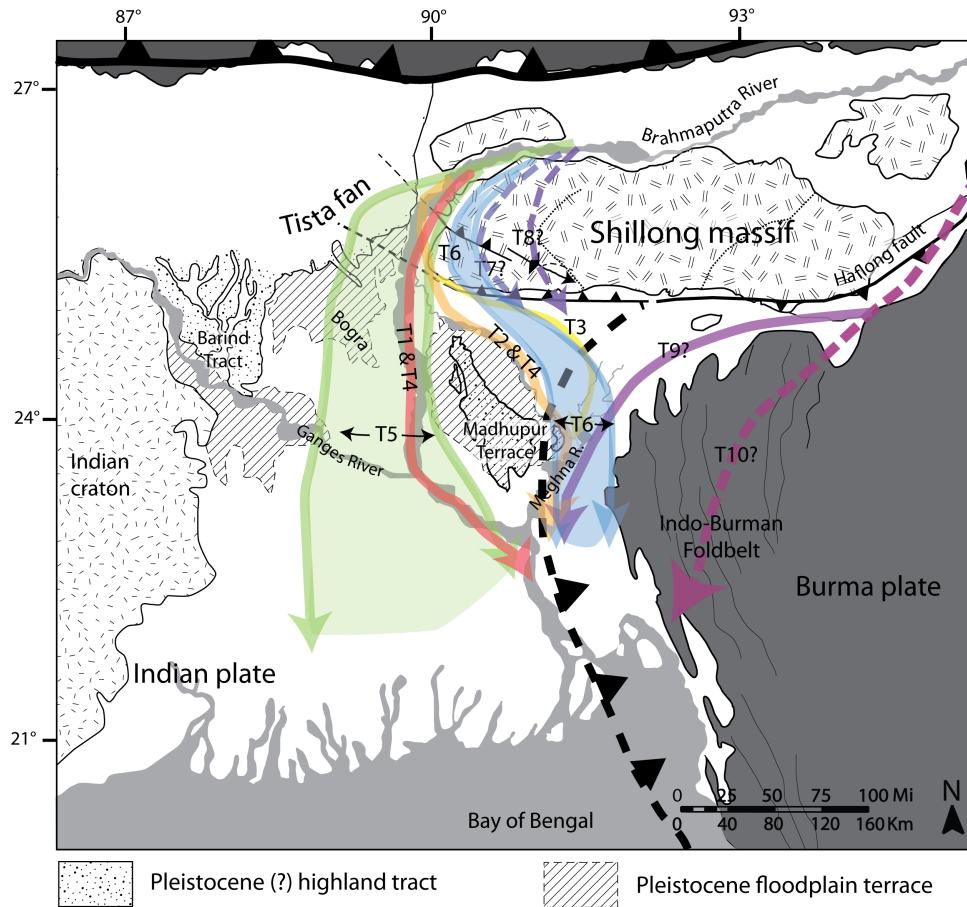
Figure 5.1: Interpreted flow paths of the Brahmaputra River from T10 (Miocene) to T1 (modern), based on work cited herein and results from this dissertation.

ago. A gap still exists, to be sure, but the flow paths presented in Fig. 5.1 make up the most comprehensive map that exists of the paleogeography of the Brahmaputra River during the Quaternary.

5.2 Contributions to the Field

In the broadest sense, the findings from the three papers contained herein suggest that, at least in this system, tectonics is the most important driver, in terms of where the river will go over the long-term ($\sim 10^5$ years), but that climate is equally important over shorter timescales, including both eustatic sea-level as a control over 10^4 year timescales, as well as extreme climate-related events such as paleofloods over 10^3–10^2 year timescales. These insights, although they are not the first nor the only findings to suggest this, offer a valuable perspective on the problem of allogenic fluvial drivers and the timescales over which they operate.

5.3 Future work

5.3.1 Luminescence Dating

Absolute ages of burial of both the terraces discussed in Ch. 3 and the uplifted Brahmaputra deposits on the margin of the Shillong Plateau discussed in Ch. 4 are currently being obtained by infrared stimulated luminescence (IRSL) dating of feldspar minerals found in the sands. Luminescence dating measures the amount of ionizing radiation (alpha, beta, and gamma rays associated with U, Th, and K decay) plus cosmic radiation that a sediment grain has accumulated internally since it's last exposure to light, which would have theoretically caused emission of any ionizing radiation accumulated prior to the resetting event. This ionizing radiation accumulates in "trap site" or luminescence centers, which are areas in the crystal lattice with charge deficits, created by atomic vacancies or substitutions. To date, eight samples have been collected from the Garo Hills (the southwest margin of

the Shillong Plateau) and the Bogra, Jamulpur, and Sherpur terraces. These samples are undergoing age analysis at the Physical Research Laboratory in Ahmedabad, India.

5.3.2 U/Pb Zircon Dating

Research is currently underway to identify delta sediments that were deposited by the early Holocene flood events presented in Ch. 2. Researchers are preparing zircon minerals picked from paleoflood sand deposits in the delta that have been identified as potential flood deposits due to their apparent mixed Brahmaputra-Shillong lithologies. If the floods were instrumental in exposing the freshly cut margins of the southwestern margin of the Shillong massif (Fig. 4.10), the Brahmaputra River would have incorporated some of these marginal Shillong sands within its sediment load, and thus may potentially contain a different suite of zircon abundances and age distributions than deposits were not associated with flood events. Evidence of detritus from the Namche Barwa (eastern Himalayan syntaxis) in the downstream Brahmaputra valley will definitively show that a major erosive event was routed through the Brahmaputra valley. Alternatively, zircon distributions that are dissimilar to those found in non-flood sediments throughout the delta will warrant further investigation, and may preliminarily be interpreted as potential flood deposits that incorporated material from the southwest Shillong margin.

5.3.3 Truncated Anticline Along the Jamuna Seismic Line

The Holocene gravel unit of Ch. 2 sits atop a dense but 'soft' (non-lithified) fluvial sand unit of latest Pleistocene age (Japan International Cooperation Agency, 1976). Deformation of these Pleistocene-aged sediments is evident in the upper 0.2 s (TWT) of the seismic profile. A particularly well imaged anticline about 100 km downstream along the seismic survey reveals that the deformation of the Pleistocene sediment is truncated by the Holocene gravel unit, indicating that the basal unconformity is erosional in some locations. In collaboration with Céline Grall, a post-doctoral researcher at Columbia University, the

horizontal resolution of the seismic line will be investigated by constructing a synthetic core log to determine if the truncation of this anticline is indeed real and not an artifact of the modern riverbed topography (i.e., a multiple that appears in just the right place to make the anticline merely appear to be truncated). We will begin working on this project in the fall of 2016.

Appendix A

Grain Size Data for Borehole Samples

Table A.1: Grain size data for BanglaPIRE samples. D [3, 2] is the surface weighted mean of the particles, and D [4, 3] is the volume weighted mean of the particles. The final 7 columns are particle size distributions for each sample, where d(0.500) is the value of the median diameter of the particle size distribution. All measurements are given in μm.

Sample ID	Field Grain Size	D [3, 2]	D [4, 3]	d(0.050)	d(0.160)	d(0.250)	d(0.0.500)	d(0.750)	d(0.840)	d(0.950)
BNGA00202	Mud	11.303	52.039	2.829	6.055	9.745	23.875	53.27	87.984	223.335
BNGA00205	Mud	11.08	70.031	2.682	5.456	8.868	26.992	91.952	150.126	280.383
BNGA00206	VF–F sand	130.811	179.076	74.917	102.857	119.431	163.708	223.627	258.171	339.65
BNGA00208	VF–F sand	229.964	326.616	122.152	171.625	202.665	289.54	413.688	487.451	664.633
BNGA00209	VF–F sand	285.604	394.454	128.201	184.077	223.429	341.757	518.159	622.03	848.875
BNGA00211	VF–F sand	327.872	431.908	165.486	235.219	278.024	393.411	549.941	639.554	840.47
BNGA00212	VF–F sand	379.685	492.365	208.202	281.052	326.902	453.292	627.361	724.862	920.298
BNGA00214	VF–F sand	335.057	449.794	157.754	232.716	279.496	407.712	584.56	684.655	892.295
BNGA00215	VF–F sand	394.029	479.032	206.953	272.566	315.912	437.128	605.553	701.166	900.339
BNGA00217	VF–F sand	450.635	535.228	242.242	315.738	364.215	498.546	678.533	774.762	954.399
BNGA00218	VF–F sand	456.529	538.856	248.029	321.701	370.043	502.973	680.278	775.235	953.742

Table A.1 – continued from previous page

Sample ID	Field Grain Size	D [3, 2]	D [4, 3]	d(0.050)	d(0.160)	d(0.250)	d(0.0.500)	d(0.750)	d(0.840)	d(0.950)
BNGA00220	VF–F sand	418.142	487.776	237.217	299.476	339.702	449.667	600.099	686.372	875.992
BNGA00223	M–C Sand	479.858	592.416	258.222	358.16	417.807	572.329	759.258	848.631	998.555
BNGA00226	M–C Sand	463.606	556.71	240.077	324.028	378.332	525.654	714.745	810.34	977.81
BNGA00229	VF–F sand	375.375	430.328	221.758	274.801	308.274	397.717	517.819	587.309	754.412
BNGA00230	VF–F sand	251.499	292.811	143.524	180.819	204.839	270.005	357.607	407.248	520.762
BNGA00502	Mud	10.422	99.047	2.507	5.503	9.243	27.599	116.767	228.268	443.008
BNGA00503	Mud	9.874	110.546	2.388	5.445	9.258	27.415	124.964	246.729	517.586
BNGA00505	VF–F sand	28.396	252.78	4.782	20.581	57.741	221.701	374.822	460.756	666.794
BNGA00506	VF–F sand	36.476	268.63	6.399	30.008	87.899	239.641	391.12	476.637	679.886
BNGA00508	VF–F sand	232.278	467.578	141.257	248.351	299.829	433.414	611.842	711.17	911.848
BNGA00511	VF–F sand	199.562	357.834	140.243	205.633	239.857	328.889	448.511	517.94	685.076
BNGA00514	VF–F sand	213.06	304.531	115.985	165.007	194.498	275.088	386.564	451.033	600.391
BNGA00517	M–C Sand	12.291	27.371	3.565	7.271	10.546	21.04	37.312	47.531	73.725
BNGA00520	M–C Sand	312.427	574.37	259.036	358.847	413.596	554.522	730.045	818.757	978.07
BNGA00523	M–C Sand	296.181	504.929	179.172	278.452	331.73	472.717	659.458	759.627	947.103
BNGA00526	M–C Sand	226.867	474.073	115.199	250.939	304.451	441.879	624.229	724.682	922.789
BNGA00529	M–C Sand	191.307	437.183	73.752	217.736	268.918	400.5	579.809	681.867	893.301

Table A.1 – continued from previous page

Sample ID	Field Grain Size	D [3, 2]	D [4, 3]	d(0.050)	d(0.160)	d(0.250)	d(0.0.500)	d(0.750)	d(0.840)	d(0.950)
BNGA00532	M–C Sand	258.343	346.634	155.034	207.403	238.331	320.295	429.594	491.85	636.374
BNGA00535	M–C Sand	290.134	330.86	170.187	212.168	238.905	310.135	402.413	452.745	562.377
BNGA00538	M–C Sand	85.581	291.714	29.434	154.078	186.732	268.115	376.801	439.727	589.532
BNGA00540	M–C Sand	10.43	80.735	2.985	5.634	8.018	16.942	41.625	131.666	462.108
BNGA00541	M–C Sand	85.733	199.721	66.745	99.185	117.012	166.719	243.438	295.396	454.124
BNGA00543	M–C Sand	84.895	196.231	56.044	88.069	105.459	154.906	234.743	292.595	496.947
BNGA00546	M–C Sand	39.341	186.633	7.321	64.719	92.854	154.174	246.48	308.162	476.395
BNGA00802	Mud	13.575	39.76	4.272	7.934	10.839	21.007	41.531	57.789	113.504
BNGA00803	Mud	8.905	54.783	2.659	4.512	6.234	14.587	49.011	81.786	209.078
BNGA00805	Mud	7.505	32.413	2.509	4.115	5.507	10.818	22.34	32.09	75.873
BNGA00806	Mud	12.213	29.973	3.531	6.966	10.075	21.346	40.918	53.565	86.1
BNGA00808	Mud	10.412	37.944	2.857	5.674	8.609	19.39	37.272	50.03	112.081
BNGA00809	Mud	9.161	35.59	2.669	4.744	6.879	16.523	34.579	47.099	94.364
BNGA00811	VF–F sand	10.872	43.845	2.929	5.646	8.526	21.55	49.35	70.636	144.286
BNGA00812	VF–F sand	273.36	392.392	133.65	201.838	242.29	351.929	503.977	593.078	800.836
BNGA00814	VF–F sand	267.828	354.621	150.286	200.594	232	318.501	440.249	512.772	690.545
BNGA00815	VF–F sand	331.556	413.161	168.887	227.461	265.791	372.055	519.838	606.011	806.024

Table A.1 – continued from previous page

Sample ID	Field Grain Size	D [3, 2]	D [4, 3]	d(0.050)	d(0.160)	d(0.250)	d(0.0.500)	d(0.750)	d(0.840)	d(0.950)
BNGA00817	VF–F sand	358.442	443.778	184.496	245.545	286.025	399.923	560.814	654.485	861.489
BNGA00818	VF–F sand	384.165	461.925	207.179	268.167	308.449	420.533	576.591	666.875	866.438
BNGA00820	VF–F sand	210.134	326.57	98.192	143.438	174.47	270.21	425.01	523.053	760.339
BNGA00823	M–C Sand	437.365	560.577	238.347	329.815	385.494	533.559	721.311	815.707	980.521
BNGA01102	Mud	10.592	39.442	3.29	5.936	8.206	16.53	33.115	46.124	103.772
BNGA01105	Mud	9.48	34.375	3.214	5.529	7.359	13.457	24.513	32.917	72.291
BNGA01108	VF–F sand	20.16	84.817	4.627	11.247	19.025	56.868	119.965	158.962	262.041
BNGA01109	M–C Sand	377.825	469.969	190.977	258.727	303.143	427.209	599.946	698.021	901.001
BNGA01111	M–C Sand	456.758	573.462	248.392	342.801	399.485	548.819	735.513	827.906	987.177
BNGA01112	M–C Sand	385.054	506.398	198.275	284.018	334.931	471.3	653.139	751.724	940.229
BNGA01114	M–C Sand	433.631	517.128	234.09	302.65	348.392	476.937	654.094	751.555	939.493
BNGA01115	M–C Sand	380.193	459.124	204.311	264.279	304.143	416.225	574.269	666.246	868.806
BNGA01117	M–C Sand	418.961	504.832	221.782	291.271	337.071	464.646	639.815	736.955	928.571
BNGA01118	M–C Sand	464.915	555.341	243.77	324.109	377.099	522.845	711.692	807.591	976.215
BNGA01120	VF–F sand	378.21	455.23	204.284	263.718	303.11	413.327	567.737	657.44	857.729
BNGA01121	VF–F sand	370.455	438.251	207.363	262.905	299.059	398.856	537.915	619.753	811.956
BNGA01123	VF–F sand	315.449	355.494	190.018	234.374	261.926	334.221	427.129	478.372	593.352

109

Table A.1 – continued from previous page

Sample ID	Field Grain Size	D [3, 2]	D [4, 3]	d(0.050)	d(0.160)	d(0.250)	d(0.0.500)	d(0.750)	d(0.840)	d(0.950)
BNGA01124	VF–F sand	303.737	350.578	174.918	220.068	248.872	325.993	427.443	483.933	610.4
BNGA01126	VF–F sand	334.908	395.216	188.147	238.522	271.13	360.373	482.845	554.046	724.369
BNGA01402	Mud	17.659	38.516	5.236	11.248	15.806	29.778	51.818	65.808	101.818
BNGA01403	Mud	15.326	49.314	4.454	9.146	12.991	25.935	49.648	67.39	136.648
BNGA01405	Mud	14.169	50.768	3.892	7.795	11.487	26.954	58.388	80.274	149.142
BNGA01406	VF–F sand	317.222	383.283	170.621	221.225	254.622	347.337	475.161	548.944	721.198
BNGA01408	VF–F sand	154.03	220.245	74.543	113.688	136.256	196.868	280.697	330.06	448.544
BNGA01409	VF–F sand	188.507	254.947	94.615	136.65	162.321	231.644	325.35	378.471	497.902
BNGA01411	VF–F sand	232.344	275.719	126.873	163.799	187.984	254.244	342.835	391.978	498.482
BNGA01412	VF–F sand	222.063	260.25	124.787	158.778	180.662	239.957	319.455	364.329	465.795
BNGA01414	VF–F sand	265.842	313.152	148.703	189.52	215.833	287.362	384.101	439.242	566.373
BNGA01415	VF–F sand	337.457	426.776	169.57	227.514	266.786	379.852	543.354	639.533	853.11
BNGA01417	VF–F sand	195.627	230.23	110.363	139.67	158.623	210.344	280.95	321.85	418.786
BNGA01418	M–C Sand	272.995	390.846	123.662	170.358	204.709	320.47	526.56	649.363	888.148
BNGA01420	M–C Sand	434.337	527.087	223.974	300.019	350.33	490.08	676.665	775.323	956.445
BNGA01423	M–C Sand	547.368	623.817	308.489	396.691	453.423	603.179	783.46	868.248	1008.101
BNGA01426	M–C Sand	461.823	584.013	278.36	368.013	421.295	560.933	735.908	823.913	981.213

Table A.1 – continued from previous page

Sample ID	Field Grain Size	D [3,2]	D [4,3]	d(0.050)	d(0.160)	d(0.250)	d(0.0.500)	d(0.750)	d(0.840)	d(0.950)
BNGA01429	VF–F sand	322.881	466.467	156.118	251.335	300.604	430.186	605.307	703.723	905.493
BNGA01432	VF–F sand	375.786	500.845	196.544	277.42	327.303	463.684	647.898	747.9	938.74
BNGA01703	Mud	5.992	59.997	2.024	3.186	4.224	8.452	19.501	32.91	485.873
BNGA01705	Mud	14.731	55.513	3.692	8.511	13.556	31.257	59.411	78.173	140.611
BNGA01706	VF–F sand	81.432	179.08	32.517	76.029	96.748	151.395	230.05	279.315	413.424
BNGA01708	VF–F sand	164.273	265.505	79.715	113.278	136.079	207.277	333.582	423.96	669.762
BNGA01709	VF–F sand	16.268	47.342	4.334	9.951	14.91	30.693	56.413	73.792	127.503
BNGA01711	VF–F sand	142.375	252.953	68.601	96.752	116.163	179.256	310.497	423.36	726.181
BNGA01712	VF–F sand	164.263	275.375	77.679	111.361	134.704	210.023	351.144	453.128	715.372
BNGA01715	M–C Sand	528.672	608.769	292.813	379.829	435.976	585.55	768.636	856.18	1002.216
BNGA01720	M–C Sand	466.735	587.549	260.214	355.136	413.119	565.603	752.727	843.155	995.696
BNGA01723	M–C Sand	507.435	592.433	274.218	359.773	415.647	566.552	754.06	844.608	996.713
BNGA01729	M–C Sand	500.608	586.279	269.622	354.547	409.857	559.175	746.43	838	993.128
BNGA02003	VF–F sand	7.34	43.394	2.456	4.034	5.387	10.413	21.356	31.606	187.724
BNGA02005	VF–F sand	251.12	329.778	126.553	185.972	219.552	306.338	418.327	479.982	614.997
BNGA02006	VF–F sand	180.572	209.53	103.227	130.18	147.466	194.002	255.743	290.421	369.131
BNGA02008	VF–F sand	191.102	225.022	107.533	136.297	154.916	205.761	275.093	315.061	408.942

Table A.1 – continued from previous page

Sample ID	Field Grain Size	D [3, 2]	D [4, 3]	d(0.050)	d(0.160)	d(0.250)	d(0.0.500)	d(0.750)	d(0.840)	d(0.950)
BNGA02009	VF–F sand	253.802	294.934	145.47	182.825	206.883	272.053	359.626	409.367	523.343
BNGA02011	VF–F sand	230.352	277.715	124.564	160.673	184.625	251.572	344.623	398.298	521.676
BNGA02012	VF–F sand	359.473	475.739	172.479	250.872	300.171	435.298	619.558	721.428	921.715
BNGA02014	VF–F sand	408.489	492.924	217.414	282.985	326.879	450.627	623.451	720.855	917.339
BNGA02015	M–C Sand	335.781	410.309	177.982	232.35	268.368	369.211	510.984	594.35	790.688
BNGA02017	M–C Sand	443.961	526.253	240.96	311.648	358.381	488.116	664.122	760.041	944.025
BNGA02018	M–C Sand	362.438	413.151	215.835	266.806	298.783	383.66	495.875	559.946	712.374
BNGA02020	M–C Sand	508.623	590.333	279.567	362.178	416.346	563.006	747.451	838.074	992.634
BNGA02302	VF–F sand	231.66	318.172	112.827	163.35	195.037	282.49	404.924	476.86	649.035
BNGA02305	VF–F sand	164.349	199.526	89.985	115.404	131.937	177.664	241.968	280.669	380.704
BNGA02308	VF–F sand	344.126	402.444	195.17	247.073	280.291	369.958	490.547	559.676	722.823
BNGA02309	VF–F sand	294.395	342.306	167.606	211.974	240.388	316.864	418.297	475.204	604.416
BNGA02314	VF–F sand	304.601	353.763	174.691	219.627	248.495	326.503	430.943	490.181	626.409
BNGA02327	VF–F sand	384.04	469.95	200.356	264.25	306.739	426.455	594.892	691.477	894.475
BNGA02329	VF–F sand	208.288	281.217	105.776	147.625	174.875	251.287	358.168	419.973	562.312
BNGA02332	M–C Sand	520.711	597.178	294.339	374.226	426.723	569.329	750.299	839.837	993.294
BNGA02335	VF–F sand	219.292	336.521	102.87	153.359	185.945	282.333	434.617	532.275	771.377

112

Table A.1 – continued from previous page

Sample ID	Field Grain Size	D [3, 2]	D [4, 3]	d(0.050)	d(0.160)	d(0.250)	d(0.0.500)	d(0.750)	d(0.840)	d(0.950)
BNGA02340	VF–F sand	349.05	486.972	150.257	252.185	307.736	452.351	642.325	744.515	937.909
BNGA02346	VF–F sand	354.485	468.867	176.452	256.428	303.587	430.092	602.519	700.059	902.113
BNGA02602	VF–F sand	82.717	137.169	36.522	59.423	73.967	116.153	179.632	218.467	312.239
BNGA02603	VF–F sand	271.202	316.943	151.731	193.643	220.858	294.534	391.466	444.594	559.024
BNGA02605	VF–F sand	359.512	436.004	192.112	249.402	287.505	394.199	543.92	631.293	831.01
BNGA02606	VF–F sand	277.776	329.351	152.296	196.005	224.664	303.309	408.724	467.501	596.294
BNGA02608	VF–F sand	331.277	446.341	147.509	221.785	270.334	403.753	585.622	687.626	896.761
BNGA02609	M–C Sand	364.856	477.176	173.844	258.454	308.341	440.151	616.062	713.813	911.919
BNGA02611	M–C Sand	325.235	449.712	148.606	231.954	280.738	410.306	585.638	684.729	891.512
BNGA02612	VF–F sand	239.01	285.065	132.183	169.057	192.919	258.542	349.284	402.411	529.684
BNGA02614	VF–F sand	207.491	240.563	118.535	149.605	169.546	223.198	294.167	333.786	422.594
BNGA02615	VF–F sand	204.548	253.751	106.782	140.092	162.428	225.751	316.198	369.924	498.571
BNGA02617	VF–F sand	234.782	281.145	126.133	164.547	189.638	258.453	350.734	402.207	514.677
BNGA02618	VF–F sand	178.811	239.144	88.83	118.272	138.526	198.853	294.361	357.47	531.899
BNGA02620	VF–F sand	218.358	308.636	98.078	139.589	169.091	258.818	397.159	483.141	697.734
BNGA02623	M–C Sand	392.643	509.028	192.033	275.449	328.362	472.86	664.117	765.159	951.37
BNGA02626	M–C Sand	495.147	578.517	269.675	350.763	403.896	548.895	734.167	826.608	986.47

Table A.1 – continued from previous page

Sample ID	Field Grain Size	D [3, 2]	D [4, 3]	d(0.050)	d(0.160)	d(0.250)	d(0.0.500)	d(0.750)	d(0.840)	d(0.950)
BNGA02629	M–C Sand	439.921	522.959	237.914	307.933	354.382	484.047	660.895	757.569	942.949
BNGA02632	M–C Sand	447.99	519.009	255.931	321.605	364.312	481.592	641.168	730.616	914.745
BNGA02635	M–C Sand	272.694	371.471	136.62	194.851	231.364	332.02	472.333	554.559	749.673
BNGA02638	M–C Sand	263.421	391.654	121.162	182.403	222.792	340.458	514.96	618.975	848.048
BNGA02641	M–C Sand	197.932	229.354	113.051	142.927	161.998	213.087	280.344	317.794	401.671
BNGA02643	M–C Sand	210.559	346.407	82.614	139.557	178.527	293.495	464.074	566.524	802.918
BNGA02802	VF–F sand	236.993	282.142	129.503	166.639	191.138	258.709	350.348	401.93	515.903
BNGA02806	VF–F sand	270.342	371.21	133.532	190.949	227.486	329.312	473.392	558.762	761.962
BNGA02809	VF–F sand	230.802	266.334	132.72	167.062	189.037	247.957	325.309	368.165	462.931
BNGA02811	VF–F sand	155.913	183.253	87.635	111.355	126.662	168.211	224.162	256.081	330.505
BNGA02812	VF–F sand	303.985	417.153	134.184	207.146	252.677	375.208	542.615	639.115	852.4
BNGA02815	M–C Sand	448.563	534.776	239.709	313.039	361.737	497.453	680.237	777.61	957.323
BNGA02818	M–C Sand	451.309	535.738	242.826	316.449	364.905	499.076	678.914	775.144	954.756
BNGA02823	M–C Sand	375.405	488.545	188.216	269.206	318.423	450.997	629.506	728.042	923.397
BNGA02826	VF–F sand	337.14	393.213	191.951	242.382	274.758	362.155	479.178	545.802	701.599
BNGA02829	VF–F sand	250.392	327.575	122.687	166.72	196.625	283.529	412.898	492.211	688.669
BNGA02832	M–C Sand	432.567	504.888	243.962	309.212	351.397	466.943	624.493	713.627	901.592

114

Table A.1 – continued from previous page

Sample ID	Field Grain Size	D [3, 2]	D [4, 3]	d(0.050)	d(0.160)	d(0.250)	d(0.0.500)	d(0.750)	d(0.840)	d(0.950)
BNGA02837	VF–F sand	391.292	460.171	219.936	278.687	316.751	421.188	565.411	649.475	841.952
BNGA02838	VF–F sand	207.745	260.826	107.277	141.295	164.236	229.895	325.174	382.591	522.268
BNGA02840	VF–F sand	164.081	232.932	86.036	118.582	139.566	199.464	289.037	345.836	498.623
BNGA02841	VF–F sand	260.296	362.479	125.623	187.468	224.428	324.458	462.666	543.635	736.219
BNGA02844	M–C Sand	485.064	570.405	261.298	342.334	395.315	539.831	725.45	819.027	982.252
BNGA02847	M–C Sand	428.605	509.116	233.277	300.804	345.386	469.444	639.648	734.603	924.919
BNGA02850	M–C Sand	389.053	458.512	217.918	276.765	314.88	419.446	563.889	648.084	841.083
BNGA02853	M–C Sand	370.067	484.922	192.747	269.763	317.114	446.126	622.445	720.89	918.154
BNGA03102	VF–F sand	197.344	296.202	87.293	140.19	172.601	260.433	382.468	454.666	630.315
BNGA03103	VF–F sand	178.011	252.035	82.679	125.521	152.319	225.374	325.525	383.116	515.079
BNGA03105	VF–F sand	268.47	367.442	126.858	195.039	233.168	333.097	467.648	545.402	728.915
BNGA03106	VF–F sand	206.948	258.477	105.992	141.181	164.671	231.109	325.004	379.72	506.048
BNGA03108	VF–F sand	219.463	247.779	131.977	162.691	181.932	232.466	297.968	334.216	416.043
BNGA03109	VF–F sand	277.857	344.777	143.845	190.649	221.689	308.801	430.997	502.32	670.347
BNGA03111	VF–F sand	350.46	421.477	189.268	245.304	282.019	383.372	522.622	603.027	789.616
BNGA03112	VF–F sand	317.106	366.759	181.748	229.367	259.754	341.012	447.722	507.084	640.344
BNGA03114	VF–F sand	161.22	189.738	91.727	115.377	130.677	172.491	229.86	263.441	345.776

Table A.1 – continued from previous page

Sample ID	Field Grain Size	D [3, 2]	D [4, 3]	d(0.050)	d(0.160)	d(0.250)	d(0.0.500)	d(0.750)	d(0.840)	d(0.950)
BNGA03115	VF–F sand	166.258	192.576	95.796	120.12	135.757	177.944	234.22	266.087	339.637
BNGA03117	VF–F sand	158.977	179.905	95.095	117.644	131.736	168.727	216.5	242.968	302.832
BNGA03118	VF–F sand	181.207	216.367	99.77	127.916	146.192	196.525	265.873	306.203	401.591
BNGA03120	VF–F sand	324.086	433.635	159.932	229.018	272.175	391.092	557.121	653.164	863.169
BNGA03123	VF–F sand	424.881	511.205	224.863	295.642	342.245	471.734	648.592	745.811	935.065
BNGA03126	VF–F sand	388.887	467.909	208.634	271.565	312.797	427.147	585.314	676.011	874.088
BNGA03129	VF–F sand	361.648	411.428	216.207	266.709	298.38	382.403	493.356	556.555	706.724
BNGA03132	VF–F sand	367.139	428.798	208.551	263.639	298.983	394.536	523.171	596.929	770.401
BNGA03135	VF–F sand	336.826	408.543	179.667	234.378	270.354	370.169	507.944	587.694	773.914
BNGA03138	VF–F sand	427.298	504.979	234.964	301.616	345.278	465.957	630.896	723.51	913.748
BNGA03141	VF–F sand	265.676	308.573	151.678	191.278	216.747	285.653	377.445	428.863	544.395
BNGA03144	VF–F sand	424.92	505.827	230.292	297.884	342.461	466.083	635.711	730.502	921.842
BNGA03147	VF–F sand	367.105	484.271	183.359	260.141	308.862	443.966	628.991	730.613	928.016
BNGA03150	VF–F sand	473.496	555.039	259.454	334.599	384.175	520.812	701.224	795.67	967.421
BNGA03153	VF–F sand	450.014	519.471	258.86	324.481	366.896	482.752	639.664	727.714	911.023
BNGA03155	VF–F sand	463.153	533.722	266.165	334.094	378.041	497.896	659.113	748.286	927.971
BNGA03603	VF–F sand	218.653	252.713	125.149	158.134	179.172	235.413	309.066	349.822	439.759

Table A.1 – continued from previous page

Sample ID	Field Grain Size	D [3, 2]	D [4, 3]	d(0.050)	d(0.160)	d(0.250)	d(0.0.500)	d(0.750)	d(0.840)	d(0.950)
BNGA03606	VF–F sand	222.595	251.737	132.832	164.765	184.62	236.693	303.608	340.364	422.21
BNGA03609	VF–F sand	286.72	355.881	149.904	196.496	227.651	316.158	443.104	518.765	701.385
BNGA03612	VF–F sand	146.026	236.552	62.985	103.615	129.66	204.264	311.489	374.551	522.688
BNGA03615	VF–F sand	193.519	274.214	100.702	138.907	163.696	234.762	341.688	409.588	590.162
BNGA03618	VF–F sand	170.918	200.613	96.234	122.224	138.957	184.334	245.359	280.115	360.966
BNGA03621	VF–F sand	139.666	206.396	66.425	98.213	118.485	176.348	262.27	315.565	452.333
BNGA03624	VF–F sand	173.559	229.806	91.106	125.629	147.458	207.431	290.135	337.906	448.49
BNGA03627	M–C Sand	366.372	444.758	194.846	254.102	293.307	402.772	556.024	645.255	846.669
BNGA03635	M–C Sand	346.13	427.252	180.811	237.514	275.339	382.521	536.209	627.361	836.284
BNGA03638	M–C Sand	364.955	487.594	180.139	261.296	311.372	448.609	635.096	736.97	932.671
BNGA03641	M–C Sand	248.581	309.935	128.749	169.58	197.076	275.476	387.689	453.961	610.489
BNGA03643	M–C Sand	426.192	509.698	228.652	297.414	342.941	469.737	643.798	740.387	930.731
BNGA03647	M–C Sand	293.604	344.287	164.831	210.064	239.08	317.428	422.142	481.281	616.323
BNGA03650	M–C Sand	442.182	528.794	235.056	308.335	356.686	491.06	672.383	769.809	952.173
BNGA03653	M–C Sand	364.731	438.92	196.901	254.945	293.099	398.746	545.277	630.437	826.224
BNGA03656	M–C Sand	426.135	542.151	221.401	312.635	367.346	512.388	698.774	794.973	967.967
BNGA04002	VF–F sand	189.956	245.361	103.849	143.775	167.266	229.005	309.18	353.029	446.824

Table A.1 – continued from previous page

Sample ID	Field Grain Size	D [3, 2]	D [4, 3]	d(0.050)	d(0.160)	d(0.250)	d(0.0.500)	d(0.750)	d(0.840)	d(0.950)
BNGA04003	VF–F sand	176.798	236.86	86.857	131.311	155.799	219.135	301.716	347.578	448.519
BNGA04005	VF–F sand	280.966	328.584	157.856	200.188	227.966	303.894	405.281	461.546	584.543
BNGA04006	VF–F sand	163.031	237.435	66.843	105.556	132.531	208.278	312.112	371.979	511.31
BNGA04008	VF–F sand	194.533	235.546	103.694	135.363	156.255	214.148	293.579	338.916	441.485
BNGA04009	VF–F sand	225.444	282.667	113.46	153.652	180.294	254.758	357.598	416.318	548.963
BNGA04011	VF–F sand	244.726	294.079	132.152	171.045	196.751	268.033	365.737	421.271	546.229
BNGA04012	VF–F sand	188.307	218.207	108.003	136.02	153.948	202.118	265.987	301.9	383.794
BNGA04014	VF–F sand	169.911	192.605	101.042	125.539	140.801	180.789	232.245	260.625	324.419
BNGA04015	VF–F sand	172.378	228.4	86.409	114.995	134.394	191.143	279.092	336.946	501.115
BNGA04017	VF–F sand	321.781	455.289	135.846	233.464	285.707	419.356	595.704	694.176	897.779
BNGA04018	VF–F sand	167.09	195.045	94.733	119.99	136.207	179.961	238.327	271.315	347.242
BNGA04020	VF–F sand	216.887	276.32	107.202	146.287	172.485	246.807	351.37	411.622	548.104
BNGA04023	VF–F sand	265.86	375.677	123.908	186.368	225.287	333.002	484.394	573.641	783.461
BNGA04026	VF–F sand	180.008	235.455	89.917	120.308	140.945	201.003	291.957	349.522	501.303
BNGA04029	VF–F sand	232.676	317.146	117.044	167.736	198.841	284.171	402.812	471.86	633.739
BNGA04032	VF–F sand	300.597	419.991	147.23	226.486	269.413	382.754	536.984	626.199	829.447
BNGA04035	VF–F sand	331.675	426.908	193.51	257.322	295.071	394.696	527.762	604.171	783.419

Table A.1 – continued from previous page

Sample ID	Field Grain Size	D [3, 2]	D [4, 3]	d(0.050)	d(0.160)	d(0.250)	d(0.0.500)	d(0.750)	d(0.840)	d(0.950)
BNGA04038	VF–F sand	264.483	382.725	122.585	189.466	229.384	339.317	495.068	587.206	801.513
BNGA04041	VF–F sand	293.503	411.871	136.2	210.495	253.93	370.937	532.284	625.89	837.037
BNGA04044	VF–F sand	372.175	483.477	196.6	271.804	318.278	444.831	617.622	714.556	911.981
BNGA04047	VF–F sand	254.423	352.093	124.207	191.674	228.002	322.581	447.94	518.966	682.349
BNGA04050	VF–F sand	202.029	306.784	92.133	138.651	168.764	257.393	394.899	481.784	700.763
BNGA04603	Mud	18.419	50.488	4.725	10.937	17.282	38.918	70.619	89.648	137.339
BNGA04604		237.926	421.009	112.256	213.611	260.604	382.996	550.015	646.334	858.042
BNGA04606	VF–F sand	230.899	311.851	134.368	181.276	209.194	284.199	386.975	447.034	590.863
BNGA04608	VF–F sand	179.149	243.805	97.865	135.373	158.079	219.958	306.085	356.696	476.815
BNGA04612	M–C Sand	309.903	357.06	178.95	224.816	254.099	332.383	435.068	492.094	619.794
BNGA04615	M–C Sand	338.357	394.806	193.326	243.285	275.408	362.496	480.18	547.847	708.298
BNGA04618	M–C Sand	389.957	478.797	201.885	267.235	310.981	434.979	609.582	708.596	910.123
BNGA04621	M–C Sand	350.86	409.182	200.447	252.338	285.683	376.066	498.074	568.148	733.605
BNGA04624	M–C Sand	327.61	379.308	188.308	236.831	267.872	351.219	461.626	523.743	666.483
BNGA04627	M–C Sand	423.757	509.085	225.35	294.365	340.245	468.773	645.411	742.915	933.248
BNGA04630	M–C Sand	411.242	491.783	221.7	288.065	331.513	451.722	616.962	710.291	904.871
BNGA04634	M–C Sand	391.478	458.713	222.094	279.733	317.121	419.854	562.035	644.993	836.535

Table A.1 – continued from previous page

Sample ID	Field Grain Size	D [3, 2]	D [4, 3]	d(0.050)	d(0.160)	d(0.250)	d(0.0.500)	d(0.750)	d(0.840)	d(0.950)
BNGA04640	M–C Sand	378.311	446.422	211.877	269.124	306.183	407.756	548.024	630.007	821.47
BNGA04646	M–C Sand	282.344	341.124	153.8	197.907	226.676	306.553	418.82	485.455	648.321
BNGA04649	M–C Sand	354.03	432.095	187.451	244.842	282.909	389.723	540.121	628.221	830.267
BNGA04654		408.487	537.219	204.274	298.542	355.673	507.838	701.519	799.628	972.243
BNGA04902	VF–F sand	261.586	293.298	158.265	195.134	218.007	277.469	352.745	393.479	482.225
BNGA04903	VF–F sand	244.292	282.239	140.333	176.612	199.842	262.339	344.916	390.861	492.907
BNGA04905	VF–F sand	247.445	279.914	147.958	183.094	205.036	262.739	337.344	378.464	470.718
BNGA04906	VF–F sand	213.628	246.308	123.276	154.796	174.959	229.07	300.406	340.136	428.703
BNGA04908	VF–F sand	214.973	253.33	120.373	153.213	174.378	232.057	310.417	355.421	459.991
BNGA04909	VF–F sand	189.318	221.312	106.334	135.708	154.49	204.959	271.681	308.929	392.592
BNGA04911	VF–F sand	198.289	273.969	102.24	142.225	168.074	241.178	346.765	410.047	562.727
BNGA04912	VF–F sand	306.423	383.553	156.692	208.853	243.687	342.092	481.46	563.542	758.438
BNGA04914	VF–F sand	297.345	364.984	155.601	205.446	238.283	329.499	455.39	527.987	697.432
BNGA04915	VF–F sand	264.352	328.402	137.771	180.819	209.792	292.229	409.807	479.201	644.225
BNGA04917	M–C Sand	329.153	407.35	170.021	226.198	263.269	366.663	510.779	594.766	790.842
BNGA04918	M–C Sand	392.141	478.503	204.734	270.324	313.854	435.988	606.315	703.061	903.352
BNGA04920	VF–F sand	298.43	343.753	172.139	216.456	244.737	320.408	419.434	474.153	595.31

Table A.1 – continued from previous page

Sample ID	Field Grain Size	D [3, 2]	D [4, 3]	d(0.050)	d(0.160)	d(0.250)	d(0.0.500)	d(0.750)	d(0.840)	d(0.950)
BNGA04923	VF–F sand	172.599	232.068	84.733	113.872	133.908	193.339	286.426	347.37	515.362
BNGA04926	M–C Sand	344.171	402.705	194.802	246.946	280.323	370.376	491.237	560.364	723.078
BNGA04929	M–C Sand	328.35	394.472	178.086	230.038	264.195	358.551	488.01	562.589	736.571
BNGA04932	M–C Sand	427.337	498.995	241.153	305.492	347.126	461.021	616.375	704.605	893
BNGA04935	M–C Sand	365.779	430.756	205.355	261.01	296.798	394.185	527.134	604.471	787.549
BNGA04946	M–C Sand	375.592	489.903	187.615	266.525	316.152	451.542	634.014	733.922	928.721
BNGA04949	VF–F sand	278.989	386.923	139.12	195.346	232.274	338.846	496.294	591.249	811.772
BNGA04952	VF–F sand	263.564	325.633	138.56	180.999	209.441	290.161	405.329	473.404	635.651
BNGA04953	VF–F sand	334.91	416.393	171.919	229.385	267.381	373.926	523.815	611.577	814.478
BNGA05202	VF–F sand	204.7	280.118	107.409	149.686	176.191	249.676	353.493	414.94	562.01
BNGA05206	VF–F sand	183.673	227.355	96.072	126.199	146.262	202.745	282.742	330.093	444.223
BNGA05212	VF–F sand	153.024	178.484	86.744	109.928	124.794	164.878	218.177	248.19	316.826
BNGA05215	VF–F sand	328.965	418.778	162.199	222.942	262.94	375.051	532.672	624.804	834.318
BNGA05221	VF–F sand	271.089	327.13	145.504	189.089	217.829	297.421	406.704	469.208	611.451
BNGA05227	VF–F sand	335.251	407.647	177.262	233.995	270.585	370.675	507.206	585.845	769.286
BNGA05235	VF–F sand	238.557	302.23	122.185	161.8	188.43	264.682	376.176	444.1	613.119
BNGA05238	VF–F sand	287.06	389.061	139.033	198.41	236.816	344.722	498.39	589.414	801.585

Table A.1 – continued from previous page

Sample ID	Field Grain Size	D [3, 2]	D [4, 3]	d(0.050)	d(0.160)	d(0.250)	d(0.0.500)	d(0.750)	d(0.840)	d(0.950)
BNGA05502	Mud	14.276	43.816	4.084	8.331	11.901	24.352	49.67	71.859	160.088
BNGA05503	Mud	15.352	56.189	4.104	8.637	12.745	29.14	72.074	108.605	202.841
BNGA05505	Mud	12.058	29.771	3.548	7.002	10.005	20.228	37.95	50.106	85.041
BNGA05506	Mud	10.407	54.131	2.788	5.292	7.96	20.154	55.25	106.001	239.751
BNGA05508	VF–F sand	203.564	245.494	109.879	142.049	163.335	222.598	304.63	351.899	460.836
BNGA05509	VF–F sand	172.634	234.339	89.887	130.856	154.154	215.598	297.244	343.142	446.047
BNGA05511	VF–F sand	189.04	229.729	100.85	131.397	151.54	207.61	285.394	330.478	435.498
BNGA05512	VF–F sand	192.293	228.291	106.327	136.267	155.634	208.521	280.559	321.988	418.473
BNGA05514	VF–F sand	171.38	233.162	99.924	136.306	157.822	214.97	291.338	334.634	433.865
BNGA05515	VF–F sand	187.158	240.089	108.752	144.338	165.801	222.694	297.85	339.992	435.27
BNGA05517	VF–F sand	232.734	282.142	123.829	161.603	186.634	256.252	352.13	406.789	529.996
BNGA05518	M–C Sand	318.691	446.906	148.324	221.658	269.517	403.542	588.248	691.433	900.81
BNGA05520	M–C Sand	321.118	443.122	149.801	221.2	267.791	398.531	580.857	684.222	896.292
BNGA05521	M–C Sand	378.739	464.255	195.907	262.132	305.099	423.349	586.065	679.162	880.242
BNGA05523	VF–F sand	295.375	389.462	157.125	216.407	253.178	352.977	489.554	568.738	755.625
BNGA05524	VF–F sand	269.888	369.341	135.283	190.797	226.576	327.124	470.206	555.051	757.565
BNGA05526	VF–F sand	223.892	307.151	119.056	163.16	191.379	270.804	385.618	454.954	625.373

Table A.1 – continued from previous page

Sample ID	Field Grain Size	D [3, 2]	D [4, 3]	d(0.050)	d(0.160)	d(0.250)	d(0.0.500)	d(0.750)	d(0.840)	d(0.950)
BNGA05527	Mud	302.807	412.121	160.331	221.574	260.393	368.97	523.696	615.257	825.487
BNGA05529	VF–F sand	312.515	375.886	169.157	218.649	251.269	341.524	465.359	536.456	701.628
BNGA05530	VF–F sand	341.757	423.748	176.698	233.831	271.948	379.749	533.125	623.426	830.286
BNGA05532	M–C Sand	469.463	583.612	245.8	344.794	405.088	562.216	752.534	843.643	996.29
BNGA05534		432.044	524.067	223.483	298.385	348.038	486.317	672.055	770.884	953.723
BNGA05535	M–C Sand	412.344	496.231	220.118	286.067	330.104	454.233	627.223	724.505	919.92
BNGA05537		395.46	475.99	212.659	275.186	316.785	433.499	597.217	691.309	891.367
BNGA05538	M–C Sand	367.331	432.836	206.784	261.812	297.42	394.97	529.591	608.43	795.843
BNGA05540		454.071	540.949	241.816	317.348	367.148	505.077	688.738	785.489	962.179
BNGA05541	M–C Sand	412.329	480.574	234.664	295.71	335.158	442.811	589.866	674.327	863.226
BNGA05543		403.046	470.565	229.232	288.757	327.265	432.548	576.901	660.284	849.578
BNGA05544	VF–F sand	290.363	387.321	152.156	209.946	246.292	346.651	488.214	572.311	773.128
BNGA05546		304.769	364.414	165.964	214.198	245.793	332.552	450.576	517.956	672.711
BNGA05547	VF–F sand	321.843	398.067	166.829	221.734	257.691	357.719	497.654	579.776	774.036
BNGA05549		289.433	343.66	158.564	204.108	233.986	315.832	425.896	487.499	624.496
BNGA05550	VF–F sand	294.697	341.878	167.57	212.605	241.273	317.879	418.299	474.019	598.405
BNGA05552		461.074	541.703	253.11	325.394	373.126	505.315	682.641	777.69	955.677

Table A.1 – continued from previous page

Sample ID	Field Grain Size	D [3, 2]	D [4, 3]	d(0.050)	d(0.160)	d(0.250)	d(0.0.500)	d(0.750)	d(0.840)	d(0.950)
BNGA05553	M–C Sand	473.75	558.345	255.985	333.62	384.613	524.987	709.017	804.021	973.531
BNGA05555		473.267	554.231	260.24	334.746	383.884	519.543	699.492	794.099	966.566
BNGA05556	M–C Sand	464.539	546.052	254.342	327.401	375.824	510.064	689.621	784.943	960.854
BNGA05559	Mud	9.253	46.793	2.744	4.737	6.606	15.558	44.67	70.356	174.494
BNGA05561		418.729	531.21	229.216	310.421	360.873	497.506	678.664	775.293	955.185
BNGA05563	M–C Sand	476.118	546.813	274.411	344.127	389.23	512.035	676.06	765.581	941.115
BNGA05564		506.07	575.3	295.185	368.673	416.023	544.106	710.929	798.88	963.604
BNGA05566	M–C Sand	434.705	514.022	238.15	306.586	351.411	475.283	644.358	738.397	926.43
BNGA05567	M–C Sand	525.921	595.809	306.167	384.215	434.251	568.142	738.21	824.556	980.624
BNGA05569	M–C Sand	526.432	595.674	307.507	385.058	434.795	567.901	737.135	823.301	979.611
BNGA05570	M–C Sand	531.713	610.664	296.198	382.973	438.888	587.517	769.597	856.766	1002.394
BNGA05903	Mud	11.505	55.162	2.939	5.768	8.875	26.047	72.049	106.323	209.225
BNGA05905	VF–F sand	245.321	307.377	147.757	194.197	221.157	290.676	379.054	427.009	530.753
BNGA05906	VF–F sand	19.706	98.42	4.73	11.782	18.789	44.555	95.419	139.549	459.79
BNGA05908	VF–F sand	351.911	411.254	199.411	251.693	285.787	378.761	503.683	574.304	735.555
BNGA05915	VF–F sand	233.888	268.41	135.406	170.084	192.186	251.046	327.514	369.386	460.898
BNGA05921	VF–F sand	177.794	210.607	98.294	126.248	144.246	193.117	258.984	296.549	383.415

Table A.1 – continued from previous page

Sample ID	Field Grain Size	D [3, 2]	D [4, 3]	d(0.050)	d(0.160)	d(0.250)	d(0.0.500)	d(0.750)	d(0.840)	d(0.950)
BNGA05927	M–C Sand	417.627	502.525	221.765	291.164	336.576	462.449	635.287	731.694	924.427
BNGA05934	M–C Sand	343.777	419.084	183.511	238.058	274.316	376.385	521.564	607.639	809.464
BNGA05940	M–C Sand	472.433	545.478	268.797	339.913	385.824	510.786	677.252	767.614	943.416
BNGA05946	M–C Sand	433.91	516.614	234.482	303.628	349.472	477.228	652.067	748.346	936.173
BNGA05952	M–C Sand	418.385	542.692	211.976	309.437	365.899	514.41	703.675	800.324	971.887
BNGA05956	M–C Sand	491.046	573.64	268.017	349.389	401.895	543.884	725.541	817.552	980.117
BNGA06202	VF–F sand	8.664	80.205	2.395	4.176	5.95	16.401	95.297	191.475	371.007
BNGA06203	VF–F sand	8.299	29.976	2.635	4.461	6.089	12.752	28.75	41.773	83.93
BNGA06205	VF–F sand	8.542	31.855	2.651	4.537	6.251	13.573	31.721	45.86	89.922
BNGA06206	VF–F sand	10.041	24.366	3.344	5.575	7.465	14.787	30.706	42.65	76.582
BNGA06208	VF–F sand	146.587	189.387	73.489	98.214	115.031	163.939	236.996	282.062	394.681
BNGA06209	VF–F sand	137.642	160.358	78.111	98.95	112.31	148.275	195.988	222.801	284.118
BNGA06211	VF–F sand	168.17	254.308	78.895	118.782	144.796	219.726	329.235	394.811	551.842
BNGA06212	VF–F sand	135.544	170.051	70.006	92.303	107.313	150.119	211.743	248.701	339.266
BNGA06214	VF–F sand	201.402	272.727	96.638	147.262	175.643	249.807	348.19	403.664	528.347
BNGA06215	VF–F sand	219.42	277.44	113.12	149.259	173.434	242.455	343.738	406.054	563.978
BNGA06217	VF–F sand	210.214	257.08	112.295	145.484	167.588	229.888	318.408	370.942	496.955

Table A.1 – continued from previous page

Sample ID	Field Grain Size	D [3, 2]	D [4, 3]	d(0.050)	d(0.160)	d(0.250)	d(0.0.500)	d(0.750)	d(0.840)	d(0.950)
BNGA06218	VF–F sand	222.002	283.005	113.514	150.179	174.843	245.894	351.568	417.049	582.36
BNGA06220	VF–F sand	374.715	450.712	202.132	261.8	301.099	410.034	561.197	648.819	846.604
BNGA06223	VF–F sand	210.989	258.106	111.844	145.689	168.288	231.985	321.742	374.059	495.198
BNGA06226	VF–F sand	190.626	249.665	98.33	128.134	148.409	207.86	301.141	364.129	552.647
BNGA06229	M–C Sand	415.086	472.78	247.366	305.186	341.694	439.032	569.496	644.52	819.905
BNGA06232	M–C Sand	361.45	408.485	218.524	268.2	299.29	381.286	488.528	549.098	691.316
BNGA06235	M–C Sand	454.587	540.065	243.379	318.718	368.161	504.347	685.591	781.675	959.086
BNGA06238	M–C Sand	366.085	425.67	209.81	263.827	298.484	392.118	517.999	590.123	759.797
BNGA06241	M–C Sand	427.202	513.156	226.862	296.562	343.059	473.295	651.623	749.221	937.605
BNGA06244	M–C Sand	471.12	544.003	267.932	339.03	384.889	509.475	675.079	765.079	940.982
BNGA06247	M–C Sand	459.387	542.513	248.986	323.384	372.256	506.929	686.194	781.468	958.321
BNGA06250	M–C Sand	479.242	552.561	272.623	345.033	391.847	518.98	686.83	776.888	949.657
BNGA06253	M–C Sand	387.432	454.066	219.07	276.828	314.184	416.301	556.333	637.572	825.548
BNGA06256	M–C Sand	407.512	514.368	195.301	276.571	330.317	478.397	672.181	773.032	956.192
BNGA06602	Mud	11.151	23.638	3.454	6.606	9.205	17.656	31.509	40.562	64.793
BNGA06603	Mud	8.274	30.476	2.745	4.714	6.369	12.092	22.393	29.854	57.109
BNGA06605	Mud	9.495	19.568	3.154	5.535	7.461	13.996	25.58	33.533	55.558

Table A.1 – continued from previous page

Sample ID	Field Grain Size	D [3,2]	D [4,3]	d(0.050)	d(0.160)	d(0.250)	d(0.0.500)	d(0.750)	d(0.840)	d(0.950)
BNGA06606	VF–F sand	269.288	309.365	155.805	195.589	221.008	289.001	377.626	426.325	532.739
BNGA06608	VF–F sand	246.445	285.397	141.528	177.928	201.31	264.381	348.36	395.506	501.708
BNGA06609	VF–F sand	270.277	312.736	154.895	195.281	221.113	290.537	382.182	433.193	546.915
BNGA06611	VF–F sand	287.166	396.507	148.504	208.376	246.458	353.143	505.398	595.592	805.831
BNGA06612	VF–F sand	306.883	356.098	175.262	221.377	250.855	330.085	434.976	493.709	626.265
BNGA06614	VF–F sand	299.73	353.872	167.834	213.38	242.829	323.288	433.001	496.216	644.963
BNGA06615	VF–F sand	234.222	272.577	132.842	168.496	191.286	252.626	333.941	379.405	481.245
BNGA06617	VF–F sand	286.894	345.772	154.553	200.089	230.27	314.281	429.741	495.694	645.835
BNGA06618	VF–F sand	335.233	418.933	171.441	228.523	266.548	374.356	528.436	619.442	827.84
BNGA06620	VF–F sand	303.447	370.947	161.193	209.957	242.37	333.224	460.7	535.4	712.709
BNGA07002	Mud	10.195	33.517	3.102	5.852	8.219	16.274	30.453	40.657	77.144
BNGA07003	VF–F sand	440.393	509.345	253.391	317.154	358.43	471.576	626.204	714.121	900.744
BNGA07005	VF–F sand	288.73	332.608	166.776	209.313	236.544	309.613	405.715	459.044	577.525
BNGA07006	VF–F sand	282.45	326.553	161.997	204.063	231.029	303.495	398.985	452.053	570.485
BNGA07009	VF–F sand	300.036	336.932	181.354	223.551	249.763	318.114	405.031	452.284	556.703
BNGA07011	VF–F sand	302.215	338.01	184.245	226.015	251.992	319.562	405.372	451.933	554.49
BNGA07012	VF–F sand	278.562	313.675	167.466	206.944	231.482	295.75	377.764	422.554	521.031

Table A.1 – continued from previous page

Sample ID	Field Grain Size	D [3, 2]	D [4, 3]	d(0.050)	d(0.160)	d(0.250)	d(0.0.500)	d(0.750)	d(0.840)	d(0.950)
BNGA07014	VF–F sand	261.716	294.964	157.216	194.181	217.295	277.792	355.387	397.76	491.528
BNGA07015	VF–F sand	254.638	295.582	145.419	183.463	207.907	273.835	361.405	410.437	520.556
BNGA07017	VF–F sand	297.901	366.488	156.8	205.2	237.486	328.392	456.374	531.392	709.347
BNGA07018	VF–F sand	429.19	500.66	242.949	306.841	348.321	462.217	618.32	707.093	896.102
BNGA07020	VF–F sand	413.132	486.284	230.541	293.483	334.338	446.84	602.049	691.048	883.99
BNGA07023	VF–F sand	310.335	360.572	177.285	223.657	253.406	333.522	439.976	499.894	636.808
BNGA07024	VF–F sand	324.187	394.283	173.303	225.106	259.441	355.265	489.274	567.714	753.842
BNGA07026	M–C Sand	532.188	611.104	296.447	383.008	438.997	587.997	770.386	857.534	1002.843
BNGA07027	M–C Sand	554.905	630.87	313.353	403.4	460.986	611.909	791.594	875.226	1011.564
BNGA07029	M–C Sand	566.522	639.204	325.752	413.698	470.615	620.614	798.945	881.404	1014.613
BNGA07030	M–C Sand	224.871	566.256	205.435	332.116	393.227	549.577	741.179	834.303	991.597
BNGA07032	M–C Sand	434.613	561.937	246.701	335.09	389.249	534.308	720.214	814.412	979.695
BNGA07033	M–C Sand	355.313	462.719	206.858	274.499	315.518	426.084	577.481	664.919	860.063
BNGA07035	M–C Sand	368.857	486.174	202.619	274.794	320.28	446.235	620.903	719.212	917.118
BNGA07036	M–C Sand	362.045	489.978	193.931	271.03	318.807	450.691	632.379	733.007	929.28
BNGA07038	M–C Sand	348.252	482.931	180.67	261.533	310.411	444.112	627	728.098	926.002
BNGA07039	M–C Sand	395.719	525.816	202.849	295.959	350.222	494.35	682.246	780.677	959.974

Table A.1 – continued from previous page

Sample ID	Field Grain Size	D [3, 2]	D [4, 3]	d(0.050)	d(0.160)	d(0.250)	d(0.0.500)	d(0.750)	d(0.840)	d(0.950)
BNGA07041	M–C Sand	422.416	562.695	198.515	314.573	379.016	542.583	739.173	833.486	991.576
BNGA07042	M–C Sand	305.014	407.508	162.845	222.381	260.368	366.181	515.126	602.671	806.203
BNGA07044	M–C Sand	399.466	512.108	219.9	296.166	344.135	475.425	653.082	750.286	938.159
BNGA07045	M–C Sand	444.95	552.341	261.102	341.381	390.572	522.177	694.004	785.06	956.47
BNGA07047	M–C Sand	385.703	498.796	209.703	284.529	331.527	460.531	636.842	734.676	927.872
BNGA07048	M–C Sand	465.39	549.664	251.754	326.869	376.622	514.46	697.598	793.544	967.136
BNGA07050	M–C Sand	384.303	491.599	222.264	294.372	338.145	455.969	615.632	705.933	896.725
BNGA07051	M–C Sand	428.049	512.397	228.939	298.389	344.387	472.626	648.368	745.293	934.559
BNGA07053	M–C Sand	419.811	534.705	231.177	312.107	362.841	501.099	684.435	781.391	959.545
BNGA07054	M–C Sand	424.446	505.718	230.199	296.98	341.325	465.216	636.323	732.005	923.935
BNGA07056		365.62	442.872	195.981	253.89	292.366	400.345	552.503	641.627	844.024
BNGA07057	M–C Sand	257.893	299.717	146.038	185.577	210.87	278.702	367.726	416.925	525.344
BNGA07059	M–C Sand	283.429	363.935	141.01	190.173	223.506	319.603	459.52	543.446	745.36
BNGA07060	M–C Sand	305.061	433.055	140.272	211.177	257.162	387.036	570.285	674.787	890.603
BNGA07062	M–C Sand	495.563	577.526	271.772	352.124	404.602	547.476	730.849	823.213	984.274
BNGA07063	M–C Sand	403.61	499.67	203.012	276.133	324.411	459.155	643.26	743.804	936.333
BNGA07064	M–C Sand	467.65	550.07	254.993	329.23	378.526	514.89	696.055	791.319	965.042

Table A.1 – continued from previous page

Sample ID	Field Grain Size	D [3, 2]	D [4, 3]	d(0.050)	d(0.160)	d(0.250)	d(0.0.500)	d(0.750)	d(0.840)	d(0.950)
BNGA07065		465.338	547.006	254.522	327.978	376.634	511.278	690.971	786.198	961.645
BNGA07102	Mud	6.995	26.534	2.177	3.677	5.138	11.683	24.798	33.576	59.497
BNGA07103	Mud	8.135	33.384	2.348	4.194	6.125	15.065	31.783	42.771	75.051
BNGA07105	Mud	9.043	34.266	2.472	4.599	6.972	18.229	38.621	53.04	111.778
BNGA07106	Mud	8.633	37.53	2.396	4.358	6.482	17.06	38.491	54.419	118.437
BNGA07108	Mud	8.225	30.732	2.356	4.14	5.974	15.511	38.101	55.067	109.211
BNGA07109	Mud	7.8	40.532	2.311	3.918	5.509	13.912	36.152	52.2	102.975
BNGA07111	Mud	7.916	26.292	2.307	3.993	5.7	14.659	36.049	50.517	88.37
BNGA07112	Mud	8.237	32.722	2.34	4.138	6.013	15.849	38.22	54.182	104.317
BNGA07114	VF–F sand	347.072	454.38	172.138	244.003	289.297	413.346	583.75	680.665	885.862
BNGA07115	VF–F sand	285.226	388.894	140.59	206.048	245.064	350.296	495.141	579.631	778.42
BNGA07117	VF–F sand	307.285	369.055	165.333	215.598	248.286	337.605	458.031	526.091	681.149
BNGA07118	VF–F sand	307.285	354.119	176.968	223.068	252.318	330.207	431.868	488.048	613.118
BNGA07120	VF–F sand	324.374	393.458	173.027	225.834	260.547	356.499	488.557	564.879	743.922
BNGA07121	VF–F sand	314.874	372.139	175.642	224.302	255.552	340.379	455.167	521.22	678.115
BNGA07123	VF–F sand	276.193	320.921	156.648	198.888	225.884	298.276	393.444	446.199	563.204
BNGA07124	VF–F sand	265.991	309.71	150.857	191.257	217.123	286.819	379.331	431.117	547.452

Table A.1 – continued from previous page

Sample ID	Field Grain Size	D [3, 2]	D [4, 3]	d(0.050)	d(0.160)	d(0.250)	d(0.0.500)	d(0.750)	d(0.840)	d(0.950)
BNGA07126	VF–F sand	293.893	362.304	153.364	202.495	234.964	325.592	451.934	525.475	699.04
BNGA07127	VF–F sand	334.763	389.087	191.822	241.563	273.359	358.853	472.985	537.908	690.301
BNGA07129	VF–F sand	273.797	323.891	150.241	193.615	221.932	299.139	401.953	458.901	582.952
BNGA07130	M–C Sand	405.667	525.262	208.798	296.783	350.025	492.579	679.062	777.211	957.37
BNGA07132	M–C Sand	513.098	597.87	277.55	365.943	422.688	573.756	759.442	848.689	998.589
BNGA07133		448.643	541.129	232.368	311.706	363.658	506.573	694.364	791.871	966.887
BNGA07135	M–C Sand	474.854	566.056	248.372	333.203	388.096	536.535	725.144	819.417	982.808
BNGA07136		524.101	605.662	287.989	375.619	432.099	582.348	766.163	854.154	1001.201
BNGA07137	M–C Sand	8.283	31.851	2.312	4.217	6.334	16.354	34.573	46.721	84.096
BNGA07138	M–C Sand	539.492	618.189	300.637	389.533	446.553	597.099	778.704	864.435	1006.262
BNGA07139		455.269	569.867	243.503	336.92	393.774	544.283	732.881	826.196	986.62
BNGA07141	M–C Sand	450.763	537.572	239.796	314.916	364.431	501.407	684.072	780.836	959.012
BNGA07142		455.884	537.613	248.685	321.287	369.081	500.98	678.158	773.529	953.083
BNGA07144		474.129	557.131	257.888	334.313	384.68	523.383	705.766	800.488	970.919
BNGA07145	M–C Sand	429.627	512.21	231.673	300.582	346.058	472.67	646.019	742.025	931.312
BNGA07147	M–C Sand	451.004	532.739	245.945	317.179	364.293	495.227	672.124	767.785	949.393
BNGA07148		453.298	535.052	247.192	318.96	366.421	497.974	675.092	770.623	951.142

Table A.1 – continued from previous page

Sample ID	Field Grain Size	D [3,2]	D [4,3]	d(0.050)	d(0.160)	d(0.250)	d(0.0.500)	d(0.750)	d(0.840)	d(0.950)
BNGA07150	M–C Sand	465.362	581.13	266.152	355.017	409.91	556.096	740.209	831.52	988.913
BNGA07151		478.007	561.196	259.882	337.202	388.249	528.308	711.25	805.53	974.008
BNGA07153	M–C Sand	422.18	508.426	223.638	292.892	338.943	468.023	645.465	743.321	933.872
BNGA07154		320.32	371.829	183.877	231.025	261.324	343.176	452.613	514.649	657.82
BNGA07156	VF–F sand	296.309	353.277	162.247	208.369	238.74	322.562	436.935	502.067	650.533
BNGA07157		360.92	435.937	194.134	251.402	289.221	394.741	542.341	628.511	826.66
BNGA07159	VF–F sand	314.764	399.846	158.698	212.486	248.59	352.506	505.261	597.453	812.912
BNGA07160		474.895	566.755	247.631	333.025	388.269	537.509	726.719	821.02	983.858
BNGA07162		461.8	548.729	245.999	323.545	374.482	514.547	698.719	794.617	967.685
BNGA07163	M–C Sand	412.071	500.015	215.869	284.676	330.412	458.8	636.146	734.532	928.15
BNGA07165		350.753	459.384	181.751	254.319	298.83	419.831	585.843	680.592	883.323
BNGA07166	M–C Sand	327.238	446.056	155.369	236.894	283.32	406.836	575.343	671.721	878.616
BNGA07168		416.121	495.581	226.148	291.747	335.042	455.306	621.012	714.607	908.488
BNGA07169	M–C Sand	369.503	447.309	197.387	256.823	296.107	405.628	558.589	647.572	848.216
BNGA07171	M–C Sand	378.557	441.527	216.388	271.856	307.64	405.129	538.122	615.39	797.702
BNGA07172		382.095	459.916	205.855	266.488	306.553	418.353	574.26	664.48	864.318
BNGA07174		401.51	468.267	228.383	288.068	326.554	431.232	573.631	655.522	842.208

Table A.1 – continued from previous page

Sample ID	Field Grain Size	D [3, 2]	D [4, 3]	d(0.050)	d(0.160)	d(0.250)	d(0.0.500)	d(0.750)	d(0.840)	d(0.950)
BNGA07175	M–C Sand	374.492	449.82	202.915	261.702	300.586	408.849	559.628	647.127	845.019
BNGA07177		354.028	465.689	192.69	263.261	306.947	426.421	591.127	685.264	886.258
BNGA07178	M–C Sand	451.494	571.857	241.743	338.538	396.267	547.772	736.238	829.027	988.094
BNGA07180		491.366	574.669	267.25	348.153	400.984	544.603	728.605	821.324	983.199
BNGA07181		421.858	504.529	226.873	294.342	339.065	464.079	636.336	732.42	924.521
BNGA07202	Mud	8.829	65.109	2.359	4.45	6.836	19.588	47.715	75.078	358.17
BNGA07203	Mud	7.761	36.349	2.206	4.257	6.493	17.439	38.548	53.779	117.46
BNGA07205	Mud	7.957	46.825	2.278	4.175	6.116	15.916	42.651	70.135	192.005
BNGA07206	Mud	7.176	40.413	2.17	3.707	5.174	12.429	40.219	77.259	187.055
BNGA07208	Mud	21.691	133.299	4.128	12.893	26.249	113.971	206.421	253.485	356.266
BNGA07209	VF–F sand	207.588	286.121	106.635	150.737	178.453	255.468	363.8	427.073	574.788
BNGA07211	M–C Sand	284.445	381.076	152.674	210.312	245.92	343.41	479.201	558.905	748.164
BNGA07212	M–C Sand	278.639	372.827	143.377	202.762	239.045	337.307	471.482	548.885	730.129
BNGA07214	M–C Sand	242.589	326.619	129.743	178.785	209.585	294.481	412.096	480.152	638.388
BNGA07215	M–C Sand	342.149	472.379	156.28	249.556	301.383	436.464	615.665	714.769	913.826
BNGA07217	M–C Sand	332.949	435.404	194.836	260.391	298.927	401.251	539.772	620.244	808.642
BNGA07220	M–C Sand	444.769	563.604	247.154	335.46	389.985	535.898	722.11	816.12	980.636

Table A.1 – continued from previous page

Sample ID	Field Grain Size	D [3, 2]	D [4, 3]	d(0.050)	d(0.160)	d(0.250)	d(0.0.500)	d(0.750)	d(0.840)	d(0.950)
BNGA07223	M–C Sand	345.315	454.687	183.23	252.587	295.837	414.497	578.412	672.418	875.73
BNGA07226	M–C Sand	388.106	503.652	211.33	288.459	336.343	466.87	643.376	740.585	931.154
BNGA07229	M–C Sand	520.958	597.717	293.541	374.398	427.392	570.58	751.056	840.131	993.14
BNGA07232	M–C Sand	526.501	605.161	293.761	378.438	433.337	580.498	762.587	850.603	999.138
BNGA07235	M–C Sand	422.904	508.204	224.728	294.363	340.315	468.451	643.817	740.611	930.548
BNGA07238	M–C Sand	512.013	595.94	278.036	365.44	421.581	571.188	755.956	845.392	996.622
BNGA07241	M–C Sand	401.996	526.447	205.308	293.317	347.517	493.888	684.508	783.428	961.948
BNGA07244	VF–F sand	276.525	320.734	157.713	199.493	226.159	297.751	392.335	445.102	563.112
BNGA07247	VF–F sand	288.871	331.359	167.806	210.264	237.309	309.504	403.715	455.626	570.029
BNGA07250	VF–F sand	258.966	329.749	130.047	175.312	205.484	291.148	414.086	487.26	664.009
BNGA07253	VF–F sand	283.501	346.572	149.594	196.001	226.783	312.904	432.356	501.084	659.578
BNGA07256	VF–F sand	260.661	318.717	137.557	180.06	208.355	287.691	398.096	461.68	607.322
BNGA07259	M–C Sand	353.125	466.165	175.465	251.137	298.06	426.073	601.026	699.443	901.999
BNGA08102	Mud	10.666	20.893	3.766	6.471	8.479	14.811	25.53	33.084	57.209
BNGA08105	Mud	21.199	70.742	5.005	13.115	22.029	50.02	91.912	119.483	202.85
BNGA08108	Mud	15.428	52.526	4.03	8.783	13.516	30.96	61.524	82.358	146.414
BNGA08109	Mud	15.428	52.526	4.03	8.783	13.516	30.96	61.524	82.358	146.414

Table A.1 – continued from previous page

Sample ID	Field Grain Size	D [3, 2]	D [4, 3]	d(0.050)	d(0.160)	d(0.250)	d(0.0.500)	d(0.750)	d(0.840)	d(0.950)
BNGA08111	VF–F sand	263.471	321.189	138.943	182.712	211.512	291.38	401.139	463.787	606.53
BNGA08114	VF–F sand	275.724	328.06	149.837	194.107	223.091	302.305	408.069	466.844	595.162
BNGA08117	VF–F sand	454.268	540.749	242.373	317.696	367.348	504.808	688.003	784.671	961.573
BNGA08120	VF–F sand	333.776	388.457	191.945	240.587	271.854	356.68	471.458	537.521	694.801
BNGA08123	M–C Sand	478.605	549.225	276.178	345.883	391.122	514.55	679.313	768.871	943.58
BNGA08126	M–C Sand	531.585	607.613	301.033	383.272	437.127	582.252	763.058	850.785	999.135
BNGA08130	M–C Sand	504.317	592.571	268.179	357.196	414.643	568.15	756.75	847.102	998.144
BNGA08132	M–C Sand	242.104	331.586	122.542	173.34	205.355	294.379	420.244	494.678	672.899
BNGA08134	M–C Sand	265.984	396.336	121.509	191.935	234.405	351.28	517.144	615.078	836.02
BNGA08138	M–C Sand	501.785	623.274	291.958	393.198	453.734	609.164	791.637	875.851	1012.143
BNGA08141	M–C Sand	171.069	586.535	81.639	339.35	413.328	585.737	779.271	867.291	1008.829
BNGA08143	M–C Sand	499.892	580.134	276.876	355.772	407.79	549.914	732.719	824.677	984.977
BNGA08146	VF–F sand	344.775	430.161	176.407	234.705	273.755	384.861	543.974	637.583	847.618
BNGA08149	VF–F sand	469.376	556.911	249.656	329.307	381.45	524.222	710.047	805.365	974.561
BNGA08152	VF–F sand	317.206	373.911	178.087	226.158	257.224	341.953	457.181	523.434	679.86
BNGA08158	VF–F sand	317.016	391.321	167.073	217.632	251.551	348.167	487.445	570.894	770.907
BNGA08166	M–C Sand	432.777	502.388	247.661	310.456	351.362	463.862	618.507	706.707	895.191

Table A.1 – continued from previous page

Sample ID	Field Grain Size	D [3, 2]	D [4, 3]	d(0.050)	d(0.160)	d(0.250)	d(0.0.500)	d(0.750)	d(0.840)	d(0.950)
BNGA08172	M–C Sand	403.641	539.803	191.302	294.205	354.777	513.186	710.462	808.534	977.974
BNGA08175	M–C Sand	331.501	443.563	178.369	245.432	287.16	402.287	563.591	657.325	863.95
BNGA08302	VF–F sand	194.479	270.971	95.105	145.595	173.763	247.907	346.847	402.632	527.495
BNGA08303	VF–F sand	146.173	188.032	87.079	115.575	132.225	175.696	232.277	263.824	335.261
BNGA08305	VF–F sand	118.298	202.879	52.66	99.187	122.034	181.299	262.459	310.265	425.218
BNGA08306	VF–F sand	213.246	274.362	121.694	163.27	188.299	254.564	341.798	390.493	499.14
BNGA08308	VF–F sand	275.002	336.603	143.112	190.511	221.446	306.533	421.931	487.126	634.281
BNGA08309	VF–F sand	224.627	270.602	121.119	156.661	180.196	245.797	336.411	388.275	506.103
BNGA08311	VF–F sand	375.865	489.872	186.51	266.836	316.82	452.165	633.69	733.028	927.453
BNGA08312	VF–F sand	419.079	501.464	224.662	293.505	338.359	462.152	631.168	725.65	917.483
BNGA08314	VF–F sand	378.154	441.698	215.627	271.148	307.032	404.936	538.787	616.677	800.208
BNGA08315	VF–F sand	341.048	395.737	196.048	246.464	278.662	365.267	480.808	546.525	700.515
BNGA08317	VF–F sand	375.774	442.199	211.149	267.965	304.661	404.835	541.956	621.606	808.159
BNGA08318	VF–F sand	399.517	466.931	226.477	286.148	324.589	429.38	572.529	655.102	843.318
BNGA08320	VF–F sand	264.45	307.031	150.271	190.629	216.359	285.324	376.071	426.441	538.187
BNGA08321	VF–F sand	257.926	297.848	148.248	186.626	211.175	277.118	363.957	412.118	518.75
BNGA08323	VF–F sand	256.638	297.075	146.906	185.342	209.934	276.018	363.233	411.741	519.625

Table A.1 – continued from previous page

Sample ID	Field Grain Size	D [3, 2]	D [4, 3]	d(0.050)	d(0.160)	d(0.250)	d(0.0.500)	d(0.750)	d(0.840)	d(0.950)
BNGA08324	M–C Sand	282.223	369.695	136.375	187.366	222.113	323.07	470.917	559.651	771.244
BNGA08326	M–C Sand	462.339	545.738	250.409	325.687	375.001	510.713	690.631	785.727	961.082
BNGA08327	M–C Sand	413.926	495.225	222.924	288.967	332.743	454.609	622.702	717.411	911.646
BNGA08329	M–C Sand	450.992	534.534	243.548	316.771	364.845	497.794	676.145	772.022	952.327
BNGA08330	M–C Sand	394.238	474.461	211.503	274.695	316.502	433.018	594.886	687.625	886.277
BNGA08332	M–C Sand	348.226	420.25	187.7	242.978	279.455	380.713	521.422	603.374	794.74
BNGA08333		362.673	425.314	205.267	259.583	294.558	389.721	519.318	594.3	772.191
BNGA08335	M–C Sand	342.483	401.903	193.395	245.101	278.336	368.458	490.407	560.656	727.196
BNGA08336		332.453	444.346	158.759	232.647	278.37	402.87	574.16	671.918	880.2
BNGA08338	M–C Sand	420.459	505.869	223.017	293.061	338.932	466.278	640.418	736.847	927.517
BNGA08339		373.449	496.596	173.657	260.129	313.921	459.777	653.02	755.68	946.003
BNGA08341	M–C Sand	400.201	481.139	214.763	279.003	321.373	439.656	604.064	697.864	895.84
BNGA08342		388.108	468.383	206.754	270.577	312.319	427.756	587.012	678.187	876.476
BNGA08344		344.439	454.172	180.551	252.226	295.801	414.433	578.117	672.159	875.775
BNGA08345	VF–F sand	216.316	252.033	123.366	155.485	176.158	232.222	307.656	350.509	449.095
BNGA08347	VF–F sand	205.316	266.244	110.977	151.444	176.698	245.083	336.443	387.14	497.424
BNGA08348		234.724	280.1	126.755	164.809	189.71	258.011	349.391	400.066	509.887

Table A.1 – continued from previous page

Sample ID	Field Grain Size	D [3, 2]	D [4, 3]	d(0.050)	d(0.160)	d(0.250)	d(0.0.500)	d(0.750)	d(0.840)	d(0.950)
BNGA08350	VF–F sand	252.83	322.852	142.865	191.546	220.976	298.967	401.64	459.065	588.985
BNGA08351		262.909	340.834	128.213	176.067	208.257	300.108	431.525	509.402	696.541
BNGA08353	VF–F sand	304.616	414.768	146.477	211.761	253.596	370.416	535.112	631.221	845.432
BNGA08354		365.198	479.799	183.522	260.996	309.071	440.368	619.444	718.971	917.505
BNGA08356	VF–F sand	325.979	419.165	158.721	219.466	259.781	373.777	535.936	630.963	843.885
BNGA08357		392.741	515.773	187.313	276.029	331.479	481.745	677.543	778.799	960.309
BNGA08359	M–C Sand	410.437	507.177	206.156	281.551	331.014	468.231	653.486	753.422	942.382
BNGA08360		294.011	444.75	116.446	199.096	253.112	402.368	603.064	711.48	919.534
BNGA08362		408.839	493.302	216.758	284.379	328.824	452.45	623.066	719.087	914.371
BNGA08363	M–C Sand	345.972	486.844	145.884	240.291	298.397	452.005	650.324	754.454	946.115
BNGA08365		370.126	493.213	179.579	264.919	316.571	456.015	642.858	744.183	937.152
BNGA08366	M–C Sand	431.814	517.463	229.628	301.478	348.524	478.867	655.843	752.661	939.44
BNGA08368		369.321	482.594	192.919	269.971	316.988	444.325	617.718	714.826	912.251
BNGA08369	M–C Sand	373.227	460.727	191.715	256.301	298.869	417.88	584.132	679.517	883.408
BNGA08371	M–C Sand	324.4	397.993	170.078	224.3	259.953	358.976	496.518	576.59	764.592
BNGA08372		313.522	400.73	155.259	211.814	249.276	355.606	508.265	598.948	809.79
BNGA08374		263.42	362.547	132.733	185.531	219.772	317.37	460.424	547.444	758.682

138

Table A.1 – continued from previous page

Sample ID	Field Grain Size	D [3, 2]	D [4, 3]	d(0.050)	d(0.160)	d(0.250)	d(0.0.500)	d(0.750)	d(0.840)	d(0.950)
BNGA08375	M–C Sand	458.37	540.685	249.146	323.347	371.836	505.042	682.518	777.419	955.268
BNGA08377		459.807	542.045	250.115	324.522	373.108	506.601	684.213	779.003	956.262
BNGA08378	M–C Sand	420.902	505.322	223.898	294.048	339.776	466.089	638.298	733.979	925.069
BNGA08380		371.21	495.178	188.128	276.996	327.291	460.356	637.852	735.479	927.891
BNGA08381	M–C Sand	343.843	452.757	174.855	248.219	292.907	413.621	578.281	672.207	875.089
BNGA08383		261.998	356.613	122.509	169.954	203.152	303.601	458.942	554.628	782.091
BNGA08384	VF–F sand	169.852	233.724	83.391	111.444	130.79	188.79	283.54	349.428	548.827
BNGA08386		235.768	322.56	115.59	164.287	196.004	285.216	411.115	484.935	660.794
BNGA08387	VF–F sand	316.784	421.331	161.366	230.281	271.605	382.75	534.843	622.945	824.568
BNGA08389		348.322	425.41	183.285	241.507	279.624	385.05	531.26	616.375	813.56
BNGA08390	VF–F sand	383.23	468.233	200.467	264.575	306.895	425.501	591.538	686.757	888.816
BNGA08503	VF–F sand	148.564	173.576	83.983	106.575	121.084	160.233	212.345	241.719	308.885
BNGA08506	VF–F sand	242.637	279.646	139.784	175.765	198.777	260.48	341.483	386.33	485.351
BNGA08509	M–C Sand	320.19	402.816	162.748	217.603	254.164	358.12	507.596	596.499	804.783
BNGA08512	M–C Sand	282.451	371.317	136.649	186.618	220.976	322.298	473.668	565.354	782.966
BNGA08515	M–C Sand	379.682	505.293	171.758	269.486	326.264	473.248	661.93	761.622	947.689
BNGA08518	M–C Sand	329.499	399.09	176.497	229.591	264.522	361.341	495.164	572.802	755.257

Table A.1 – continued from previous page

Sample ID	Field Grain Size	D [3, 2]	D [4, 3]	d(0.050)	d(0.160)	d(0.250)	d(0.0.500)	d(0.750)	d(0.840)	d(0.950)
BNGA08521	M–C Sand	387.089	482.158	194.111	263.733	309.937	439.696	619.442	719.659	918.964
BNGA08523	M–C Sand	191.43	274.28	104.192	144.745	170.233	241.956	345.953	408.767	561.966
BNGA08524	M–C Sand	340.989	420.537	176.881	234.979	273.125	379.29	527.407	613.749	813.206
BNGA08526	M–C Sand	420.486	539.344	214.523	306.113	361.587	509.179	698.697	795.992	969.421
BNGA08527	M–C Sand	246.067	301.284	129.857	170.042	196.687	271.268	375.627	436.273	576.87
BNGA08530	M–C Sand	303.727	348.929	175.621	220.834	249.582	326.132	425.621	480.288	600.386
BNGA08535	M–C Sand	417.511	501.432	222.333	291.966	337.232	462.129	632.633	727.623	919.372
BNGA08538	M–C Sand	273.668	336.784	144.715	188.611	217.894	300.479	417.932	487.563	654.965
BNGA08541	M–C Sand	225.757	262.955	127.879	162.305	184.342	243.607	322.16	366.11	464.677
BNGA08544	M–C Sand	280.884	404.362	132.002	191.923	231.775	350.37	531.678	639.671	868.682
BNGA08547	M–C Sand	443.869	571.524	238.32	340.449	398.395	548.692	735.56	828	987.293
BNGA08550	M–C Sand	351.51	466.758	169.661	251.192	299.403	428.175	602.425	700.47	902.66
BNGA08553	M–C Sand	312.411	420.642	157.146	228.511	270.183	381.971	535.267	624.218	827.319
BNGA08556	M–C Sand	326.714	431.446	172.552	237.631	278.395	390.524	546.844	637.878	843.279
BNGA08557		377.89	499.878	180.45	267.315	320.408	463.711	653.667	755.086	944.664
BNGA08802	VF–F sand	186.23	239.627	110.646	147.652	169.116	224.87	297.006	336.793	424.613
BNGA08803	VF–F sand	201.483	227.491	120.932	149.359	167.085	213.67	273.712	306.877	381.266

Table A.1 – continued from previous page

Sample ID	Field Grain Size	D [3, 2]	D [4, 3]	d(0.050)	d(0.160)	d(0.250)	d(0.0.500)	d(0.750)	d(0.840)	d(0.950)
BNGA08805	VF–F sand	207.196	273.47	102.368	137.382	161.342	232.368	342.516	412.191	588.151
BNGA08806	VF–F sand	194.737	240.625	103.077	134.105	154.77	213.223	297.323	348.128	474.133
BNGA08808	VF–F sand	232.171	286.814	121.389	159.203	184.585	256.628	358.823	418.487	556.949
BNGA08809	VF–F sand	191.376	252.177	106.286	142.887	165.62	227.688	313.998	364.752	486.195
BNGA08811	VF–F sand	365.245	425.701	209.046	262.758	297.293	390.962	517.976	591.379	765.589
BNGA08812	VF–F sand	392.016	457.932	222.614	280.942	318.579	421.049	560.569	640.941	826.282
BNGA08814	VF–F sand	344.943	411.75	188.611	242.629	278.05	375.44	508.461	584.913	762.857
BNGA08815	VF–F sand	380.425	464.795	198.05	263.107	305.753	423.864	586.482	679.122	878.739
BNGA08817	VF–F sand	407.426	494.02	213.911	282.109	327.149	452.904	626.5	723.67	918.83
BNGA08818	VF–F sand	326.006	417.527	160.167	219.506	259.134	371.73	532.858	627.497	840.581
BNGA08820	VF–F sand	476.094	562.207	254.893	335.961	388.461	530.82	714.665	808.679	975.833
BNGA08823	VF–F sand	470.832	542.302	269.925	339.539	384.538	507.182	671.281	761.062	937.812
BNGA08826	VF–F sand	336.599	442.343	174.431	246.551	289.48	404.442	560.767	650.741	851.858
BNGA08829	M–C Sand	427.279	508.148	232.02	299.687	344.309	468.339	638.695	733.852	924.719
BNGA08832	VF–F sand	439.223	500.491	260.44	322.183	361.217	465.816	606.258	686.46	865.829
BNGA08835	VF–F sand	396.001	474.753	214.015	276.556	317.972	433.401	593.844	685.933	884.192
BNGA08838	M–C Sand	478.251	570	249.508	336.146	391.907	541.797	730.362	823.85	985.109

Table A.1 – continued from previous page

Sample ID	Field Grain Size	D [3, 2]	D [4, 3]	d(0.050)	d(0.160)	d(0.250)	d(0.0.500)	d(0.750)	d(0.840)	d(0.950)
BNGA08841	M–C Sand	555.335	629.551	316.951	404.05	460.367	609.251	788.298	872.241	1010.032
BNGA08844	M–C Sand	569.167	642.173	326.418	416.206	473.891	624.8	802.617	884.389	1016.011
BNGA08847	VF–F sand	412.628	497.261	218.68	287.257	332.25	457.123	628.403	724.148	917.565
BNGA08850	VF–F sand	379.673	456.843	204.469	265.017	304.901	415.895	569.974	658.881	857.296
BNGA08853	VF–F sand	346.591	420.007	185.308	241.35	278.187	380.393	522.194	604.725	797.102
BNGA09103	VF–F sand	136.508	185.794	71.986	98.794	115.753	162.721	229.56	270.152	375.734
BNGA09109	M–C Sand	249.066	314.218	123.761	170.226	200.49	283.885	397.71	462.5	609.715
BNGA09118	VF–F sand	234.043	298.31	118.691	157.987	184.532	260.992	373.167	441.119	607.689
BNGA09124	VF–F sand	114.857	178.747	59.806	85.281	100.916	145.038	212.036	256.887	408.714
BNGA09127	VF–F sand	150.882	210.087	84.995	114.07	132.098	182.031	254.948	301.159	431.971
BNGA09134	M–C Sand	289.985	380.057	139.4	192.776	228.922	333.445	485.571	576.209	788.823
BNGA09140	M–C Sand	460.603	580.996	246.136	345.308	404.508	559.118	748.386	839.932	994.232
BNGA09152	M–C Sand	391.852	531.217	179.281	288.207	348.544	504.173	699.356	797.988	971.447
BNGA09155	M–C Sand	372.4	451.977	198.144	258.215	297.967	409.426	566	657.07	859.612
BNGA09158	M–C Sand	366.895	505.052	187.643	275.042	327.205	469.275	659.741	761.343	949.266
BNGA09161	M–C Sand	294.558	406.52	151.098	213.699	252.983	362.591	519.231	612.116	825.553
BNGA09164	M–C Sand	247.667	490.229	143.909	250.455	307.503	457.241	653.253	756.908	947.695

Table A.1 – continued from previous page

Sample ID	Field Grain Size	D [3, 2]	D [4, 3]	d(0.050)	d(0.160)	d(0.250)	d(0.0.500)	d(0.750)	d(0.840)	d(0.950)
BNGA09167	M–C Sand	397.69	526.386	199.3	296.55	351.502	495.868	682.975	780.944	959.786
BNGA09173	M–C Sand	247.689	290.899	139.212	176.979	201.276	267.241	356.363	407.156	524.315
BNGA09176	M–C Sand	327.954	471.085	136.795	221.532	277.292	431.679	635.685	742.909	940.199
BNGA09402	Mud	7.403	19.771	2.393	3.973	5.403	11.251	24.576	35.02	66.665
BNGA09403	Mud	8.57	34.115	2.669	4.619	6.393	13.556	28.895	40.811	87.985
BNGA09405	Mud	8.118	42.802	2.511	4.301	5.955	12.876	28.873	42.224	117.001
BNGA09406	Mud	8.162	45.367	2.528	4.243	5.831	13.003	32.261	49.228	129.09
BNGA09408	Mud	11.485	41.088	3.202	6.209	9.152	21.402	45.318	62.022	114.659
BNGA09409	Mud	11.597	25.716	3.528	6.865	9.629	18.666	33.834	44.032	72.427
BNGA09411	Mud	9.834	69.126	2.514	5.04	8.035	21.423	46.635	68.341	427.703
BNGA09412	Mud	8.544	49.108	2.34	4.421	6.709	17.915	40.083	56.95	174.809
BNGA09414	Mud	7.274	30.272	2.332	3.903	5.305	11.069	25.12	37.261	82.601
BNGA09415	Mud	6.465	28.98	2.321	3.593	4.661	8.66	17.408	25.134	61.742
BNGA09417	Mud	11.529	57.643	3.065	5.698	8.418	24.941	80.051	122.94	221.366
BNGA09418	VF–F sand	12.577	76.296	3.06	6.1	9.579	35.196	106.48	158.277	289.119
BNGA09420	VF–F sand	258.567	345.537	154.821	212.104	243.649	324.744	429.096	486.797	616.085
BNGA09423	VF–F sand	183.819	258.641	97.712	137.665	162.3	230.801	328.11	385.564	520.591

Table A.1 – continued from previous page

Sample ID	Field Grain Size	D [3, 2]	D [4, 3]	d(0.050)	d(0.160)	d(0.250)	d(0.0.500)	d(0.750)	d(0.840)	d(0.950)
BNGA09426	VF–F sand	217.591	302.121	116.766	165.976	195.361	274.82	383.164	445.096	586.322
BNGA09429	VF–F sand	353.968	421.373	195.192	249.439	285.143	383.831	519.678	598.115	780.984
BNGA09432	VF–F sand	243.074	325.88	138.006	184.962	213.855	293.002	404.237	470.438	632.719
BNGA09435	VF–F sand	457.664	543.775	244.454	320.887	370.989	508.77	691.107	787.024	962.525
BNGA09438	VF–F sand	296.572	408.855	153.096	212.832	251.573	362.263	523.663	619.797	837.09
BNGA09441	M–C Sand	368.736	460.924	186.988	249.587	292.08	414.607	590.323	690.792	898.096
BNGA09444	M–C Sand	365.746	519.137	161.522	280.017	339.251	491.122	684.562	784.301	963.187
BNGA09447	M–C Sand	240.727	274.528	141.084	176.059	198.305	257.456	333.96	375.748	466.446
BNGA09450	M–C Sand	244.73	280.668	141.879	178.066	201.132	262.604	342.438	386.137	481.32
BNGA09453	M–C Sand	346.806	425.905	182.531	238.732	276.22	382.284	533.405	622.494	827.062
BNGA09456	M–C Sand	253.437	499.953	72.408	215.052	308.073	486.444	690.207	791.481	968.62
BNGA09702	Mud	9.007	41.66	2.814	4.893	6.711	13.705	30.599	49.551	194.093
BNGA09703		158.608	209.769	94.61	127.072	145.95	195.391	260.269	296.649	379.087
BNGA09705		190.531	230.539	101.938	132.371	152.652	209.271	287.462	332.112	432.859
BNGA09706		160.803	180.445	97.449	119.919	133.901	170.296	216.619	241.907	298.036
BNGA09708		229.866	269.977	129.623	164.284	186.632	247.497	330.17	377.562	487.929
BNGA09709		232.378	261.066	140.731	173.074	193.181	245.935	313.614	350.694	433.192

144

Table A.1 – continued from previous page

Sample ID	Field Grain Size	D [3, 2]	D [4, 3]	d(0.050)	d(0.160)	d(0.250)	d(0.0.500)	d(0.750)	d(0.840)	d(0.950)
BNGA09711		350.909	435.484	180.434	239.859	279.463	391.34	549.98	642.639	850.013
BNGA09712		362.352	448.355	186.667	247.905	288.79	404.273	567.421	662.089	868.778
BNGA09714		356.668	405.59	213.217	263.111	294.448	377.297	486.36	548.354	694.95
BNGA09715		368.951	432.77	208.666	264.046	299.663	396.511	528.599	605.324	786.918
BNGA09717		425.369	515.105	221.434	294.928	343.132	476.578	657.031	755.089	942.205
BNGA09718		312.908	385.784	164.676	214.855	248.579	344.243	480.793	561.771	755.063
BNGA09720		343.619	425.827	178.798	234.669	272.353	380.253	535.992	628.137	837.777
BNGA09721		429.105	513.838	229.259	298.852	345.064	474.17	650.896	747.919	936.349
BNGA09723		448.481	521.528	253.765	320.666	364.26	484.105	646.941	737.635	921.454
BNGA09724		454.12	539.941	242.889	318.123	367.537	503.976	685.952	782.38	959.873
BNGA09726		422.325	505.019	227.665	294.484	338.977	463.96	637.19	733.97	926.478
BNGA09727		410.671	496.003	217.232	285.107	329.925	455.015	627.718	724.507	919.264
BNGA09729	M–C Sand	354.232	406.125	209.262	259.502	291.105	375.49	488.202	553.085	709.28
BNGA09730		361.772	425.098	203.977	258.577	293.706	389.269	519.538	594.972	774.097
BNGA09732		253.864	298.838	141.116	180.924	206.534	275.749	367.993	419.72	536.053
BNGA09734		237.338	275.463	134.902	170.998	194.096	256.089	337.628	382.802	482.736
BNGA09735		367.94	479.928	170.975	244.251	294.203	437.038	632.841	738.136	935.774

145

Table A.1 – continued from previous page

Sample ID	Field Grain Size	D [3, 2]	D [4, 3]	d(0.050)	d(0.160)	d(0.250)	d(0.0.500)	d(0.750)	d(0.840)	d(0.950)
BNGA09737		397.281	482.263	209.393	274.695	318.117	439.971	609.818	706.222	905.394
BNGA09738		366.484	431.95	205.516	261.22	297.132	395.062	529.016	606.9	791.135
BNGA09739		251.064	296.707	141.124	178.646	203.001	269.889	362.192	416.093	545.012
BNGA09741		355.517	414.196	202.944	256.015	289.965	381.465	504.211	574.472	740.001
BNGA09742		422.216	484.636	247.753	307.725	345.798	448.59	588.218	668.824	852.049
BNGA09744		392.615	459.86	222.407	280.663	318.373	421.605	563.598	646.123	836.162
BNGA09745		424.719	513.811	222.169	293.914	341.491	474.4	655.427	753.896	941.677
BNGA09747		362.224	445.179	188.085	249.489	290.012	403	560.525	651.757	854.971
BNGA09748		454.973	541.096	243.077	318.223	367.897	505.367	688.147	784.473	961.064
BNGA09750		345.71	465.08	161.56	241.808	291.39	425.466	606.438	706.968	909.596
BNGA09751		356.154	422.8	197.594	252.439	287.879	385.033	519.03	597.37	783.832
BNGA09753	M–C Sand	6.872	42.557	2.356	3.7	4.865	9.511	21.368	33.332	190.697
BNGA09754	Mud	388.288	471.932	203.924	269.506	312.354	430.887	594.443	687.89	887.463
BNGA09756		439.656	529.858	229.328	306.094	356.116	493.593	676.612	774.053	954.833
BNGA09757		507.198	588.24	279.629	361.54	415.143	560.363	743.811	834.535	990.458
BNGA09759		421.584	502.722	227.895	295.068	339.453	462.851	632.132	726.771	918.589
BNGA09761		459.81	545.792	245.898	322.575	372.849	511.062	693.614	789.457	964.129

146

Sample ID	Field Grain Size	D [3, 2]	D [4, 3]	d(0.050)	d(0.160)	d(0.250)	d(0.0.500)	d(0.750)	d(0.840)	d(0.950)
BNGA09763	M–C Sand	493.148	575.118	270.35	349.985	402.163	544.615	727.866	820.491	982.629
BNGA10002	VF–F sand	138.158	155.635	83.012	102.643	114.863	146.722	187.3	209.463	258.626
BNGA10003	VF–F sand	112.327	144.244	65.506	87.489	100.519	134.679	179.029	203.576	258.38
BNGA10004	VF–F sand	17.059	44.51	4.443	10.284	15.905	34.331	61.889	78.67	120.973
BNGA10005	VF–F sand	159.961	186.649	90.639	114.906	130.448	172.303	228.045	259.547	332.039
BNGA10006	M–C Sand	294.394	347.759	160.764	208.921	239.925	323.162	431.859	491.274	619.396
BNGA10008	M–C Sand	229.183	269.301	127.476	163.382	186.515	249.062	332.14	378.344	480.847
BNGA10009	M–C Sand	234.536	290.053	122.432	161.069	186.81	259.396	362.132	422.444	564.18
BNGA10011	M–C Sand	200.162	230.794	115.638	145.056	163.889	214.475	281.211	318.441	402.162
BNGA10012	M–C Sand	336.732	459.53	146.147	220.252	271.571	416.692	612.571	718.674	922.846
BNGA10014	M–C Sand	259.63	311.437	139.851	181.774	209.26	285.037	387.812	445.833	574.814
BNGA10015	M–C Sand	293.52	364.636	152.892	201.218	233.393	324.378	454.324	531.757	718.854
BNGA10017	M–C Sand	339.121	410.384	180.771	237.548	274.08	373.745	509.55	587.75	769.93
BNGA10018	M–C Sand	265.667	320.7	142.026	184.959	213.374	292.161	399.806	460.804	597.781
BNGA10020	M–C Sand	346.282	406.466	195.402	247.901	281.56	372.676	495.911	566.941	736.239
BNGA10023	M–C Sand	290.546	359.429	149.76	199.965	232.977	324.45	450.188	522.45	690.145
BNGA10026	M–C Sand	275.242	322.455	153.98	196.994	224.482	298.49	396.41	451.01	573.416

147

Table A.1 – continued from previous page

Sample ID	Field Grain Size	D [3, 2]	D [4, 3]	d(0.050)	d(0.160)	d(0.250)	d(0.0.500)	d(0.750)	d(0.840)	d(0.950)
BNGA10029	M–C Sand	373.169	447.726	201.214	262.22	301.671	409.445	556.519	640.832	832.129
BNGA10032	M–C Sand	388.342	522.6	167.413	287.802	347.002	495.386	683.063	780.807	959.395
BNGA10035	M–C Sand	310.579	362.816	175.29	223.012	253.466	335.354	444.009	505.105	644.436
BNGA10038	M–C Sand	313.502	368.462	175.319	224.119	255.308	339.398	451.528	514.986	661.128
BNGA10041	M–C Sand	292.315	386.479	144.329	208.353	246.802	349.644	489.676	570.836	761.474
BNGA10044	M–C Sand	413.587	491.087	226.271	290.933	333.485	451.182	613.058	704.968	898.864
BNGA10047	M–C Sand	445.908	570.26	239.26	340.563	398.006	547.055	732.731	825.035	985.244
BNGA10050	M–C Sand	527.163	606.471	293.048	379.156	434.645	582.604	764.571	852.238	999.9
BNGA10053	M–C Sand	547.41	622.476	310.929	397.611	453.315	600.882	780.023	865.021	1006.294
BNGA10056	M–C Sand	396.732	514.241	211.367	296.028	346.238	480.461	658.486	755.002	940.496
BNGA10059	M–C Sand	433.799	551.048	237.716	324.474	377.84	521.175	706.582	801.953	972.24
BNGA10063	M–C Sand	377.353	492.374	191.639	274.873	324.192	456.04	632.898	730.437	924.152
BNGA10066	M–C Sand	417.228	532.701	217.328	305.437	358.653	500.873	686.302	783.408	960.808
BNGA10302	Mud	15.267	101.856	3.47	7.613	12.581	51.419	141.629	197.159	359.755
BNGA10305	Mud	52.309	211.926	10.267	74.54	112.39	190.812	291.7	349.497	483.085
BNGA10306	VF–F sand	192.769	260.44	101.456	140.029	164.757	233.493	329.654	385.628	515.866
BNGA10308	VF–F sand	284.043	339.857	153.707	199.403	229.318	311.39	422.177	484.515	624.148

Table A.1 – continued from previous page

Sample ID	Field Grain Size	D [3, 2]	D [4, 3]	d(0.050)	d(0.160)	d(0.250)	d(0.0.500)	d(0.750)	d(0.840)	d(0.950)
BNGA10314	VF–F sand	268.153	318.21	146.461	189.116	217.044	293.348	395.313	451.892	575.729
BNGA10320	M–C Sand	367.755	442.604	198.762	256.973	295.272	401.688	550.062	636.635	834.849
BNGA10321	VF–F sand	175.023	212.703	96.005	122.745	140.2	188.75	257.937	300.147	410.424
BNGA10326	VF–F sand	214.738	275.812	122.48	163.221	188.097	254.514	343.042	393.027	506.391
BNGA10327	VF–F sand	191.91	227.399	106.438	136.077	155.301	207.862	279.388	320.475	415.854
BNGA10329	VF–F sand	268.606	329.366	140.155	185.49	215.398	298.46	412.524	477.598	625.656
BNGA10330	M–C Sand	401.704	492.941	206.348	276.007	322.146	451.446	629.917	728.933	924.659
BNGA10338	M–C Sand	458.266	543.946	245.681	321.206	370.973	508.425	691.185	787.466	963.231
BNGA10344	M–C Sand	463.423	535.071	264.743	333.674	378.213	499.557	662.213	751.727	930.685
BNGA10350	M–C Sand	517.96	588.634	300.2	377.183	426.693	559.801	730.119	817.48	976.381
BNGA10356	M–C Sand	406.774	490.054	216.584	282.898	326.774	449.066	618.002	713.201	909.095
BNGA10363	M–C Sand	431.786	517.964	229.182	300.927	348.122	479.198	657.288	754.561	941.265
BNGA10369	M–C Sand	359.855	478.287	176.122	256.293	305.238	438.626	620.73	721.755	921.264
BNGA10375	M–C Sand	449.543	569.845	238.577	335.955	393.746	545.51	734.538	827.698	987.475
BNGA10381	M–C Sand	428.589	550.168	218.617	315.483	372.544	522.792	712.851	808.766	976.969
BNGA10382	M–C Sand	308.931	434.641	132.661	194.712	240.831	383.815	587.65	698.445	912.052
BNGA10387	M–C Sand	430.642	552.704	215.076	314.468	372.997	526.374	718.492	814.336	980.44

149

Table A.1 – continued from previous page

Sample ID	Field Grain Size	D [3, 2]	D [4, 3]	d(0.050)	d(0.160)	d(0.250)	d(0.0.500)	d(0.750)	d(0.840)	d(0.950)
BNGA10388	M–C Sand	411.689	528.865	211.51	296.495	349.819	495.063	686.104	785.413	963.811
BNGA10391	M–C Sand	416.438	500.632	222.21	289.667	334.405	459.518	632.785	729.712	923.629
BNGA10603	Mud	23.381	107.183	5.093	14.734	27.329	65.216	119.55	158.916	385.737
BNGA10605	VF–F sand	98.851	136.372	50.829	73.622	87.285	124.049	173.664	201.81	265.764
BNGA10606	Mud	12.59	47.202	3.585	7.269	10.496	21.719	42.523	58.317	127.547
BNGA10608	Mud	16.455	44.848	4.255	9.696	15.064	33.943	62.849	80.306	123.769
BNGA10609	Mud	14.298	39.124	3.956	8.215	12.099	26.428	52.23	69.438	116.561
BNGA10611	Mud	18.113	64.287	4.477	10.675	17.059	39.904	77.648	103.233	184.897
BNGA10612	Mud	13.221	48.268	3.777	7.353	10.469	22.942	53.762	79.165	162.539
BNGA10614	M–C Sand	125.872	176.195	65.567	84.551	97.409	134.825	194.247	237.88	458.785
BNGA10615	M–C Sand	336.095	387.053	194.184	244.127	275.861	360.432	471.025	532.474	670.954
BNGA10618	VF–F sand	184.218	231.819	93.964	124.989	145.873	205.462	290.981	341.609	461.552
BNGA10620	VF–F sand	236.377	305.485	124.901	173.42	203.045	282.14	386.317	443.877	569.236
BNGA10623	VF–F sand	247.32	367.551	113.652	173.888	212.274	320.961	478.051	572.032	792.684
BNGA10626	M–C Sand	258.074	296.03	149.558	187.708	212.052	276.967	361.425	407.646	508.158
BNGA10629	M–C Sand	484.63	565.667	266.535	343.743	394.486	533.431	714.324	807.463	974.486
BNGA10632	M–C Sand	412.061	490.309	224.895	289.179	331.637	449.73	613.007	705.831	900.79

Sample ID	Field Grain Size	D [3, 2]	D [4, 3]	d(0.050)	d(0.160)	d(0.250)	d(0.0.500)	d(0.750)	d(0.840)	d(0.950)
BNGA10635	VF–F sand	386.027	452.965	217.929	275.742	313.077	415.084	555.07	636.466	825.193
BNGA10638	VF–F sand	265.404	367.673	120.279	187.329	226.546	330.632	471.881	553.664	746.245
BNGA10641	M–C Sand	441.366	528.244	233.996	307.742	356.289	490.824	671.801	768.937	951.22
BNGA10644	VF–F sand	373.207	443.965	205.295	263.195	301.101	405.416	548.717	631.447	821.535
BNGA10647	VF–F sand	366.958	435.494	202.55	259.453	296.525	398.301	537.133	616.977	801.4
BNGA10650	VF–F sand	409.908	521.498	240.061	319.879	366.551	489.837	653.375	743.644	925.624
BNGA10653	VF–F sand	357.82	427.281	195.61	251.766	288.489	389.557	528.071	607.997	793.873
BNGA10656	VF–F sand	267.07	342.777	142.255	201.413	234.864	321.141	431.469	491.47	620.77
BNGA10659	VF–F sand	306.623	356.846	173.058	219.713	250.009	331.898	439.453	498.473	626.227
BNGA10663	VF–F sand	331.879	404.605	175.591	230.342	266.276	365.777	503.624	583.772	771.999
BNGA10666	VF–F sand	333.777	387.186	191.635	241.073	272.708	357.778	471.112	535.229	683.653
BNGA10669	VF–F sand	331.952	404.388	177.237	230.236	265.368	363.745	502.376	584.025	777.346
BNGA10672	VF–F sand	275.884	365.94	145.572	205.978	241.117	334.515	460.225	532.165	699.179
BNGA10675	VF–F sand	300.181	352.814	167.088	213.425	243.624	325.93	435.619	496.587	630.933
BNGA10678	VF–F sand	295.619	338.588	172.051	215.482	243.103	316.674	412.421	465.028	580.437
BNGA10681	VF–F sand	308.969	426.076	146.665	226.879	270.791	387.122	546.786	639.354	846.613
BNGA10684	M–C Sand	345.323	513.507	115.152	250.036	325.08	493.133	692.472	792.467	968.495

151

Table A.1 – continued from previous page

Sample ID	Field Grain Size	D [3, 2]	D [4, 3]	d(0.050)	d(0.160)	d(0.250)	d(0.0.500)	d(0.750)	d(0.840)	d(0.950)
BNGA10687	M–C Sand	295.634	416.273	140.556	211.837	255.03	373.643	539.086	635.183	848.276
BNGA10690	M–C Sand	358.124	497.458	162.058	272.67	326.624	465.513	647.807	746.523	936.523
BNGA10693	M–C Sand	402.358	522.364	218.948	302.605	352.975	488.755	669.269	766.15	949.063
BNGA10902	VF–F sand	176.275	199.322	105.72	130.557	146.053	186.834	239.632	268.997	335.605
BNGA10903	Mud	10.753	37.559	2.82	5.372	8.2	24.772	55.507	72.904	114.516
BNGA10905	Mud	13.924	56.848	3.265	7.166	11.97	39.777	84.572	109.685	169.663
BNGA10906	M–C Sand	186.895	474.249	81.389	173.177	250.025	450.128	675.257	783.174	966.769
BNGA10908	Mud	14.578	55.578	3.475	7.799	12.859	37.92	79.691	104.767	168.558
BNGA10909	Mud	14.518	47.376	3.588	8.077	12.98	33.32	67.16	87.819	139.818
BNGA10911	Mud	12.984	70.172	3.188	6.611	10.479	32.601	80.481	111.628	212.434
BNGA10912	Mud	14.747	47.436	3.752	8.452	13.303	30.74	60.146	80.475	144.64
BNGA10914	Mud	12.158	47.118	3.2	6.534	10.009	25.01	53.075	71.507	125.057
BNGA10915	Mud	11.104	36.412	3.141	6.167	9.018	19.866	39.939	53.77	95.855
BNGA10917	M–C Sand	247.449	286.124	141.734	178.751	202.468	266.167	350.041	396.549	499.237
BNGA10918	M–C Sand	245.259	283.837	140.389	177.019	200.503	263.73	347.249	393.676	496.625
BNGA10920	M–C Sand	201.843	229.088	119.876	148.935	167.038	214.711	276.367	310.49	387.371
BNGA11002	Mud	9.111	25.773	2.689	4.831	6.89	15.775	34.699	47.885	82.901

Table A.1 – continued from previous page

Sample ID	Field Grain Size	D [3, 2]	D [4, 3]	d(0.050)	d(0.160)	d(0.250)	d(0.0.500)	d(0.750)	d(0.840)	d(0.950)
BNGA11003	Mud	7.165	28.585	2.419	3.916	5.194	10.139	21.882	33.419	91.04
BNGA11005	Mud	5.898	28.56	2.179	3.333	4.279	7.709	14.819	20.872	58.008
BNGA11006	Mud	11.068	52.415	2.918	5.555	8.362	23.501	66.134	97.558	187.507
BNGA11008	M–C Sand	50.952	464.62	8.184	129.199	250.348	454.635	678.37	785.881	968.404
BNGA11009	Mud	9.042	31.874	2.629	4.694	6.694	15.815	39.817	59.678	117.093
BNGA11011	Mud	10.998	45.537	2.648	5.467	9.047	32.244	69.146	89.142	134.828
BNGA11012	Mud	16.201	53.746	3.612	9.141	17.382	45.469	78.32	96.493	138.393
BNGA11014	Mud	8.536	37.859	2.388	4.338	6.387	16.879	40.12	56.94	110.981
BNGA11015	Mud	9.658	35.413	2.62	4.907	7.37	19.678	46.639	66.546	123.447
BNGA11017	Mud	7.722	25.108	2.297	3.964	5.601	13.486	32.693	46.99	87.571
BNGA11018	Mud	6.52	23.153	2.083	3.523	4.862	10.745	24.36	34.926	73.068
BNGA11020	Mud	6.688	36.952	2.146	3.535	4.836	10.612	23.708	33.46	70.119
BNGA11021	Mud	6.524	36.646	2.232	3.589	4.766	9.265	18.57	25.997	64.487
BNGA11023	Mud	6.11	33.545	2.148	3.413	4.484	8.395	16.312	22.967	67.556
BNGA11024	VF–F sand	245.628	306.869	132.326	169.373	193.946	264.381	371.54	441.53	636.571
BNGA11026	VF–F sand	10.769	46.79	2.919	5.761	8.621	20.633	45.211	63.36	128.64
BNGA11027	VF–F sand	300.64	350.604	169.415	214.831	244.526	325.306	432.196	491.092	618.856

Table A.1 – continued from previous page

Sample ID	Field Grain Size	D [3, 2]	D [4, 3]	d(0.050)	d(0.160)	d(0.250)	d(0.0.500)	d(0.750)	d(0.840)	d(0.950)
BNGA11029	VF–F sand	3.024	21.35	0.815	1.466	2.168	5.817	17.857	30.916	91.553
BNGA11030	VF–F sand	223.124	311.819	113.643	169.956	201.774	285.747	397.679	460.759	602.484
BNGA11032	VF–F sand	210.52	279.1	125.612	169.901	195.487	261.988	347.811	394.887	497.682
BNGA11034		188.618	274.293	99.353	138.941	164.666	238.886	348.803	415.29	575.641
BNGA11035	VF–F sand	254.673	323.94	150.046	197.273	225.854	301.529	400.884	456.234	580.065
BNGA11037		166.038	425.118	166.938	241.226	281.996	390.098	538.175	624.774	825.067
BNGA11038	VF–F sand	379.26	492.142	210.88	284.143	329.704	454.288	624.677	720.341	914.808
BNGA11039	M–C Sand	409.852	529.069	215.637	299.295	351.936	495.385	684.16	782.744	961.364
BNGA11041	M–C Sand	405.769	539.265	225.913	312.91	365.846	508.398	694.493	791.364	966.127
BNGA11042	M–C Sand	330.836	448.752	165.191	235.151	279.993	405.307	580.78	680.904	889.911
BNGA11044	M–C Sand	231.59	445.859	108.199	207.122	263.017	407.773	599.826	705.393	913.125
BNGA11045	M–C Sand	149.865	463.714	110.801	222.777	277.519	426.333	628.206	736.344	936.834
BNGA11047	M–C Sand	267.292	538.441	158.621	303.374	364.083	516.875	707.6	804.132	974.343
BNGA11048	M–C Sand	413.258	549.585	212.792	315.219	373.009	523.674	713.602	809.412	977.35
BNGA11050	M–C Sand	269.837	516.233	118.261	270.052	335.025	493.367	689.126	788.75	965.961
BNGA11051	M–C Sand	117.599	485.372	40.796	232.895	300.892	462.449	664.836	769.123	956.145
BNGA11053	M–C Sand	351.946	483.033	176.198	262.366	312.353	446.209	626.346	725.809	922.534

Table A.1 – continued from previous page

Sample ID	Field Grain Size	D [3, 2]	D [4, 3]	d(0.050)	d(0.160)	d(0.250)	d(0.0.500)	d(0.750)	d(0.840)	d(0.950)
BNGA11054	M–C Sand	259.675	484.357	153.294	258.537	311.443	450.385	635.901	737.19	932.44
BNGA11056	M–C Sand	292.507	536.835	148.916	293.1	356.988	515.704	710.895	808.302	977.5
BNGA11057	M–C Sand	350.881	485.599	180.575	265.149	314.668	448.359	629.45	729.348	925.753
BNGA11059	M–C Sand	456.229	575.504	230.923	333.043	394.397	553.882	746.913	839.476	994.416
BNGA11061		460.564	576.172	235.242	332.743	393.441	553.5	747.855	840.667	995.266
BNGA11063	M–C Sand	497.903	584.305	267.126	352.804	408.233	557.266	744.091	835.729	991.721
BNGA11064		450.787	558.037	234.707	324.535	380.322	529.457	718.942	814.169	980.056
BNGA11202	Mud	10.018	133.116	2.579	4.827	7.269	22.385	84.737	273.308	774.88
BNGA11203	M–C Sand	114.78	281.078	72.348	108.467	132.441	209.03	358.288	474.457	766.087
BNGA11205	M–C Sand	343.316	510.461	122.172	219.623	299.6	490.934	703.632	805.256	977.543
BNGA11209	Mud	10.823	99.31	2.712	5.269	8.138	26.142	82.374	128.009	626.12
BNGA11211	M–C Sand	87.519	577.417	21.483	302.757	403.62	593.681	790.238	876.978	1013.665
BNGA11212	Mud	19.938	102.029	3.916	11.47	24.411	85.399	152.392	189.269	274.347
BNGA11214	M–C Sand	270.862	413.499	111.632	162.04	201.689	346.824	583.049	705.692	924.736
BNGA11218	Mud	8.904	37.464	2.423	4.434	6.606	18.512	46.993	69.003	140.528
BNGA11221	Mud	6.843	37.395	2.197	3.58	4.83	10.133	28.14	56.844	190.889
BNGA11227	Mud	10.137	46.113	2.735	5.131	7.617	20.035	55.428	83.147	173.43

Table A.1 – continued from previous page

Sample ID	Field Grain Size	D [3, 2]	D [4, 3]	d(0.050)	d(0.160)	d(0.250)	d(0.0.500)	d(0.750)	d(0.840)	d(0.950)
BNGA11228		131.777	206.926	57.746	93.417	115.27	176.769	267.189	322.778	461.953
BNGA11230	VF–F sand	282.578	339.476	151.336	198.13	228.507	311.281	422.464	484.913	624.798
BNGA11241	VF–F sand	427.386	513.473	226.74	297.598	344.261	474.005	651.322	748.714	937.418
BNGA11250	M–C Sand	401.669	531.874	192.752	296.32	353.835	503.368	693.792	791.698	966.848
BNGA11256	M–C Sand	449.26	562.811	248.776	335.619	389.433	534.132	720.225	814.594	979.961
BNGA11402	Mud	7.669	39.077	2.505	4.149	5.581	11.133	24.536	38.856	152.36
BNGA11403	Mud	6.563	35.571	2.246	3.565	4.705	9.127	19.421	29.751	170.935
BNGA11405	Mud	11.156	89.081	2.702	5.234	8.154	33.853	125.269	179.228	331.787
BNGA11406	VF–F sand	84.809	255.566	62.014	118.194	143.556	214.51	324.247	396.466	594.763
BNGA11408	Mud	9.46	24.049	2.966	5.306	7.334	14.779	29.361	40.342	77.2
BNGA11409	Mud	23.623	112.601	4.667	14.729	34.422	91.007	151.753	187.088	282.131
BNGA11411	Mud	4.844	63.348	1.658	2.606	3.397	6.969	39.144	113.936	351.996
BNGA11412	M–C Sand	293.547	399.846	134.123	191.488	230.85	347.291	521.802	625.874	853.557
BNGA11414	M–C Sand	96.721	289.303	65.001	106.41	129.939	202.102	362.108	522.369	841.992
BNGA11415	Mud	14.574	67.4	3.428	7.719	13.164	37.251	79.515	113.662	251.428
BNGA11417	Mud	15.803	105.757	3.525	8.012	13.732	53.002	136.853	190.859	379.135
BNGA11418	M–C Sand	109.651	439.425	36.459	142.743	212.398	406.339	640.594	754.519	951.634

Table A.1 – continued from previous page

Sample ID	Field Grain Size	D [3, 2]	D [4, 3]	d(0.050)	d(0.160)	d(0.250)	d(0.0.500)	d(0.750)	d(0.840)	d(0.950)
BNGA11420	Mud	332.17	447.622	149.666	216.416	263.093	400.222	593.527	700.403	910.468
BNGA11421	Mud	8.203	38.834	2.426	4.271	6.059	14.127	32.803	48.17	133.049
BNGA11423	Mud	7.699	39.948	2.294	3.954	5.54	13.077	35.161	54.308	129.986
BNGA11424	Mud	12.686	53.799	3.07	6.495	10.482	33.316	78.983	106.159	171.924
BNGA11427	Mud	11.789	50.305	2.966	6.083	9.556	27.876	63.675	85.887	147.175
BNGA11429	Mud	10.934	43.767	2.871	5.942	9.23	23.413	50.657	71.329	148.991
BNGA11430	Mud	7.288	28.87	2.476	4.073	5.43	10.368	20.121	27.75	59.337
BNGA11432	Mud	6.437	37.242	2.073	3.407	4.626	10.02	25.764	41.831	128.508
BNGA11434	Mud	13.827	62.51	3.164	7.064	12.222	40.946	86.24	113.004	183.617
BNGA11435	VF–F sand	158.509	212.49	90.792	123.031	142.55	194.791	265.173	305.481	398.891
BNGA11437	VF–F sand	120.981	187.67	72.106	100.308	117.33	164.317	232.189	274.241	386.212
BNGA11438	VF–F sand	221.367	281.77	127.838	168.948	194.115	261.197	349.799	399.317	510.366
BNGA11441	VF–F sand	215.345	422.881	171.353	244.812	284.708	389.45	531.637	614.576	809.114
BNGA11444	VF–F sand	240.829	295.782	127.413	165.982	191.77	264.652	368.159	429.032	572.371
BNGA11447	VF–F sand	273.279	329.743	145.178	190.891	220.698	302.317	411.834	473.039	608.779
BNGA11450	VF–F sand	444.878	528.937	239.146	312.029	359.834	491.708	669.25	765.179	947.653
BNGA11453	VF–F sand	314.965	394.079	159.995	215.665	252.196	353.758	495.307	577.982	772.662

157

Table A.1 – continued from previous page

Sample ID	Field Grain Size	D [3, 2]	D [4, 3]	d(0.050)	d(0.160)	d(0.250)	d(0.0.500)	d(0.750)	d(0.840)	d(0.950)
BNGA11456	M–C Sand	534.746	612.095	300.011	385.678	441.124	588.763	769.852	856.688	1002.171
BNGA11463	M–C Sand	422.223	546.262	219.125	313.318	369.429	517.837	707.07	803.378	973.718
BNGA11605	Mud	12.254	78.379	2.942	5.776	9.077	40.288	117.305	160.891	271.334
BNGA11606	VF–F sand	222.432	267.987	118.9	155.101	178.981	245.052	334.891	385.402	496.56
BNGA11608	VF–F sand	252.532	369.123	113.386	158.065	190.042	295.252	492.195	618.836	871.674
BNGA11618	Mud	12.467	92.209	2.775	5.994	10.353	46.616	122.068	167.387	315.826
BNGA11623	Mud	8.589	49.711	2.519	4.338	6.087	14.64	43.079	75.549	215.22
BNGA11628		296.402	393.145	141.874	194.44	230.902	340.034	506.641	607.606	835.266
BNGA11632	Mud	5.925	130.464	1.922	2.976	3.921	8.576	42.588	360.124	826.012
BNGA11635	VF–F sand	60.21	140.674	22.041	61.499	78.403	122.889	185.314	222.536	313.383
BNGA11637	M–C Sand	234.406	319.564	112.726	152.642	180.399	264.868	402.686	493.75	727.224
BNGA11641	M–C Sand	422.856	556.664	186.504	295.59	363.157	536.463	740.105	835.714	993.457
BNGA11647	Mud	12.647	195.77	2.923	5.861	9.368	43.903	235.694	547.557	873.331
BNGA11649	VF–F sand	20.318	124.782	4.099	12.08	23.359	74.797	153.09	206.206	452.969
BNGA11652	VF–F sand	148.066	224.301	67.728	108.747	132.548	197.321	288.643	343.118	475.715
BNGA11655	VF–F sand	326.562	437.546	163.008	237.288	280.894	398.076	559.087	652.054	857.887
BNGA11666	M–C Sand	296.489	395.518	150.626	213.125	251.38	355.724	500.862	586.193	787.224

Table A.1 – continued from previous page

Sample ID	Field Grain Size	D [3, 2]	D [4, 3]	d(0.050)	d(0.160)	d(0.250)	d(0.0.500)	d(0.750)	d(0.840)	d(0.950)
BNGA11673	M–C Sand	386.622	515.535	185.768	278.581	333.874	482.183	676.081	777.127	959.27
BNGA11677	M–C Sand	420.297	536.354	219.481	306.977	360.598	504.59	691.986	789.385	965.089
BNGA11902	Mud	8.578	37.418	2.626	4.662	6.494	13.657	29.535	43.028	102.977
BNGA11903	Mud	17.286	82.408	3.634	9.554	18.643	59.963	117.709	153.106	246.247
BNGA11905	Mud	9.16	31.025	2.669	4.817	6.854	15.878	39.201	58.356	112.021
BNGA11906	Mud	11.263	66.035	2.96	5.522	8.067	24.887	100.71	142.232	239.814
BNGA11908	Mud	12.247	79.758	3.043	5.921	9.053	32.282	117.771	166.139	289.641
BNGA11909	Mud	11.173	64.516	2.876	5.431	8.137	26.25	93.512	135.823	239.593
BNGA11911	Mud	11.422	40.784	3.011	5.931	9.029	24.221	55.52	76.158	133.381
BNGA11912	Mud	11.64	32.838	3.293	6.623	9.709	20.615	39.86	53.688	99.858
BNGA11914	Mud	11.377	38.89	2.976	6.018	9.318	23.806	52.387	72.479	127.471
BNGA11915	VF–F sand	244.422	310.334	124.137	165.145	192.882	272.697	388.773	458.405	626.901
BNGA11917	Mud	9.843	66.282	2.551	4.774	7.158	23.136	76.598	114.008	251.957
BNGA11918	Mud	18.49	85.835	3.805	10.46	21.119	68.423	126.757	159.969	238.575
BNGA11920	Mud	10.553	31.423	2.977	5.73	8.435	19.129	39.351	53.654	97.818
BNGA11921	Mud	7.263	46.537	2.432	3.985	5.323	10.308	20.971	30.92	257.505
BNGA11923	Mud	6.344	26.241	2.297	3.56	4.604	8.39	16.38	23.568	68.942

Table A.1 – continued from previous page

Sample ID	Field Grain Size	D [3, 2]	D [4, 3]	d(0.050)	d(0.160)	d(0.250)	d(0.0.500)	d(0.750)	d(0.840)	d(0.950)
BNGA12103	Mud	9.633	84.982	2.64	4.779	6.865	17.824	85.556	158.146	416.695
BNGA12105	VF–F sand	174.342	202.847	98.801	125.335	142.365	188.179	248.643	282.315	357.579
BNGA12106	Mud	8.636	24.049	2.663	4.63	6.43	13.874	30.895	43.758	79.384
BNGA12108	M–C Sand	358.393	472.633	164.36	235.6	285.024	428.324	626.074	732.497	932.69
BNGA12112	M–C Sand	453.239	587.713	238.95	349.743	411.738	570.268	759.96	849.9	999.553
BNGA12113		8.079	18.012	2.648	4.427	6.021	12.395	24.588	32.451	52.157
BNGA12115	Mud	7.117	40.325	2.302	3.796	5.136	10.652	24.22	36.477	114.867
BNGA12121	Mud	8.281	67.119	2.474	4.203	5.803	13.124	44.886	115.111	351.844
BNGA12122	VF–F sand	230.175	299.27	115.523	153.824	179.962	256.53	372.988	446.27	634.263
BNGA12126	Mud	14.053	96.333	3.238	7.369	12.312	37.695	113.198	173.575	397.716
BNGA12126.5	M–C Sand	238.329	337.909	109.527	151.509	181.51	276.233	436.402	540.892	789.134
BNGA12129	VF–F sand	13.602	50.535	3.357	7.029	11.216	34.891	75.001	97.452	150.692
BNGA12130	M–C Sand	395.473	551.475	150.205	277.28	354.735	537.643	742.841	838.093	994.674
BNGA12134	Mud	17.075	73.4	3.739	9.264	17.762	54.102	93.712	116.384	177.063
BNGA12135	VF–F sand	295.774	421.531	136.073	203.002	246.83	372.661	554.968	660.64	881.688
BNGA12136	Mud	17.321	117.755	3.483	9.285	18.096	79.626	164.582	214.8	367.442
BNGA12137	VF–F sand	297.98	450.147	120.451	176.982	223.185	395.661	641.461	758.286	955.232

Table A.1 – continued from previous page

Sample ID	Field Grain Size	D [3, 2]	D [4, 3]	d(0.050)	d(0.160)	d(0.250)	d(0.0.500)	d(0.750)	d(0.840)	d(0.950)
BNGA12140	Mud	10.788	63.753	2.793	5.366	8.061	23.675	79.087	121.031	237.091
BNGA12302	Mud	10.13	53.482	2.676	5.023	7.493	21.865	65.142	99.725	216.136
BNGA12303	Mud	9.368	65.922	2.535	4.614	6.765	19.34	58.411	93.756	323.955
BNGA12305	Mud	12.863	62.872	3.056	6.459	10.642	36.242	82.832	115.172	226.014
BNGA12306	Mud	14.46	61.253	3.286	7.423	13.287	43.623	81.861	105.055	177.094
BNGA12308	Mud	12.802	62.834	3.132	6.559	10.62	32.504	68.553	92.251	200.868
BNGA12309	Mud	10.439	49.89	2.732	5.161	7.747	24.194	64.511	89.918	165.694
BNGA12311	Mud	7.968	27.513	2.45	4.148	5.712	12.828	33.636	51.559	103.889
BNGA12312	Mud	10.504	82.983	2.552	5.046	8.105	27.729	88.42	146.138	366.735
BNGA12314	Mud	12.687	103.756	2.794	6.419	11.659	56.143	153.214	209.678	356.588
BNGA12315	Mud	17.764	87.099	3.866	9.891	17.474	56.765	129.675	172.307	272.077
BNGA12317	M–C Sand	379.751	507.424	176.536	264.721	320.456	472.379	670.748	773.367	957.622
BNGA12318	M–C Sand	449.219	575.694	211.79	325.273	391.143	557.788	753.718	845.757	997.961
BNGA12320	M–C Sand	407.647	562.425	166.336	296.469	370.069	548.491	751.357	845.102	998.285
BNGA12321	Mud	8.506	46.43	2.569	4.333	5.984	14.004	39.086	77.728	242.955
BNGA12324	Mud	17.653	165.727	3.527	8.595	16.793	116.69	275.22	346.634	492.555
BNGA12327	Mud	8.849	48.141	2.695	4.633	6.404	14.048	36.18	62.77	236.18

161

Table A.1 – continued from previous page

Sample ID	Field Grain Size	D [3, 2]	D [4, 3]	d(0.050)	d(0.160)	d(0.250)	d(0.0.500)	d(0.750)	d(0.840)	d(0.950)
BNGA12330	Mud	6.917	34.443	2.274	3.684	4.933	10.036	23.229	37.551	159.734
BNGA12334	Mud	8.201	23.026	2.582	4.401	6.057	12.874	28.035	39.852	78.051
BNGA12337	Mud	7.481	26.357	2.344	3.926	5.361	11.567	30.229	48.852	103.659
BNGA12340	Mud	8.109	26.655	2.629	4.37	5.894	12.108	27.619	42.149	105.923
BNGA12343	Mud	8.417	46.918	2.533	4.458	6.245	13.69	31.626	48.99	246.112
BNGA12346	Mud	10.165	35.659	2.854	5.372	7.853	18.929	42.156	58.107	109.085
BNGA12349	Mud	11.734	71.294	3.061	5.835	8.603	25.274	103.711	155.53	275.46
BNGA12353	VF–F sand	20.19	126.464	3.736	11.04	28.741	106.916	185.645	231.32	342.992
BNGA12356	VF–F sand	273.593	354.526	134.675	182.821	215.433	309.577	447.708	531.441	735.65
BNGB00502	Mud	12.056	23.037	3.984	7.698	10.248	17.872	30.124	38.235	60.288
BNGB00505	Mud	15.971	46.094	4.704	10.116	14.079	26.823	49.626	66.08	119.046
BNGB00509	VF–F Sand	397.745	440.849	250.538	301.976	333.492	415.06	520.21	579.324	719.598
BNGB00511	VF–F sand	248.3	481.811	230.868	318.26	358.887	459.885	590.491	664.902	836.731
BNGB00515	Mud	9.384	42.738	2.461	4.794	7.425	19.064	43.047	61.94	140.501
BNGB00902	Mud	21.517	43.968	1.875	2.231	2.529	3.782	8.347	13.158	27.433
BNGB00908	Mud	14.398	40.938	1.651	1.949	2.189	3.08	5.128	7.011	15.154
BNGB00912	Mud	19.058	49.304	1.816	2.112	2.377	3.369	5.882	8.595	20.907

Table A.1 – continued from previous page

Sample ID	Field Grain Size	D [3, 2]	D [4, 3]	d(0.050)	d(0.160)	d(0.250)	d(0.0.500)	d(0.750)	d(0.840)	d(0.950)
BNGB00914	VF–F sand	116.413	284.578	2.366	2.583	2.818	3.742	5.753	7.735	22.944
BNGB00918	M–C Sand	104.75	319.958	2.376	2.611	2.871	3.824	5.677	7.148	14.51
BNGB00921	Mud	8.092	24.548	1.488	1.703	1.893	2.55	3.911	5.028	9.157
BNGB00925	Mud	7.122	17.872	1.585	1.858	2.081	2.844	4.322	5.457	9.33
BNGB00927	M–C Sand	194.964	434.485	3.722	4.059	4.437	5.964	9.264	12.644	44.682
BNGB00935	Mud	7.639	32.334	1.393	1.633	1.814	2.427	3.638	4.621	8.346
BNGB00941	VF–F sand	112.593	284.645	2.353	2.546	2.739	3.519	4.987	6.153	15.268
BNGB00949	M–C Sand	324.348	425.666	27.445	31.732	35.899	55.223	270.293	329.365	470.445
BNGB01302	Mud	19.879	64.245	4.831	12.893	20.011	42.086	79.062	104.597	186.537
BNGB01305	Mud	21.767	53.905	1.877	2.241	2.539	3.647	6.297	9.093	23.557
BNGB01306	Mud	7.9	22.844	2.509	4.181	5.713	12.451	27.966	39.03	72.178
BNGB01308	Mud	4.946	14.746	1.837	2.866	3.686	7.089	18.516	27.928	52.963
BNGB01309	Mud	9.048	18.858	1.615	1.903	2.138	3.018	5.017	6.716	12.583
BNGB01311	VF–F sand	14.78	60.475	3.744	7.685	12.207	31.846	84.095	124.648	211.686
BNGB01315	VF–F sand	120.821	182.455	61.766	90.443	108.403	159.282	233.309	277.894	386.104
BNGB01320	VF–F sand	331.209	430.739	31.817	36.352	40.774	60.653	284.318	343.887	483.613
BNGB01323	VF–F sand	168.456	195.662	96.364	121.533	137.62	180.899	238.445	270.93	345.707

Sample ID	Field Grain Size	D [3, 2]	D [4, 3]	d(0.050)	d(0.160)	d(0.250)	d(0.0.500)	d(0.750)	d(0.840)	d(0.950)
BNGB01330	VF–F sand	241.791	324.87	17.551	20.933	24.019	35.815	187.835	236.301	347.407
BNGB01337	VF–F sand	304.34	397.454	27.721	32.414	36.426	50.93	258.624	316.187	439.995
BNGB01340	Mud	10.736	31.931	3.183	6.342	9.043	17.531	30.893	39.715	67.791
BNGB01341	Mud	9.958	22.65	1.586	1.865	2.1	2.988	5.048	6.833	13.157
BNGB01350	Mud	8.591	18.966	1.586	1.863	2.093	2.931	4.755	6.287	11.689
BNGB01356	VF–F sand	74.961	183.748	2.034	2.219	2.41	3.137	4.721	6.431	17.27
BNGB01702	VF–F sand	83.903	123.178	41.973	55.997	65.453	92.631	133.295	159.724	253.865
BNGB01705	VF–F sand	85.915	131.307	33.049	55.05	70.66	114.432	174.175	208.501	288.729
BNGB01709	Mud	25.197	57.749	7.806	20.193	26.521	44.49	73.267	92.709	149.512
BNGB01712	Mud	19.041	40.981	4.906	14.385	19.979	34.321	54.88	67.532	99.406
BNGB01714	M–C Sand	220.008	278.131	139.399	181.791	205.259	264.69	339.543	380.289	470.448
BNGB01717	Mud	23.934	83.524	5.724	15.877	24.563	59.384	118.42	153.938	243.378
BNGB01721	M–C Sand	120.521	177.887	64.188	89.55	105.86	152.98	224.178	268.698	381.681
BNGB01724	M–C Sand	211.146	472.182	62.412	201.686	292.392	454.565	647.328	749.083	940.694
BNGB01726	M–C Sand	77.111	238.973	19.269	117.891	150.169	224.821	318.977	370.569	482.371
BNGB01732	Mud	19.711	46.129	5.512	13.238	18.805	35.547	62.202	79.26	123.235
BNGB01735	M–C Sand	92.525	378.03	24.798	140.082	213.382	348.213	519.579	618.529	839.769

Table A.1 – continued from previous page

Sample ID	Field Grain Size	D [3, 2]	D [4, 3]	d(0.050)	d(0.160)	d(0.250)	d(0.0.500)	d(0.750)	d(0.840)	d(0.950)
BNGB017375	Mud	13.42	49.075	3.706	7.812	11.433	24.023	47.673	66.329	157.849
BNGB01759	M–C Sand	154.971	304.799	55.507	116.127	159.825	270.498	411.537	491.408	678.561
BNGB01763	M–C Sand	143.006	321.802	44.653	142.705	190.751	296.222	428.445	502.951	675.352

Appendix B

Geochemical Data for Borehole Samples

Table B.1: Geochemical data for BanglaPIRE samples. Strontium (Sr) concentration is measured in parts per million (ppm), and silicon dioxide (SiO_2) and calcium oxide (CaO) are measured in percentage of the total sample weight (bulk weight %).

Sample ID	Field Grain Size	Sr	SiO$_2$	CaO
BNGA00202	Mud	65.58	64.36	1.37
BNGA00205	Mud	89.67	65.13	1.5
BNGA00206	VF–F sand	127.48	77.43	1.84
BNGA00208	VF–F sand	138.39	78.28	1.85
BNGA00211	VF–F sand	117	85.11	1.7
BNGA00214	VF–F sand	147.12	78.86	2.04
BNGA00217	VF–F sand	140.5	81.37	1.91
BNGA00220	VF–F sand	143.86	78.24	1.9
BNGA00223	M–C Sand	122.33	83.04	1.79
BNGA00226	M–C Sand	121.76	81.68	1.62
BNGA00229	VF–F sand	182.75	77.29	1.97
BNGA00802	Mud	82.43	59.14	1.41
BNGA00805	Mud	99.04	58.65	1.49
BNGA00808	Mud	77.63	69.54	1.51
BNGA00809	Mud	96.93	63.97	1.72
BNGA00811	VF–F sand	99.75	61.87	1.6
BNGA00814	VF–F sand	158.29	75.96	1.93
BNGA00817	VF–F sand	163.17	77.99	2.08
BNGA00820	VF–F sand	151.4	74.57	1.89

Table B.1 – continued from previous page

Sample ID	Field Grain Size	Sr	SiO$_2$	CaO
BNGA00823	M–C Sand	122.12	82.5	1.65
BNGA01402	Mud	85.84	60.1	1.57
BNGA01405	Mud	87.4	60.2	1.49
BNGA01406	VF–F sand	136.75	79.46	1.85
BNGA01408	VF–F sand	141.95	73.7	2.02
BNGA01411	VF–F sand	138.62	77.13	2.02
BNGA01414	VF–F sand	133.63	77.25	1.91
BNGA01417	VF–F sand	143.47	75.83	2.23
BNGA01420	M–C Sand	127.77	81.03	1.77
BNGA01423	M–C Sand	104.99	83.01	1.61
BNGA01426	M–C Sand	126.16	83.52	1.73
BNGA01429	VF–F sand	122.54	75.19	1.84
BNGA01432	VF–F sand	133.63	78.46	1.71
BNGA02002	VF–F sand	115.55	64.44	1.72
BNGA02003	VF–F sand	80.4	56.96	1.37
BNGA02005	VF–F sand	164.4	76.03	2.2
BNGA02008	VF–F sand	169.38	73.93	2.26
BNGA02011	VF–F sand	169.32	73.3	2.27
BNGA02014	VF–F sand	146.81	79.28	1.89
BNGA02017	M–C Sand	138.72	78.83	1.73
BNGA02020	M–C Sand	116.95	82.52	1.71
BNGA02602	VF–F sand	140.72	67.87	2.06
BNGA02605	VF–F sand	148.74	79.35	1.95
BNGA02608	VF–F sand	141.12	80.47	1.96
BNGA02611	M–C Sand	125.8	78.91	1.74

Sample ID	Field Grain Size	Sr	SiO$_2$	CaO
BNGA02614	VF–F sand	174.48	74.94	2.48
BNGA02617	VF–F sand	169.62	74.49	2.36
BNGA02620	VF–F sand	167.58	74.32	2.42
BNGA02623	M–C Sand	126.38	82.79	1.7
BNGA02626	M–C Sand	113.57	84.44	1.63
BNGA02629	M–C Sand	137.19	82.27	1.89
BNGA02632	M–C Sand	137.74	80.76	1.76
BNGA02635	M–C Sand	153.58	76.41	2.12
BNGA02638	M–C Sand	143.29	71.4	1.82
BNGA02641	M–C Sand	149.57	76.73	1.98
BNGA02643	M–C Sand	149.64	75.44	2.05
BNGA03102	VF–F sand	157.34	73.93	2.14
BNGA03105	VF–F sand	152.57	75.31	1.97
BNGA03108	VF–F sand	162.15	75.07	2.22
BNGA03111	VF–F sand	144.32	80.93	2.01
BNGA03114	VF–F sand	189.69	73.26	2.83
BNGA03117	VF–F sand	185.11	75.9	2.6
BNGA03120	VF–F sand	137.69	82.39	2.01
BNGA03123	VF–F sand	129.35	81.46	1.7
BNGA03126	VF–F sand	141.49	80.01	2.04
BNGA03129	VF–F sand	152.36	78.82	2.22
BNGA03132	VF–F sand	148.85	79.04	2.03
BNGA03135	VF–F sand	147.65	80.11	2.14
BNGA03138	VF–F sand	134.94	82.17	1.97
BNGA03141	VF–F sand	146.62	77.42	2.07

Table B.1 – continued from previous page

Sample ID	Field Grain Size	Sr	SiO$_2$	CaO
BNGA03144	VF–F sand	163.59	78.11	2.44
BNGA03147	VF–F sand	150.79	80.14	1.84
BNGA03150	VF–F sand	154.34	81.03	2.04
BNGA03153	VF–F sand	162.67	77.02	2.49
BNGA03155	VF–F sand	159.29	81.81	2.08
BNGA04002	VF–F sand	165.09	72.63	2.16
BNGA04005	VF–F sand	162.29	76.77	2.17
BNGA04008	VF–F sand	171.59	73.86	2.72
BNGA04011	VF–F sand	171.19	75.87	2.39
BNGA04014	VF–F sand	172.15	75.2	2.64
BNGA04017	VF–F sand	138.92	80.03	1.89
BNGA04020	VF–F sand	164.8	76.21	2.4
BNGA04023	VF–F sand	150.44	77.27	2.01
BNGA04026	VF–F sand	161.25	71.47	2.24
BNGA04029	VF–F sand	157.64	76.29	2.13
BNGA04032	VF–F sand	155.59	78.23	2.12
BNGA04035	VF–F sand	159.58	77.12	1.88
BNGA04038	VF–F sand	152.41	78.33	2.23
BNGA04041	VF–F sand	160.27	78.03	2.11
BNGA04044	VF–F sand	159.09	77.87	1.98
BNGA04047	VF–F sand	169.04	78	2.22
BNGA04050	VF–F sand	156.14	72.07	2.14
BNGA04052	VF–F sand	154.41	71.79	2.14
BNGA04902	VF–F sand	148.14	79.5	2.07
BNGA04905	VF–F sand	157.57	75.73	2.31

Table B.1 – continued from previous page

Sample ID	Field Grain Size	Sr	SiO$_2$	CaO
BNGA04908	VF–F sand	158.71	74.95	1.99
BNGA04911	VF–F sand	154.46	72.89	2.03
BNGA04914	VF–F sand	147.62	78.34	1.87
BNGA04917	M–C Sand	146.01	79.47	1.9
BNGA04920	VF–F sand	151.7	77.76	2.02
BNGA04923	VF–F sand	158.11	73.88	2.29
BNGA04926	M–C Sand	145.53	77.76	1.98
BNGA04930	M–C Sand	150.77	78.16	2.05
BNGA04932	M–C Sand	139.79	81.41	1.88
BNGA04935	M–C Sand	152.93	77.6	1.98
BNGA04938	VF–F sand	158.9	77.84	1.91
BNGA04941	VF–F sand	156.17	76.91	2.04
BNGA04944	M–C Sand	158.03	77.54	2.07
BNGA04947	M–C Sand	146.35	78.15	1.99
BNGA04950	VF–F sand	153.97	78.69	2.05
BNGA04953	VF–F sand	155.15	77.42	1.84
BNGA05502	Mud	167.5	65.75	2.42
BNGA05505	Mud	159.24	59.64	2.29
BNGA05508	VF–F sand	166.1	74.29	2.37
BNGA05511	VF–F sand	107.54	84.88	1.53
BNGA05514	VF–F sand	145.86	82.61	2
BNGA05517	VF–F sand	167.06	77.84	2.69
BNGA05520	M–C Sand	138.09	81.08	1.83
BNGA05523	VF–F sand	144.68	80.06	1.79
BNGA05526	VF–F sand	149.48	75.5	2.11

Sample ID	Field Grain Size	Sr	SiO$_2$	CaO
BNGA05527	Mud	134.15	63.77	1.86
BNGA05529	VF–F sand	147.43	79.83	2.06
BNGA05532	M–C Sand	163.14	74.28	2.39
BNGA05535	M–C Sand	133.94	82.57	1.85
BNGA05538	M–C Sand	142.56	80.61	1.98
BNGA05541	M–C Sand	138.64	80.35	1.75
BNGA05544	VF–F sand	146.45	76.47	1.83
BNGA05547	VF–F sand	145.46	76.47	1.76
BNGA05550	VF–F sand	151	79.46	2.03
BNGA05553	M–C Sand	137.01	81.07	1.72
BNGA05556	M–C Sand	171.99	72.85	3.09
BNGA05559	Mud	110.44	61.97	1.73
BNGA05563	M–C Sand	154.73	81.48	2.02
BNGA05566	M–C Sand	156.4	79.96	2.22
BNGA05569	M–C Sand	138.69	81.86	1.75
BNGA05570	M–C Sand	130.91	84.64	1.75
BNGA06202	VF–F sand	131.4	66.58	1.81
BNGA06205	VF–F sand	145.81	63.03	1.89
BNGA06208	VF–F sand	156.73	72.14	2.29
BNGA06211	VF–F sand	144.32	67.29	1.88
BNGA06214	VF–F sand	156.99	73.75	2.11
BNGA06217	VF–F sand	158.11	72.22	2.36
BNGA06220	VF–F sand	150.56	80.37	2.05
BNGA06223	VF–F sand	157.81	74.88	2.24
BNGA06226	VF–F sand	158.45	70.1	2.2

Table B.1 – continued from previous page

Sample ID	Field Grain Size	Sr	SiO$_2$	CaO
BNGA06229	M–C Sand	145.11	81.46	1.88
BNGA06232	M–C Sand	155.78	79.64	2.15
BNGA06235	M–C Sand	157.34	80.01	2
BNGA06238	M–C Sand	171.69	76.69	2.16
BNGA06241	M–C Sand	151.25	79.48	2.09
BNGA06244	M–C Sand	154.96	80.62	1.97
BNGA06247	M–C Sand	153.38	80.96	1.91
BNGA06250	M–C Sand	156.69	82.16	1.86
BNGA06253	M–C Sand	161.68	75.53	1.93
BNGA06256	M–C Sand	139.43	81.81	1.95
BNGA06258	M–C Sand	135.33	79.28	2.04
BNGA07002	Mud	141.32	60.54	1.98
BNGA07005	VF–F sand	171.08	77.47	2.4
BNGA07009	VF–F sand	150.3	81.82	1.92
BNGA07015	VF–F sand	166.98	78.73	2.21
BNGA07018	VF–F sand	155.77	80.32	1.99
BNGA07023	VF–F sand	165.05	79.26	2.11
BNGA07026	M–C Sand	109.49	84.48	1.53
BNGA07029	M–C Sand	105.68	85.75	1.51
BNGA07032	M–C Sand	132.49	80.83	1.75
BNGA07035	M–C Sand	167.86	77.79	2.21
BNGA07038	M–C Sand	123.65	76.96	1.71
BNGA07041	M–C Sand	131.6	82.39	1.67
BNGA07044	M–C Sand	144.8	79.8	1.92
BNGA07047	M–C Sand	145.19	81	1.89

Sample ID	Field Grain Size	Sr	SiO$_2$	CaO
BNGA07050	M–C Sand	156.32	79.69	1.76
BNGA07053	M–C Sand	158.94	0	1.81
BNGA07056		163.5	80.5	1.94
BNGA07059	M–C Sand	170.44	77.54	2.1
BNGA07064	M–C Sand	170.63	78.12	2.32
BNGA07102	Mud	43.76	65	1.21
BNGA07105	Mud	41.63	63.78	1.22
BNGA07108	Mud	52.02	64.55	1.25
BNGA07111	Mud	71.41	62.96	1.34
BNGA07114	VF–F sand	124.89	83.36	1.61
BNGA07117	VF–F sand	159.9	79.25	1.89
BNGA07120	VF–F sand	163.78	78.49	2.09
BNGA07123	VF–F sand	163.09	76.25	2.09
BNGA07126	VF–F sand	162.65	78.13	1.96
BNGA07129	VF–F sand	166.48	77.84	2.19
BNGA07132	M–C Sand	138.39	82.03	1.69
BNGA07135	M–C Sand	142.28	81.52	1.74
BNGA07138	M–C Sand	136.34	82.55	1.75
BNGA07141	M–C Sand	162	80.52	1.93
BNGA07144		164.78	74.63	1.84
BNGA07147	M–C Sand	165.95	78.98	1.89
BNGA07150	M–C Sand	150.4	80.87	1.83
BNGA07153	M–C Sand	176.24	77.28	2.16
BNGA07156	VF–F sand	156.02	78.73	1.78
BNGA07159	VF–F sand	148.62	78.73	1.94

Sample ID	Field Grain Size	Sr	SiO$_2$	CaO
BNGA07162		145.92	76.83	1.88
BNGA07165		159.12	77.76	2.11
BNGA07168		149.59	77.84	1.87
BNGA07171	M–C Sand	160.99	77.77	2.02
BNGA07174		160.6	77.21	2.03
BNGA07177		156.46	77.08	2.08
BNGA07180		122.37	81.52	1.78
BNGA07202	Mud	41.48	59.42	1.22
BNGA07205	Mud	40.76	60.5	1.18
BNGA07208	Mud	92.14	63.46	1.42
BNGA07211	M–C Sand	127.04	77.64	1.64
BNGA07214	M–C Sand	136.33	75.67	1.76
BNGA07217	M–C Sand	151.92	78.9	1.88
BNGA07220	M–C Sand	141.94	80.99	1.79
BNGA07223	M–C Sand	154.49	78.21	1.8
BNGA07226	M–C Sand	152.77	77.58	1.69
BNGA07229	M–C Sand	146.47	82.2	1.89
BNGA07232	M–C Sand	143.86	81.71	1.77
BNGA07235	M–C Sand	154.16	79.79	1.85
BNGA07238	M–C Sand	136.28	82	1.75
BNGA07244	VF–F sand	187.46	73.27	2.13
BNGA07247	VF–F sand	188.18	77.11	2.28
BNGA07250	VF–F sand	156.41	73.23	1.81
BNGA07253	VF–F sand	165.87	75.49	2.22
BNGA07256	VF–F sand	155.81	71.68	1.84

Table B.1 – continued from previous page

Sample ID	Field Grain Size	Sr	SiO$_2$	CaO
BNGA07259	M–C Sand	148.92	79.06	1.79
BNGA07261		166.21	77.35	1.99
BNGA08302	VF–F sand	167.81	75.35	2.28
BNGA08305	VF–F sand	172.73	73.86	2.33
BNGA08308	VF–F sand	168.25	77.42	2.16
BNGA08311	VF–F sand	155.06	80.28	1.97
BNGA08314	VF–F sand	164.5	79.33	2.09
BNGA08317	VF–F sand	161.76	79.99	2.13
BNGA08323	VF–F sand	162.48	76.02	2.03
BNGA08326	M–C Sand	145.85	81.9	1.77
BNGA08329	M–C Sand	152.36	81.56	1.91
BNGA08332	M–C Sand	166.27	79.25	2.02
BNGA08335	M–C Sand	165.48	79.63	2.05
BNGA08338	M–C Sand	156.98	80.76	2
BNGA08341	M–C Sand	158.21	79.17	2.09
BNGA08344		158.95	79.34	2.01
BNGA08347	VF–F sand	150.19	75.7	1.91
BNGA08350	VF–F sand	147.19	75.4	1.75
BNGA08353	VF–F sand	158.38	77.2	1.98
BNGA08356	VF–F sand	140.25	80.6	2.01
BNGA08359	M–C Sand	133.23	82.06	1.78
BNGA08365		149.17	80.12	1.95
BNGA08368		150.41	79.84	1.92
BNGA08371	M–C Sand	165.42	77.58	2.12
BNGA08374		162.06	76.59	2.05

Sample ID	Field Grain Size	Sr	SiO$_2$	CaO
BNGA08380		152.06	80.77	1.93
BNGA08383		160.95	77.09	2.06
BNGA08386		162.76	75.62	2.18
BNGA08389		158.79	78	2.05
BNGA08802	VF–F sand	167.73	74.47	2.28
BNGA08805	VF–F sand	169.06	74.25	2.29
BNGA08808	VF–F sand	173.39	76.29	2.36
BNGA08811	VF–F sand	160.67	77.56	2.04
BNGA08814	VF–F sand	161.9	77.63	2.02
BNGA08817	VF–F sand	148.89	79.17	1.95
BNGA08820	VF–F sand	155.5	80.82	2.02
BNGA08823	VF–F sand	157.49	80.61	2.03
BNGA08826	VF–F sand	168.58	76.07	2.14
BNGA08829	M–C Sand	161.16	80.41	1.93
BNGA08832	VF–F sand	164.33	80.07	2.12
BNGA08835	VF–F sand	166.85	78.94	2.15
BNGA08838	M–C Sand	128.35	82.53	1.73
BNGA08841	M–C Sand	131.78	81.59	1.75
BNGA08844	M–C Sand	146.59	80.68	1.86
BNGA08847	VF–F sand	177.5	77.59	2.16
BNGA08850	VF–F sand	181.11	77.41	2.24
BNGA08853	VF–F sand	184.14	76.77	2.16
BNGA09402	Mud	126.33	58.54	1.69
BNGA09405	Mud	124.37	58.27	1.63
BNGA09406	Mud	130.42	66.95	1.85

Table B.1 – continued from previous page

Sample ID	Field Grain Size	Sr	SiO$_2$	CaO
BNGA09408	Mud	134.53	63.33	1.76
BNGA09411	Mud	41.66	61.74	1.19
BNGA09414	Mud	40.11	57.01	1.15
BNGA09417	Mud	132.07	68.16	1.65
BNGA09420	VF–F sand	138.85	77.75	1.77
BNGA09423	VF–F sand	134.73	75.31	1.79
BNGA09426	VF–F sand	139.31	71.47	1.79
BNGA09429	VF–F sand	147.61	78	1.96
BNGA09432	VF–F sand	150.6	76.07	2.06
BNGA09435	VF–F sand	151.43	78.44	1.8
BNGA09438	VF–F sand	152.72	75.36	1.97
BNGA09441	M–C Sand	142.75	75.26	1.76
BNGA09444	M–C Sand	144.82	78.18	1.82
BNGA09447	M–C Sand	145.47	75.99	2.03
BNGA09450	M–C Sand	143.08	75.4	1.81
BNGA09453	M–C Sand	151.65	75.29	1.84
BNGA09456	M–C Sand	132.34	78.41	1.7
BNGA09459	M–C Sand	120.02	74.06	1.86
BNGA09702	Mud	128.6	62.11	1.71
BNGA09705		182.68	74.92	2.19
BNGA09708		181.62	74.13	2.25
BNGA09711		142.54	78.16	1.8
BNGA09714		171.36	77.52	2.15
BNGA09717		155.89	0	0
BNGA09720		161.77	79.01	1.94

Sample ID	Field Grain Size	Sr	SiO$_2$	CaO
BNGA09723		145.01	81.61	1.89
BNGA09726		151.88	79.92	1.92
BNGA09729	M–C Sand	167.36	78.59	2.05
BNGA09732		162	77.27	2.04
BNGA09735		147.38	76.43	1.8
BNGA09741		165.68	77.96	2.23
BNGA09744		167.51	78.64	2.19
BNGA09747		162.62	79.14	2.06
BNGA09750		153.77	79.76	1.92
BNGA09753	M–C Sand	78.7	61.55	1.34
BNGA09756		155.73	80.14	1.94
BNGA09759		171.11	77.5	2.33
BNGA09763	M–C Sand	158.39	79.38	2.06
BNGA10002	VF–F sand	195.28	74.64	3.33
BNGA10004	VF–F sand	151.51	62.16	2.08
BNGA10005	VF–F sand	188.93	73.13	2.82
BNGA10008	M–C Sand	180.07	74.37	2.57
BNGA10011	M–C Sand	186.65	74.15	2.63
BNGA10014	M–C Sand	175.63	75.15	2.41
BNGA10017	M–C Sand	167.22	78.59	1.92
BNGA10020	M–C Sand	168.82	76.33	1.88
BNGA10023	M–C Sand	180.33	75.63	2.45
BNGA10026	M–C Sand	170.22	74.45	2.22
BNGA10029	M–C Sand	172.19	77.97	2.17
BNGA10032	M–C Sand	149.67	81.73	2.01

Sample ID	Field Grain Size	Sr	SiO$_2$	CaO
BNGA10035	M–C Sand	124.73	82.76	1.81
BNGA10038	M–C Sand	172.46	76.03	2.42
BNGA10041	M–C Sand	169.63	75.17	2.33
BNGA10044	M–C Sand	168.36	76.94	1.98
BNGA10047	M–C Sand	140.38	80.83	1.82
BNGA10050	M–C Sand	129.95	81.79	1.69
BNGA10053	M–C Sand	148.52	80.22	1.99
BNGA10056	M–C Sand	164.03	76.63	1.93
BNGA10059	M–C Sand	162.11	76.97	1.84
BNGA10063	M–C Sand	174.35	73.23	1.98
BNGA10066	M–C Sand	161.65	77.15	2.07
BNGA10069	M–C Sand	158.74	76.69	2.1
BNGA10070	M–C Sand	128.63	79.21	1.85
BNGA10602	Mud	148.12	65.72	2.14
BNGA10605	VF–F sand	165.89	69.21	2.3
BNGA10608	Mud	148.51	61.68	2.04
BNGA10611	Mud	144.29	59.01	2.04
BNGA10614	M–C Sand	177.57	74.01	2.56
BNGA10615	M–C Sand	169.25	77.21	2.13
BNGA10617	Mud	141.58	69.32	1.92
BNGA10620	VF–F sand	177.87	76.24	2.49
BNGA10623	VF–F sand	161.39	70.04	2.22
BNGA10626	M–C Sand	174.13	75.66	2.52
BNGA10629	M–C Sand	146.95	81.25	1.76
BNGA10632	M–C Sand	164.67	79.62	2.15

Table B.1 – continued from previous page

Sample ID	Field Grain Size	Sr	SiO$_2$	CaO
BNGA10635	VF–F sand	170.97	78.67	2.07
BNGA10638	VF–F sand	168.43	76.76	2.17
BNGA10641	M–C Sand	143.63	81.61	1.9
BNGA10644	VF–F sand	168.11	78.87	1.95
BNGA10647	VF–F sand	170.08	77.32	2.21
BNGA10650	VF–F sand	161.74	79.53	2.06
BNGA10653	VF–F sand	171.7	77.88	2.02
BNGA10656	VF–F sand	173.2	77.88	2.28
BNGA10659	VF–F sand	175.36	77.05	2.52
BNGA10663	VF–F sand	163.26	75.7	2.07
BNGA10666	VF–F sand	166.27	77.07	2.19
BNGA10669	VF–F sand	158.92	77.58	2.01
BNGA10672	VF–F sand	165.91	76.23	2.04
BNGA10675	VF–F sand	172.31	77.53	2.18
BNGA10678	VF–F sand	162.5	78.85	2.12
BNGA10681	VF–F sand	168.83	77.28	2.17
BNGA10684	M–C Sand	137.93	80.11	1.84
BNGA10687	M–C Sand	164.67	77.31	1.95
BNGA10690	M–C Sand	164.97	78.2	2.07
BNGA10693	M–C Sand	161.83	78.93	2.1
BNGA10695	M–C Sand	153.19	78.36	1.94
BNGA11002	Mud	73.58	71.01	1.16
BNGA11005	Mud	100.54	59.72	1.35
BNGA11008	M–C Sand	17	101.22	1.08
BNGA11011	Mud	34.15	81.99	1.1

Table B.1 – continued from previous page

Sample ID	Field Grain Size	Sr	SiO$_2$	CaO
BNGA11014	Mud	54.67	70.59	1.24
BNGA11017	Mud	59.43	66.91	1.2
BNGA11020	Mud	54.43	65.42	1.23
BNGA11023	Mud	78.81	57.74	1.22
BNGA11027	VF–F sand	165.65	80.24	2.3
BNGA11029	VF–F sand	165.57	78.58	2.05
BNGA11032	VF–F sand	185.12	72.56	2.79
BNGA11035	VF–F sand	182.44	75.89	2.08
BNGA11038	VF–F sand	172.81	78.85	2.18
BNGA11041	M–C Sand	158.48	80.57	2
BNGA11044	M–C Sand	152.37	80.22	2.09
BNGA11047	M–C Sand	165.62	81.71	2.11
BNGA11050	M–C Sand	163.43	82.73	2.15
BNGA11053	M–C Sand	156.01	82.73	1.85
BNGA11056	M–C Sand	148.74	83.56	1.87
BNGA11059	M–C Sand	116.88	85.91	1.7
BNGA11063	M–C Sand	125.05	85.28	1.77
BNGA11402	Mud	79.87	64.48	1.13
BNGA11405	Mud	47.64	76.9	1.09
BNGA11406	VF–F sand	28.22	68.86	1.06
BNGA11408	Mud	61.9	0	1.1
BNGA11411	Mud	99.64	60.72	1.12
BNGA11414	M–C Sand	19.61	97.76	1.06
BNGA11415	Mud	48.01	77.96	1.1
BNGA11416	Mud	17.44	101.97	1.05

Table B.1 – continued from previous page

Sample ID	Field Grain Size	Sr	SiO$_2$	CaO
BNGA11418	M–C Sand	28.23	93.63	1.08
BNGA11419	Mud	84.66	57.99	1.38
BNGA11420	Mud	65.52	59.17	1.21
BNGA11423	Mud	62.55	65.37	1.21
BNGA11426	VF–F sand	16.39	100.33	1.07
BNGA11429	Mud	49.12	66.35	1.12
BNGA11432	Mud	83.64	60.27	1.37
BNGA11435	VF–F sand	130.1	77.01	2.05
BNGA11438	VF–F sand	155	74.58	2.12
BNGA11441	VF–F sand	136.31	75.13	1.97
BNGA11444	VF–F sand	162.08	76.41	2.14
BNGA11447	VF–F sand	174.16	76.58	2.21
BNGA11450	VF–F sand	156.92	80.52	1.98
BNGA11453	VF–F sand	161	77.92	1.96
BNGA11456	M–C Sand	108.11	84.59	1.56
BNGA11459	M–C Sand	130.9	84.11	1.75
BNGA11463	M–C Sand	154.39	80.69	1.97
BNGA11902	Mud	68.8	63.13	1.09
BNGA11905	Mud	57.48	69.55	1.1
BNGA11908	Mud	42.48	83.72	1.07
BNGA11911	Mud	55.48	72.12	1.12
BNGA11914	Mud	39.02	78.41	1.1
BNGA11915	VF–F sand	15.43	106.84	1.06
BNGA11917	Mud	46.36	77.14	1.16
BNGA11920	Mud	65.01	71.46	1.21

Table B.1 – continued from previous page

Sample ID	Field Grain Size	Sr	SiO$_2$	CaO
BNGA11923	Mud	60.22	72.21	1.26
BNGA12302	Mud	66.83	63.15	1.1
BNGA12305	Mud	64.27	67.63	1.1
BNGA12308	Mud	66.07	65.59	1.09
BNGA12311	Mud	77.9	66.26	1.09
BNGA12314	Mud	43.07	63.32	1.08
BNGA12317	M–C Sand	12.67	105.54	1.04
BNGA12320	M–C Sand	9.38	104.01	1.04
BNGA12323	Mud	44.45	68.25	1.16
BNGA12326	Mud	41.59	70.78	1.16
BNGA12329	Mud	48.51	71.88	1.14
BNGA12332	Mud	89.96	59.2	1.21
BNGA12335	Mud	92.52	59.59	1.18
BNGA12338	Mud	85.36	63.62	1.17
BNGA12341	Mud	60.17	64.8	1.14
BNGA12344	Mud	78.98	65.1	1.16
BNGA12347	Mud	62.35	65.79	1.13
BNGA12350	Mud	67.83	0	0
BNGA12353	VF–F sand	31.9	78.27	1.1
BNGA12356	VF–F sand	17.63	99.45	1.06
BNGA12359	Mud	54.09	66.99	1.22
BNGB00102	Mud	62.32	47.114713	0.309697
BNGB00111	Mud	41.84	47.108756	0.272341
BNGB00114	VF–F sand	62.99	49.623441	0.255779
BNGB00120	VF–F sand	74.68	56.145325	0.285212

Table B.1 – continued from previous page

Sample ID	Field Grain Size	Sr	SiO$_2$	CaO
BNGB00124	VF–F sand	73.28	54.665225	0.256864
BNGB00502	Mud	88.52	39.843441	0.70376
BNGB00505	Mud	120.14	48.036147	1.102295
BNGB00509	VF–F sand	11.67	64.257519	<LOD
BNGB00515	Mud	65.01	38.661331	0.415577
BNGB00523	VF–F sand	33.49	59.932638	0.13412
BNGB00527	Mud	77.82	44.424925	1.200954
BNGB00530	Mud	80.07	52.283319	0.379063
BNGB00537	VF–F sand	139.22	47.2577	1.222348
BNGB00544	Mud	87.49	44.073813	1.409262
BNGB00547	Mud	78.97	50.329466	0.295665
BNGB00902	Mud	111.06	46.423697	0.518951
BNGB00905	Mud	20.23	<LOD	<LOD
BNGB00908	Mud	117.42	44.192463	0.724854
BNGB00912	Mud	122	48.683081	0.797699
BNGB00914	VF–F sand	45.74	66.9883	0.103892
BNGB00918	M–C Sand	40.49	69.775363	0.079904
BNGB00920	Mud	96.32	47.871516	0.918448
BNGB00921	Mud	99.35	44.646022	0.381536
BNGB00925	Mud	90.15	42.752509	0.25929
BNGB00927	M–C Sand	104.7	66.544763	0.388754
BNGB00930	M–C Sand	97.08	51.270534	0.551368
BNGB00935	Mud	58.62	47.996484	0.186528
BNGB00937	Mud	47.08	52.515963	0.442427
BNGB00941	VF–F sand	47.74	70.315694	0.109578

Sample ID	Field Grain Size	Sr	SiO$_2$	CaO
BNGB00949	M–C Sand	51.07	71.776006	0.11779
BNGB01302	Mud	91.39	35.103088	1.086593
BNGB01305	Mud	131.04	54.792931	0.943095
BNGB01309	Mud	102.43	49.367697	0.445004
BNGB01311	VF–F sand	104.52	33.943706	1.285407
BNGB01314	VF–F sand	123.48	54.432994	0.759435
BNGB01315	VF–F sand	110.26	38.012484	1.054638
BNGB01317	VF–F sand	107.26	54.297956	1.25672
BNGB01320	VF–F sand	51.78	69.017531	0.185906
BNGB01323	VF–F sand	114.47	41.2177	0.958452
BNGB01326	VF–F sand	127.54	50.4775	0.977067
BNGB01330	VF–F sand	94.74	69.846775	0.430166
BNGB01337	VF–F sand	120.12	70.3881	0.730683
BNGB01341	Mud	90.08	44.146878	0.327061
BNGB01350	Mud	90.9	46.258084	0.292752
BNGB01356	VF–F sand	50.53	72.200306	0.123989
BNGB01702	VF–F sand	121.42	42.127791	1.359878
BNGB01705	VF–F sand	142.53	54.299069	1.259415
BNGB01709	Mud	139.95	51.620997	1.487887
BNGB01712	Mud	106.48	37.11305	1.05863
BNGB01714	M–C Sand	104.9	59.595019	0.799005
BNGB01717	Mud	116.51	42.158753	1.215
BNGB01718	Mud	126.96	47.005563	1.430865
BNGB01721	M–C Sand	112.42	44.090941	1.098347
BNGB01724	M–C Sand	29.35	53.690494	0.282283

Table B.1 – continued from previous page

Sample ID	Field Grain Size	Sr	SiO$_2$	CaO
BNGB01726	M–C Sand	35.4	43.821309	0.245817
BNGB01729	Mud	117.19	46.011922	1.560382
BNGB01732	Mud	123.81	45.704103	1.919637
BNGB01735	M–C Sand	75.87	52.165894	0.447042
BNGB017375	Mud	116.23	46.761775	0.797154
BNGB01738	M–C Sand	92.13	51.081913	0.489439
BNGB01743	M–C Sand	103.95	47.800594	0.669595
BNGB01750	M–C Sand	72.94	40.776872	0.356458
BNGB01758	M–C Sand	68.13	43.739359	0.447032
BNGB01763	M–C Sand	75.72	50.586559	0.465017
BNGB01770	M–C Sand	89.33	47.918619	0.709669
BNGB01778	M–C Sand	69.95	49.568878	0.308453
BNGB01782	M–C Sand	77.44	51.592719	0.330148
BNGB01785	M–C Sand	87.26	48.8574	0.735325
BNGB02103	Mud	124.84	51.082328	1.827065
BNGB02108	Mud	112.02	51.760644	1.023605
BNGB02112	Mud	120.98	54.3286	1.068311
BNGB02115	Mud	131.35	51.340625	1.329451
BNGB02117	Mud	127.41	52.259619	1.250859
BNGB02123	VF–F sand	129.18	58.31725	1.296294
BNGB02126	VF–F sand	156.79	54.173044	1.50084
BNGB02129	Mud	93.57	28.963397	1.139855
BNGB02132	VF–F sand	143.1	49.794022	0.961562
BNGB02135	Mud	124.05	47.623228	1.14302
BNGB02141	Mud	59.55	58.126288	0.31499

Sample ID	Field Grain Size	Sr	SiO$_2$	CaO
BNGB02144	Mud	86.84	53.096144	0.625838
BNGB02146	M–C Sand	53.18	62.580031	0.117683
BNGB02147	Mud	95.34	37.654275	1.64701
BNGB02155	VF–F sand	63.09	53.076656	0.194542
BNGB02163	VF–F sand	67.16	50.619813	0.402604
BNGB02169	VF–F sand	69.3	53.589981	0.282173
BNGB02502		86.17	38.992119	0.695998
BNGB02505	VF–F sand	150.43	52.85855	1.858225
BNGB02509	VF–F sand	140.21	66.092644	1.094665
BNGB02514	VF–F sand	152.98		
BNGB02518	VF–F sand	161.46	66.673356	1.330875
BNGB02524	Mud	120.46	47.251331	0.769114
BNGB02529	M–C Sand	116.08	44.671269	0.726263
BNGB02534	M–C Sand	108.46	58.921669	0.920892
BNGB02537	Mud	117.96	46.377919	0.722789
BNGB02538	Mud	65.9	46.47495	0.100927
BNGB02543	M–C Sand	63.94	65.720238	0.146543
BNGB02549	VF–F sand	85.25	63.823744	0.318191
BNGB02558	M–C Sand	67.88	64.935119	0.161974
BNGB02564	VF–F sand	77.17	70.991081	0.287674
BNGB02572	M–C Sand	63.79	67.970438	0.166007
BNGB02579	VF–F sand	85.5	69.663269	0.348544
BNGB02903	Mud	118.52	47.560263	1.105377
BNGB02908	Mud	115.95	41.70355	1.316822
BNGB02911	VF–F sand	146.9	54.739056	1.323614

Table B.1 – continued from previous page

Sample ID	Field Grain Size	Sr	SiO$_2$	CaO
BNGB02915	Mud	113.03	31.213947	1.187396
BNGB02917	VF–F sand	138.46	41.382316	1.453399
BNGB02922	Mud	95.23	32.434106	1.018079
BNGB02926	VF–F sand	138.76	53.143088	1.014051
BNGB02930	VF–F sand	152.89	49.581247	1.036815
BNGB02935	M–C Sand	105.38	47.850475	1.16947
BNGB02940	Mud	125.63	47.578444	2.287893
BNGB02943	M–C Sand	44.84	53.159038	0.27721
BNGB029435	Mud	61.35	49.580313	0.400191
BNGB02946	Mud	82.67	45.350763	1.94204
BNGB02952	M–C Sand	68.71	53.351231	0.50945
BNGB02961	M–C Sand	54.5	49.390538	0.301149
BNGB02972	M–C Sand	61.59	50.503394	0.305784
BNGB03502		147.05	40.758244	1.285772
BNGB03505	Mud	149.38	45.911166	1.804448
BNGB03506	VF–F sand	154.49	42.729638	1.782913
BNGB03511	M–C Sand	135.63	46.620384	0.84665
BNGB03517	M–C Sand	162.5	52.465975	1.515568
BNGB03521	M–C Sand	130.68	42.096172	1.128789
BNGB03526	M–C Sand	138	42.536403	1.141435
BNGB03529	M–C Sand	145.35	52.897588	1.336805
BNGB03534	M–C Sand	125.9	41.403781	1.218393
BNGB03537	M–C Sand	141.2	50.483031	1.117417
BNGB03541	M–C Sand	141.42	49.371613	1.173749
BNGB03543	Mud	118.34	47.561356	1.152738

Table B.1 – continued from previous page

Sample ID	Field Grain Size	Sr	SiO$_2$	CaO
BNGB03546	M–C Sand	89.23	48.260916	0.74948
BNGB03550	M–C Sand	110.47	43.972809	0.760083
BNGB03555	M–C Sand	128.02	48.232647	1.095203
BNGB03558	Mud	123.02	46.900034	1.202969
BNGB03564	M–C Sand	45.44	54.74095	0.179408
BNGB03572	M–C Sand	83.48	53.450606	0.088688
BNGB03576	M–C Sand	59.92	51.146316	0.359036
BNGB03578	Mud	69.74	47.278166	0.274227
BNGB03902	Mud	130.14	44.975663	1.176931
BNGB03903	VF–F sand	164.79	58.339969	1.384371
BNGB03908	M–C Sand	164.7	56.583219	1.0967
BNGB03912	M–C Sand	168.42	52.836581	1.114268
BNGB03917	M–C Sand	144.22	33.593384	0.99824
BNGB03921	M–C Sand	170.35	55.921431	1.495847
BNGB03926	M–C Sand	149.6	55.239544	0.914005
BNGB03929	M–C Sand	161.72	57.619263	1.047867
BNGB03934	Mud	134.54	46.099334	1.057743
BNGB03936	Mud	123.6	44.365888	0.83373
BNGB03937	M–C Sand	63.48	70.041738	0.170265
BNGB03941	Mud	119.99	42.099791	0.79794
BNGB03946	Mud	139.46	51.480228	1.571526
BNGB03953	Mud	128.85	46.454403	1.905732
BNGB03959	Mud	133.6	45.035447	0.960908
BNGB03964	M–C Sand	54.43	70.505106	0.095158
BNGB03967	Mud	93.9	55.298738	0.358345

Table B.1 – continued from previous page

Sample ID	Field Grain Size	Sr	SiO$_2$	CaO
BNGB04302	Mud	84.55	24.974094	0.849779
BNGB04303	VF–F sand	169.04	47.166747	1.316758
BNGB04308	M–C Sand	161.15	48.100291	1.080864
BNGB04314	M–C Sand	149.2	47.692306	1.029288
BNGB04317	M–C Sand	142.91	50.170319	1.243946
BNGB04320	M–C Sand	163.27	52.276703	1.178278
BNGB04323	M–C Sand	163.46	52.132103	1.838346
BNGB04327	M–C Sand	116.33	57.042863	0.716462
BNGB04330	M–C Sand	99.7		
BNGB04335	M–C Sand	88.5	52.395478	0.667208
BNGB04338	M–C Sand	60.03	53.640744	0.597017
BNGB04340	Mud	134.08	45.004684	2.198528
BNGB04344	M–C Sand	48.79	56.514838	0.310083
BNGB04349	VF–F sand	58.99	40.206431	0.311132
BNGB04352	VF–F sand	75.99	38.871088	0.455606
BNGB04358	M–C Sand	72.96	40.910141	0.322508
BNGB043635	Mud	75.74	39.045944	0.265843
BNGB04370	M–C Sand	71.23	50.264259	0.314268
BNGB04378	M–C Sand	77.03	46.250422	0.459876
BNGB04703	M–C Sand	167.73	60.146038	1.106904
BNGB04708	M–C Sand	148.14	36.494334	1.132746
BNGB04712	M–C Sand	160.72	39.502241	1.453664
BNGB04717	M–C Sand	169.82	60.384394	1.346251
BNGB04720	M–C Sand	145.09	39.2779	1.501494
BNGB04726	M–C Sand	164.44	62.415425	1.105285

Table B.1 – continued from previous page

Sample ID	Field Grain Size	Sr	SiO$_2$	CaO
BNGB04730	M–C Sand	141.23	65.19245	0.80469
BNGB04735	M–C Sand	146.32	62.942906	0.90454
BNGB04741	M–C Sand	148.32	63.970156	0.86916
BNGB04746	M–C Sand	72.66	61.024269	0.291985
BNGB04764	VF–F sand	70.12	66.503238	0.213378
BNGB04778	VF–F sand	58.25	68.250163	0.124124
BNGB04902	Mud	53.62	50.122478	0.544863
BNGB04905	Mud	123.61	38.726297	3.353587
BNGB04909	Mud	64.18	45.458972	1.056212
BNGB04912	M–C Sand	86.68	50.305125	0.287983
BNGB04914	Mud	91.14	38.740266	0.377727
BNGB04915	M–C Sand	75.38	55.734938	0.555988
BNGB05706	Mud	98		
BNGB05712	Mud	45.05	49.894906	0.078417
BNGB05715	M–C Sand	60.53	49.104334	0.244104
BNGB05717	M–C Sand	65.69	49.935159	0.285713
BNGB05720	M–C Sand	69.43	51.703188	0.106248
BNGB05723	M–C Sand	89.2	46.920509	0.538802
BNGB05726	M–C Sand	88.44	50.462069	0.485427
BNGB05729	M–C Sand	107.98	44.933709	0.594456
BNGB05735	M–C Sand	65.07	38.159722	0.603128
BNGB05743	Mud	53.82	41.094091	0.300975
BNGB05749	VF–F sand	72.37	42.1665	0.522787
BNGB05759	M–C Sand	106.81	45.195438	0.284399
BNGB05903	VF–F sand	156.63	48.021953	1.42906

Table B.1 – continued from previous page

Sample ID	Field Grain Size	Sr	SiO$_2$	CaO
BNGB05908	M–C Sand	133.07	37.343422	1.330292
BNGB05914	M–C Sand	148.5	49.367422	0.913179
BNGB05918	Mud	69.12	45.858016	0.439103
BNGB05920	Mud	155.39	52.993881	1.661736
BNGB05924	Mud	71.72	41.380013	0.614933
BNGB05926	VF–F sand	74.82	41.813603	0.570119
BNGB05932	VF–F sand	72.83	45.894041	0.589002
BNGB05937	M–C Sand	54.29	45.230594	0.392736
BNGB05946	M–C Sand	58.25	47.629238	0.300125
BNGB05949		63.78	45.029306	0.390715
BNGB05952	M–C Sand	64.47	45.300244	0.395029
BNGB05958	M–C Sand	70.8	47.582972	0.384186
BNGB05967	M–C Sand	39.98	46.566328	0.427134
BNGB05973	M–C Sand	45.73	49.262991	0.178521
BNGB06302	Mud	140.23	51.6427	1.364698
BNGB06306	M–C Sand	182	56.966688	1.358918
BNGB06312	M–C Sand	162.17	49.2795	0.86127
BNGB06317	M–C Sand	168.08	49.805347	1.645955
BNGB06321	M–C Sand	167.25	48.943388	1.428638
BNGB06326	M–C Sand	127.47	60.34175	0.526081
BNGB06329	M–C Sand	142.54	52.031559	1.050887
BNGB06332	Mud	113.35	47.106728	0.671191
BNGB06338	M–C Sand	78.43	65.126306	0.227588
BNGB06343	Mud	83.4	48.443369	0.231087
BNGB06349	Mud	76.04	56.9705	0.240155

Table B.1 – continued from previous page

Sample ID	Field Grain Size	Sr	SiO$_2$	CaO
BNGB06350	Mud	77.68	48.015556	0.20024
BNGB06355	M–C Sand	96.48	65.593575	0.426039
BNGB06361	M–C Sand	87.65	66.908569	0.296022
BNGB06365	Mud	79.03	47.883375	0.225102
BNGB06703	Mud	124.74	41.938913	1.16899
BNGB06706	VF–F sand	168.02	50.030347	1.409903
BNGB06709	VF–F sand	127.84	36.648569	1.06661
BNGB06712	VF–F sand	164.85	51.685141	1.445368
BNGB06717	Mud	106.75	52.618013	0.819344
BNGB06720	Mud	80	38.728881	0.76392
BNGB06724	Mud	96.92	48.746288	0.623581
BNGB06729	Mud	101.32	50.064041	1.5956
BNGB06732	VF–F sand	93.98	56.862288	0.894283
BNGB06737	M–C Sand	96.75	56.092513	0.530856
BNGB06740	Mud	114.06	40.341091	0.914814
BNGB06741	VF–F sand	107.62	45.350609	0.836861
BNGB06743	VF–F sand	104.88	44.002797	0.829225
BNGB06747	M–C Sand	105.99	47.326147	0.780621
BNGB06753	M–C Sand	94.79	43.017884	0.604848
BNGB06758	M–C Sand	96.44	43.997081	0.595932
BNGB06761	Mud	89.01	51.907381	0.540558
BNGB07103	M–C Sand	75.65	54.267175	0.332054
BNGB07106	Mud	42.17	47.335894	0.095699
BNGB07109	M–C Sand	71.11	45.587222	0.30082
BNGB07111	M–C Sand	78.25	39.433513	0.342429

Sample ID	Field Grain Size	Sr	SiO$_2$	CaO
BNGB07114	Mud	100.45	33.39435	4.096514
BNGB07118	Mud	93.18	45.210956	0.661667
BNGB07124	Mud	110.22	37.730206	3.153814
BNGB07129	Mud	127.62	43.479903	0.92637
BNGB07132	M–C Sand	120.48	45.067375	0.834893
BNGB07503	Mud	113.93	49.057191	1.775154
BNGB07512	Mud	72.06	46.250338	0.669642
BNGB07518	VF–F sand	103.26	50.1504	0.574574
BNGB07523	VF–F sand	97.04	49.471616	0.525342
BNGB07524	M–C Sand	78.57	50.447497	0.41047
BNGB07527	Mud	79.01	51.3926	0.432089
BNGB07530	Mud	97.61	48.096297	0.672118
BNGB07535	Mud	105.35	47.214309	0.756857
BNGB07538	M–C Sand	64.4	57.218456	0.293352
BNGB07546	VF–F sand	73.65	54.19265	0.318644
BNGB07550	M–C Sand	143.95	44.572831	0.863972
BNGB07555	Mud	51.33	50.694797	0.676267
BNGB07558	VF–F sand	71	54.392869	0.196957
BNGB07567	VF–F sand	88.64	49.539047	0.310409
BNGB07573	VF–F sand	94.9	48.869113	0.683127
BNGB07903	Mud	150.62	49.316238	1.230259
BNGB07906	M–C Sand	127.13	67.001956	0.734431
BNGB07909	Mud	122.6		
BNGB07914	Mud	99.47	47.491019	0.446575
BNGB07918	Mud	108.82	30.20435	3.440254

Table B.1 – continued from previous page

Sample ID	Field Grain Size	Sr	SiO$_2$	CaO
BNGB07923	Mud	66.34	53.499188	0.218312
BNGB07926	Mud	102.09	51.779603	0.692853
BNGB07930	VF–F sand	119.82	48.878197	0.691869
BNGB07934	VF–F sand	108.82	64.889819	0.533287
BNGB07937.5	Mud	63.04	39.771022	0.481237
BNGB07938	VF–F sand	99.1	68.340569	0.450693
BNGB07939	Mud	71.13	46.537072	0.48493
BNGB07941	VF–F sand	104.37	69.447913	0.590742
BNGB07943.5	Mud	88.11	46.300809	0.426957
BNGB07946	Mud	109.3	59.565688	0.547892
BNGB07949	Mud	102.34	52.579231	0.511818
BNGB07952	M–C Sand	117.53	67.692425	0.5861
BNGB07953	Mud	94.83	49.769069	0.44193
BNGB07956	M–C Sand	42.12	58.119756	0.090418
BNGB07959	M–C Sand	62.32	56.059575	0.228522
BNGB07961	M–C Sand	50.34	55.901069	0.250357
BNGB07966	M–C Sand	69.55	74.852844	0.160315
BNGB07972	VF–F sand	95.67	66.659075	0.293766
BNGB07975	VF–F sand	96.97	49.862347	0.356964
BNGB07982	VF–F sand	85.02	71.142744	0.302467
BNGB08205	Mud	104.37	50.593006	0.640885
BNGB08209	Mud	43.56	47.222141	0.078849
BNGB08214	VF–F sand	81.09	41.756616	0.453796
BNGB08218	M–C Sand	103.13	48.388778	0.518456
BNGB08224	M–C Sand	129.27	43.627056	0.980675

Table B.1 – continued from previous page

Sample ID	Field Grain Size	Sr	SiO$_2$	CaO
BNGB08229	M–C Sand	145.11	40.031213	1.429223
BNGB08235	M–C Sand	154.69	44.722503	0.654188
BNGB08238	Mud	133.83	46.292541	1.032411
BNGB08240	VF–F sand	155.35	42.963806	1.291812
BNGB08243	VF–F sand	128.24	44.955297	0.796443
BNGB08247	M–C Sand	76.5	54.343694	0.230877
BNGB08252	M–C Sand	90.31	51.227328	0.381599
BNGB08255	M–C Sand	106.95	50.114306	0.550386
BNGB082585	Mud	78.26	43.053681	1.145962
BNGB08506	Mud	37.96	20.940056	0.562918
BNGB08509	Mud	124.84	45.958713	0.56398
BNGB08515	VF–F sand	136.56	41.112556	0.854128
BNGB08521	M–C Sand	164.51	47.156675	1.373875
BNGB08530	M–C Sand	111.7	47.858531	0.682345
BNGB08541	M–C Sand	150.86	53.365788	0.794055
BNGB08546	M–C Sand	134.51	50.361859	0.886181
BNGB08550	VF–F sand	135.88	54.166888	0.774413
BNGB08552	VF–F sand	157.97	43.689716	1.457711
BNGB08553	VF–F sand	149.56	41.969819	0.91263
BNGB08556	M–C Sand	126.94	53.045144	0.707273
BNGB08561	M–C Sand	125.34	50.776897	1.15821
BNGB08566	M–C Sand	105.78	54.457338	0.515057
BNGB08570	M–C Sand	107.37	53.616963	0.753699
BNGB08578	M–C Sand	108.68	52.874438	0.818147
BNGB09003	Mud	107.07	45.233888	0.776758

Table B.1 – continued from previous page

Sample ID	Field Grain Size	Sr	SiO$_2$	CaO
BNGB09008	Mud	105.97	51.107128	0.808055
BNGB09014	Mud	103.34		
BNGB09020	Mud	96.32		
BNGB09032	Mud	86.46	50.776134	0.857815
BNGB09035	M–C Sand	109.38	45.311294	0.583442
BNGB09037	M–C Sand	132.09	48.993978	0.812288
BNGB09038	M–C Sand	144.03	49.249984	0.777273
BNGB09406	Mud	46.39	51.234322	0.130842
BNGB09409	Mud	91.95	49.664063	0.455018
BNGB09414	Mud	79.48	50.384969	0.346311
BNGB09420	Mud	97.69	52.243963	0.481248
BNGB09429	Mud	78.59	46.2112	0.388739
BNGB09434	Mud	39.19	48.863478	0.047735
BNGB09438	VF–F sand	57.81		
BNGB09441	VF–F sand	54.49	50.090919	0.111429
BNGB09444	M–C Sand	81.13	67.764681	0.232634
BNGB09446	VF–F sand	77.34	48.908931	0.304934
BNGB09449	VF–F sand	80.36	46.089884	0.322281
BNGB09453	VF–F sand	102.83	66.360956	0.372164
BNGB09458	VF–F sand	103.59	46.354075	0.535362
BNGB09464	VF–F sand	95.14	67.102806	0.28604
BNGB09803	Mud	43.51	40.6439	0.325266
BNGB09806	Mud	49.73	42.887444	0.097348
BNGB09809	Mud	90.22	49.756644	0.530911
BNGB09814	Mud	105.9	41.071584	0.844353

Sample ID	Field Grain Size	Sr	SiO$_2$	CaO
BNGB09818	Mud	91.43	38.146647	0.558578
BNGB09821	Mud	99.62	43.09805	1.866548
BNGB09826	Mud	70.75	38.789019	1.231474
BNGC00103	Mud	86.02	51.944069	0.172748
BNGC00105	VF–F sand	66.19	70.732744	0.142484
BNGC00108.5	Mud	81.08	45.945663	0.090198
BNGC00116A	Mud	79.27	67.767031	0.202816
BNGC00117	Mud	79.31	49.880491	0.101092
BNGC00123	M–C Sand	29.03	74.934744	0
BNGC00126	Mud	63.25	52.965256	0.14904
BNGC00127	VF–F sand	56.75	59.918325	0.094555
BNGC00133	Mud	51.37	54.617269	0.109515
BNGC00146	VF–F sand	55.3	59.3607	0.090928
BNGC00503	Mud	80.64	49.892216	0.663265
BNGC00511	Mud	106.2	51.230666	0.715449
BNGC00518	Mud	89.88	52.473063	0.262068
BNGC00524	M–C Sand	23.05	56.119325	0
BNGC00532	M–C Sand	70.39	54.653431	0.336933
BNGC00534	M–C Sand	67.14	45.653291	0.38016
BNGC00540	VF–F sand	92.56	43.409194	0.510389
BNGC00543	VF–F sand	91.67	45.787947	0.487633
BNGC00544	VF–F sand	114.72	44.729997	0.914142
BNGC00546	M–C Sand	107.39	40.840822	0.540358
BNGC00550	VF–F sand	111.76	44.207869	0.828654
BNGC005525	M–C Sand	42.46	37.427716	0.106515

Table B.1 – continued from previous page

Sample ID	Field Grain Size	Sr	SiO$_2$	CaO
BNGC00555	Mud	108.79	24.217608	1.531679
BNGC00903	Mud	87.6	52.262188	0.294303
BNGC00909	Mud	85.69	47.417397	0.133304
BNGC00911	Mud	89.33	48.049003	0.242769
BNGC00914	Mud	95.11	51.795225	0.34631
BNGC00917	VF–F sand	70.16	67.838844	0.168308
BNGC00920	M–C Sand	55.24	72.749344	0.07223
BNGC00924	VF–F sand	54.25	56.745225	0.14354
BNGC00926	VF–F sand	48.04	53.281719	0.061482
BNGC00934	VF–F sand	75.19	52.228028	0.232106
BNGC00940	VF–F sand	86.35	65.423944	0.303742
BNGC00943	VF–F sand	86.3	64.848844	0.366828
BNGC00947	VF–F sand	69.59	64.394081	0.185008
BNGC00953	Mud	83.9	51.751822	0.266637
BNGC00956	VF–F sand	125.86	65.718481	0.54544
BNGC01311	Mud	60.38	38.276038	0.065094
BNGC01314	VF–F sand	106.63	44.796178	0.609642
BNGC01318	VF–F sand	133.99	49.174503	0.69495
BNGC01323	M–C Sand	121.76	43.786888	0.614692
BNGC01330	VF–F sand	149.02	44.463828	0.860221
BNGC01335	M–C Sand	146.87	40.776478	0.802699
BNGC01340	VF–F sand	148.88	46.691994	1.002122
BNGC01341	M–C Sand	147.55	40.906913	1.090094
BNGC01344	M–C Sand	148.6	46.918144	1.148801
BNGC01347	VF–F sand	152.04	41.991853	1.184497

Table B.1 – continued from previous page

Sample ID	Field Grain Size	Sr	SiO$_2$	CaO
BNGC01350	VF–F sand	169.14	46.1529	1.070084
BNGC01359	M–C Sand	151.17	53.347144	1.048176
BNGC01364	Mud	69.22	39.262525	1.69992
BNGC01375	M–C Sand	133.91	45.281413	0.818443
BNGC01703	VF–F sand	68.63	49.204956	0.295593
BNGC01711	Mud	114.49	50.037316	1.140708
BNGC01714	M–C Sand	68.15	54.535594	0.492908
BNGC01720	M–C Sand	69.41	45.200194	0.379333
BNGC01721	M–C Sand	82.04	42.104213	0.38999
BNGC01726	VF–F sand	109.22	42.9191	0.848124
BNGC01732	M–C Sand	91.85	41.413441	0.60723
BNGC01738	VF–F sand	95.08	40.505663	0.752647
BNGC01745	Mud	87.03	47.239756	0.498567
BNGC01747	VF–F sand	84.97	45.316941	0.399075
BNGC01755	VF–F sand	99.3	44.546016	0.443634
BNGC01758	VF–F sand	99.68	40.608722	0.776126
BNGC01767	VF–F sand	116.72	37.693934	0.918767
BNGC02102	Mud	104.81	41.738284	0.999433
BNGC02106	Mud	127.47	52.723594	1.19442
BNGC02111	VF–F sand	146.5	41.243647	0.808992
BNGC02114	VF–F sand	126.64	47.283716	1.160821
BNGC02118	VF–F sand	135.13	55.373875	1.261319
BNGC02121	M–C Sand	74.7	49.016406	0.965958
BNGC02126	M–C Sand	62.24	74.449813	0.236658
BNGC02134	Mud	124.95	47.362053	1.1429

Table B.1 – continued from previous page

Sample ID	Field Grain Size	Sr	SiO$_2$	CaO
BNGC02143	M–C Sand	53.14	65.343656	0.230102
BNGC02146	VF–F sand	124.51	51.803931	1.086035
BNGC02147	M–C Sand	31.24	75.394569	
BNGC02155	VF–F sand	61.73	40.965419	0.309421
BNGC02162	Mud	72.3	49.089575	0.212025
BNGC02167	VF–F sand	70.71	65.998	0.291366
BNGC02173	VF–F sand	73.61	68.397844	0.480256
BNGC02191	VF–F sand	77.85	66.903563	0.337175
BNGC02503	Mud	106.45	40.502613	0.725611
BNGC02506	VF–F sand	139.41	44.690947	1.100234
BNGC02509	VF–F sand	123.71	47.944625	1.045141
BNGC02514	VF–F sand	158.14	52.140581	1.755969
BNGC02518	VF–F sand	118.28	50.576884	0.639115
BNGC025205	VF–F sand	66.26	47.694431	0.435737
BNGC025235	Mud	128.73	42.287625	1.60801
BNGC02527	M–C Sand	55.67	53.6882	0.216284
BNGC02534	M–C Sand	119.12	39.691756	0.988854
BNGC02538	Mud	138.9	49.874784	1.369254
BNGC02544	Mud	65.14	53.640469	0.458871
BNGC02549	VF–F sand	70.19	53.986931	0.334107
BNGC025525	Mud	81.71	54.606131	0.368501
BNGC02561	VF–F sand	67.41	54.364381	0.27745
BNGC02564	M–C Sand	72.8	56.655475	0.307115
BNGC02568	Mud	77.3		
BNGC02570	M–C Sand	61.68	53.490963	0.256354

Sample ID	Field Grain Size	Sr	SiO$_2$	CaO
BNGC02903	Mud	124.68	54.423706	1.12105
BNGC02905	VF–F sand	135.92	47.927172	1.205693
BNGC02908	VF–F sand	124.97	41.836266	1.210182
BNGC02909	VF–F sand	133	48.806247	1.174352
BNGC02914	VF–F sand	120.9	45.51075	1.304758
BNGC02915	VF–F sand	139.4	40.473806	1.693268
BNGC02916	Mud	132.41	44.974081	1.233231
BNGC02917	VF–F sand	125.8	41.008178	1.343412
BNGC02918	VF–F sand	110.72	51.035581	1.023044
BNGC02921	VF–F sand	104.27	67.1651	0.750004
BNGC02923	Mud	119.91	51.728191	1.17134
BNGC02926	VF–F sand	82.6	56.598144	0.519127
BNGC02929	VF–F sand	108	42.951244	0.98943
BNGC02932	Mud	117.92	46.976475	0.931144
BNGC02935	VF–F sand	131.01	47.743988	1.115894
BNGC02937	Mud	127.89	51.366956	1.307113
BNGC029375	Mud	123.58	48.739359	1.081812
BNGC02938	VF–F sand	77.59	56.826588	0.56017
BNGC02941	Mud	120.51	45.880094	1.973568
BNGC02946	Mud	116.49	46.949359	1.001759
BNGC02947	M–C Sand	69.59	68.489138	0.377943
BNGC02948	M–C Sand	92.05	53.560881	0.44771
BNGC02952	VF–F sand	124.41	66.266381	0.876995
BNGC02953	VF–F sand	100.99	51.496456	0.857889
BNGC02955	VF–F sand	115.3	51.733859	0.677347

Table B.1 – continued from previous page

Sample ID	Field Grain Size	Sr	SiO$_2$	CaO
BNGC02958	Mud	98.27	39.546256	1.789938
BNGC02961	M–C Sand	59.93	53.794294	0.220841
BNGC02962	Mud	86.14	45.877288	0.278125
BNGC02963	M–C Sand	61.55	71.767838	0.247716
BNGC02965	M–C Sand	39.83	52.254644	0.237013
BNGC02967	M–C Sand	65.9	60.086438	0.41669
BNGC03303	VF–F sand	140.04	50.273581	1.217093
BNGC03308	VF–F sand	134.43	54.361069	1.227416
BNGC03314	VF–F sand	136.03	49.118028	1.116588
BNGC03318	VF–F sand	115.7	56.405844	0.641465
BNGC03323	Mud	124.35	46.683378	1.200449
BNGC03334	Mud	124.14	45.172031	1.085196
BNGC03337	Mud	110.17	50.594756	0.850435
BNGC03346	Mud	126.75	46.564213	2.328741
BNGC03349	M–C Sand	87.65	51.858938	0.633652
BNGC03350	M–C Sand	68.06	50.368931	0.603496
BNGC03353	VF–F sand	92.53	48.181963	0.872873
BNGC03356	M–C Sand	96.67	43.374916	0.853823
BNGC03363	M–C Sand	52.53	43.243284	0.482828
BNGC03364	M–C Sand	69.42	45.559772	0.514427
BNGC03369	VF–F sand	76.86	45.608438	0.456485
BNGC03372	M–C Sand	87.19	46.305138	0.767534
BNGC03378	VF–F sand	96.94	44.682606	0.857235
BNGC03382	VF–F sand	86.53	53.718731	0.503691
BNGC03702		132.76	55.188806	1.319643

Table B.1 – continued from previous page

Sample ID	Field Grain Size	Sr	SiO$_2$	CaO
BNGC03705	Mud	115.49	48.29825	0.997565
BNGC03708	VF–F sand	135.23	40.863031	0.987016
BNGC03711	VF–F sand	145.11	47.981981	1.20408
BNGC03712	Mud	126.74	46.036831	1.438845
BNGC03715	VF–F sand	143.95	59.032731	1.233449
BNGC03720	Mud	130.97	46.620697	0.960713
BNGC03724	VF–F sand	142.19	62.279206	1.100023
BNGC03727	Mud	117.26	32.010769	0.951741
BNGC03730	M–C Sand	116.77	69.599131	1.37642
BNGC03734	VF–F sand	99.72	55.981519	0.565656
BNGC03741	Mud	116.75	47.623119	0.988201
BNGC03747	Mud	114.99	46.747994	0.963393
BNGC03749	M–C Sand	111.13	48.9384	0.946994
BNGC03751	M–C Sand	82.69	72.348819	0.461491
BNGC03756	M–C Sand	65.54	77.100031	0.275664
BNGC037585	VF–F sand	80.87	50.956316	0.490287
BNGC03759	Mud	88.4	54.412269	0.404408
BNGC03762	VF–F sand	83.67	50.98745	0.728581
BNGC03769	Mud	93.83	50.634472	0.532881
BNGC04102	Mud	103.75	40.685556	0.953508
BNGC04105	Mud	123.5	48.070556	1.764846
BNGC04109	VF–F sand	135.09	48.844366	0.939104
BNGC04115	VF–F sand	138.59	52.014378	1.160931
BNGC04118	Mud	108.95	47.061578	0.855909
BNGC04123	VF–F sand	143.29	48.850778	1.233382

Sample ID	Field Grain Size	Sr	SiO$_2$	CaO
BNGC04126	VF–F sand	143.18	46.985559	1.391827
BNGC04127	Mud	132.36	51.577675	1.264976
BNGC04137	Mud	102.25	43.195188	0.586839
BNGC04143	VF–F sand	127.47	42.93605	1.206708
BNGC04146	VF–F sand	136.55	46.7001	1.226345
BNGC04146.5		110.2	36.558188	1.123321
BNGC04147	Mud	86.85	31.336684	0.909456
BNGC04149	Mud	80.25	48.882322	0.366023
BNGC04150	M–C Sand	82.71	46.873103	0.80515
BNGC04152	M–C Sand	105.19	46.006528	1.134753
BNGC04153	Mud	63.05	36.525281	0.271378
BNGC04154	M–C Sand	64.74	54.619938	0.353467
BNGC04163	Mud	84.7	42.655819	0.71137
BNGC04166	VF–F sand	68.33	53.878119	0.318594
BNGC04170	M–C Sand	69.93	47.872359	0.662495
BNGC04502	Mud	124.19	44.07625	1.184626
BNGC04505	Mud	120.19	42.175534	1.22196
BNGC04511	VF–F sand	138.9	55.0654	1.153434
BNGC04517	VF–F sand	148.56	48.631666	1.262006
BNGC04521	VF–F sand	159.26	47.383644	1.26655
BNGC04524	Mud	141.92	40.637441	1.31286
BNGC04526	VF–F sand	147.45	49.174191	1.365072
BNGC04527	Mud	152.14	44.195947	1.788371
BNGC04530	VF–F sand	123.05	41.4275	0.963457
BNGC04534	M–C Sand	94.54	55.867044	0.363329

Table B.1 – continued from previous page

Sample ID	Field Grain Size	Sr	SiO$_2$	CaO
BNGC04535	Mud	109.84	46.397216	0.959665
BNGC04537	VF–F sand	155.51	48.822622	1.249678
BNGC04538	Mud	109.73	48.018903	0.822831
BNGC04541	M–C Sand	64.06	54.928969	0.339803
BNGC04543	M–C Sand	85.68	47.052256	0.491633
BNGC04546	Mud	109.38	44.371863	1.600051

Appendix C

Geochronological Data for Borehole Samples

Table C.1: Geochronological data for BanglaPIRE samples. Sample IDs correspond to those used in App. A and B. Ages were measured at the National Ocean Sciences Accelerator Mass Spectrometry Facility (NOSAMS) at the Woods Hole Oceanographic Institution. All ages were calibrated using CALIB 6.0 software (Stuiver and Reimer, 1993) with the intcal90.^{14}C curve.

Sample ID	Material	Lab ID	^{14}C age BP	Error	cal yr BP	2θ lower	2θ upper
BNGB00517	Organic	OS-99280	7710.0	90	8492	8415	8582
BNGB00925	Organic	OS-99281	6890.0	80	7722	7656	7830
BNGB01330	Organic	OS-99282	4400.0	60	4962	4866	5047
BNGB04905	Organic	OS-99314	5390.0	60	6217	6026	6045
BNGB04914	Organic	OS-99391	8370.0	110	9392	9255	9519
BNGB07914	Organic	OS-99390	6020.0	80	6863	6747	6959
BNGB08205	Organic	OS-99317	6050.0	100	6903	6748	6769
BNGC00108	Organic	OS-99319	3070.0	50	3298	3218	3231
BNGC00116	Organic	OS-99320	7060.0	90	7892	7794	7966
BNGC00910	Organic	OS-99323	3340.0	60	3577	3477	3640
BNGC00920	Organic	OS-99324	7190.0	80	7999	7938	8060
BNGC01305.5	Organic	OS-99394	5110.0	60	5817	5750	5829
BNGC02143	Organic	OS-99395	7040.0	100	7877	7757	7965
BNGC02532	Organic	OS-99396	5410.0	70	6233	6031	6037
BNGC02541	Organic	OS-99397	43500.0	9400	45902	39359	50000
BNGC03769	Organic	OS-99456	40100.0	7600	43924	37789	50000
BNGC04956	Organic	OS-99452	9570.0	130	10929	10708	11156
BNGC04961	Organic	OS-99453	10000.0	140	11494	11245	11767
BNGC06111	Organic	OS-99454	5550.0	70	6346	6292	6402
BNGC06521	Organic	OS-99457	5000.0	70	5728	5645	5770
BNGC08121	Organic	OS-99458	6420.0	110	7351	7258	7429
BNGD00109	Organic	OS-103163	5620.0	70	6397	6311	6472

Table C.1 – continued from previous page

Sample ID	Material	Lab ID	^{14}C age BP	Error	cal yr BP	2θ lower	2θ upper
BNGD00321	Organic	OS-102897	6480.0	70	7381	7316	7442
BNGD00327	Organic	OS-102898	6260.0	60	7208	7029	7041
BNGD00510	Organic	OS-102899	5510.0	60	6304	6221	6231
BNGD02509	Organic	OS-106697	4110.0	50	4626	4526	4654
BNGD03729.5	Organic	OS-106698	1560.0	40	1471	1403	1524
BNGD03732	Organic	OS-110748	1900.0	35	1847	1734	1902
BNGD05726.5	Organic	OS-106699	1530.0	50	1415	1353	1424
BNGD06706	Organic	OS-106700	4540.0	50	5154	5054	5188
BNGD06737	Organic	OS-106701	8850.0	70	9982	9769	9975
BNGD07706	Organic	OS-106702	3100.0	50	3304	3243	3376
BNGD08209	Organic	OS-106703	4430.0	50	5012	4877	4942
BNGD08243.5	Organic	OS-106704	8840.0	80	9926	9710	9715
BNGD08508	Organic	OS-106705	2820.0	50	2920	2859	2980
BNGD08809	Organic	OS-102900	3870.0	50	4312	4183	4197
BNGD08844	Organic	OS-102901	8660.0	110	9620	9528	9776
BNGD08847	Organic	OS-102902	8970.0	80	10161	9923	10065
BNGD09109	Organic	OS-106706	3000.0	60	3186	3075	3252
BNGD09409	Organic	OS-102903	4030.0	60	4485	4422	4572
BNGD09421	Organic	OS-102904	47800.0	1500	47800		
BNGD09435	Organic	OS-102905	8160.0	70	9092	9011	9144
BNGD09809	Organic	OS-103600	3740.0	60	4097	3984	4157
BNGD09812	Organic	OS-102906	4560.0	50	5183	5059	5113
BNGD09820	Organic	OS-102907	7340.0	60	8131	8032	8201
BNGD10015	Organic	OS-103254	4510.0	60	5162	5047	5200
BNGD10020	Organic	OS-102910	6030.0	60	6875	6789	6952
BNGD10024	Organic	OS-102911	7300.0	70	8104	8025	8177
BNGD10211	Organic	OS-106730	4130.0	60	4674	4532	4558
BNGE13114	Organic	OS-106733	6200.0	80	7093	6994	7184
BNGE13209	Organic	OS-106708	4000.0	50	4479	4420	4455
BNGE13606	Organic	OS-106710	3610.0	60	3919	3838	3984
BNGF16020	Organic	OS-124748	6060.0	30	6916	6799	6817

Table C.1 – continued from previous page

Sample ID	Material	Lab ID	^{14}C age BP	Error	cal yr BP	2θ lower	2θ upper
BNGF16532	Organic	OS-114306	5110.0	25	5815	5753	5826
BNGF16552	Organic	OS-124757	9580.0	50	10935	10734	11133
BNGF18727	Organic	OS-114307	7990.0	35	8872	8719	9002
BNGF19240	Organic	OS-124744	8730.0	35	9687	9556	9821
BNGF19249	Organic	OS-124750	9630.0	35	10947	10787	10973
BNGH701011	Organic	OS-110728	40000.0	2	43577	43270	43934
BNGP00034	Organic	OS-102912	7470.0	60	8295	8199	8270
BNGP00043	Organic	OS-102913	8450.0	80	9481	9422	9532
BNGP00312	Organic	OS-102914	150.0	50	173	-3	37
BNGP00327	Organic	OS-102915	3660.0	50	3983	3901	4013
BNGP00366	Organic	OS-102916	8200.0	70	9158	9030	9270
BNGP00440	Organic	OS-102917	3960.0	60	4431	4296	4331
BNGP00456	Organic	OS-102918	9250.0	80	10425	10275	10523
BNGP00485	Organic	OS-102919	9470.0	80	10713	10581	10793
BNGP00863	Organic	OS-102920	8500.0	70	9507	9470	9537
BNGP00888	Mollusc	OS-102990	9670.0	80	11110	10796	10850
BNGP00906	Organic	OS-102921	240.0	50	290	-1	10
BNGP00914	Organic	OS-102975	4270.0	60	4845	4728	4750
BNGP00925	Organic	OS-102976	7230.0	70	8039	7970	8074
BNGP00944	Organic	OS-102977	7760.0	70	8542	8448	8598
BNGP01230	Organic	OS-102978	7660.0	70	8446	8395	8523
BNGP01267	Organic	OS-102979	8400.0	90	9437	9303	9365
BNGP01315	Organic	OS-102980	2780.0	80	2878	2778	2966
BNGP01330	Organic	OS-102981	7590.0	70	8396	8346	8432
BNGP01352	Organic	OS-102982	8180.0	80	9121	9020	9261
BNGP01711	Organic	OS-102983	4340.0	60	4907	4845	4972
BNGP01732	Organic	OS-102984	7760.0	80	8538	8433	8600
BNGP01755	Organic	OS-102985	7950.0	80	8823	8646	8983
BNGP01761	Organic	OS-102986	44000.0	1020	47030	45860	48623
BNGP02323	Organic	OS-102987	7170.0	70	7985	7935	8037
BNGP02337	Organic	OS-102988	7860.0	110	8670	8541	8797

Table C.1 – continued from previous page

Sample ID	Material	Lab ID	^{14}C age BP	Error	cal yr BP	2θ lower	2θ upper
BNGP02355	Mollusc	OS-102989	3340.0	60	3577	3477	3640
BNGP02720	Organic	OS-103248	6000.0	70	6840	6747	6934
BNGP02726	Organic	OS-103249	7360.0	70	8177	8040	8219
BNGS00108	Organic	OS-124754	6640.0	30	7528	7468	7576
BNGS01211	Organic	OS-124753	7100.0	35	7937	7851	7908
BNGS01615	Organic	OS-124745	7410.0	30	8255	8178	8323
BNGS02120	Organic	OS-124743	6520.0	25	7437	7339	7350
BNGS02411	Organic	OS-124752	5950.0	25	6773	6679	6682
BNGSH209526.5	Organic	OS-124742	2520.0	20	2593	2498	2595
BNGSH308535	Organic	OS-124756	980.0	20	912	799	815
BNGSH308546.5	Organic	OS-124751	9030.0	35	10212	10177	10242
BNGSH407834	Organic	OS-124749	2360.0	20	2356	2340	2433
BNGSH410020	Organic	OS-124746	48000.0	0	48000		
BNGSH504118	Organic	OS-124758	6500.0	25	7426	7329	7396
BNGSH505118	Organic	OS-124741	3790.0	25	4174	4090	4133
BNGSH506134	Organic	OS-124747	5630.0	35	6410	6317	6481
BNGSH507117.5	Organic	OS-124755	7990.0	35	8872	8719	9002
BNGSH702017	Organic	OS-110729	4240.0	30	4831	4654	4668
BNGSH702521	Organic	OS-110730	5450.0	30	6247	6204	6300
BNGSH703034	Organic	OS-110731	5020.0	30	5771	5659	5771
BNGSH703037	Organic	OS-110732	5770.0	35	6573	6487	6659
BNGSH703556	Organic	OS-110733	9450.0	55	10691	10522	10533
BNGSH705752	Organic	OS-110734	10050.0	70	11576	11273	11830
BNGSH708064	Organic	OS-110735	10150.0	60	11811	11408	11440
BNGSH708508	Organic	OS-110736	605.0	25	604	546	573
BNGSH708518	Organic	OS-110737	490.0	20	522	507	537
BNGSH708525	Organic	OS-110738	4640.0	30	5410	5308	5334
BNGSH708553	Organic	OS-110739	9470.0	55	10723	10572	10834
BNGSH709514E	Organic	OS-110740	3730.0	25	4081	3986	4051
BNGSH710025	Organic	OS-110741	5350.0	35	6133	6002	6086
BNGSH710558	Organic	OS-110742	9910.0	60	11327	11212	11500

Table C.1 – continued from previous page

Sample ID	Material	Lab ID	^{14}C age BP	Error	cal yr BP	2θ lower	2θ upper
BNGSH712020	Organic	OS-110743	3860.0	25	4288	4160	4170
BNGSH712306E	Organic	OS-110744	5010.0	35	5743	5654	5772
BNGSH712606	Organic	OS-110745	4530.0	30	5156	5053	5190
BNGSH713217	Organic	OS-110746	3740.0	35	4096	3982	4160
CHUA29	Organic	OS-103250	4890.0	70	5625	5585	5664
JESS46	Organic	OS-103251	6110.0	80	6989	6890	7157
JESS76	Organic	OS-103252	26900.0	240	31259	31084	31438
KUST24 47	Organic	OS-103164	7270.0	80	8094	8007	8173
NARA20	Organic	OS-103253	3980.0	70	4467	4299	4327
NARA29 49	Organic	OS-103165	6470.0	80	7375	7291	7440
BNGF00715	Organic	OS-121363	5770.0	25	6575	6495	6641
BNGF00723	Organic	OS-121364	5740.0	25	6534	6468	6633
BNGF01338	Organic	OS-121365	6170.0	25	7078	6995	7163
BNGF04935	Organic	OS-121397	8540.0	30	9526	9490	9545
BNGF06117	Organic	OS-121398	4450.0	20	5060	4971	5070
BNGF07559	Organic	OS-121399	37900.0	390	42166	41615	42702
BNGF11323	Organic	OS-121497	4270.0	25	4845	4828	4863
BNGG00715	Organic	OS-121287	7170.0	25	7985	7950	8019
BNGG00769	Organic	OS-121209	9230.0	35	10393	10269	10505
BNGG01344	Organic	OS-121337	7870.0	25	8640	8592	8728
BNGG03940	Organic	OS-121338	6210.0	20	7092	7011	7128
BNGG04521	Organic	OS-121339	4760.0	20	5526	5469	5584
BNGG04556	Organic	OS-121340	33800.0	270	38249	37285	38867
BNGG06035	Organic	OS-121341	8160.0	25	9083	9014	9137
BNGG06515	Organic	OS-121342	6800.0	25	7640	7594	7676
BNGG10014	Organic	OS-121343	370.0	15	454	330	359
BNGG10024	Organic	OS-121344	525.0	20	535	514	553
BNGG10040	Organic	OS-121345	5310.0	25	6085	5999	6181
BNGG10064	Organic	OS-121346	7940.0	35	8791	8641	8815
BNGG11050	Organic	OS-121347	3680.0	25	4029	3926	3951
BNGG12038	Organic	OS-123351	8090.0	40	9022	8785	8831

Table C.1 – continued from previous page

Sample ID	Material	Lab ID	^{14}C age BP	Error	cal yr BP	2θ lower	2θ upper
BNGG12050	Organic	OS-123352	8970.0	35	10169	9930	9994
BNGG12088	Organic	OS-123353	10050.0	35	11558	11361	11372
BNGG13040	Organic	OS-123354	3260.0	20	3482	3446	3561
BNGG14020	Organic	OS-123355	7170.0	30	7985	7943	8024
BNGG14059	Organic	OS-123356	9030.0	40	10211	10163	10248
BNGG15729	Organic	OS-123357	6950.0	30	7776	7690	7848
BNGG15750	Organic	OS-123358	7910.0	30	8714	8602	8791
BNGG15769	Organic	OS-123359	8860.0	30	10016	9786	9848
BNGG16934	Organic	OS-123360	7750.0	30	8530	8451	8592
BNGG16963	Organic	OS-123309	9610.0	40	10938	10774	11040
BNGG18791	Organic	OS-123310	10700.0	50	12662	12572	12721
BNGG19332	Organic	OS-123361	8010.0	30	8850	8774	9006
BNGG19376	Organic	OS-123362	9230.0	35	10393	10269	10505
BNGG22738	Organic	OS-123402	8840.0	95	9916	9610	10192
BNGSH707352	Organic	OS-111020	9650.0	210	10982	10304	10313
BNGSH800518	Organic	OS-121348	3110.0	20	3337	3251	3303
BNGSH800544	Organic	OS-121349	8920.0	30	10040	9917	10090
BNGSH801726	Organic	OS-121350	5800.0	20	6607	6537	6666
BNGSH802146	Organic	OS-121739	9960.0	45	11382	11248	11508
BNGSH802417	Organic	OS-121351	5790.0	20	6596	6506	6516
BNGSH803930	Organic	OS-121288	3150.0	20	3377	3275	3282
BNGSH803956	Organic	OS-121359	9990	30	11446	11285	11512
BNGSH805938	Organic	OS-121360	8940	30	10054	9919	10070
BNGT100141	Organic	OS-121401	710	20	670	654	685
BNGT116217	Organic	OS-121402	500	20	526	510	540
BNGT209217	Organic	OS-121403	3070	20	3291	3224	3356
BNGT209826	Organic	OS-121404	1750	20	1659	1604	1714
BNGT211440	Organic	OS-121405	3960	25	4431	4298	4327
BNGT301315	Organic	OS-121406	4130	20	4674	4550	4553

Appendix D

Qualitative GRADISTAT statistics for Transect A

Table D.1: Qualitative grain size statistics generated for BanglaPIRE samples using GRADISTAT software (Blott and Pye, 2001) and laser particle size analysis results (App. A.)

Sample ID	Mode and sorting	Sedimentology	Mean grain size class	Skewness	Kurtosis
BNGA00202	Unimodal, Poorly Sorted	Very Fine Sandy Coarse Silt	Coarse Silt	Symmetrical	Mesokurtic
BNGA00205	Bimodal, Very Poorly Sorted	Fine Sandy Coarse Silt	Coarse Silt	Symmetrical	Platykurtic
BNGA00502	Bimodal, Very Poorly Sorted	Medium Sandy Coarse Silt	Very Coarse Silt	Coarse Skewed	Platykurtic
BNGA00503	Bimodal, Very Poorly Sorted	Medium Sandy Coarse Silt	Very Coarse Silt	Coarse Skewed	Platykurtic
BNGA00505	Bimodal, Very Poorly Sorted	Very Coarse Silty Medium Sand	Fine Sand	Very Fine Skewed	Leptokurtic
BNGA00506	Bimodal, Very Poorly Sorted	Very Coarse Silty Medium Sand	Fine Sand	Very Fine Skewed	Leptokurtic
BNGA00517	Unimodal, Poorly Sorted	Coarse Silt	Coarse Silt	Fine Skewed	Mesokurtic
BNGA00540	Bimodal, Very Poorly Sorted	Medium Sandy Medium Silt	Coarse Silt	Very Coarse Skewed	Leptokurtic
BNGA00546	Unimodal, Poorly Sorted	Medium Silty Fine Sand	Fine Sand	Fine Skewed	Very Leptokurtic
BNGA00802	Unimodal, Poorly Sorted	Very Fine Sandy Coarse Silt	Coarse Silt	Symmetrical	Mesokurtic
BNGA00803	Unimodal, Very Poorly Sorted	Very Fine Sandy Medium Silt	Coarse Silt	Coarse Skewed	Platykurtic
BNGA00805	Unimodal, Poorly Sorted	Medium Silt	Medium Silt	Coarse Skewed	Mesokurtic
BNGA00806	Unimodal, Poorly Sorted	Very Fine Sandy Coarse Silt	Coarse Silt	Fine Skewed	Mesokurtic

213

Table D.1 – continued from previous page

Sample ID	Mode and sorting	Sedimentology	Mean grain size class	Skewness	Kurtosis
BNGA00808	Unimodal, Poorly Sorted	Very Fine Sandy Coarse Silt	Coarse Silt	Symmetrical	Mesokurtic
BNGA00809	Unimodal, Poorly Sorted	Coarse Silt	Medium Silt	Symmetrical	Mesokurtic
BNGA00811	Unimodal, Poorly Sorted	Very Fine Sandy Coarse Silt	Coarse Silt	Symmetrical	Mesokurtic
BNGA01102	Unimodal, Poorly Sorted	Very Fine Sandy Coarse Silt	Coarse Silt	Symmetrical	Mesokurtic
BNGA01105	Unimodal, Poorly Sorted	Medium Silt	Medium Silt	Symmetrical	Mesokurtic
BNGA01108	Unimodal, Poorly Sorted	Very Fine Sandy Very Coarse Silt	Very Coarse Silt	Fine Skewed	Mesokurtic
BNGA01402	Unimodal, Poorly Sorted	Very Fine Sandy Very Coarse Silt	Coarse Silt	Fine Skewed	Mesokurtic
BNGA01403	Unimodal, Poorly Sorted	Very Fine Sandy Coarse Silt	Coarse Silt	Symmetrical	Mesokurtic
BNGA01405	Unimodal, Poorly Sorted	Very Fine Sandy Very Coarse Silt	Coarse Silt	Symmetrical	Mesokurtic
BNGA01703	Bimodal, Very Poorly Sorted	Coarse Sandy Fine Silt	Medium Silt	Very Coarse Skewed	Leptokurtic
BNGA01705	Unimodal, Poorly Sorted	Very Fine Sandy Very Coarse Silt	Coarse Silt	Fine Skewed	Mesokurtic
BNGA01709	Unimodal, Poorly Sorted	Very Fine Sandy Very Coarse Silt	Coarse Silt	Fine Skewed	Mesokurtic
BNGA02003	Unimodal, Poorly Sorted	Medium Silt	Medium Silt	Coarse Skewed	Leptokurtic
BNGA04603	Unimodal, Poorly Sorted	Very Fine Sandy Very Coarse Silt	Very Coarse Silt	Fine Skewed	Mesokurtic
BNGA05502	Unimodal, Poorly Sorted	Very Fine Sandy Coarse Silt	Coarse Silt	Symmetrical	Mesokurtic
BNGA05503	Unimodal, Poorly Sorted	Very Fine Sandy Coarse Silt	Coarse Silt	Symmetrical	Mesokurtic
BNGA05505	Unimodal, Poorly Sorted	Very Fine Sandy Coarse Silt	Coarse Silt	Symmetrical	Mesokurtic
BNGA05506	Bimodal, Very Poorly Sorted	Fine Sandy Coarse Silt	Coarse Silt	Coarse Skewed	Mesokurtic
BNGA05526-27	Unimodal, Poorly Sorted	Very Fine Sandy Coarse Silt	Coarse Silt	Symmetrical	Mesokurtic
BNGA05559	Unimodal, Poorly Sorted	Very Fine Sandy Medium Silt	Coarse Silt	Coarse Skewed	Platykurtic

Table D.1 – continued from previous page

Sample ID	Mode and sorting	Sedimentology	Mean grain size class	Skewness	Kurtosis
BNGA05903	Unimodal, Poorly Sorted	Very Fine Sandy Very Coarse Silt	Coarse Silt	Symmetrical	Platykurtic
BNGA05906	Bimodal, Poorly Sorted	Very Fine Sandy Very Coarse Silt	Very Coarse Silt	Symmetrical	Leptokurtic
BNGA06202	Bimodal, Very Poorly Sorted	Fine Sandy Fine Silt	Coarse Silt	Coarse Skewed	Platykurtic
BNGA06203	Unimodal, Poorly Sorted	Medium Silt	Medium Silt	Symmetrical	Mesokurtic
BNGA06205	Unimodal, Poorly Sorted	Medium Silt	Medium Silt	Symmetrical	Platykurtic
BNGA06206	Unimodal, Poorly Sorted	Medium Silt	Medium Silt	Symmetrical	Mesokurtic
BNGA06602	Unimodal, Poorly Sorted	Coarse Silt	Coarse Silt	Symmetrical	Mesokurtic
BNGA06603	Unimodal, Poorly Sorted	Medium Silt	Medium Silt	Symmetrical	Mesokurtic
BNGA06605	Unimodal, Poorly Sorted	Medium Silt	Medium Silt	Symmetrical	Mesokurtic
BNGA07002	Unimodal, Poorly Sorted	Coarse Silt	Coarse Silt	Symmetrical	Mesokurtic
BNGA07102	Unimodal, Poorly Sorted	Coarse Silt	Medium Silt	Symmetrical	Platykurtic
BNGA07103	Unimodal, Poorly Sorted	Coarse Silt	Medium Silt	Symmetrical	Platykurtic
BNGA07105	Unimodal, Poorly Sorted	Very Fine Sandy Coarse Silt	Coarse Silt	Symmetrical	Mesokurtic
BNGA07106	Unimodal, Poorly Sorted	Very Fine Sandy Coarse Silt	Coarse Silt	Symmetrical	Mesokurtic
BNGA07108	Unimodal, Poorly Sorted	Very Fine Sandy Coarse Silt	Medium Silt	Symmetrical	Platykurtic
BNGA07109	Bimodal, Poorly Sorted	Very Fine Sandy Fine Silt	Medium Silt	Symmetrical	Platykurtic
BNGA07111	Bimodal, Poorly Sorted	Very Fine Sandy Coarse Silt	Medium Silt	Symmetrical	Platykurtic
BNGA07112	Unimodal, Poorly Sorted	Very Fine Sandy Coarse Silt	Medium Silt	Symmetrical	Platykurtic
BNGA07137	Unimodal, Poorly Sorted	Coarse Silt	Medium Silt	Fine Skewed	Platykurtic
BNGA07202	Bimodal, Very Poorly Sorted	Very Fine Sandy Coarse Silt	Coarse Silt	Symmetrical	Mesokurtic

Table D.1 – continued from previous page

Sample ID	Mode and sorting	Sedimentology	Mean grain size class	Skewness	Kurtosis
BNGA07203	Unimodal, Poorly Sorted	Very Fine Sandy Coarse Silt	Coarse Silt	Symmetrical	Mesokurtic
BNGA07205	Unimodal, Poorly Sorted	Very Fine Sandy Medium Silt	Coarse Silt	Symmetrical	Mesokurtic
BNGA07206	Unimodal, Very Poorly Sorted	Very Fine Sandy Fine Silt	Medium Silt	Coarse Skewed	Platykurtic
BNGA07208	Bimodal, Very Poorly Sorted	Very Coarse Silty Fine Sand	Very Fine Sand	Very Fine Skewed	Platykurtic
BNGA08102	Unimodal, Poorly Sorted	Medium Silt	Medium Silt	Symmetrical	Mesokurtic
BNGA08105	Unimodal, Poorly Sorted	Very Fine Sandy Very Coarse Silt	Very Coarse Silt	Fine Skewed	Mesokurtic
BNGA08109	Unimodal, Poorly Sorted	Very Fine Sandy Very Coarse Silt	Very Coarse Silt	Fine Skewed	Mesokurtic
BNGA09402	Unimodal, Poorly Sorted	Medium Silt	Medium Silt	Symmetrical	Mesokurtic
BNGA09403	Unimodal, Poorly Sorted	Medium Silt	Medium Silt	Symmetrical	Mesokurtic
BNGA09405	Unimodal, Poorly Sorted	Medium Silt	Medium Silt	Symmetrical	Mesokurtic
BNGA09406	Unimodal, Poorly Sorted	Very Fine Sandy Medium Silt	Medium Silt	Coarse Skewed	Mesokurtic
BNGA09408	Unimodal, Poorly Sorted	Very Fine Sandy Coarse Silt	Coarse Silt	Symmetrical	Mesokurtic
BNGA09409	Unimodal, Poorly Sorted	Coarse Silt	Coarse Silt	Symmetrical	Mesokurtic
BNGA09411	Bimodal, Very Poorly Sorted	Very Fine Sandy Coarse Silt	Coarse Silt	Symmetrical	Leptokurtic
BNGA09412	Unimodal, Poorly Sorted	Very Fine Sandy Coarse Silt	Coarse Silt	Symmetrical	Mesokurtic
BNGA09414	Unimodal, Poorly Sorted	Medium Silt	Medium Silt	Coarse Skewed	Mesokurtic
BNGA09415	Unimodal, Poorly Sorted	Fine Silt	Medium Silt	Coarse Skewed	Mesokurtic
BNGA09417	Bimodal, Very Poorly Sorted	Very Fine Sandy Medium Silt	Coarse Silt	Symmetrical	Platykurtic
BNGA09418	Bimodal, Very Poorly Sorted	Very Fine Sandy Very Coarse Silt	Very Coarse Silt	Symmetrical	Platykurtic
BNGA09702	Unimodal, Poorly Sorted	Very Fine Sandy Medium Silt	Medium Silt	Coarse Skewed	Leptokurtic

216

Table D.1 – continued from previous page

Sample ID	Mode and sorting	Sedimentology	Mean grain size class	Skewness	Kurtosis
BNGA09753	Unimodal, Poorly Sorted	Fine Silt	Medium Silt	Coarse Skewed	Leptokurtic
BNGA10004	Unimodal, Poorly Sorted	Very Fine Sandy Very Coarse Silt	Coarse Silt	Fine Skewed	Mesokurtic
BNGA10302	Bimodal, Very Poorly Sorted	Fine Sandy Medium Silt	Very Coarse Silt	Fine Skewed	Platykurtic
BNGA10305	Unimodal, Poorly Sorted	Very Coarse Silty Fine Sand	Fine Sand	Very Fine Skewed	Very Leptokurtic
BNGA10603	Unimodal, Poorly Sorted	Very Coarse Silty Very Fine Sand	Very Coarse Silt	Fine Skewed	Leptokurtic
BNGA10606	Unimodal, Poorly Sorted	Very Fine Sandy Coarse Silt	Coarse Silt	Symmetrical	Mesokurtic
BNGA10608	Unimodal, Poorly Sorted	Very Fine Sandy Very Coarse Silt	Coarse Silt	Fine Skewed	Mesokurtic
BNGA10609	Unimodal, Poorly Sorted	Very Fine Sandy Very Coarse Silt	Coarse Silt	Fine Skewed	Mesokurtic
BNGA10611	Unimodal, Poorly Sorted	Very Fine Sandy Very Coarse Silt	Very Coarse Silt	Fine Skewed	Mesokurtic
BNGA10612	Unimodal, Poorly Sorted	Very Fine Sandy Coarse Silt	Coarse Silt	Symmetrical	Mesokurtic
BNGA10903	Unimodal, Poorly Sorted	Very Fine Sandy Very Coarse Silt	Coarse Silt	Fine Skewed	Platykurtic
BNGA10905	Unimodal, Poorly Sorted	Very Fine Sandy Very Coarse Silt	Very Coarse Silt	Fine Skewed	Platykurtic
BNGA10908	Unimodal, Poorly Sorted	Very Fine Sandy Very Coarse Silt	Very Coarse Silt	Fine Skewed	Platykurtic
BNGA10909	Unimodal, Poorly Sorted	Very Fine Sandy Very Coarse Silt	Coarse Silt	Fine Skewed	Mesokurtic
BNGA10911	Unimodal, Poorly Sorted	Very Fine Sandy Very Coarse Silt	Coarse Silt	Fine Skewed	Platykurtic
BNGA10912	Unimodal, Poorly Sorted	Very Fine Sandy Very Coarse Silt	Coarse Silt	Fine Skewed	Mesokurtic
BNGA10914	Unimodal, Poorly Sorted	Very Fine Sandy Very Coarse Silt	Coarse Silt	Fine Skewed	Platykurtic
BNGA10915	Unimodal, Poorly Sorted	Very Fine Sandy Coarse Silt	Coarse Silt	Symmetrical	Mesokurtic
BNGA11002	Unimodal, Poorly Sorted	Coarse Silt	Medium Silt	Symmetrical	Platykurtic
BNGA11003	Unimodal, Poorly Sorted	Medium Silt	Medium Silt	Coarse Skewed	Mesokurtic

217

Table D.1 – continued from previous page

Sample ID	Mode and sorting	Sedimentology	Mean grain size class	Skewness	Kurtosis
BNGA11005	Unimodal, Poorly Sorted	Fine Silt	Medium Silt	Coarse Skewed	Mesokurtic
BNGA11006	Unimodal, Poorly Sorted	Very Fine Sandy Coarse Silt	Coarse Silt	Symmetrical	Platykurtic
BNGA11008	Unimodal, Poorly Sorted	Medium Silty Coarse Sand	Medium Sand	Very Fine Skewed	Very Leptokurtic
BNGA11009	Unimodal, Poorly Sorted	Very Fine Sandy Medium Silt	Coarse Silt	Symmetrical	Platykurtic
BNGA11011	Unimodal, Poorly Sorted	Very Fine Sandy Very Coarse Silt	Coarse Silt	Fine Skewed	Platykurtic
BNGA11012	Unimodal, Poorly Sorted	Very Fine Sandy Very Coarse Silt	Very Coarse Silt	Very Fine Skewed	Mesokurtic
BNGA11014	Unimodal, Poorly Sorted	Very Fine Sandy Coarse Silt	Coarse Silt	Symmetrical	Platykurtic
BNGA11015	Unimodal, Poorly Sorted	Very Fine Sandy Coarse Silt	Coarse Silt	Symmetrical	Platykurtic
BNGA11017	Unimodal, Poorly Sorted	Very Fine Sandy Medium Silt	Medium Silt	Symmetrical	Platykurtic
BNGA11018	Unimodal, Poorly Sorted	Medium Silt	Medium Silt	Symmetrical	Mesokurtic
BNGA11020	Unimodal, Poorly Sorted	Medium Silt	Medium Silt	Symmetrical	Mesokurtic
BNGA11021	Unimodal, Poorly Sorted	Medium Silt	Medium Silt	Symmetrical	Mesokurtic
BNGA11023	Unimodal, Poorly Sorted	Fine Silt	Medium Silt	Coarse Skewed	Mesokurtic
BNGA11026	Unimodal, Poorly Sorted	Very Fine Sandy Coarse Silt	Coarse Silt	Symmetrical	Mesokurtic
BNGA11029	Unimodal, Very Poorly Sorted	Fine Silt	Fine Silt	Coarse Skewed	Mesokurtic
BNGA11202	Bimodal, Very Poorly Sorted	Coarse Sandy Medium Silt	Coarse Silt	Coarse Skewed	Mesokurtic
BNGA11209	Trimodal, Very Poorly Sorted	Very Fine Sandy Medium Silt	Coarse Silt	Symmetrical	Mesokurtic
BNGA11212	Unimodal, Poorly Sorted	Very Coarse Silty Fine Sand	Very Coarse Silt	Very Fine Skewed	Mesokurtic
BNGA11218	Unimodal, Poorly Sorted	Very Fine Sandy Coarse Silt	Coarse Silt	Symmetrical	Platykurtic
BNGA11221	Unimodal, Poorly Sorted	Very Fine Sandy Fine Silt	Medium Silt	Coarse Skewed	Mesokurtic

Table D.1 – continued from previous page

Sample ID	Mode and sorting	Sedimentology	Mean grain size class	Skewness	Kurtosis
BNGA11227	Unimodal, Poorly Sorted	Very Fine Sandy Medium Silt	Coarse Silt	Symmetrical	Platykurtic
BNGA11402	Unimodal, Poorly Sorted	Very Fine Sandy Medium Silt	Medium Silt	Coarse Skewed	Leptokurtic
BNGA11403	Unimodal, Poorly Sorted	Fine Silt	Medium Silt	Coarse Skewed	Leptokurtic
BNGA11405	Bimodal, Very Poorly Sorted	Fine Sandy Fine Silt	Very Coarse Silt	Symmetrical	Platykurtic
BNGA11408	Unimodal, Poorly Sorted	Medium Silt	Medium Silt	Symmetrical	Mesokurtic
BNGA11409A	Bimodal, Poorly Sorted	Very Coarse Silty Very Fine Sand	Very Fine Sand	Very Fine Skewed	Leptokurtic
BNGA11411	Bimodal, Very Poorly Sorted	Fine Sandy Fine Silt	Medium Silt	Very Coarse Skewed	Mesokurtic
BNGA11414A	Bimodal, Poorly Sorted	Very Fine Sandy Very Coarse Silt	Coarse Silt	Symmetrical	Platykurtic
BNGA11415	Unimodal, Poorly Sorted	Very Fine Sandy Very Coarse Silt	Very Coarse Silt	Fine Skewed	Mesokurtic
BNGA11417	Unimodal, Very Poorly Sorted	Very Fine Sandy Very Coarse Silt	Very Coarse Silt	Fine Skewed	Platykurtic
BNGA11418A	Unimodal, Poorly Sorted	Very Fine Sandy Medium Silt	Medium Silt	Symmetrical	Mesokurtic
BNGA11421	Unimodal, Poorly Sorted	Very Fine Sandy Medium Silt	Medium Silt	Symmetrical	Mesokurtic
BNGA11423	Unimodal, Poorly Sorted	Very Fine Sandy Medium Silt	Medium Silt	Coarse Skewed	Mesokurtic
BNGA11424	Unimodal, Poorly Sorted	Very Fine Sandy Very Coarse Silt	Coarse Silt	Fine Skewed	Platykurtic
BNGA11427	Unimodal, Poorly Sorted	Very Fine Sandy Very Coarse Silt	Coarse Silt	Fine Skewed	Platykurtic
BNGA11429	Unimodal, Poorly Sorted	Very Fine Sandy Coarse Silt	Coarse Silt	Symmetrical	Mesokurtic
BNGA11429A	Bimodal, Poorly Sorted	Very Fine Sandy Very Coarse Silt	Coarse Silt	Symmetrical	Platykurtic
BNGA11430	Unimodal, Poorly Sorted	Medium Silt	Medium Silt	Symmetrical	Mesokurtic
BNGA11430A	Unimodal, Poorly Sorted	Fine Silt	Medium Silt	Coarse Skewed	Mesokurtic
BNGA11432	Unimodal, Poorly Sorted	Very Fine Sandy Fine Silt	Medium Silt	Coarse Skewed	Mesokurtic

Table D.1 – continued from previous page

Sample ID	Mode and sorting	Sedimentology	Mean grain size class	Skewness	Kurtosis
BNGA11434	Unimodal, Poorly Sorted	Very Fine Sandy Very Coarse Silt	Very Coarse Silt	Fine Skewed	Platykurtic
BNGA11437A	Bimodal, Very Poorly Sorted	Very Fine Sandy Very Coarse Silt	Very Coarse Silt	Symmetrical	Platykurtic
BNGA11605	Bimodal, Very Poorly Sorted	Very Fine Sandy Medium Silt	Very Coarse Silt	Fine Skewed	Platykurtic
BNGA11618	Bimodal, Very Poorly Sorted	Very Fine Sandy Very Coarse Silt	Very Coarse Silt	Fine Skewed	Platykurtic
BNGA11623	Unimodal, Very Poorly Sorted	Very Fine Sandy Medium Silt	Coarse Silt	Coarse Skewed	Mesokurtic
BNGA11632	Bimodal, Very Poorly Sorted	Coarse Sandy Fine Silt	Coarse Silt	Very Coarse Skewed	Mesokurtic
BNGA11635	Unimodal, Poorly Sorted	Very Coarse Silty Fine Sand	Very Fine Sand	Fine Skewed	Leptokurtic
BNGA11647	Trimodal, Very Poorly Sorted	Coarse Sandy Medium Silt	Very Coarse Silt	Symmetrical	Platykurtic
BNGA11649	Unimodal, Very Poorly Sorted	Very Coarse Silty Very Fine Sand	Very Coarse Silt	Fine Skewed	Mesokurtic
BNGA11902	Unimodal, Poorly Sorted	Medium Silt	Medium Silt	Symmetrical	Mesokurtic
BNGA11903	Unimodal, Poorly Sorted	Very Fine Sandy Very Coarse Silt	Very Coarse Silt	Very Fine Skewed	Mesokurtic
BNGA11905	Unimodal, Poorly Sorted	Very Fine Sandy Medium Silt	Coarse Silt	Symmetrical	Platykurtic
BNGA11906	Bimodal, Very Poorly Sorted	Very Fine Sandy Medium Silt	Coarse Silt	Symmetrical	Platykurtic
BNGA11908	Bimodal, Very Poorly Sorted	Fine Sandy Medium Silt	Very Coarse Silt	Symmetrical	Platykurtic
BNGA11909	Bimodal, Very Poorly Sorted	Very Fine Sandy Medium Silt	Coarse Silt	Symmetrical	Platykurtic
BNGA11911	Unimodal, Poorly Sorted	Very Fine Sandy Very Coarse Silt	Coarse Silt	Symmetrical	Platykurtic
BNGA11912	Unimodal, Poorly Sorted	Very Fine Sandy Coarse Silt	Coarse Silt	Symmetrical	Mesokurtic
BNGA11914	Unimodal, Poorly Sorted	Very Fine Sandy Very Coarse Silt	Coarse Silt	Fine Skewed	Platykurtic
BNGA11917	Bimodal, Very Poorly Sorted	Very Fine Sandy Medium Silt	Coarse Silt	Symmetrical	Platykurtic
BNGA11918	Unimodal, Poorly Sorted	Very Coarse Silty Very Fine Sand	Very Coarse Silt	Very Fine Skewed	Mesokurtic

220

Table D.1 – continued from previous page

Sample ID	Mode and sorting	Sedimentology	Mean grain size class	Skewness	Kurtosis
BNGA11920	Unimodal, Poorly Sorted	Very Fine Sandy Coarse Silt	Coarse Silt	Symmetrical	Mesokurtic
BNGA11921	Unimodal, Poorly Sorted	Medium Silt	Medium Silt	Coarse Skewed	Leptokurtic
BNGA11923	Unimodal, Poorly Sorted	Fine Silt	Medium Silt	Coarse Skewed	Mesokurtic
BNGA12103	Bimodal, Very Poorly Sorted	Fine Sandy Medium Silt	Coarse Silt	Coarse Skewed	Platykurtic
BNGA12106	Unimodal, Poorly Sorted	Medium Silt	Medium Silt	Symmetrical	Platykurtic
BNGA12113	Unimodal, Poorly Sorted	Medium Silt	Medium Silt	Symmetrical	Platykurtic
BNGA12115	Unimodal, Poorly Sorted	Medium Silt	Medium Silt	Coarse Skewed	Mesokurtic
BNGA12121	Bimodal, Very Poorly Sorted	Fine Sandy Medium Silt	Coarse Silt	Very Coarse Skewed	Mesokurtic
BNGA12126	Unimodal, Very Poorly Sorted	Very Fine Sandy Very Coarse Silt	Very Coarse Silt	Symmetrical	Platykurtic
BNGA12129	Unimodal, Poorly Sorted	Very Fine Sandy Very Coarse Silt	Coarse Silt	Fine Skewed	Platykurtic
BNGA12134	Bimodal, Poorly Sorted	Very Fine Sandy Very Coarse Silt	Very Coarse Silt	Very Fine Skewed	Mesokurtic
BNGA12136	Unimodal, Very Poorly Sorted	Very Coarse Silty Fine Sand	Very Coarse Silt	Very Fine Skewed	Platykurtic
BNGA12140	Bimodal, Very Poorly Sorted	Very Fine Sandy Medium Silt	Coarse Silt	Symmetrical	Platykurtic
BNGA12302	Bimodal, Very Poorly Sorted	Very Fine Sandy Medium Silt	Coarse Silt	Symmetrical	Platykurtic
BNGA12303	Bimodal, Very Poorly Sorted	Very Fine Sandy Medium Silt	Coarse Silt	Coarse Skewed	Mesokurtic
BNGA12305	Unimodal, Poorly Sorted	Very Fine Sandy Very Coarse Silt	Coarse Silt	Fine Skewed	Platykurtic
BNGA12306	Bimodal, Poorly Sorted	Very Fine Sandy Very Coarse Silt	Very Coarse Silt	Very Fine Skewed	Mesokurtic
BNGA12308	Unimodal, Poorly Sorted	Very Fine Sandy Very Coarse Silt	Coarse Silt	Fine Skewed	Mesokurtic
BNGA12309	Bimodal, Poorly Sorted	Very Fine Sandy Very Coarse Silt	Coarse Silt	Symmetrical	Platykurtic
BNGA12311	Unimodal, Poorly Sorted	Very Fine Sandy Medium Silt	Medium Silt	Coarse Skewed	Platykurtic

Table D.1 – continued from previous page

Sample ID	Mode and sorting	Sedimentology	Mean grain size class	Skewness	Kurtosis
BNGA12312	Unimodal, Very Poorly Sorted	Very Fine Sandy Very Coarse Silt	Coarse Silt	Symmetrical	Platykurtic
BNGA12314	Unimodal, Very Poorly Sorted	Fine Sandy Very Coarse Silt	Very Coarse Silt	Fine Skewed	Platykurtic
BNGA12315	Unimodal, Poorly Sorted	Very Fine Sandy Very Coarse Silt	Very Coarse Silt	Fine Skewed	Platykurtic
BNGA12321	Bimodal, Very Poorly Sorted	Fine Sandy Medium Silt	Coarse Silt	Coarse Skewed	Mesokurtic
BNGA12324	Bimodal, Very Poorly Sorted	Medium Silty Medium Sand	Very Fine Sand	Very Fine Skewed	Platykurtic
BNGA12327	Unimodal, Poorly Sorted	Very Fine Sandy Medium Silt	Coarse Silt	Coarse Skewed	Mesokurtic
BNGA12330	Unimodal, Poorly Sorted	Very Fine Sandy Fine Silt	Medium Silt	Coarse Skewed	Leptokurtic
BNGA12334	Unimodal, Poorly Sorted	Medium Silt	Medium Silt	Symmetrical	Mesokurtic
BNGA12337	Unimodal, Poorly Sorted	Very Fine Sandy Medium Silt	Medium Silt	Coarse Skewed	Mesokurtic
BNGA12340	Unimodal, Poorly Sorted	Very Fine Sandy Medium Silt	Medium Silt	Coarse Skewed	Mesokurtic
BNGA12343	Unimodal, Poorly Sorted	Very Fine Sandy Medium Silt	Medium Silt	Coarse Skewed	Leptokurtic
BNGA12346	Unimodal, Poorly Sorted	Very Fine Sandy Coarse Silt	Coarse Silt	Symmetrical	Platykurtic
BNGA12349	Bimodal, Very Poorly Sorted	Fine Sandy Medium Silt	Coarse Silt	Symmetrical	Platykurtic
BNGA12353	Bimodal, Very Poorly Sorted	Very Coarse Silty Fine Sand	Very Fine Sand	Very Fine Skewed	Mesokurtic

Location and Facies of Garo Hills Outcrops

Table E.1: Outcrop locations of the Garo Hills given by GPS coordinates. All alluvial outcrops were divided into one of four facies: Amalgamated, cross-stratified, sand bodies (Acs); Homogeneous sand bodies (Hs); Heterolithic sand, silt, mud bodies (Hssm); or Graded, poorly sorted, alluvial bodies (Gpsa), as described in Sec. 4.4.3.1 and summarized in Table 4.3. Likewise, weathering extent for each alluvial outcrop was assigned using Table 4.2.

Outcrop ID	Latitude	Longitude	Environment	Facies	Weathering stage
20130117-01	25.74180298	90.40058901	Alluvial	Gpsa	4
20130120-08	25.81459302	89.97600303	Non-alluvial	Basement	
20130117-04	25.63481997	90.32746503	Alluvial	Gpsa	4
20130120-07	25.80837901	89.980038	Non-alluvial	Basement	
20130120-05	25.80693799	89.98202501	Non-alluvial	Basement	
20130118-01	25.46068903	90.21899298	Alluvial	Hssm	4
20130118-02	25.46019701	90.21937603	Alluvial	Hs	4
20130118-04	25.43310796	90.21848504	Alluvial	Hs	4
20130118-05	25.35708997	90.22301696	Alluvial	Hs	4
20130118-06	25.34822501	90.21976696	Alluvial	Hssm	4
20130117-03	25.692883	90.34827604	Non-alluvial	Basement	
20130118-07	25.34726503	90.21874798	Alluvial	Hssm	4
20130118-08	25.26055601	90.212166	Alluvial	Hs	4
20130118-09	25.19941899	90.33415002	Alluvial	Hssm	4
20130118-10	25.200485	90.33666601	Alluvial	Hs	4
20130118-11	25.16894398	90.42092602	Alluvial	Hs	4
20130117-05	25.60570501	90.29202199	Non-alluvial	Basement	

Outcrop ID	Latitude	Longitude	Environment	Facies	Weathering stage
20130118-12	25.16743499	90.42769801	Alluvial	Gpsa	4
20130120-01	25.51555596	90.21174699	Alluvial	Hssm	4
20130120-02	25.580508	90.03072001	Alluvial	Hssm	4
20130123-05	25.57984499	90.23779401	Non-alluvial	Basement	
20130123-07	25.579775	90.22073801	Non-alluvial	Basement	
20130123-08	25.579545	90.21865703	Non-alluvial	Basement	
20130123-04	25.57925399	90.23782703	Non-alluvial	Basement	
20130120-03	25.62664703	89.98621898	Alluvial	Gpsa	4
20130119-01	25.57221503	90.30145196	Non-alluvial	Basement	
20130119-07	25.56797898	90.30285501	Non-alluvial	Basement	
20130119-03	25.56257098	90.35081701	Non-alluvial	Basement	
20130119-04	25.56111203	90.35116302	Non-alluvial	Basement	
20130119-05	25.560992	90.351894	Non-alluvial	Basement	
20130119-06	25.559022	90.360723	Non-alluvial	Basement	
20130119-02	25.55205002	90.33183896	Non-alluvial	Basement	
20130124-02	25.55177199	90.37927299	Non-alluvial	Basement	
20130124-03	25.55166001	90.37950198	Non-alluvial	Basement	
20130124-04	25.55138801	90.37915296	Non-alluvial	Basement	
20130120-04	25.61356799	90.01339604	Alluvial	Hssm	4
20130122-08	25.54692297	90.37965696	Non-alluvial	Basement	
20130122-09	25.54617397	90.37895104	Non-alluvial	Basement	
20130122-10	25.54544801	90.37905799	Non-alluvial	Basement	
20130122-11	25.545388	90.37894098	Non-alluvial	Basement	
20130120-06	25.80616199	89.98156602	Alluvial	Hs	4
20130123-02	25.54296697	90.22624098	Non-alluvial	Basement	
20130122-02	25.54017504	90.39054698	Non-alluvial	Basement	
20130122-01	25.54000304	90.39014499	Non-alluvial	Basement	

Outcrop ID	Latitude	Longitude	Environment	Facies	Weathering stage
20130122-05	25.53940197	90.38731501	Non-alluvial	Basement	
20130124-01	25.53918899	90.38748499	Non-alluvial	Basement	
20130122-06	25.53915203	90.38756998	Non-alluvial	Basement	
20130122-03	25.539105	90.38900999	Non-alluvial	Basement	
20130122-04	25.53894298	90.38828697	Non-alluvial	Basement	
20130123-09	25.538573	90.23163297	Non-alluvial	Basement	
20130122-07	25.53746701	90.38765598	Non-alluvial	Basement	
20130120-09	25.81448003	89.97725898	Alluvial	Acs	1
20130123-10	25.52499801	90.22844701	Non-alluvial	Basement	
20130123-11	25.52076699	90.227741	Non-alluvial	Basement	
20130120-10	25.74444403	89.99990503	Alluvial	Hs	2
20130123-13	25.52033499	90.22726902	Non-alluvial	Basement	
20130123-14	25.52029501	90.22613796	Non-alluvial	Basement	
20130120-11	25.74234998	89.99885202	Alluvial	Hs	2
20130121-01	25.57451804	89.98377297	Alluvial	Gpsa	3
20130123-16	25.50815801	90.21551902	Non-alluvial	Basement	
20130121-02	25.54730502	89.98604799	Alluvial	Hssm	3
20130121-03	25.39361302	89.91540598	Alluvial	Hssm	3
20130121-04	25.36445104	89.86218802	Alluvial	Hssm	2
20130118-03	25.46015301	90.21969899	Non-alluvial	Basement	
20130121-05	25.36248498	89.86059898	Alluvial	Hssm	3
20130121-06	25.34385704	89.84030002	Alluvial	Gpsa	3
20130121-07	25.33331604	89.84723403	Alluvial	Hssm	4
20130121-08	25.323046	89.848232	Alluvial	Hs	4
20130121-09	25.32400601	89.84208503	Alluvial	Acs	1
20130121-10	25.33111998	89.849615	Alluvial	Hssm	4
20130121-11	25.49391699	89.943108	Alluvial	Hssm	4

Table E.1 – continued from previous page

Outcrop ID	Latitude	Longitude	Environment	Facies	Weathering stage
20130123-01	25.53681498	90.227855	Alluvial	Hssm	4
20130123-03	25.54329101	90.22608399	Alluvial	Hssm	4
20130123-06	25.58441397	90.19392899	Alluvial	Hssm	4
20130123-12	25.52037497	90.22560798	Alluvial	Hs	4
20130123-15	25.51383399	90.21822704	Alluvial	Acs	4
A20130125-01	25.18976944	90.22369167	Alluvial	Hssm	3
A20130126-01	25.17322778	90.14691111	Alluvial	Gpsa	3
A20130126-02	25.2429	90.04240556	Alluvial	Gpsa	3
A20130126-03	25.25625	89.98179167	Alluvial	Hssm	3
A20130126-04	25.256825	89.98013611	Alluvial	Hs	2
A20130127-01	25.26016667	89.98433611	Alluvial	Hs	2
A20130127-02	25.25043889	89.97905556	Alluvial	Hs	2
A20130127-03	25.249825	89.97853056	Alluvial	Hs	3
A20130127-04	25.24973056	89.97681667	Alluvial	Acs	1
A20130127-05	25.24508889	89.95891667	Alluvial	Hs	3
A20130127-06	25.24748333	89.95641944	Alluvial	Hssm	4
A20130127-07	25.25199167	89.957725	Alluvial	Acs	2
A20130127-08	25.26093333	89.976725	Alluvial	Acs	2
20131119-01	25.19935	90.645533	Alluvial	Gpsa	0
20131119-02	25.199393	90.645943	Alluvial	Hs	4
20131120-01	25.18274	90.496336	Alluvial	Gpsa	3
20131120-02	25.193487	90.355666	Alluvial	Hs	3
20131120-03	25.194369	90.335098	Alluvial	Hssm	3
20131120-04	25.223456	90.22361	Alluvial	Acs	3
20131120-05	25.224156	90.254253	Alluvial	Hs	4
20131122-01	25.588438	90.023652	Alluvial	Hssm	3
20131122-02	25.649989	89.962371	Alluvial	Gpsa	3

Table E.1 – continued from previous page

Outcrop ID	Latitude	Longitude	Environment	Facies	Weathering stage
20131122-03	25.743969	89.885108	Alluvial	Acs	0
20131122-04	25.814941	89.976279	Alluvial	Hs	2
20131122-05	25.689918	89.937414	Alluvial	Hssm	4
20131123-01	25.298172	89.840636	Alluvial	Acs	1
20131123-02	25.324143	89.842054	Alluvial	Acs	1
20131123-03	25.384045	89.823618	Alluvial	Hssm	4
20131123-04	25.375515	89.821987	Alluvial	Hssm	4
20131123-05	25.364567	89.825026	Alluvial	Hssm	4
20131123-06	25.360281	89.830201	Alluvial	Hssm	4
20131123-07	25.322153	89.843724	Alluvial	Hs	3
20131123-08	25.328678	89.837822	Alluvial	Acs	3
20131123-09	25.403909	89.828778	Alluvial	Gpsa	3
20131124-01	25.318396	89.868587	Alluvial	Gpsa	2
20131124-02	25.309307	89.878719	Alluvial	Hs	2
20131124-03	25.296552	90.012622	Alluvial	Gpsa	3
20151013-01	25.260711	89.981558	Alluvial	Hs	2
20151013-02	25.259334	89.976037	Alluvial	Hssm	4
20151014-01	25.276645	89.935727	Alluvial	Hs	2
20151014-02	25.288176	89.90546	Alluvial	Hssm	4
20151014-03	25.289158	89.902986	Alluvial	Acs	1

REFERENCES

Aftabuzzaman, M., Kabir, S., Islam, M. K., and Alam, M. S. (2013). Clay Mineralogy of the Pleistocene Soil Horizon in Barind Tract, Bangladesh. *Journal Geological Society of India*, 81(May):677–684.

Aitken, M. (1998). *An introduction to optical dating.* Oxfor University Press, New York.

Alam, M., Alam, M. M., Curray, J. R., Chowdhury, M. L. R., and Gani, M. R. (2003). An overview of the sedimentary geology of the Bengal Basin in relation to the regional tectonic framework and basin-fill history. *Sedimentary Geology*, 155(3-4):179–208.

Alam, M. S., Keppens, E., and Paepet, R. (1997). The use of oxygen and carbon isotope composition of pedogenic carbonates from Pleistocene palaeosols in NW Bangladesh, as palaeoclimatic indicators. *Quaternary Science Reviews*, 16(96):161–168.

Allen, J. R. L. (1963). The classification of cross-stratified units, with notes on their origin. *Sedimentology*, 2(1 963):93–114.

Allen, J. R. L. (1965). The classification of cross-stratified units, further discussion. *Sedimentology*, 5:249–254.

Allen, P. A. (2008). From landscapes into geological history. *Nature*, 451:274–276.

Allen, R., Najman, Y., Carter, A., Barfod, D., Bickle, M., Chapman, H., Garzanti, E., Vezzoli, G., Ando, S., and Parrish, R. (2008). Provenance of the Tertiary sedimentary rocks of the Indo-Burman Ranges, Burma (Myanmar): Burman arc or Himalayan-derived? *Journal of the Geological Society*, 165(6):1045–1057.

Allison, M. A., Khan, S. R., Jr, S. L. G., and Kuehl, S. A. (2003). Stratigraphic evolution of the late Holocene Ganges – Brahmaputra lower delta plain. *Sedimentary Geology*, 155:317–342.

Anbeek, C., Van Breemen, N., Meijer, E. L., and Van Der Plas, L. (1994). The dissolution of naturally weathered feldspar and quartz. *Geochimica et Cosmochimica Acta*, 58(21):4601–4613.

Archer, A. W. and Greb, S. F. (1995). An Amazon-Scale Drainage System in the Early Pennsylvanian of Central North America.

Ardies, G. W., Dalrymple, R. W., and Zaitlin, B. A. (2002). Controls on the geometry of incised valleys in the Basal Quartz unit (Lower Cretaceous), Western Canada Sedimentary Basin. *Journal of Sedimentary Research*, 72(5):602–618.

Armitage, J. J., Duller, R. A., Whittaker, A. C., and Allen, P. A. (2011). Transformation of tectonic and climatic signals from source to sedimentary archive. *Nature Geoscience*, 4(4):231–235.

Aslan, A. and Blum, M. D. (1999). Constrasting Styles of Holocene Avulsion, Texas Gulf Coastal Plain, USA. In *Fluvial Sedimentology VI*, pages 193–209. Blackwell Publishing Ltd.

Baker, V. R. (2013). *Global Late Quaternary Fluvial Paleohydrology: With Special Emphasis on Paleofloods and Megafloods*, volume 9. Elsevier Ltd.

Baki, A. B. M. and Gan, T. Y. (2012). Riverbank migration and island dynamics of the braided Jamuna River of the Ganges-Brahmaputra basin using multi-temporal Landsat images. *Quaternary International*, 263:148–161.

Beerbower, J. R. (1964). Cyclothems and Cyclic Depositional Mechanisms in Alluvial Plain Sedimentation. In Merriam, D., editor, *Symposium on cyclic sedimentation*, pages 31–42. Kansas Geological Survey, Bulletin.

Berger, A., Crucifix, M., Hodell, D. A., Mangili, C., McManus, J. F., Otto-Bliesner, B., Pol, K., Raynaud, D., Skinner, L. C., Tzedakis, P. C., Wolff, E. W., Yin, Q., Abe-Ouchi, A., Barbante, C., Brovkin, V., Cacho, I., Capron, E., Ferretti, P., Ganopolski, A., Grimalt, J. O., Hönisch, B., Kawamura, K., Landais, A., Margari, V., Martrat, B., Masson-Delmotte, V., Mokeddem, Z., Parrenin, F., Prokopenko, A. A., Rashid, H., Schulz, M., and Vazquez Riveiros, N. (2015). Interglacials of the last 800,000 years. *Reviews of Geophysics*, 1622:n/a–n/a.

Berger, A. and Loutre, M. F. (1991). Insolation values for the climate of the last 10 million years. *Quaternary Science Reviews*, 10(4):297–317.

Best, J. L., Ashworth, P. J., Bristow, C. S., and Roden, J. (2003). Three-Dimensional Sedimentary Architecture of a Large, Mid-Channel Sand Braid Bar, Jamuna River, Bangladesh. *Journal of Sedimentary Research*, 73(4):516–530.

Best, J. L., Ashworth, P. J., Sarker, M. H., and Roden, J. E. (2007). The Brahmaputra-Jamuna River, Bangladesh. In Gupta, A., editor, *Large Rivers: Geomorphology and Management*, pages 395–433. John Wiley & Sons, Ltd.

Bilham, R. (2001). Plateau pop-up during the 1897 Assam earthquake. *Nature*, 9:1–7.

Bilham, R., Bali, B. S., Ahmad, S., and Schiffman, C. (2013). Oldham's Lost Fault. *Seismological Research Letters*, 84(4):702–710.

Biscaye, P. E. (1965). Mineralogy and Sedimentation of Recent Deep-Sea Clay in the Atlantic Ocean and Adjacent Seas and Oceans. *Geological Society of America Bulletin*, 76:803.

Biswas, S., Coutand, I., Grujic, D., Hager, C., Stöckli, D., and Grasemann, B. (2007). Exhumation and uplift of the Shillong plateau and its influence on the eastern Himalayas: New constraints from apatite and zircon (U-Th-[Sm])/He and apatite fission track analyses. *Tectonics*, 26(6):n/a–n/a.

Blatt, H., Middleton, G., and Murray, R. (1980). *Origin of sedimentary rocks*. Prentice-Hall, Inc., 2nd edition.

Blott, S. J. and Pye, K. (2001). GRADISTAT: A grain size distribution and statistics package for the analysis of unconsolidated sediments. *Earth Surface Processes and Landforms*, 26(11):1237–1248.

Blum, M. D., Martin, J., Milliken, K., and Garvin, M. (2013). Paleovalley systems: Insights from Quaternary analogs and experiments. In *Earth-Science Reviews*, volume 116, pages 128–169. Elsevier B.V.

Blum, M. D. and Price, D. M. (1998). Quaternary alluvial plain construction in response to glacio-eustatic and climatic controls, Texas Gulf Coastal Plain. In *Relative Role of Eustasy, Climate, and Tectonism in Continental Rocks*. SEPM Special Publication.

Blum, M. D. and Törnqvist, T. E. (2000). Fluvial responses to climate and sea-level change: a review and look forward. *Sedimentology*, 47:2–48.

Bracciali, L., Najman, Y., Parrish, R. R., Akhter, S. H., and Millar, I. (2015). The Brahmaputra tale of tectonics and erosion: Early Miocene river capture in the Eastern Himalaya. *Earth and Planetary Science Letters*, 415:25–37.

Britz, R. (2009). Danionella priapus, a new species of miniature cyprinid fish from West Bengal, India (Teleostei: Cypriniformes: Cyprinidae). *Zootaxa*, 60:53 – 60.

Brookfield, M. (1998). The evolution of the great river systems of southern Asia during the Cenozoic India-Asia collision: Rivers draining southwards. *Geomorphology*, 22:285–312.

Burr, D. M., Carling, P. A., and Baker, V. R. (2009). *Megaflooding on Earth and Mars*.

Buylaert, J. P., Murray, A. S., Thomsen, K. J., and Jain, M. (2009). Testing the potential of an elevated temperature IRSL signal from K-feldspar. *Radiation Measurements*, 44(5-6):560–565.

Cai, Y., Fung, I. Y., Edwards, R. L., An, Z., Cheng, H., Lee, J.-E., Tan, L., Shen, C.-C., Wang, X., Day, J. a., Zhou, W., Kelly, M. J., and Chiang, J. C. H. (2015). Variability of stalagmite-inferred Indian monsoon precipitation over the past 252,000 y. *Proceedings of the National Academy of Sciences of the United States of America*, 112(10):2954–9.

Carling, P. A. (2013). Freshwater megaflood sedimentation: What can we learn about generic processes? *Earth-Science Reviews*, 125:87–113.

Castelltort, S. and Van Den Driessche, J. (2003). How plausible are high-frequency sediment supply-driven cycles in the stratigraphic record? *Sedimentary Geology*, 157(1-2):3–13.

Cheel, R. J. (2005). Bedforms and stratification under unidirectional flows. *Introduction to Clastic Sedimentology*, page 126.

Chirouze, F., Huyghe, P., van der Beek, P., Chauvel, C., Chakraborty, T., Dupont-Nivet, G., and Bernet, M. (2013). Tectonics, exhumation, and drainage evolution of the eastern Himalaya since 13 Ma from detrital geochemistry and thermochronology, Kameng River Section, Arunachal Pradesh. *Geological Society of America Bulletin*, 125(3-4):523–538.

Cina, S. E., Yin, A., Grove, M., Dubey, C. S., Shukla, D. P., Lovera, O. M., Kelty, T. K., Gehrels, G. E., and Foster, D. a. (2009). Gangdese arc detritus within the eastern Himalayan Neogene foreland basin: Implications for the Neogene evolution of the Yalu–Brahmaputra River system. *Earth and Planetary Science Letters*, 285(1-2):150–162.

Clark, M. and Bilham, R. (2008). Miocene rise of the Shillong Plateau and the beginning of the end for the Eastern Himalaya. *Earth and Planetary Science Letters*, 269(3-4):337–351.

Clift, P. D. and Giosan, L. (2013). Sediment fluxes and buffering in the post-glacial Indus Basin. *Basin Research*, 26(3):369–386.

Coleman, J. (1969). Brahmaputra River: Channel processes and sedimentation. *Sedimentary Geology*, 3:129–239.

Colin, C. (2006). Evolution of weathering patterns in the Indo-Burman Ranges over the last 280 kyr: Effects of sediment provenance on 87 Sr/ 86 Sr ratios tracer. (September 2005).

Cullen, J. L. (1981). Microfossil evidence for changing salinity patterns in the bay of Bengal over the last 20 000 years. *Palaeogeography, Palaeoclimatology, Palaeoecology*, 35(C):315–356.

Dalrymple, R. W. (1994). Incised-valley systems : origin and sedimentary sequences. *SEPM Special Publication*, (51):391.

Davidson, S. K., Leleu, S., and North, C. P., editors (2011). *From river to rock record: The preservation of fluvial sediments and their subsequent interpretation*. SEPM Society for Sedimentary Geology.

Dayem, K. E., Molnar, P., Battisti, D. S., and Roe, G. H. (2010). Lessons learned from oxygen isotopes in modern precipitation applied to interpretation of speleothem records of paleoclimate from eastern Asia. *Earth and Planetary Science Letters*, 295(1-2):219–230.

Debrabant, P., Fagel, N., Chamley, H., Bout, V., and Caulet, J. P. (1993). Neogene to Quaternary clay mineral fluxes in the Central Indian basin. *Palaeogeography, Palaeoclimatology, Palaeoecology*, 103(3-4):117–131.

Derry, L. A. and France-lanord, C. (1996). Neogene Himalayan weathering history and river 87Sr/86Sr: impact on the marine Sr record. *Earth and Planetary Science Letters*, 142:59–74.

Duchaufour, R. (1982). *Pedology: Pedogenesis and classification*. Springer Science & Business Media.

Dunoyer De Segonzac, G. (1970). The transformation of clay minerals during diagenesis and low-grade metamorphism: A review. *Sedimentology*, 15(1 970):281–346.

EGIS (1997). Morphological Dynamics of the Brahmaputra-Jamuna River. Technical report, Environmental and GIS Support Project for Water Sector Planning, Dhaka.

Ethridge, F. G., Wood, L. J., and Schumm, S. A. (1998). Cyclic variables controlling fluvial sequence development: problems and perspectives. *Relative Role of Eustasy, Climate, and Tectonism in Continental Rocks*, 59(59):17–30.

Ferguson, E. K., Seeber, L., Steckler, M. S., Akhter, S. H., Mondal, D., and Lenhart, A. (2012). The Dauki Thrust Fault and the Shillong Anticline: An incipient plate boundary in NE India? *American Geophysical Union*.

Folk, R. L. and Ward, W. C. (1957). Brazos River Bar: A Study in the Significance of Grain Size Parameters. *Journal of Sedimentary Petrology*, Vol. 27(1):3–26.

Galy, V., France-Lanord, C., Peucker-Ehrenbrink, B., and Huyghe, P. (2010). Sr-Nd-Os evidence for a stable erosion regime in the Himalaya during the past 12 Myr. *Earth and Planetary Science Letters*, 290(3-4):474–480.

Gardiner, D. T. and Miller, R. W. (2004). *Soils in our Environment*. Prentice Hall, 10th edition.

Garzanti, E., Andò, S., France-Lanord, C., Vezzoli, G., Censi, P., Galy, V., and Najman, Y. (2010). Mineralogical and chemical variability of fluvial sediments 1. Bedload sand (Ganges-Brahmaputra, Bangladesh). *Earth and Planetary Science Letters*, 299:368–381.

Ghosal, U., Sikdar, P. K., and Mcarthur, J. (2014). Palaeosol Control of Arsenic Pollution: The Bengal Basin in West Bengal, India. *Groundwater*, pages 1–12.

Gibling, M. R. (2006). Width and Thickness of Fluvial Channel Bodies and Valley Fills in the Geological Record: A Literature Compilation and Classification. *Journal of Sedimentary Research*, 76(5):731–770.

Gibling, M. R., Fielding, C. R., and Sinha, R. (2015). Alluvial Valleys and Alluvial Sequences: Towards a Geomorphic Assessment. *SEPM Special Publications*, 97:423–447.

Goodbred, S. L. (2003a). Response of the Ganges dispersal system to climate change : a source-to-sink view since the last interstade. *Sedimentary Geology*, 162:83 – 104.

Goodbred, S. L. (2003b). Response of the Ganges dispersal system to climate change: A source-to-sink view since the last interstade. *Sedimentary Geology*, 162(1-2):83–104.

Goodbred, S. L. and Kuehl, S. A. (1998). Floodplain processes in the Bengal Basin and the storage of Ganges – Brahmaputra river sediment: an accretion study using 137 Cs and 210 Pb geochronology. *Sedimentary Geology*, 121:239–258.

Goodbred, S. L. and Kuehl, S. A. (1999). Holocene and modern sediment budgets for the Ganges-Brahmaputra river system: Evidence for highstand dispersal to flood-plain, shelf, and deep-sea depocenters. *Geology*, 27(6):559–562.

Goodbred, S. L. and Kuehl, S. A. (2000a). Enormous Ganges-Brahmaputra sediment discharge during strengthened early Holocene monsoon. *Geology*, 28(12):1083–1086.

Goodbred, S. L. and Kuehl, S. A. (2000b). The significance of large sediment supply, active tectonism, and eustasy on margin sequence development: Late Quaternary stratigraphy and evolution of the Ganges-Brahmaputra delta. *Sedimentary Geology*, 133:227–248.

Goodbred, S. L., Paolo, P. M., Ullah, M. S., Pate, R. D., Khan, S. R., Kuehl, S. A., Singh, S. K., and Rahaman, W. (2014). Piecing together the Ganges-Brahmaputra-Meghna river delta: Use of sediment provenance to reconstruct the history and interaction of multiple fluvial systems during Holocene delta evolution. *Bulletin of the Geological Society of America*, 126(11-12):1495–1510.

Govin, G. (2015). Constraining the timing of Shillong Plateau uplift from a study of the palaeo-Brahmaputra deposits, Siwalik Group, Samdrup Jongkhar, Eastern Bhutan. In *2015 AGU Fall Meeting*. Agu.

Grall, C., Pickering, J. L., Sincavage, R., Goodbred, S. L., Paola, C., and Steckler, M. S. (in prep). Holocene subsidence of the Ganges-Brahmaputra Delta.

Granet, M., Chabaux, F., Stille, P., Dosseto, A., France-Lanord, C., and Blaes, E. (2010). U-series disequilibria in suspended river sediments and implication for sediment transfer time in alluvial plains: The case of the Himalayan rivers. *Geochimica et Cosmochimica Acta*, 74(10):2851–2865.

Grant, K., Rohling, E., Bar-Matthews, M., Ayalon, a., Medina-Elizalde, M., Ramsey, C. B., Satow, C., and a.P. Roberts (2012). Rapid coupling between ice volume and polar temperature over the past 150,000 years. *Nature*, 491(7426):744–747.

Grant, K. M., Rohling, E. J., Ramsey, C. B., Cheng, H., Edwards, R. L., Florindo, F., Heslop, D., Marra, F., Roberts, a. P., Tamisiea, M. E., and Williams, F. (2014). Sea-level variability over five glacial cycles. *Nature communications*, 5:5076.

Greb, S. F. and Chestnut, D. R. J. (1996). Lower and lower Middle Pennsylvanian fluvial to estuarine deposition, central Appalachian Basin; effects of eustasy, tectonics, and climate. *Geological Society of America Bulletin*, 108(January):303–317.

Hampson, G., Stollhofen, H., and Flint, S. (1999). A sequence stratigraphic model for the Lower Coal Measures (Upper Carboniferous) of the Ruhr district, north-west Germany. *Sedimentology*, 46(6):1199–1231.

Hartzog, T. R. (2015). *Controls, distribution, and significance of gravel in the Holocene stratigraphy of the Brahmaputra River*. PhD thesis.

Heroy, D. C., Kuehl, S. A., and Goodbred, S. L. (2003). Mineralogy of the Ganges and Brahmaputra Rivers: Implications for river switching and Late Quaternary climate change. *Sedimentary Geology*, 155:343–359.

Hiller, K. (1988). On the petroleum geology of Bangladesh. *Das Geologische Jahrbuch*, D 90:3–32.

Holbrook, J. (2001). Origin, genetic interrelationships, and stratigraphy over the continuum of fluvial channel-form bounding surfaces: An illustration from middle Cretaceous strata, Southeastern Colorado. *Sedimentary Geology*, 144(3-4):179–222.

Holbrook, J. and Schumm, S. A. (1999). Geomorphic and sedimentary response of rivers to tectonic deformation: A brief review and critique of a tool for recognizing subtle epeirogenic deformation in modern and ancient settings. *Tectonophysics*, 305:287–306.

Holbrook, J. M. and Bhattacharya, J. P. (2012). Reappraisal of the sequence boundary in time and space: Case and considerations for an SU (subaerial unconformity) that is not a sediment bypass surface, a time barrier, or an unconformity. *Earth-Science Reviews*, 113(3-4):271–302.

Holbrook, J. M., Willis, B. J., and Bhattacharya, J. (2003). The evolution of allocyclicity and autocyclicity as sedimentary concepts. In *AAPG Annual Convention*, volume 3, Salt Lake City, Utah.

Hoque, M., McArthur, J., and Sikdar, P. (2014). New resources of low-arsenic groundwater in the Bengal Basin for arsenic mitigation. *Hydrogeology Journal*, (434).

Hoque, M., McArthur, J., and Sikdar, P. K. (2012). The palaeosol model of arsenic pollution of groundwater tested along a 32 km traverse across West Bengal, India. *The Science of the total environment*, 431:157–165.

Hu, G., Yi, C. L., Zhang, J. F., Liu, J. H., and Jiang, T. (2015). Luminescence dating of glacial deposits near the eastern Himalayan syntaxis using different grain-size fractions. *Quaternary Science Reviews*, 124:124–144.

Huang, S.-Y. Y., Chen, Y.-G. G., Burr, G. S., Jaiswal, M. K., Lin, Y. N., Yin, G., Liu, J., Zhao, S., and Cao, Z. (2014). Late Pleistocene sedimentary history of multiple glacially dammed lake episodes along the Yarlung-Tsangpo river, southeast Tibet. *Quaternary Research (United States)*, 82(2):430–440.

Irion, G., de Mello, J. A. S. N., Morais, J., Piedade, M. T. F., Junk, W. J., and Garming, L. (2010). Development of the Amazon Valley During the Middle to Late Quaternary: Sedimentological and Climatological Observations. In Junk, W. J., editor, *Amazonian Floodplain Forests: Ecophysiology, Biodiversity and Sustainable Management*, chapter 2.

Islam, S. (2012). Women and girls: Invisible force of resilience.

Japan International Cooperation Agency (1976). Vol. 6: Geology and stone material, Part 1: Geology, excerpt. Technical report, Japan International Cooperation Agency, Tokyo.

Jerolmack, D. J. and Paola, C. (2010). Shredding of environmental signals by sediment transport. *Geophysical Research Letters*, 37(19):1–5.

Johnson, S. Y. and Alam, A. M. N. (1991). Sedimentation and tectonics of the Sylhet trough, Bangladesh. *Geological Society of America Bulletin*, 103:1513–1527.

Kayal, J., Arefiev, S., and Barua, S. (2006). Shillong plateau earthquakes in northeast India region: complex tectonic model. *Current Science*, 91(1):109–114.

Khan, S. R. and Islam, B. (2008). Holocene stratigraphy of the lower Ganges-Brahmaputra river delta in Bangladesh. *Frontiers of Earth Science in China*, 2(4):393–399.

Kim, W. (2011). Decoupling allogenic forcing from autogenic processes: Experimental geomorphology and stratigraphy.

Kraus, M. J. (1999). Paleosols in clastic sedimentary rocks: their geologic applications. *Earth-Science Reviews*, 47(1-2):41–70.

Kudrass, H. R., Hofmann, A., Doose, H., Emeis, K., and Erlenkeuser, H. (2001). Modulation and amplification of climatic changes in the Northern Hemisphere by the Indian summer monsoon during the past 80 k.y. *Geology*, 29:63–66.

Lang, K. A., Huntington, K. W., and Montgomery, D. R. (2013). Erosion of the Tsangpo Gorge by megafloods, Eastern Himalaya. *Geology*, 41(9):1003–1006.

Larson, T., Howe, M., Steckler, M., Seeber, L., Kim, W.-Y., and Akhter, S. H. (2015). Determining crustal structure of Bangladesh using seismological techniques. In *American Geophysical Union Fall Meeting Scientific Program*, San Francisco, CA.

Leeder, M. R. (2011). *Sedimentology and sedimentary basins: From turbulence to tectonics*. John Wiley & Sons, Ltd, 2nd edition.

Li, Q., Lu, L., and Straub, K. M. (2016). Storage thresholds for relative sea-level signals in the stratigraphic record. *Geology*, 44(3):179–182.

Liu, Z., Shen, F., Zhu, X., Li, F., and Tan, M. (2015). Formation Conditions and Sedimentary Characteristics of a Triassic Shallow Water Braided Delta in the Yanchang Formation, Southwest Ordos Basin, China. *Plos One*, 10(6):e0119704.

Lupker, M., France-Lanord, C., Galy, V., Lavé, J., and Kudrass, H. R. (2013). Increasing chemical weathering in the Himalayan system since the Last Glacial Maximum. *Earth and Planetary Science Letters*, 365:243–252.

Martin, J., Cantelli, A., Paola, C., Blum, M. D., and Wolinsky, M. (2011). Quantitative Modeling of the Evolution and Geometry of Incised Valleys. *Journal of Sedimentary Research*, 81(1):64–79.

McArthur, J., Ravenscroft, P., Banerjee, D., Milsom, J., Hudson-Edwards, K., Sengupta, S., Bristow, C., Sarkar, A., Tonkin, S., and Purohit, R. (2008). How paleosols influence groundwater flow and arsenic pollution: A model from the Bengal Basin and its worldwide implication. *Water Resources Research*, 44(11):30.

Métivier, F., Gaudemer, Y., Tapponnier, P., and Klein, M. (1999). Mass accumulation rates in Asia during the Cenozoic. *Geophysical Journal International*, 137(2):280–318.

Miall, A. (2014). *Fluvial Depositional Systems*. Springer International Publishing, Switzerland.

Miall, A. D. (1985). Architectural-element analysis: A new method of facies analysis applied to fluvial deposits. *Earth-Science Reviews*, 22(4):261–308.

Miall, A. D. (2000). *Principles of Sedimentary Basin Analysis*. Springer-Verlag, Heidelberg, Germany, 3rd edition.

Milana, J. P. and Tietze, K. W. (2002). Three-dimensional analogue modelling of an alluvial basin margin affected by hydrological cycles: Processes and resulting depositional sequences. *Basin Research*, 14(3):237–264.

Milliman, J. D. and Meade, R. H. (1983). World-wide delivery of river sediment to the oceans. *The Journal of Geology*, 91(1):1–21.

Milliman, J. D. and Syvitski, J. P. M. (1992). Geomorphic/Tectonic Control of Sediment Discharge to the Ocean: The Importance of Small Mountainous Rivers. *The Journal of Geology*, 100(5):525–544.

Mitra, S., Priestley, K., Bhattacharyya, A. K., and Gaur, V. K. (2005). Crustal structure and earthquake focal depths beneath northeastern India and southern Tibet. *Geophysical Journal International*, 160(1):227–248.

Molnar, P. (1987). The Distribution of Intensity Associated With the Great 1897 Assam Earthquake and Bounds on the Extent of the Rupture Zone. *Geological Society of India*, 30(1):13–27.

Montgomery, D. R., Hallet, B., Yuping, L., Finnegan, N., Anders, A., Gillespie, A., and Greenberg, H. M. (2004). Evidence for Holocene megafloods down the Tsangpo River gorge, southeastern Tibet. *Quaternary Research*, 62(2):201–207.

Morgan, J. P. and McIntire, W. G. (1959). Quaternary Geology of the Bengal Basin, East Pakistan and India. *Bulletin of the Geological Society of America*, 70(March):319–342.

Najman, Y., Bracciali, L., Parrish, R. R., Chisty, E., and Copley, A. (2016). Evolving strain partitioning in the Eastern Himalaya: The growth of the Shillong Plateau. *Earth and Planetary Science Letters*, 433:1–9.

NASA Modis Rapid Response Team (2007). Floods in Bangladesh.

Nittrouer, C. and Driscoll, N. (1999). Source to Sink. *MARGINS Newsletter 3*, pages 2–3.

Oldham, R. (1899). Report of the great earthquake of12th June, 1897. *Memoirs of the Geological Survey of India*, 29.

Owen, L. A., Finkel, R. C., and Caffee, M. W. (2002). A note on the extent of glaciation throughout the Himalaya during the global Last Glacial Maximum. *Quaternary Science Reviews*, 21(1-3):147–157.

Pate, R. D. (2008). *Multiple-proxy records of delta evolution and dispersal system behavior: fluvial and coastal borehole evidence from the Bengal Basin, Bangladesh*. M.sci. thesis, Vanderbilt University.

Patrick, M. (2016). *Co-evolution of Arsenic and Stratrigraphy in Ganges-Brahmaputra lower delta plain*. Msc, Vanderbilt University.

Pickering, J. L., Goodbred, S. L., Reitz, M. D., Hartzog, T. R., Mondal, D. R., and Hossain, M. S. (2014). Late Quaternary sedimentary record and Holocene channel avulsions of the Jamuna and Old Brahmaputra River valleys in the upper Bengal delta plain. *Geomorphology*, 227:123–136.

Ponce, V. M. (1989). *Engineering Hydrology, Principles and Practices*. Prentice Hall.

Posamentier, H. W. (2001). Lowstand alluvial bypass systems: Incised vs. unincised. *AAPG Bulletin*, 85(10):1771–1793.

Posamentier, H. W., Jervey, M. T., and Vail, P. (1988). Eustatic Controls on Clastic Deposition I—Conceptual Framework. In *Sea-Level Changes: An Integrated Approach*, number 42, pages 109–124. SEPM Special Publication.

Posamentier, H. W. and Vail, P. R. (1988). Eustatic Controls on Clastic Deposition II — Sequence and Systems Tract Models. In *Sea-Level Changes: An Integrated Approach*, number 42, page 918985. SEPM Special Publication.

Prell, W. L. and Kutzbach, J. E. (1987). Monsoon variability over the past 150,000 years. *Journal of Geophysical Research*, 92(D7):8411.

Railsback, L. B., Gibbard, P. L., Head, M. J., Voarintsoa, N. R. G., and Toucanne, S. (2015). An optimized scheme of lettered marine isotope substages for the last 1.0 million years, and the climatostratigraphic nature of isotope stages and substages. *Quaternary Science Reviews*, 111(0):94–106.

Rajendran, C. P., Rajendran, K., Duarah, B. P., Baruah, S., and Earnest, A. (2004). Interpreting the style of faulting and paleoseismicity associated with the 1897 Shillong, northeast India, earthquake: Implications for regional tectonism. *Tectonics*, 23(4):n/a–n/a.

Reinfelds, I. and Bishop, P. (1998). Palaeohydrology, Palaeodischarges and Palaeochannel Dimensions: Research Strategies for Meandering Alluvial Rivers. *Palaeohydrology and Environmental Change*, (i):27–42.

Rennell, J. and Dury, A. (1776). An actual survey, of the provinces of Bengal, Bahar. Laurie & Whittle, London.

Robinson, R. A. J., Brezina, C. A., Parrish, R. R., Horstwood, M. S. A., Bird, M. I., Walters, A. S., and Oliver, G. J. H. (2013). Large rivers and orogens: The evolution of the Yarlung Tsangpo–Irrawaddy system and the eastern Himalayan syntaxis. *Gondwana Research*, 26(1):112–121.

Roden, J. (1998). *The Sedimentology and Dynamics of Mega-Dunes, Jamuna River, Bangladesh.* Phd, University of Leeds.

Rogers, K. G., Goodbred, S. L., and Mondal, D. R. (2013). Monsoon sedimentation on the 'abandoned ' tide-influenced Ganges-Brahmaputra delta plain. *Estuarine, Coastal and Shelf Science*, pages 1–13.

Romans, B. W., Castelltort, S., Covault, J. A., Fildani, A., and Walsh, J. P. (2014). Environmental signal propagation in sedimentary systems across timescales. *Earth-Science Reviews*, 153:7–29.

Romans, B. W. and Graham, S. A. (2011). A Deep-Time Perspective of Land-Ocean Linkages in the Sedimentary Record. *Annual Review of Marine Science*, 5(1):69–94.

Rüber, L., Britz, R., Kullander, S. O., and Zardoya, R. (2004). Evolutionary and biogeographic patterns of the Badidae (Teleostei: Perciformes) inferred from mitochondrial and nuclear DNA sequence data. *Molecular Phylogenetics and Evolution*, 32(3):1010–1022.

Rubin, D. M. and McCulloch, D. S. (1980). Single and superimposed bedforms: a synthesis of San Francisco Bay and flume observations. *Sedimentary Geology*, 26(1-3):207–231.

Rudoy, A. N. and Baker, V. R. (1993). Sedimentary effects of cataclysmic late Pleistocene glacial outburst flooding, Altay Mountains, Siberia. *Sedimentary Geology*, 85(1-4):53–62.

Sarkar, A., Sengupta, S., McArthur, J. M., Ravenscroft, P., Bera, M. K., Bhushan, R., Samanta, A., and Agrawal, S. (2009). Evolution of Ganges-Brahmaputra western delta plain: Clues from sedimentology and carbon isotopes. *Quaternary Science Reviews*, 28:2564–2581.

Schumm, S. A. (1977). *The Fluvial System*. John Wiley & Sons, Inc., New York.

Schumm, S. A., Dumont, J. F., and Holbrook, J. M. (2000). *Active Tectonics and Alluvial Rivers*. Cambridge University Press, New York, N.Y.

Schumm, S. A. and Ethridge, F. G. (1994). Origin, evolution, and morphology of fluvial valleys. In *Incised-valley Systems: Origin and Sedimentary Sequences*, number 51. SEPM Special Publication.

Shanley, K. and McCabe, P. (1994). Perspectives on the sequence stratigraphy of continental strata. *AAPG bulletin*.

Siddall, M., Rohling, E. J., Almogi-Labin, A., Hemleben, C., Meischner, D., Schmelzer, I., and Smeed, D. A. (2003). Sea-level fluctuations during the last glacial cycle. *Nature*, 423(6942):853–858.

Sincavage, R., Pickering, J. L., and Goodbred, S. L. (in review). Holocene Brahmaputra River path selection and variable sediment bypass as indicators of fluctuating hydrologic and climate conditions in Sylhet Basin, Bangladesh.

Sincavage, R., Wilson, C., Liang, M., Passalacqua, P., and Goodbred, S. L. (2015). Comparing morphologic and stratigraphic field data from a tectonic basin on the Ganges-Brahmaputra River delta with results from a reduced-complexity model for river delta formation. In *Community Surface Dynamics Modeling System Annual Meeting*.

Singh, S. K., Kumar, A., and France-lanord, C. (2006). Sr and 87Sr/86Sr in waters and sediments of the Brahmaputra river system: Silicate weathering, CO2 consumption and Sr flux. *Chemical Geology*, 234:308–320.

Sømme, T. O., Helland-Hansen, W., Martinsen, O. J., and Thurmond, J. B. (2009). Relationships between morphological and sedimentological parameters in source-to-sink systems: A basis for predicting semi-quantitative characteristics in subsurface systems. *Basin Research*, 21(4):361–387.

Song, B., Li, Z., Saito, Y., Okuno, J., Lu, A., Hua, D., Li, J., Li, Y., and Nakashima, R. (2013). Initiation of the Changjiang (Yangtze) delta and its response to the mid-Holocene sea level change. *Palaeogeography, Palaeoclimatology, Palaeoecology*, 388:81–97.

Srivastava, P., Bhakuni, S. S., Luirei, K., and Misra, D. K. (2009). Morpho-sedimentary records at the Brahmaputra River exit , NE Himalaya : climate – tectonic interplay during the Late Pleistocene – Holocene. *Journal of Quaternary Science*, 24(July 2008):175–188.

Stanley, D. J. and Hait, A. (2000). Holocene depositional patterns, neotectonics, and Sundarban mangroves in the western Ganges-Brahmaputra delta. *Journal of Coastal Research*, 16(1):26–39.

Steckler, M. S., Mondal, D. R., Akhter, S. H., Seeber, L., Feng, L., Gale, J., Hill, E. M., and Howe, M. (2016). Locked and loading megathrust linked to active subduction beneath the Indo-Burman Ranges. *Nature Geoscience*, (July).

Stouthamer, E. and Berendsen, H. J. (2007). Avulsion: The relative roles of autogenic and allogenic processes. *Sedimentary Geology*, 198(3-4):309–325.

Strong, N. and Paola, C. (2008). Valleys That Never Were: Time Surfaces Versus Stratigraphic Surfaces. *Journal of Sedimentary Research*, 80(1):4–5.

Stuiver, M. and Reimer, P. (1993). Extended 14C data base and revised CALIB 3.0 14C age calibration program. *Radiocarbon*, 35:215–230.

Syvitski, J. P. M., Vo, C. J., Kettner, A. J., and Green, P. (2005). Impact of humans on the flux of terrestrial sediment to the global coastal ocean. *Science*, 308(5720):376–380.

Tennant, E. (2005). *Late Quaternary climage and provenance signals of the Ganges-Brahmaputra Delta Plain, Bangladesh*. Hons. thesis, William and Mary.

Thiel, C., Buylaert, J. P., Murray, A., Terhorst, B., Hofer, I., Tsukamoto, S., and Frechen, M. (2011). Luminescence dating of the Stratzing loess profile (Austria) - Testing the potential of an elevated temperature post-IR IRSL protocol. *Quaternary International*, 234(1-2):23–31.

Uddin, A. and Lundberg, N. (1999). A paleo-Brahmaputra? Subsurface lithofacies analysis of Miocene deltaic sediments in the Himalayan-Bengal system, Bangladesh. *Sedimentary Geology*, 123(3-4):239–254.

Uddin, A. and Lundberg, N. (2004). Miocene sedimentation and subsidence during continent–continent collision, Bengal basin, Bangladesh. *Sedimentary Geology*, 164(1-2):131–146.

Ullah, M. S. (2010). *Provenance Analysis and Depositional System of the Late Quaternary Sediment From the Ganges-Brahmaputra (G-B) Delta, Bangladesh: Application of Strontium Geochemistry*. M.sci. thesis, Vanderbilt University.

Umitsu, M. (1987). Late Quaternary sedimentary environment and landform evolution in the Bengal lowland. *Geographical Review of Japan*, 60:164–178.

Vail, P., Mitchum, Jr., R., and Thompson, III, S. (1977). Seismic stratigraphy and global changes of sea level, part 3: relative changes of sea level from coastal onlap. In *M 26: Seismic Stratigraphy–Applications to Hydrocarbon Exploration*, chapter Seismic st, pages 63–81.

Van Wagoner, J., Posamentier, H., Mitchum, R., Vail, P., Sarg, J., Loutit, T., and Hardenbol, J. (1988). An overview of sequence stratigraphy and key definitions. *The Society of Economic Paleontologists and Mineralogists*, (42):39–45.

Van Wagoner, J. C., Mitchum, R. M., Campion, K. M., and Rahmanian, V. D. (1990). Siliciclastic sequence stratigraphy in well logs, cores, and outcrops: concepts for high-resolution correlation of time and facies. *Methods in Exploration Series 7: Siliciclastic Sequence Stratigraphy in Well Logs, Cores, and Outcrops: Concepts for High-Resolution Correlation of Time and Facies*, (7):III–55.

Veevers, J. J. and Powell, C. M. (1987). Late Paleozoic glacial episodes in Gondwanaland reflected in transgressive-regressive depositional sequences in Euramerica. *Geological Society of America Bulletin*, 98(4).

Velde, B. (1992). *Introduction to Clay Minerals: Chemistry, Origins, Uses and Envronmental Significance*. Chapman & Hall, London, 1st edition.

Vernant, P., Bilham, R., Szeliga, W., Drupka, D., Kalita, S., Bhattacharyya, a. K., Gaur, V. K., Pelgay, P., Cattin, R., and Berthet, T. (2014). Clockwise rotation of the Brahmaputra Valley relative to India: Tectonic convergence in the eastern Himalaya, Naga Hills, and Shillong Plateau. (Figure 1):6558–6571.

Wang, Y., Cheng, H., Edwards, R. L., Kong, X., Shao, X., Chen, S., Wu, J., Jiang, X., Wang, X., and An, Z. (2008). Millennial- and orbital-scale changes in the East Asian monsoon over the past 224,000 years. *Nature*, 451(7182):1090–3.

Wang, Y. J., Cheng, H., Edwards, R. L., An, Z. S., Wu, J. Y., Shen, C. C., and Dorale, J. a. (2001). A high-resolution absolute-dated late Pleistocene Monsoon record from Hulu Cave, China. *Science (New York, N.Y.)*, 294(5550):2345–2348.

Weaver, C. and Pollard, L. (1973). The chemistry of clay minerals. *Developments in Sedimentology*, 15:213.

Weber, M., Wiedicke-Hombach, M., Kudrass, H., and Erlenkeuser, H. (2003). Bengal Fan sediment transport activity and response to climate forcing inferred from sediment physical properties. *Sedimentary Geology*, 155(3-4):361–381.

Williams, L. A. (2014). *Late Quaternary stratigraphy and infilling of the Meghna River valley along the tectonically active eastern margin of the Ganges-Brahmaputra-Meghna delta*. Thesis, Vanderbilt University.

Wilson, C. A. and Goodbred, S. L. (2015). Construction and Maintenance of the Ganges-Brahmaputra-Meghna Delta: Linking Process, Morphology, and Stratigraphy. *Annual Reviews of Marine Science*, 7:67–88.

Wintle, A. G. (1997). Luminescence dating: laboratory procedures and protocols. *Radiation Measurements*, 27(5-6):769–817.

Wittmann, H., von Blanckenburg, F., Maurice, L., Guyot, J. L., Filizola, N., and Kubik, P. W. (2011). Sediment production and delivery in the Amazon River basin quantified by in situ-produced cosmogenic nuclides and recent river loads. *Bulletin of the Geological Society of America*, 123(5):934–950.

Zaitlin, B. A., Dalrymple, R. W., and Boyd, R. (1994). The stratigraphic organization of incised-valley systems associated with relative sea-level change. *SEPM Special Publications*, 51(51):45–60.

Zhu, S., Wu, Z., Zhao, X., and Xiao, K. (2013). Glacial dammed lakes in the Tsangpo River during late Pleistocene, southeastern Tibet. *Quaternary International*, 298:114–122.